A SIMPLE MODEL OF OCEAN-ATMOSPHERE INTERACTIONS IN THE TROPICAL CLIMATE SYSTEM

by Michael A. Kelly

David A. Randall, Principal Investigator

Colorado State University

DEPARTMENT OF ATMOSPHERIC SCIENCE

PAPER NO. **678**

A SIMPLE MODEL OF OCEAN-ATMOSPHERE INTERACTIONS IN THE TROPICAL CLIMATE SYSTEM

by

Michael A Kelly

Research supported by the
National Atmospheric and Space Administration
under Grant number NAG1-1266
and the National Science Foundation
under Grant number ATM-9214981

Department of Atmospheric Science
Colorado State University
Fort Collins, CO

May 1999

Atmospheric Science Paper No. 678

Abstract

A Simple Model of Ocean-Atmosphere Interactions in the Tropical Climate System

The tropical sea surface temperature (SST) distribution strongly modulates the global atmospheric circulation. Although the mechanisms which generate SST anomalies have been the subject of intense scrutiny in recent years [see Neelin et al. (1998) for a review], the steady tropical climate has received much less attention. As a consequence, the dominant physical processes which maintain the steady tropical climate remain poorly understood. The goal of this report is to construct and use a simple, mechanistic box model of the tropical ocean-atmosphere climate system to develop ideas about the interactions among various physical processes which can be tested against observations and results from more sophisticated models.

Efforts to study the steady tropical climate have been aided by the recent emergence of box models. Pierrehumbert (1995) developed a two-box model of the tropical climate in which one box represents the ascending branch of the Hadley/Walker circulation, and the second box represents the subsiding branch. Pierrehumbert used the model to demonstrate the importance of a low-water-vapor region in exporting to space excess heat that is generated by the ascending branch. Later studies using box models have demonstrated the importance of ocean dynamics (Sun and Liu 1996) and low-level stratus clouds (Miller 1997) for regulating SST and the SST gradient. Despite their success in simulating the tropical climate, simplifying assumptions in these box models make conclusions derived from them less than robust. None of the these box models include a momentum budget for the ocean or atmosphere. Each of the box models emphasizes either the ocean or the atmosphere and settles for a highly simplified representation of the other.

We have developed a simple coupled ocean-atmosphere model of the Walker circulation which has separate boxes for the ascending and descending branches of the atmospheric circulation and separate boxes for the Cold Pool, Warm Pool, and undercurrent. This is the first box model to include explicit momentum budgets for the atmosphere and ocean components and to calculate the fractional width of the Warm Pool. The atmospheric model contains an explicit hydrologic cycle, a simplified but physically based radiative transfer

parameterization, and interactive clouds.

We first explored the conditions under which the Warm Pool can establish a radiative-convective equilibrium. Under clear skies, quasi-tropical equilibria occur for realistic prescribed SSTs and wind speeds, but realistic clear-sky equilibria of the tropical ocean-atmosphere system do not occur. If the surface temperature is allowed to vary, the model runs away. When cloud radiative effects are incorporated, the model reaches an unrealistically warm, dry radiative-convective equilibrium. For simulations in which cloud radiative effects are incorporated and realistic, lateral transports of energy and moisture are specified, equilibrium of the ocean-atmosphere system occurs for an SST of 300 K and precipitable water of 40 kg m^{-2}, which is quite realistic. We also demonstrated the sensitivity of the tropopause height and temperature to cloud radiative effects. The tropopause height and temperature are calculated based on the requirement of temperature continuity at the bottom of a two-layer stratosphere in radiative equilibrium. As the cloud optical depth or cloud fraction increase, the upward longwave flux across the tropopause decreases, and so the tropopause temperature decreases and tropopause height increases.

Our results from the fully coupled model indicate that the intensity of the tropical circulation is crucially dependent on the specified cloud fraction in the Warm-Pool region and on the amount and distribution of water vapor above the Cold-Pool boundary layer (CPBL). In response to increasing the cloud fraction above the Warm Pool, a feedback involving the tropopause height slows the Walker circulation. As the cloud fraction over the Warm Pool increases, the altitude of the tropopause increases, and so air is advected to the Cold-Pool region from higher, drier altitudes. The effects of the drier air are to reduce the radiative cooling rate above the CPBL and, therefore, to reduce the subsidence rate. Since the width of the Cold Pool remains approximately constant, a decreased subsidence rate implies a weaker Walker circulation. In order to maintain energy balance in spite of a weaker circulation, the precipitable water over the Warm Pool must increase. The radiative effect of the precipitable water contributes to an increase of SST in the Warm Pool. Our "wet troposphere" experiment shows that the Walker circulation intensifies if air which is advected to the subsiding region originates from a lower altitude in the Warm-Pool region. Because the circulation is more intense, the SST and precipitable water of the Warm Pool must decrease in order to balance the energy and moisture budgets.

Experiments using our ocean model reveal that cold-water upwelling is the dominant mechanism for regulating SST in the Cold Pool. Although the radiative effect of stratus clouds further depress SST, ocean dynamics prevent the mixed-layer temperature from warming by more than 4 K beyond the temperature of the undercurrent.

ACKNOWLEDGMENTS

I thank Professor David A. Randall for his expert advice and never-ending patience during the six years that he has served as my advisor. Professor Randall taught me how to conduct research, demonstrating the ideal blend of knowledge, curiosity, and creativity needed to be a successful scientist. He has a knack for guiding research, while still encouraging academic independence. His ability to ask a series of pertinent questions which lead to a solution is a talent which I seek to emulate. Dr. Randall has been a true mentor for me.

I also thank the other members of my committee: Drs. Graeme L. Stephens, Roland A. Madden, Wayne H. Schubert, Richard H. Johnson, and David A. Krueger. Dr. Stephens guided me in developing a simplified radiative transfer parameterization for the model. His classes and informal discussions led me to appreciate the significance of radiation-climate interactions. Dr. Madden at the National Center for Atmospheric Research assisted with my interpretation of the observations and spent many hours helping me to edit and improve this report. Dr. Schubert recommended mathematical techniques for finding an analytical solution for the model. In several illuminating discussions, Dr. Johnson helped me to evaluate results from my model based on observations from the tropics. Dr. Krueger engaged me in several fruitful discussions about underlying assumptions in the model.

My heartfelt thanks go to my wife, Missy, for her incredible patience and strong encouragement during my research. Not only did she work long hours at her job to support us financially, but she completed most of our household chores. Her hard work and sacrifice inspired me to complete this report; without her, I would not have finished. I must also express my very special gratitude to Rachel, our four-year-old daughter, for allowing me to see the world through her eyes. After her birth, her thirst for knowledge rekindled my enthusiasm for atmospheric science. Although she is too young to realize it, Rachel also sacrificed during my pursuit of a Ph.D. The long hours that Missy and I worked took away from time which we would otherwise have spent with her.

Thanks also to my parents, Keel and Barbara Kelly, for telling me as a child that no accomplishment is beyond my grasp. I thank my Dad for his support and words of encouragement, especially during the last few months of my research. My only regret is that Mom left us before she could share the joy of my completed Ph.D. This report is dedicated to her memory.

Dr. Tommy Jensen, now at the University of Hawaii and formerly at Colorado State University, patiently discussed aspects of physical oceanography and ocean modeling with me. Through formal lectures and informal discussions, Dr. Jensen provided me with the observational and theoretical foundation in oceanography which provides the basis for my understanding of ocean-atmosphere interactions. His expertise and advice during the development of my simplified ocean model were invaluable resources to me.

I also thank the members of our group who contributed to my research: Don Dazlich, Kelley Wittmeyer, Cindy Carrick, Michelle Beckman, Beth White, Cara-lyn Lappen, Todd Ringler, Mark Branson, Kevin Schaefer, and Doug Cripe. Don Dazlich kindly provided his computer subroutines and assisted me with developing and debugging Fortran code. His expertise enabled me to complete this report much sooner than would have been possible otherwise. Kelley Wittmeyer kept my computer running and responded quickly whenever I needed assistance. She devised a way to extract this report from the hard drive of my computer following a system failure. The contributions of Cindy Carrick, Michelle Beckman, and Beth White are too numerous to list, but range from completing the many forms required by the Graduate School to purchasing supplies needed to do our jobs. Without them, research in our group would come to a screeching halt. Scientific discussions with Cara-lyn Lappen helped me to clarify ideas presented in this report. Todd Ringler introduced me to the GRADS plotting program and assisted me with using ECMWF reanalysis data. Suggestions provided by Mark Branson, Kevin Schaefer and Doug Cripe during a dry run of my Ph.D. defense greatly improved my oral presentation and have since been incorporated in this report.

I am also grateful to Paul Ciesielski and John Kleist for their assistance with the TOGA COARE and ASTEX datasets, respectively. Paul Ciesielski spent his valuable time and effort in discussions with me about the limitations and biases of TOGA COARE data. His knowledge and insight have helped me immensely.

This research was sponsored under the NASA grant NAG 1-1266 and the National Science Foundation grant ATM-9214981.

Table of Contents

CHAPTER 1

Introduction

1.1 Motivation

The tropical sea surface temperature (SST) distribution strongly affects the global atmospheric circulation. Many studies have explored the processes that cause SST anomalies to develop in the tropical Pacific ocean (Cane and Zebiak 1985; Zebiak and Cane 1987; Battisti 1988; Battisti and Hirst 1989; Neelin and Jin 1993; Anderson and McCreary 1985; Schopf and Suarez 1988: Yamagata and Masumoto 1989; Graham and White 1990; and many others). Nevertheless, the physical processes that maintain the time-mean tropical climate are poorly understood. The goal of this report is to develop and apply a simple, semi-analytical model of the tropical circulation which then can be tested against observations and more sophisticated models. Below we introduce the basic characteristics of the tropical climate system and describe relevant previous studies, focusing on the issues which we hope to investigate in the course of this report.

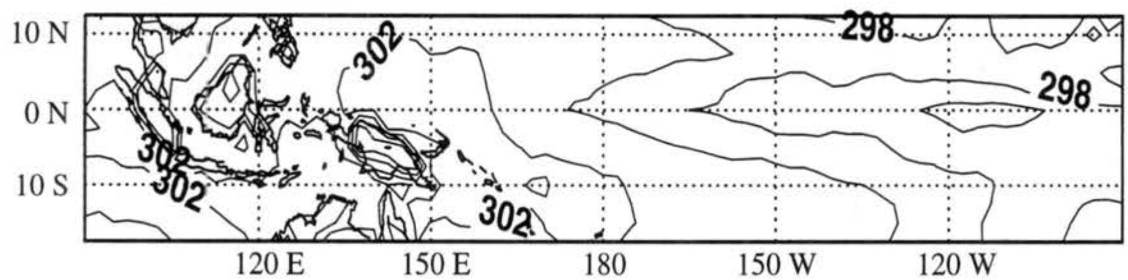

FIGURE 1.1: Tropical skin temperature for January 1989 from the ECMWF reanalysis dataset obtained from NCAR. Resolution for this dataset is 2.5° and contour interval is 2 K.

Figure 1.1 shows that an SST maximum occurs over the tropical region centered on 120° E, and for this reason the region is known as the tropical Warm Pool (WP). The cold tongue refers to a band of relatively cold waters over the equator that stretches from South America westward to near 160° E. Although a noticeable SST gradient exists along and across the cold tongue, the temperature variation is still much smaller than that which is generally observed in extratropical or polar regions of the globe. The tropical climate is characterized by sea surface and horizontal air temperature gradients which are weak compared to the corresponding mid-latitude gradients. As explained by Charney (1963), for cloud-free regions of the tropics, pressure and temperature gradients must be small compared to those of midlatitudes.

The distribution of tropical convection is strongly related to both the local SST and the SST gradient. The tropical-Pacific WP is a region of intense deep convection. In Fig. 1.2, regions in which the outgoing longwave radiation (OLR) is less than 225 W m^{-2} can be identified as areas of frequent convection (Webster 1994). The OLR threshold corresponds to a monthly mean emission temperature of 250 K. Due to longwave trapping by optically thick anvil clouds, which are produced by deep convection, the OLR is reduced and threshold values of OLR can therefore be used as surrogates to infer the presence of convection. From the figure, we see that convection occurs throughout the WP, and in the South Pacific convergence zone (SPCZ). On the other hand, the OLR is generally larger than 275 W m^{-2} across the equatorial cold tongue, indicating that convection is infrequent there.

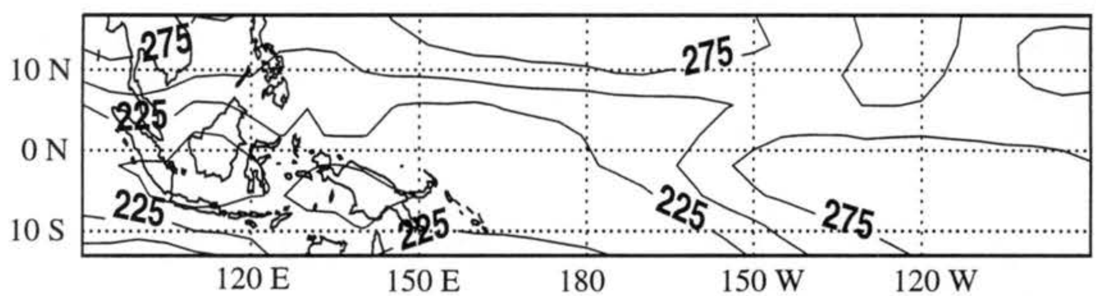

FIGURE 1.2: Tropical OLR for January averaged over 1985 to 1988. Daily means from the Earth Radiation Budget Experiment (ERBE) were averaged and interpolated onto a 5° × 4° (longitude-latitude) grid. The units are W m^{-2}.

The tropical atmosphere is not a slave to the SST distribution, because atmospheric processes can influence the SST distribution. In the eastern tropical Pacific, for instance, stratus clouds in the boundary layer intercept sunlight and strongly reduce the heat flux into the ocean below (e.g. Hartmann et al. 1992). In this way, the atmosphere helps to maintain the cooler SSTs of the eastern Pacific. Stratus clouds form preferentially over cold water (Klein and Hartmann 1993), so a positive feedback is at work here (Ma et al. 1996). Latent heat exchange between the ocean and atmosphere is influenced by the surface relative humidity and the surface winds. For fixed relative humidity and SST, the evaporative cooling of the ocean increases as the surface wind stress increases. The winds also influence the SST distribution by generating cold-water upwelling in the eastern Pacific, and along the equator in the eastern and central Pacific. The equatorial cold tongue is an example of an effect of cold-water upwelling on the SST distribution.

Despite our knowledge of these and other processes, a satisfactory understanding of the tropical climate has not yet been attained. How is the time-averaged SST distribution maintained? What are the dominant mechanisms which maintain the tropical SST distribution? How do clouds affect the SST distribution? What characteristics of the tropical climate produce the east-west Walker circulation (formally defined in the next section)? What effects does the Walker circulation have on tropical climate? What factors determine the intensity and width of the Walker circulation?

Previous investigators have dealt with some of these questions. We now review these earlier studies in quasi-chronological order, so as to show the evolution of the various theories and hypotheses. We present findings from several observational studies in order to describe the tropical climate and to provide an objective basis for assessing our model's performance. In general, we consider the reanalysis dataset from the European Centre for Medium Range Weather Forecasting (ECMWF), obtained from the National Center for Atmospheric Research (NCAR), as truth, although there are well-known biases (Sohn 1994; Heckley 1985) in fields such as specific humidity. When ECMWF data are presented, we describe any known biases which cause the analyses to be unrealistic. Finally, and most importantly, we critically review the various hypotheses and theories put forth in the literature to explain and describe the average tropical climate, with an emphasis on their weaknesses and on the remaining unanswered questions. Because we are presenting the formulation and results from a coupled ocean-atmosphere box model in Chapters 3 and 4, we concentrate on the results from recent studies which used similar box models.

1.2 Previous studies

An early description of the Walker circulation is given by Troup (1965), who described a toroidal circulation spanning the equatorial Pacific ocean. Troup presented data in which the mean 500-300 mb geopotential thickness for 120-140° E was 20 m greater than that for 80-100° W. By the thermal wind equation (e.g. Holton 1992), this east-west thickness difference implies that the meridional geostrophic wind must decrease with height. Because the vertical gradient of meridional geostrophic wind is related to the zonal temperature gradient by the thermal wind relation, it can be shown that the zonal temperature gradient drives an ascending ageostrophic flow from the warm region to cold region. As Troup noted, the resulting distribution of ageostrophic motions is complicated, because it depends on the varying temperature differences and vertical motions across the different regions of the circulation. Troup found that westerly flow between 500 and 200 mb originates over the Indonesian region and terminates over the central and eastern equatorial Pacific; this upper-level flow is balanced by an easterly return flow, which he described as frictional ageostrophic flow down the pressure gradient. He noted that descent occurs over the central and eastern Pacific, while ascent occurs over the western Pacific and Indonesia.

Bjerknes (1969) proposed the term "Walker cell" in honor of Sir Gilbert Walker, to describe an overturning in the equatorial plane with rising motion in the western Pacific and sinking motion in the eastern Pacific. He theorized that when the equatorial cold tongue is well developed, the cool, dry air just above the surface cannot ascend to join the Hadley circulation. Instead, it is heated and moistened as it moves westward until it finally undergoes large-scale moist-adiabatic ascent over the WP. If there were no mass exchange with adjacent latitudes, a simple circulation would develop in which the flow is easterly at low levels and westerly at upper levels. Furthermore, the ascending motion in the west would adjust so as to cover a smaller surface area than the descending motion, which develops as a result of the balance between subsidence warming and radiative cooling. Mass continuity demands that the region of intense rising motion must occupy a smaller area than the region of weak sinking motion. When meridional mass exchange is considered, this simple picture has to be altered, because absolute angular momentum is exported to adjacent latitudes. Under steady-state conditions, the flux divergence of angular momentum at the equator must be balanced by an easterly surface wind stress. Thus surface easterlies on the equator are stronger than those imposed by the Walker circulation. The net result is that a thermally driven Walker cell is imposed on a background of easterly flow, the intensity of which depends on the strength of the angular momentum flux divergence. Apparently, Bjerknes was unaware of the paper by Troup (1965), as no reference was made to the earlier study.

Newell et al. (1974) (hereafter NKVB) defined the Walker circulation to be the asymmetric part of the east-west tropical circulation, and the Hadley circulation to be the zonally symmetric part of the tropical circulation. NKVB discussed the zonal asymmetry of vertical velocity, precipitation, cloudiness, and SST. In particular, they observed that upward motion occurs preferentially over tropical continental regions and downward motion occurs preferentially over the tropical oceans. Noting a circulation similar to that depicted in Fig. 1.3, NKVB identified the region bordered by ascending air over the equatorial west Pacific and descending air over the equatorial east Pacific as the Walker circulation.

Figure 1.3 presents scaled u-ω wind vectors in the equatorial x-z plane for January 1989 from the ECMWF reanalysis dataset. We define u and ω as the zonal and vertical components of velocity in pressure coordinates. The vertical velocity was scaled by -300 m Pa^{-1} in order to account for the much smaller speed of the vertical motions as compared with the horizontal motions.

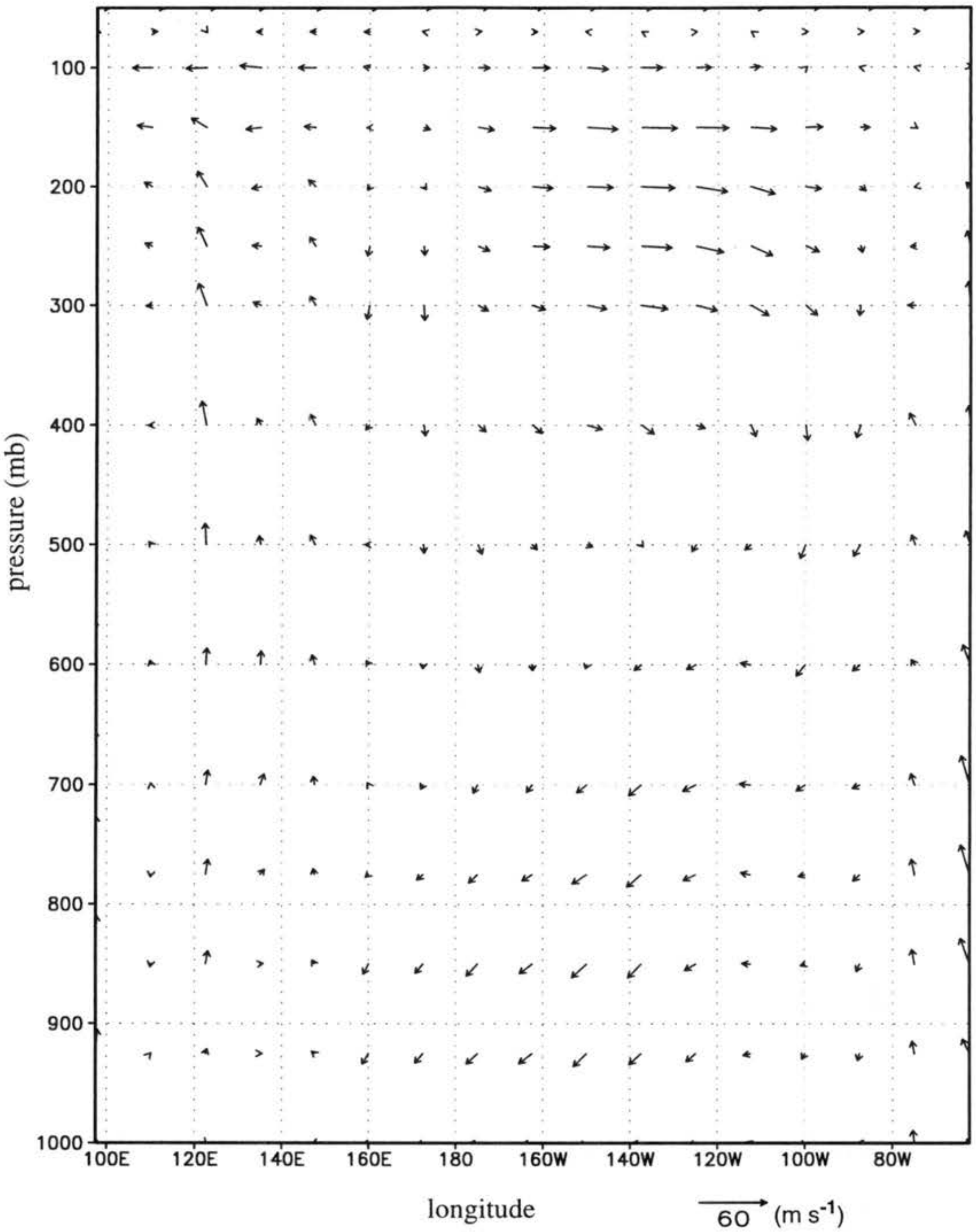

FIGURE 1.3: Monthly mean u-ω wind vectors in units of m s^{-1} on the Equator for January 1989 from the ECMWF reanalysis dataset stored at NCAR. The ω values, which were originally in units of Pa s^{-1}, were scaled by -300 m Pa^{-1}.

In the figure, we see that the rising branch of the Walker circulation is centered on 125° E, while the sinking branch is spread across a wide region between the dateline and 80° W.

Within this region, westerlies are present between 100 and 400 mb, and easterlies are confined below 700 mb. Upper-level easterly flow exists between 120˚E and 160˚E, and appears to be associated with the Australian winter monsoon. The flow is quite weak between 400 and 700 mb. NKVB also described additional cells in the equatorial plane which Bjerknes did not mention. Their data (not shown) indicated the presence of Walker-like circulations over the tropical Atlantic ocean, near the African sector, and the western branch of the Pacific Walker cell.

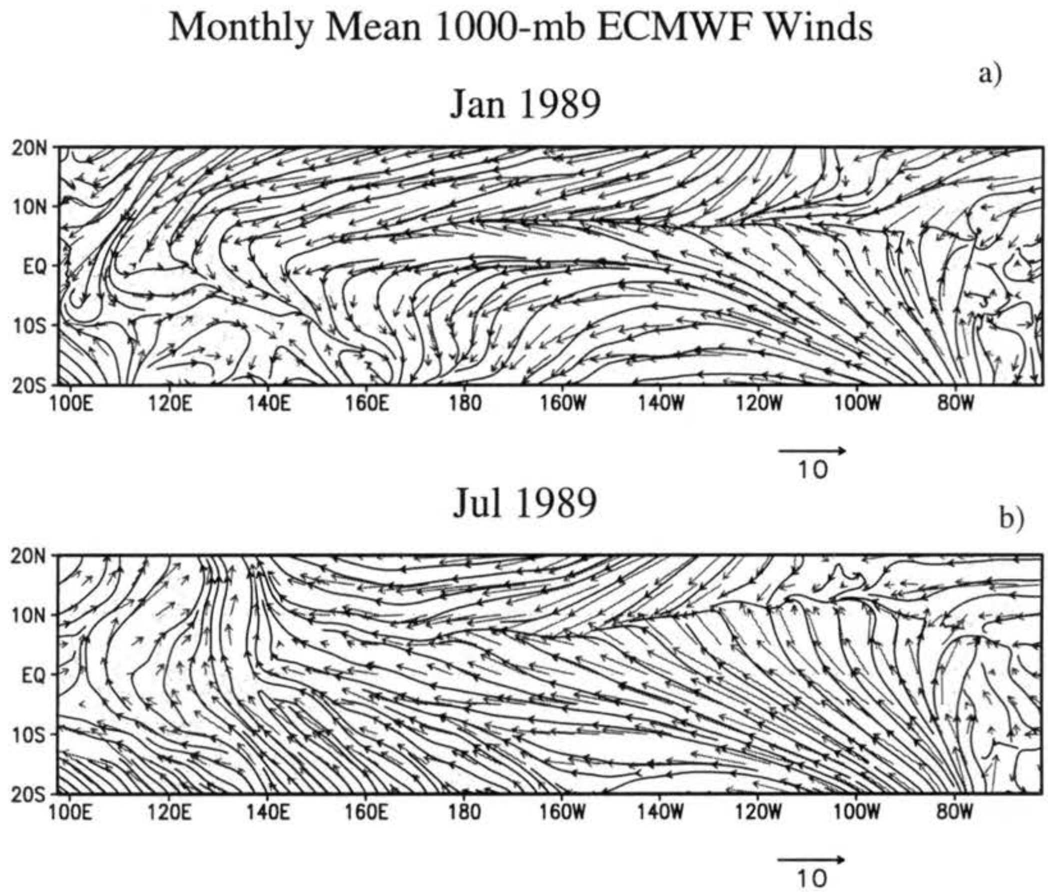

FIGURE 1.4: Mean streamlines and horizontal wind vectors for the tropical Pacific at 1000 mb for a) Jan 1989 and for b) July 1989. The wind vectors are in units of m s^{-1}. ECMWF reanalysis data were obtained from NCAR.

Figure 1.4 shows that the 1000-mb winds above the tropical Pacific (between 10˚ N and 10˚ S) have an easterly component in both solstitial seasons. For both seasons, easterly flow near the equator occurs west of about 90˚ W. In January, the easterly component is particularly strong above the central equatorial Pacific, and convergence is evident along the ITCZ near 8˚ N. In July, a notable characteristic is the strong cross-equatorial flow in the eastern Pacific. The zone of convergence at 1000 mb during the northern hemisphere (NH) summer has moved north of 10° N over the eastern Pacific. At the latitude of the ITCZ, the easterly fetch originates to the east of Central America during both seasons. If we consider the Walker circulation to occur at near-equatorial latitudes, then easterly flow at 1000 mb cannot originate over the continents because the mountains of Peru act as a vertical barrier on the eastern boundary of the ocean. However, we note that a strong southerly component is evident during both seasons.

A recent study by Newell et al. (1996; hereafter N96) takes issue with some aspects of the traditional Bjerknes-type model of the Walker circulation. N96 compared water-vapor data from the Upper Atmosphere Research Satellite (UARS) with upper-air wind data from the ECMWF reanalysis dataset to deduce horizontal and vertical motions in the tropical atmosphere. N96 used ECMWF data between September 17 and October 22, 1991 and February 7 to March 14, 1994, respectively, to correspond with the NASA Global Tropospheric Experiment, Pacific Exploratory Mission.

Both the UARS-derived water vapor and ECMWF-diagnosed vertical velocities presented in N96 indicate regions of strong ascending motion over the western Pacific WP and SPCZ. The main regions of sinking motion, which are located off South America and extend westward to the dateline just south of the equator, exhibit little seasonal movement between experiment periods. For comparison, we present in Fig. 1.5 the vertical velocity fields at 300 mb from the ECMWF reanalysis dataset for the solstitial months. Although our plots capture more of the variation associated with the seasonal cycle, the zones of vertical motion described by N96 are consistent with those depicted in Fig. 1.5. During January 1989, centers of ascending motion were located near 145° E at latitudes 5° N and 5° S. The SPCZ was clearly evident during January 1989 with a large region of ascending motion that extends southeastward from 145° E to 160° W. A region of strong sinking motion straddles the equator and extends eastward from 160° E. During July 1989, the ascending region remains fixed at 145° E, but the NH and southern hemisphere (SH) centers of ascending motion have merged on the equator. During the NH summer, the ITCZ is well developed at 5° N, and so the zone of sinking motion has slipped southward from its January position, particularly the zone over the central Pacific. Despite differences associated with the seasonal cycle, the general pattern is one in which ascending motion dominates over the tropical western Pacific, while sinking motion occurs over the tropical central and eastern Pacific. As noted by N96, this pattern generally fits the Bjerknes model of the Walker circulation, although the pattern varies with the seasonal cycle.

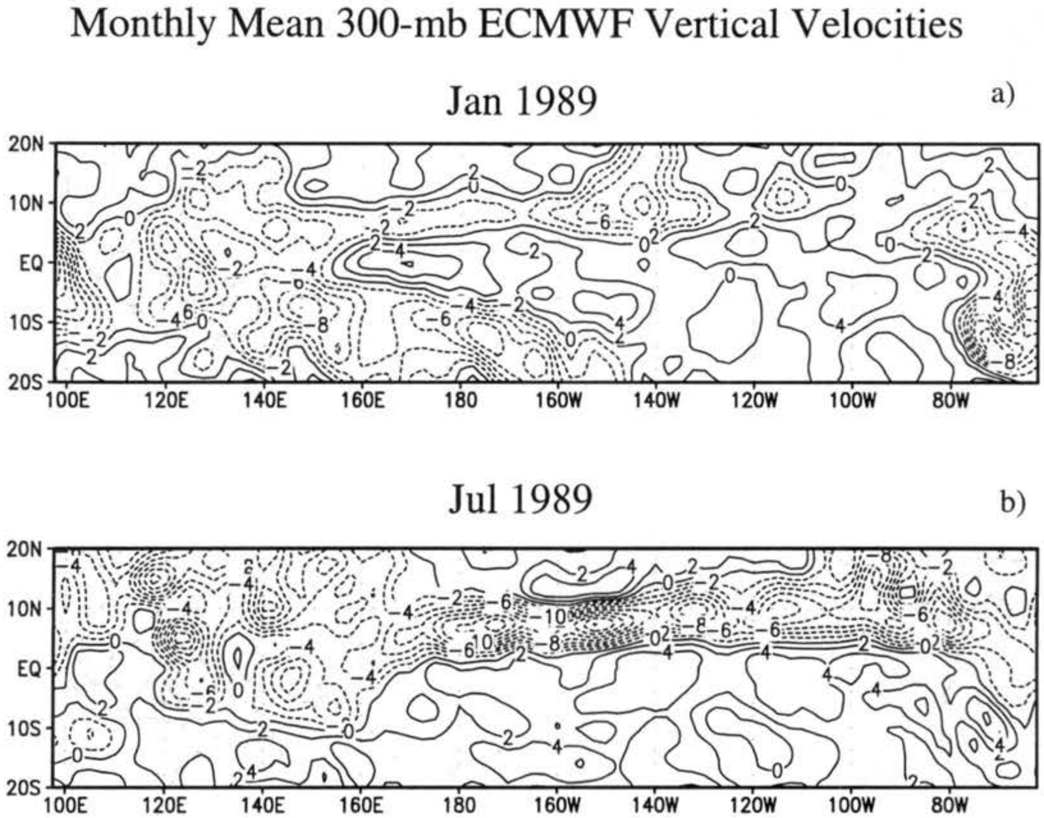

FIGURE 1.5: Contour plot of mean vertical velocity at 300 mb (units, 10^{-2} Pa s^{-1}) from the ECMWF reanalysis dataset for a) January 1989 and b) July 1989. Contour interval is 2×10^{-2} Pa s^{-1}; negative contours are dashed. Data were obtained from NCAR.

Dividing the ECMWF horizontal wind data into rotational and divergent parts, N96 showed the divergent part of the wind field to be generally consistent with the regions of vertical motion described above, but the rotational part to be at odds with the traditional conceptual model of the Walker circulation. With their analysis of the rotational wind field, N96 showed that easterlies extend across the equatorial Pacific from South America to 170° W and 160° E during the first and second experiment periods. West of 160° E, the low-level equatorial winds are very weak. However, easterlies span the equatorial Pacific at 5° S and 5° N during the first and second experimental periods, respectively. These observations indicate that the Walker circulation is not always located at the equator, but rather shifts between hemispheres over relatively short periods. Figure 1.4 shows that monthly mean easterlies for January and July 1989 are present for a 5°-latitude belt centered on the equator across the entire Pacific ocean.

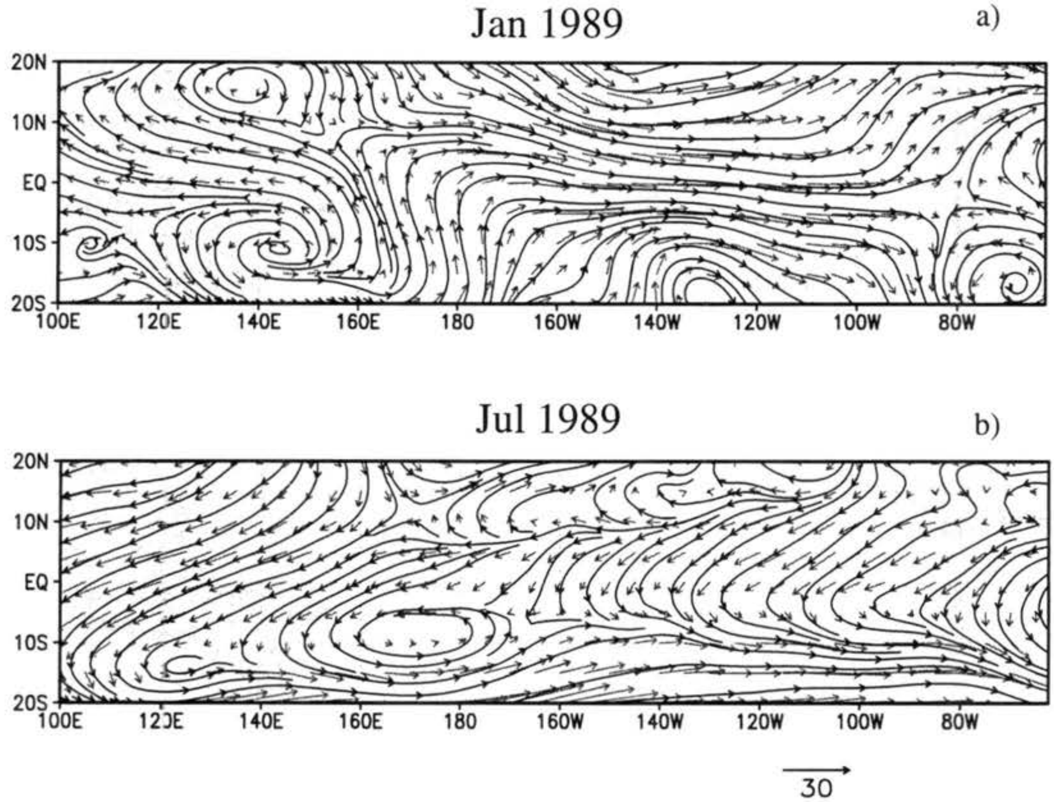

FIGURE 1.6: Same as for Fig. 1.4, except that the pressure level is 200 mb.

N96 also discussed the upper branch of the Walker circulation. West of the dateline, data presented in the form of a streamline-vector plot indicate that zonal winds over the equator were easterly during the second experiment period. This is consistent with data presented in Fig. 1.6a and agrees with our interpretation discussed in the preceding paragraph. Because a region of strong rising motion occurs offshore to the east of Indonesia, upper-level westerly flow of the Walker cell should occur to the east of the rising motion. This is precisely what we see in the figure, although comparing Fig. 1.4 and Fig. 1.6, we note that the low-level region of easterlies extends farther westward than the upper-level region of westerlies.

Figure 1.6b (and plots in N96) present a more complicated picture. During July 1989 and the first experiment period, the upper-level flow above the equatorial Pacific ocean is entirely from the east. In the NH, weak westerly flow appears between 170° W and 140° W poleward of 15° N. In the SH, a westerly component of the wind exists south of 5° S to the east of the dateline. An interpretation would be that no Walker circulation exists in July because upper-tropospheric flow on the equator is easterly. Another interpretation, however, might be that the Walker circulation has migrated southward into the SH. A reexamination of Fig. 1.5b indicates that the zone of downward vertical velocity is confined mainly to the SH, and occurs as far west as 165° W. We note that flow around an anticyclone centered over 5° S, 170° W complicates the zonal circulation, making a simple Walker circulation difficult to isolate in this instance.

Finally, N96 conducted a mass budget analysis of two regions in ascending zones and two regions in descending zones. Based on their analysis, N96 concluded that air enters the descending zones in comparable ratios from the north, south, east, and west borders of the box. This implies that water vapor from convecting regions over South America finds its way into the descending zone. These data show that the Walker circulation as envisioned by Bjerknes is somewhat of an oversimplification.

A study by Cornejo-Garrido and Stone (1977; hereafter CGS) examined the heat balance in the region of the Walker circulation. Having analyzed the various terms of the thermodynamic equation, they concluded that the primary energy balances are

$$w'\partial[\theta]/\partial z \approx Q_L'/c_p, \tag{1.1}$$

$$L\mathcal{E}' = \mathcal{S}'_S - \mathcal{R}'_S, \tag{1.2}$$

for the free troposphere and surface, respectively. The primed quantities denote deviations from a zonal average, the brackets denote a zonally averaged quantity, θ denotes potential temperature, Q_L denotes latent heating per unit mass, $\mathcal{E}$ is the evaporation rate, $\mathcal{S}_S$ is the net downward shortwave radiative flux at the surface, and $\mathcal{R}_S$ is the net upward longwave radiative flux at the surface.

Equation (1.1) states that adiabatic ascent balances positive latent heating anomalies. Based on an analysis in which the radiative fluxes are assumed to vary linearly with temperature, the heating due to radiation is neglected, which we now know to be completely unjustified. Precipitation data from Schutz and Gates (1972) were used to estimate latent heating anomalies as a function of height and longitude at 6° S. The maximum strength of the tropical precipitation anomalies at this latitude is about of 2.5 mm day^{-1}, with a maximum and a minimum near 140° E and 110° W, respectively. CGS approximated the height and longitude variations of the latent heating rate using cosine and sine functions. Consequently, the perturbation vertical velocity that they derived have the same dependencies. At 500 mb, the maximum upward vertical velocity of -18.1 mb day^{-1} occurs near 170° E, while the maximum downward vertical velocity of 17.3 mb day^{-1} occurs near 130° W. The pattern of vertical motion fits well with Bjerknes' conceptual model for the Walker circulation.

Equation (1.2) indicates that evaporative cooling at the surface is balanced by the net radiative flux into the ocean. CGS showed that precipitation anomalies are anti-correlated with evaporation anomalies over the tropical Pacific ocean. This linkage was explained as follows. The net flux of longwave radiation into the ocean tends to be small, and so the surface energy budget is actually a local balance between the shortwave and evaporative fluxes. The cloud fraction usually increases (decreases) as the precipitation rate increases (decreases). Over the western Pacific ocean where precipitation anomalies are positive, the increased cloud cover reduces the shortwave surface heating, and from (1.2), implies a decreased evaporation rate. On the other hand, negative precipitation anomalies lead to an increased evaporation rate over central and eastern regions of the Pacific ocean. Presumably, the evaporation rate changes due to changes of the surface wind stress.

CGS also showed that the large-scale tropical precipitation anomalies are locally an order of magnitude larger than the evaporation anomalies. For a vertically integrated moisture budget, the flux divergence of water vapor must be balanced in a time average by the difference between the evaporation and precipitation rates. Because anomalies of the precipitation rate dominate over those for the evaporation rate, a net moisture export from the eastern Pacific to the western Pacific is indicated. CGS contrasted this result with Bjerknes' hypothesis (1969) who implied that the low-level air of the Walker circulation is heated and moistened *after* it crosses over the WP. Clearly, the modern interpretation of Bjerknes' hypothesis has evolved to allow that the air is continuously moistened as it flows across the Pacific.

Nevertheless, the authors concluded that the driving force behind the Walker circulation is the zonal structure of the precipitation rate, and that these variations are balanced by adiabatic heating/cooling due to sinking/rising motions. In the western Pacific, latent heat release due to intense convection is balanced by adiabatic cooling and ascending motion (Webster 1987). It is the inability of radiative processes to balance the latent heating which requires a tropical circulation. The precipitation rate need not be considered at all in order to determine the vertical velocities over the Cold Pool (CP). In fact, as described later, box models of the tropical climate (Pierrehumbert 1995; Miller 1997; Larson et al. 1999) determine the mass flux over the eastern tropical Pacific from the observed balance between adiabatic sinking and radiative cooling, and neglect precipitation over the CP altogether. It seems strange to conclude that the driving force for the Walker circulation is the zonal variation of the precipitation rate, when the precipitation rate does not have to be considered in calculating the mass flux for the subsiding branch of the circulation. Instead, it has been shown that the circulation is strongly related to SST and to the SST gradient. Over the eastern tropical Pacific where the SST is relatively low, convection is infrequent, and so a balance between radiation and subsidence exists. Over the western tropical Pacific where the SST is high, convection is frequent over regions of large-scale ascending motion. As discussed by Lau et al. (1997), large-scale ascending motion tends to be correlated with regions of high SST. Thus, the SST pattern largely determines the locations and intensities of the Walker circulation. The argument of CGS rests with their assumption that the horizontal distribution of precipitation is given. The connection between the SST pattern and convection was not firmly established, and so CGS did not consider the link between tropical precipitation and the distribution of SST.

Based on the National Centers for Environmental Prediction (NCEP)-NCAR reanalysis dataset and radiosonde reports, Hastenrath (1998) analyzed the large-scale characteristics which contribute to near-equatorial jet streams of 10 m s^{-1}. Two main jet cores were observed. Centered on 1° N, a mid-tropospheric jet is observed over the eastern Pacific near 90° W, although wind speeds in excess of 6 m s^{-1} extend to the dateline. At the 925-mb pressure level, a jet is apparent near 10° N in the central Pacific, between 150° W and the dateline. Analyzing the 600/1000-mb geopotential thickness pattern, Hastenrath found that a low-level trough of geopotential heights exists along the equator. The meridional geopotential gradient is strongest at 625 mb over the eastern Pacific, while it is strongest at 925 mb and below for the central Pacific. Hence, a meridional gradient of geopotential heights, together with a small Coriolis parameter, contributes to these geostrophic jets, which are most intense during late NH winter.

We would be remiss if some discussion of the El Niño-Southern Oscillation (ENSO) phenomenon (e.g. Philander 1990; for a review of theory, see Neelin et al. 1998) were not included in this review. During an ENSO warm event, warm water from the WP shifts eastward, so that the WP occupies a larger surface area of the equatorial Pacific than at other times. The intensity of the near-surface trade winds over the central equatorial Pacific diminishes due to the decreasing SST gradient. Typically, the zones of intense convection shift with the warm water so that the regions of upper-tropospheric divergence shift also. This movement of the convective zone means that the rising branch of the Walker circulation also shifts eastward. If our model produced multiple solutions, we could identify an ENSO solution as one in which the relative area of the WP is larger than in the other solution(s). As discussed later, we have found only one solution.

We now turn our attention to theories and hypotheses of the tropical climate which were developed based on models. Gill (1980) developed a simple analytic model of the response of a resting tropical atmosphere to small heat-induced perturbations. Since much of the convective heating in the tropics is confined over three relatively small land regions

(Africa, South America, and the Indonesian region), Gill examined the atmospheric response to a relatively small-scale heating source which is centered on the equator. If the atmosphere is abruptly heated at some initial time, Kelvin waves propogate rapidly eastward and generate easterly trade winds to the east of the heating. Thus the easterly trade winds in the Pacific could result from Kelvin waves produced by convective heating over Indonesia. Similarly, Rossby waves propogate westward and generate westerlies to the west of the heating. Because the fastest Rossby wave travels at only one-third the speed of the Kelvin wave, the effects of the Rossby waves would be expected to reach only one-third as far as those of the Kelvin wave. Gill interpreted the westerlies across the Indian ocean as a response to Rossby waves generated by convective heating over Indonesia.

Gill adopted the shallow-water equations (Matsuno 1966) on an equatorial β-plane for his model. For the equatorial β-plane, the Coriolis force is approximated as βy, where $\beta \equiv df/dy$ is assumed constant and y is the northward distance from the equator. Gill included dissipation in the form of Rayleigh friction and Newtonian cooling, and for simplicity assumed that the time scales for both types were equal. Rayleigh friction is a simple parameterization of friction in which the velocity is divided by a dissipation time scale. Because the object of Gill's study was to examine the horizontal structure of the atmosphere's response, he obtained a solution for a single representative vertical mode. In order to study the horizontal structure, Gill expanded the variables in terms of parabolic cylinder functions because free solutions of the shallow water equations have this form.

Gill focused primarily on cases for which the heating is symmetric or anti-symmetric about the equator. The solution for symmetric heating resembles a Walker circulation, with lower-tropospheric inflow into the heating region and upper-tropospheric outflow. The surface easterlies cover a larger area than the surface westerlies because the phase speed of the eastward-propogating Kelvin wave is three times faster than that of the westward-moving Rossby wave. By forming a vorticity equation for the case of no momentum damping, and then substituting from the continuity equation, Gill found that

$$v = yQ, \tag{1.3}$$

where v is the north-south velocity, y is the distance from the equator, and Q is the heating rate. The signs have been chosen so that $Q > 0$ for heating and the sign of v corresponds to that near the surface. For a incompressible atmosphere with a rigid lid at $z = D$ and a constant lapse rate, the gravest mode (the mode with the largest vertical scale) has horizontal velocity components which vary as $\cos(\pi z/D)$. For $Q > 0$, (1.3) implies poleward motion in the lower layer and equatorward motion in the upper layer. This suggests that the Walker circulation produces a north-south circulation which opposes the

Hadley circulation. As discussed later, Geisler (1981) found the same result.

The solution for anti-symmetric heating consists of a mixed Rossby-gravity wave and a Rossby wave. For the heating function chosen by Gill, the only non-zero mode for the anti-symmetric case is the Q_1 mode, which does not produce the Kelvin wave (only the Q_0 mode produces a Kelvin wave for this model). Here, the subscript refers to the order of the particular parabolic cylinder function. Long mixed Rossby-gravity waves for his model do not propagate, and so the response to this wave type is largely confined to the heating region. Due to the westward propagation of Rossby waves, no response is generated to the east of the forcing region. To the west, the region of westerly flow into the heating region is limited because the dissipation rate of this particular Rossby mode ($n = 2$) is 5ε, where ε is the dissipation timescale due to Rayleigh friction, and so the wave dissipates before it can propogate far to the west. For smaller scale Rossby waves ($n > 2$), the dissipation rate is even stronger, and as a result their zone of influence is even smaller.

Gill could have considered additional modes of forcing, but he showed that the predominant response is due to the idealized symmetric and antisymmetric modes described above. The combined response to the two forcings was shown to resemble the observations. He interpreted the symmetric case as a simulation of the Walker circulation, and the asymmetric case as a simulation of the Hadley cell.

Although Gill plausibly demonstrated that heating of limited extent generates tropical waves which produce broad wind and pressure fields resembling the observations, his results must be viewed with caution due to several limitations. First, results were generated for a specified rather than predicted heating of the tropical troposphere, and so ocean-atmosphere interactions and feedbacks involving moist convection were excluded. Second, the model includes neither a moisture budget nor cloud radiative effects. Last and most important, the model was linearized about a resting atmosphere. Although linearization is appropriate, Gill's results must be interpreted as the response of the tropical atmosphere to a perturbation of a basic state, not as a prediction of the basic-state climate. Gill demonstrated the sensitivity of the tropical troposphere to the spatial distribution of heating, but his study does not really address the basic-state climate.

Geisler (1981) used a simple dynamical model in order to study the structure of the Walker circulation. He noted that previous investigators used general circulation models (GCMs) to study fluctuations of the Walker circulation rather than the maintenance of the Walker circulation itself, because of the difficulty in isolating the circulation from GCM results. Interestingly, Geisler devoted some effort to precisely defining the Walker circulation. Geisler found Bjerknes' definition of the Walker circulation to be unsatisfactory because it does not address the behavior or size of the cell. Geisler found a more satisfactory definition of the Walker circulation from NKVB who define it as the deviation of the circulation in the equatorial plane from its zonal average.

Following previous studies (Schneider 1977; Gill 1980), Geisler specified the deviation of heating from the zonal mean due to precipitation in equatorial latitudes. He specified that the horizontal deviation would have a Gaussian dependence on longitude and latitude, and that the vertical deviation would have a cubic dependence on pressure. The approach adopted for Geisler's study was similar to that of Gill (1980) in that a wave-like solution was obtained for model equations linearized about a motionless basic state. Geisler chose to use the steady primitive equations with constant static stability, and included dissipation in the form of Rayleigh friction, Newtonian cooling, vertical eddy diffusion, and cumulus friction. Following Schneider and Lindzen (1977), Geisler parameterized the effects of cumulus friction and specified a mass flux profile.

Geisler showed that the vertical structure of the zonal wavenumber-one response depends on the vertical structure of the perturbation cumulus heating and on the assumed form of dissipation. The standard case includes cumulus friction, Newtonian cooling, and a cumulus heating profile with maximum heating at 400 mb. The zero-wind level occurs at 4.5 km, which Geisler interprets as being too low. Taking the zero-wind level as that where the wind vectors are exactly vertical, Fig. 1.3 suggests that the zero-wind level occurs near 600 mb and 450 mb over the western Pacific and eastern Pacific, respectively. When Rayleigh friction replaces cumulus friction, the zero-wind level occurs over a broad layer between 350 mb and 500 mb. For this case, the responses of the free-tropospheric and boundary-layer zonal winds have amplitudes of 45 m $s^{-1}$and 10 m s^{-1}, respectively, and a phase difference between the two levels of nearly 180°.

The summed response of the zonal wind for the remaining wavenumbers resembles a Walker circulation. The heating produces inflow at low levels and outflow at upper levels. The zonal overturning to the east of the heat source is weaker and occurs over a greater x distance than that to the west. This result agrees with Gill (1980). Geisler noted Gill's interpretation of the differing longitudinal scales of the response, which is that larger group velocities allow the Kelvin waves to propagate farther east before being dissipated than the Rossby waves can propogate toward the west. For the meridional wind, the model produces a pair of cells straddling the equator to the east and west of the heating. The flow pattern of these cells opposes and enhances the Hadley circulation to the east and west of the heating, respectively. This suggests zones of enhanced and weakened convergence on either side of the heating. As Geisler noted, if the perturbation heating occurs over Indonesia, then Walker circulation appears to generate meridional flow which strengthens the Hadley cell over the Indian ocean, and weakens it over the Pacific ocean. No explanation for the meridional cells was given.

Lau and Lim (1982) presented results from a two-layer shallow water model on the equatorial β plane. Following Gill (1980), the "long wave" approximation was made, in which the waves are assumed to have a horizontal scale larger than 4, 000 km and a period larger than one day. With their model, Lau and Lim showed that specified heatings which are symmetric and anti-symmetric about the equator give Walker- and Hadley-like circulations, respectively. That is, the symmetric heating generates a zonal circulation, while the anti-symmetric heating generates a meridional circulation. These results are identical to those of Gill (1980).

Lau and Lim (1982) also suggested an interaction between the Walker and Hadley circulations and monsoon surges. According to their hypothesis, during the NH winter, cold air surges from Siberia over the Chinese southeast coast, where an intense high pressure system generates strong northeasterly flow downstream over the South China Sea. Strong subsidence over the cold Asian continent, coupled with strong equatorial flow over the South China Sea induces a strong local Hadley circulation. The northeasterly flow intensifies convergence over the maritime areas of Borneo and Indonesia which increases large-scale ascending motion, and thereby acts as a feedback on both the Hadley and Walker circulations.

Lau and Lim (1982) modeled this sequence of events by specifying a strong surface cooling at mid or subtropical latitudes (35° N or 27° N), and then a time-delayed warming at 6° S. Results from their model were consistent with their hypothesis, and details such as the tilt of the high-pressure systems were reproduced in accord with the observations. Thus, interactions between the Walker circulation and transient mid-latitude disturbances may be important for simulating the mean conditions of the tropical climate. However, as explained in more detail below, our model represents an isolated Walker circulation.

Using a model which is nearly identical to that of Geisler (1981), Rosenlof et al. (1986) examined the response of the Walker circulation to a single tropical heat source in the presence of a mean zonal wind and mean Hadley cell, which were prescribed to resemble the observations. Recall that Geisler linearized his model about a motionless basic state. The study of Rosenlof et al. (1986) was designed to examine the response of the Walker circulation to perturbations of non-resting basic states. Because Rosenlof et al. (1986) prescribed heating functions which are similar to those used by Geisler, their model produces a Walker circulation which is quantitatively very similar to those obtained by Geisler and Gill. However, Rosenlof et al. (1986) showed that interactions between the Hadley and Walker circulations might be important for correctly simulating the Walker circulation. For instance, the zero-wind level of the zonal wind rose from 670 mb for the base state to 500 mb for the case in which a Hadley circulation was specified. Rosenlof et al. (1986) showed that the advective processes associated with the zonally averaged zonal wind and vertical velocity are responsible for the change in zero-wind level. Although the zero-wind level is a detail which we only briefly consider for our model, these results illustrated interactions between the Hadley and Walker circulations.

Lindzen and Nigam (1987) used a simple model to show that SST gradients are capable of forcing low-level winds and convergence in the tropics. They simplified the horizontal momentum equation by assuming an Ekman balance such that the Coriolis force is balanced by the sum of the pressure gradient force and wind stress. The density was assumed to be a function of temperature only, i.e. essentially incompressible, SST and specific humidity were specified, and a rigid boundary-layer top was imposed. Linearizing the simplified momentum equations about a state of rest and using a drag coefficient to compute the surface wind stress, Lindzen and Nigam found a pressure field that qualitatively resembles the observations. However, the simulation produces enormous wind speeds and convergences, with maximum values for each being quantitatively very unrealistic. Lindzen and Nigam explained the discrepancies as resulting from their assumptions of a rigid boundary-layer lid and of instantaneous take-up of horizontal mass flux by cumulonimbus mass flux. If these assumptions are relaxed, the model produced better simulations of the tropical wind and divergence fields.

Neelin et al. (1998) provided a simple, interesting interpretation of the Lindzen-Nigam model which we describe briefly here. The reader should note that the description above contains no explicit relation to convective heating. Assuming that the temperature of the boundary layer follows from SST, integration of the hydrostatic equation gives

$$\hat{p} - p_T = -BT_S, \tag{1.4}$$

where $\hat{p}$ is the vertically averaged pressure perturbation in the boundary layer, p_T is the pressure perturbation at the top of the boundary layer, T_S is the SST, and B is a constant which hydrostatically relates SST to pressure perturbations. In order to close the model, an assumption regarding p_T is required. Neglect of p_T is equivalent to the rigid lid assumption discussed above, and results in extremely large wind speeds and convergences.

Consider the following steady thermodynamic equation,

$$\dot{Q} = -\alpha\omega\left(\frac{1}{\Gamma_d}\frac{dT}{dz} + 1\right), \tag{1.5}$$

in which $\dot{Q}$ is the cumulus heating rate per unit mass (units: W kg^{-1}), ω is the vertical velocity in pressure coordinates, Γ_d is the dry adiabatic lapse rate, and α is the specific volume. Equation (1.5) was derived under the assumption that vertical advection dominates over horizontal advection, and shows that the heating on the left-hand side (LHS) is related to the vertical motion and to the lapse rate. Suppose that the lapse rate in (1.5) is assumed to be zero. Then the vertical velocity would be larger than if the lapse rate were moist adiabatic. This is essentially what Lindzen and Nigam assumed for their model. Consequently, extremely large boundary-layer vertical velocities result and are associated with large horizontal convergences and strong wind speeds.

In order to relax the assumption of a rigid lid, Lindzen and Nigam hypothesized that

$$p_T = \varepsilon_C^{-1} g H \nabla \bullet \boldsymbol{v}, \tag{1.6}$$

where ε_C is an inverse time scale for horizontal convergence, H is the mean depth of the boundary layer, and $\boldsymbol{v}$ is the horizontal velocity vector. When (1.6) is inserted in (1.4) for p_T, Neelin et al. (1998) show that the result is very similar to the continuity equation for the forced shallow water equations. Thus, the model used by Lindzen and Nigam (1987) is very similar to the Gill model, which was described earlier.

A limitation of Lindzen and Nigam (1987), however, is that the SST gradients were specified in their model, rather than calculated. Consequently, air-sea interactions cannot be represented in this model. We can imagine, for instance, that regions of convergence might be associated with increased cumulonimbus activity, resulting in evaporation-wind feedbacks and/or cloud radiative effects which would affect the SST distribution. While Lindzen and Nigam demonstrated the sensitivity of the tropical wind field to SST, their study was insufficient to define the mechanisms which control the steady coupled ocean-atmosphere system.

Ramanathan and Collins (1991) postulated that cirrus clouds act as a thermostat to regulate tropical SST. Using a steady-state surface heat budget, Ramanathan and Collins examined Earth Radiation Budget Experiment (ERBE) data to deduce the inter-relationships among shortwave and longwave cloud radiative forcings and radiative forcing of the clear atmosphere. From their analysis, Ramanathan and Collins concluded that the shortwave cloud effect dominates over the longwave cloud effect in regulating SST. According to their hypothesis, as SST increases, the optical depth and altitude of cumulonimbus clouds increase which leads to stronger longwave and shortwave cloud effects. This occurs because the atmosphere warms as a result of longwave cloud radiative effects, stronger latent-heat release by convection, and a stronger SST gradient over the tropical Pacific, and leads to an amplification of the large-scale flux convergence of moisture. This amplification continues until the reflectivity of the cirrus clouds, which increases with optical depth, increases sufficiently to begin cooling the surface. Using ERBE data to estimate the slope of each term of the energy budget with respect to SST, Ramanathan and Collins calculated an upper limit for the SST of 305 K.

The main criticism of this study is that convection dynamics and large-scale air-sea interactions were not specifically considered. For instance, changes in the strength of the ocean and atmosphere circulations were not included. We can imagine that for these high SSTs, the surface winds might increase, leading to stronger cold-water upwelling and enhanced cooling of the surface. The increased surface wind stress would lead to stronger wind-driven currents which could increase the flux divergence of energy in the mixed layer. Moreover, there is nothing really special about T_S = 305 K. With the observed SST distribution, T_S = 305 K appears to be the SST at which the combined effects of cumulus convection lead to a surface cooling. However, if the SST were increased uniformly across the tropics and subtropics, then the surface wind field might not change and a strengthening of the tropical circulation would be unrealized. Thus, the feedback hypothesized by Ramanathan and Collins would not exist, because an enhanced moisture source on which the clouds could feed would not be available.

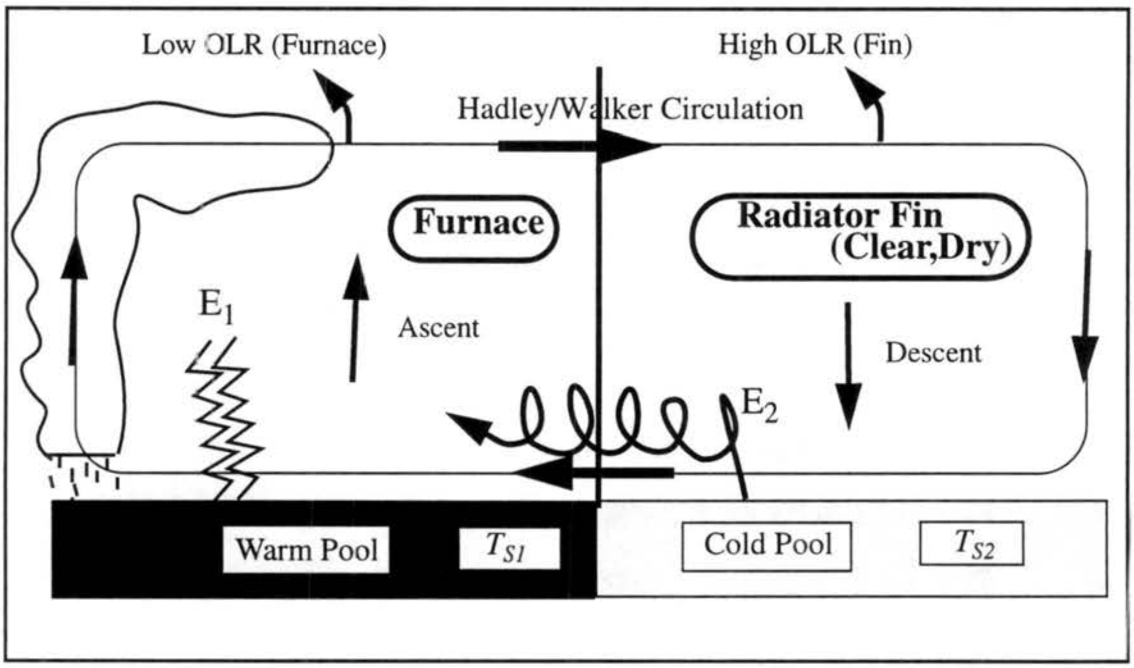

FIGURE 1.7: Reproduction of Pierrehumbert's schematic representation of the 'furnace/radiator-fin' model of the tropical circulation. The symbols E and T_S represent the evaporation rate and SST, respectively. The subscripts *1* and *2* denote the WP or furnace and the CP or radiator fin.

Pierrehumbert (1995) (hereafter P95) presented a two-box model of a Hadley/Walker circulation which has strongly influenced recent studies of the tropical climate. Figure 1.7

presents a schematic of the furnace/radiator-fin model in P95. The model has separate energy budgets for its CP and WP regions. SSTs for the CP and WP were constrained to be those which give energy balance for each box of the model atmosphere and for the CP ocean. Surface energy balance for the WP was not explicitly included in the model, even though it was discussed in detail. A vertically and horizontally uniform lapse rate was assumed, and the free-tropospheric temperature profile was assumed to be uniform across the tropics. The radiating temperature of the CP free atmosphere was assumed to be the air temperature at $z = z_T/2$, where z_T is the assumed height of the tropopause. The solution was obtained by first computing the net energy flux at the top of the WP atmosphere for a given SST and relative humidity profile. The net radiative flux at the top of the atmosphere (TOA) in the WP region was assumed to be balanced by a horizontal energy transport to the CP region. The CP SST and radiating temperature were then computed under the constraint that the net diabatic cooling must balance the energy imported laterally from the WP.

The mass flux was assumed to be that required to give a balance between adiabatic warming by dry subsidence and the net radiative cooling of the CP region. The mass flux is proportional to the sum of the net diabatic cooling of and specified mid-latitude atmospheric energy transport from the CP. The potential temperature difference between the inflow and outflow regions of the CP atmosphere was specified. Therefore, the mass flux responds only to changes to the net diabatic cooling of the CP. Because precipitation over the CP is neglected, the diabatic cooling of the CP atmosphere is purely radiative and depends on the WP and CP SSTs, and on the emissivity of the CP atmosphere, which is a prescribed parameter. P95 assumed a uniform vertical temperature profile for the atmosphere which is controlled by WP SST, and so the radiating temperature of the CP atmosphere depends on WP SST. It can be shown that the horizontal heat transport by the WP atmosphere, F_{ah1}, is proportional to the diabatic cooling of the CP atmosphere and to the ratio of CP area, A_2, and WP area, A_1. This ratio is also a prescribed parameter of the model.

The column energy budget for this model is given by

$$H = (Q_{v1} + F_{a\exp})\frac{A_1}{A_1 + A_2} + (Q_{v2} + F_{a\exp})\frac{A_2}{A_1 + A_2}, \quad (1.7)$$

where Q_v is the energy added to the CP atmospheric column due to vertical flux convergence and F_{aexp} is the specified, horizontal-mean, net horizontal, atmospheric heat transport into the column. The radiative effects of clouds were ignored. In equilibrium, $H = 0$, and so

$$(Q_{v1} + F_{a\exp})A_1 + (Q_{v2} + F_{a\exp})A_2 = 0. \quad (1.8)$$

For the case in which $F_{aexp} = F_{oh1} = F_{oh2} = 0$, where F_{oh} is the horizontal energy transport by the ocean, the net horizontal, atmospheric heat transport for the WP is given by $F_{ah1} = -Q_{v1}$. Obviously, F_{ah1} increases as the ratio A_2/A_1 increases for a fixed CP radiating temperature, and the climate cools for a fixed radiating temperature. P95 argued that Q_{v1} is bounded due to limits on the OLR in moist atmospheres, i.e. the increase of OLR with SST levels off due to the longwave-trapping effect of water vapor, which also increases with SST. As A_2 becomes much larger than A_1, the horizontal energy transport between boxes must vanish, and radiative equilibrium results. For small A_2/A_1, Q_{v2} is not bounded because the radiative temperature of the CP can be increased as much as needed in order to yield a finite energy transport between boxes, no matter how small A_2 becomes. Since the WP SST controls the CP radiating temperature, the WP becomes extremely hot in this limit.

P95 also showed that for very small values of the emissivity, the WP SST runs away, because the CP cannot radiate enough energy to balance the WP. Thus, a runaway greenhouse (Ingersoll 1969) is simulated for small values of the emissivity. As the CP's emissivity is increased, the SSTs of the WP and CP decrease and increase, respectively. Hence the temperature difference between the two boxes decreases with increasing CP emissivity.

In fact, the model breaks down for some value of the CP emissivity less than one and A_2/A_1 greater than two but less than four. For this case, the SST of the "Cold" Pool can exceed that of the "Warm" Pool. For fixed, lateral atmospheric energy transport, a larger A_2/A_1 implies a smaller Q_{v2}, which can be seen from (1.8). It can be shown that a smaller Q_{v2} leads to a reduced CP mass flux. Because the CP mass flux was assumed to be proportional to the CP surface evaporation rate, increasing A_2/A_1 warms the CP SST. On the other hand, as the CP emissivity increases, the radiating temperature of the CP atmosphere must decrease in order to radiate the same amount of energy. Because the WP controls the vertical temperature profile, the equilibrium SST of the WP must decrease as the CP radiating temperature decreases. As the CP emissivity increases, the WP SST must therefore decrease. Under the conditions of large CP emissivity and $A_2/A_1 > 2$, the model produces a warmer SST in the "Cold" Pool than in the "Warm" Pool.

Although the model contains simplified parameterizations and extreme assumptions, it captures important aspects of the tropical climate. For instance, simulated CP and WP SSTs resemble the present-day climate for a range of conditions, even if lateral energy transport by the ocean is ignored. The diagnosed CP mass flux is realistic although the potential temperature difference between inflow and outflow regions of the CP atmosphere was specified. In spite of these successes, the model suffers from shortcomings, as the results described above for large CP emissivity and A_2/A_1 demonstrate. A thermally indirect Walker/Hadley circulation is impossible. However, the results would no doubt change if moisture and momentum budgets were included. We would, for instance, expect boundary layer winds to reverse their direction if the temperature gradient reversed.

A further serious criticism of this model is that it fails to account for cloud-radiative effects in the WP region. P95 assumed that the shortwave and longwave cloud radiative effects cancel at the top of the atmosphere. Because he obtained realistic results without including cloud radiative effects, he concluded that cloud radiative effects do not significantly affect the tropical climate. We reject this approach for three reasons: 1) While such a near-cancellation is observed in the present-day tropics, the shortwave radiative forcing affects the surface primarily, and the longwave cloud forcing mainly influences the atmosphere; 2) Cancellation should be predicted, not assumed; 3) Cancellation may not occur in other climate states.

The observation that cloud shortwave forcing primarily affects the surface makes Pierrehumbert's results suspect. P95 argues that enhanced shortwave forcing at the surface is generally negated by a decreased evaporative cooling so that SST changes little in response to increasing high-cloud cover. But this idea rests on the premise that the evaporation rate decreases in response to decreased solar heating at the surface. Pierrehumbert quotes several studies to show that the dominant energy balance at the surface is between solar heating and evaporation. In nature, as the TOGA COARE observations (Webster 1994) show, gusty winds tend to accompany convectively active periods, and we might expect the stronger winds to increase the evaporation rate during the onset of the convectively active period. The combined effects of decreased solar heating and increased evaporative cooling would therefore tend to decrease the SST. As the system moves toward equilibrium, the dominant balance between solar heating and evaporative cooling could reestablish itself, but perhaps not before SST has decreased significantly. This might be an example in which a steady-state model cannot represent the processes which control SST.

We now consider the findings of Battisti and Ovens (1995), who used the Community Climate Model-Version 1 (CCM1), a GCM developed at NCAR, to examine the dependence of the low-level equatorial easterly jet on the Hadley and Walker circulations. Battisti and Ovens described the jet, based on ship reports and observations from Hastenrath (1971) and Bunker (1971), as a near-equatorial region of maximum wind speeds of nearly 10 m s^{-1}, which is located between 120° and 150° W and centered vertically about 850 mb. This easterly jet is essentially the low-level branch of the Walker circulation, and is noteworthy because it is confined to a shallow layer. As described above, the mechanisms which induce the formation of this jet have since been analyzed by Hastenrath (1998), based on the NCEP-NCAR reanalysis dataset.

Several idealized GCM experiments were performed with different SST distributions to examine the response of this jet. For each case, the lower boundary was specified by the authors to be uniform ocean. CCM1 experiments with a zonally symmetric SST distribution produce a wind field which resembles the Hadley circulation. For the cases with a Hadley cell, equatorial easterlies and low-level easterly jets on the poleward side of the ITCZ were produced, but no low-level easterly jet resulted. The CCM1 simulated geostrophic jets between 10° and 15°, which are the latitudes of the strongest meridional pressure gradient. Even though easterly winds form near the equator, the maximum wind speed is 7 m s^{-1} and the easterlies extend between 850 mb and 500 mb. Battisti and Ovens interpret this behavior based on Ekman theory, which is an extremely crude representation of the boundary layer. According to Ekman theory, the depth of the friction layer is proportional to f^{-1}, which is the inverse of the Coriolis parameter. Close to the equator, the depth of the friction layer increases strongly, and so the strong winds are not confined to a shallow layer.

Superimposing a zonal wavenumber-one SST anomaly on the zonally symmetric SST distribution results in a simulated wind field which includes both Hadley and Walker circulations. For this case, a strong equatorial easterly jet appears which resembles the horizontal and vertical scale of the observed easterly equatorial jet. According to the authors, the Walker circulation induces a Kelvin-wave meridional pressure distribution which produces the dominant geostrophic component of the zonal flow. An ageostrophic zonal component associated with the zonal pressure gradient also contributes to the easterlies. Battisti and Ovens also found that a deep layer of strong westerlies in the free troposphere is produced by the Walker circulation, which dominates over the weak easterlies produced by the Hadley circulation. The subsidence of this deep westerly layer provides the mechanism for confining the low-level easterlies below 800 mb. Hence, the CCM1 experiments provide strong evidence that the equatorial low-level easterly jet is associated with the Walker circulation.

The assumptions used to derive our box model are basically consistent with the findings of Battisti and Ovens (1995). Our assumption that the low-level easterlies and upper-level westerlies over the equator result mainly from the Walker circulation are supported by this study. Their results also provide justification for our assumption that the strong easterly mass flux simulated by our model is mainly confined beneath the trade-wind layer. However, Battisti and Ovens also showed that the easterlies and westerlies have significant geostrophic components, and therefore depend on the meridional pressure gradient. This is one aspect of their findings which we cannot simulate at present, as meridional variations are not included in our model. Our results should still be realistic because we consider only motions in the equatorial plane; hence the Coriolis parameter f vanishes in this case, and motions directly over the equator are necessarily ageostrophic.

Next, we discuss an appealingly simple box model developed by Sun and Liu (1996; hereafter SL) to demonstrate the role of dynamic ocean-atmosphere coupling in SST regulation for the tropical Pacific ocean. Because P95 neglected the influence of ocean currents and still realistically simulated the tropical climate, the role of ocean dynamics in regulating the tropical climate became murky. Although it is well known that ocean currents between the tropical eastern and western Pacific ocean are driven by surface winds, which are in turn driven by the SST difference between the two regions, the significance of this mechanism for the tropical climate was clarified by SL.

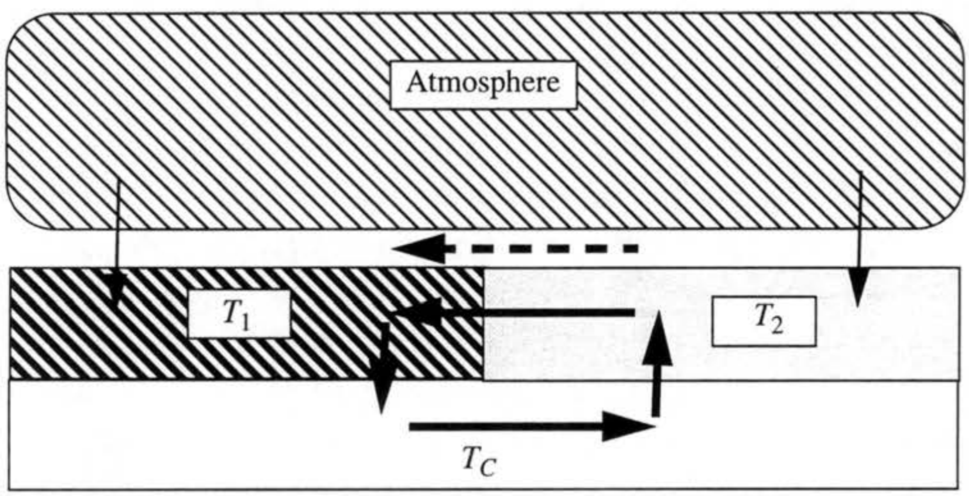

FIGURE 1.8: Schematic of the Sun-Liu coupled model. The boxes represent the atmosphere (light hatching), the WP (heavy hatching), the CP (stippling), and the undercurrent (clear box). Heavy arrows denote ocean currents, light arrows denote local heating and the dashed arrow represents the surface winds.

SL constructed a three-box model (Fig. 1.8) of the tropical Pacific ocean, which is coupled to a very simple model of the atmosphere. Two adjacent equal-volume boxes represent the surface layer of the eastern and western Pacific ocean regions, respectively, and a sub-surface box represents the equatorial undercurrent. Water is assumed to be advected into the western box from the eastern box, which is fed by upwelling of the equatorial undercurrent. Water returns to the equatorial undercurrent by subduction from the western box. The temperature of the equatorial undercurrent, T_c, was specified based on observations. The temperature tendencies for the two surface-layer boxes were assumed to be controlled by dynamical ocean-atmosphere processes and by thermal advection in the ocean. SL crudely parameterized the dynamical processes as a relaxation toward an equatorial equilibrium temperature T_e, with inverse time scale c. In order to determine T_e, the feedbacks due to surface emission, the clear-sky greenhouse effect, the greenhouse effect of clouds, and the cloud shortwave forcing with respect to an SST perturbation at $T_0 = 300$ K (i.e. the partial derivatives) were estimated. Except for the value of the surface emission feedback which is easily calculated, values for the other feedbacks were taken from published estimates. The difference between T_e and T_0 was then computed by taking the quotient of the net heating of the ocean-atmosphere column which was evaluated at T_0 and the summed feedbacks for an SST perturbation.

The advective temperature tendency can be shown to be proportional to the temperature difference between water entering and departing each box. The advection proportionality parameter, q, was in turn assumed to be proportional to the temperature difference between the two surface boxes with a specified constant of proportionality, α. Thus, the advective temperature tendencies for the WP and CP are given by $\alpha(T_1\text{-}T_2)^2$ and $\alpha(T_1\text{-}T_2)(T_c\text{-}T_2)$, respectively. The rationale for this form of q is that the strength of the ocean currents is proportional to the surface wind speed, which is assumed to be proportional to the east-west SST gradient.

SL found that the solution of their model is completely determined by a non-dimensional parameter $\beta = (\alpha/c)(T_e - T_c)$, which gives the strength of the dynamic coupling relative to the thermodynamic forcing. As seen in Fig. 1.9, the east-west SST gradient and the ocean currents are zero for $\beta < 1$, and hence the tropical Pacific ocean-atmosphere column is in radiative-convective equilibrium, with equilibrium temperatures $T_1 = T_2 = T_e$. This solution contrasts with those of P95 and Chapter 2 of this report which show that, due to the strong greenhouse effect, the WP ocean-atmosphere column cannot establish radiative-convective equilibrium unless the SST is very warm and the atmosphere is very dry. For $\beta < 1$, the SL model can reach a radiative-convective equilibrium for any $T_e \neq T_c$, and thus does not really account for the greenhouse effect. In fact, because the actual value of the temperatures depends on T_e, the radiative-convective solution is essentially specified in advance.

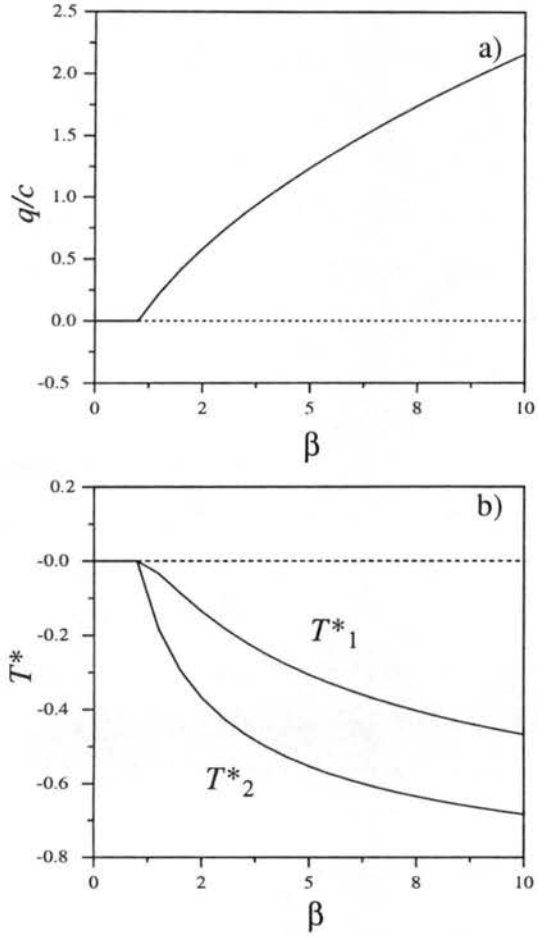

FIGURE 1.9: The equilibrium solution from the Sun-Liu coupled model for (a) current strength as measured by *q/c*, and for (b) non-dimensionalized SST as given by $T^*_1 = (T_1 - T_e)/(T_c - T_e)$ and $T^*_2 = (T_1 - T_e)/(T_c - T_e)$, as functions of β.

For $\beta > 1$, two solutions were found. The radiative-convective solution still holds, but is unstable to perturbations. As a numerical integration of the model shows, a perturbation of the radiative-convective equilibrium causes the system to evolve to the second solution. The second solution produces a finite east-west temperature difference, and the SSTs of the two surface boxes are colder than the radiative-convective equilibrium. As shown in Fig. 1.9, finite ocean currents develop for $\beta > 1$, and advection from the undercurrent to the CP and from the CP to the WP leads to colder SSTs in the CP and WP, respectively. The "Warm" Pool becomes warmer than the "Cold" Pool because water advected from the CP to the WP is warmer than water upwelled to the CP from the undercurrent. As described in Liu and Huang (1997), this destabilization of the radiative-convective equilibrium can be interpreted as a wind-cold water upwelling positive feedback. SL argued that T_e increases and c decreases due to positive radiative feedbacks in the atmosphere, such as those from water vapor and clouds. Since β increases with increasing T_e and decreasing c, SL asserted that strong positive feedbacks of the atmosphere play a role in the evolution of the system from radiative-convective equilibrium. The ocean circulation transports heat from the subsurface to surface ocean, and leads to cooler SSTs. SL also showed that as T_e increases, the difference between WP SST and T_e increases. This represents a regulation of the WP SST, and does not explicitly depend on an atmospheric circulation. Results from a simplified coupled ocean-atmosphere GCM support these conclusions.

In an extension of SL, Liu and Huang (1997) demonstrated with a model that the east-west SST difference is limited to 25% of the SST difference between the tropics and subtropics. Their results were generated with essentially the same model as that used by SL, except that a box representing the subtropics is included. Water is assumed to flow from the two tropical surface boxes to the subtropical surface box, where it is subducted to the equatorial undercurrent. Water from the equatorial undercurrent is then fed to the eastern surface box by upwelling, just as in SL.

Liu and Huang (1997) found that when $A_W \equiv \tilde{A}(T_e - T_m)/(cm_1)$, which is analogous to α in SL, is increased slightly from zero, the system is in a local radiative-convective equilibrium with no east-west temperature gradient, no ocean circulation, and no Walker circulation. In the definition of A_W, $\tilde{A}$ is the Walker coupling parameter, T_m is the prescribed equilibrium temperature of the mid-latitudes, and m_1 is the volume of the two surface boxes. Liu and Huang interpret A_W as a measure of the strength of ocean-atmosphere feedbacks such that increasing A_W corresponds to intensifying feedbacks. For $A_W > 1$, the SST gradient becomes finite and increases with increasing A_W. Liu and Huang attribute this transition to a destabilization of the local equilibrium due to a wind-cold water upwelling positive feedback. As described above, even though both surface boxes relax toward the same temperature (T_e), a temperature gradient forms because cold water is upwelled into the eastern (CP) box while warm water is advected from the eastern box to the western (WP) box. As A_W increases, the rate of cold-water upwelling continues to increase, and so the SST gradient increases until $A_W = 3$, in which case the gradient has maximized. Further increases of A_W result in a decrease of the SST gradient. Because the ocean circulation is so intense for $A_W > 3$, local relaxation has a negligible effect on the temperature of the water being advected from the CP to the WP. Thus, the temperatures of the water being transported to the two surface boxes are not too different, and the resulting gradient becomes small. Results from a simplified atmosphere model coupled to an ocean GCM generally support the conclusions of Liu and Huang (1997). The transition to the oversaturation regime for the simple model may be accomplished by decreasing c, but the response of the GCM to increasing c is different. Although the zonal SST gradient decreases, the ocean circulation weakens, which differs from the response of the box model. Liu and Huang speculate that the response may be modulated by the thermohaline circulation, which is not simulated by the box model.

Miller (1997; hereafter M97) extended Pierrehumbert's model by studying the radiative effect of low clouds in the CP region. Following the basic concepts of P95, Miller constructed a three-box model, which includes energy- and moisture-balance equations for the boundary layer and free troposphere and a surface energy budget for each of three boxes: the updraft region, the WP, and the CP. Taking advantage of the small surface area covered by the updrafts, M97 simplified the model for the limit of vanishing updraft surface area. M97 demonstrated that in this limit, the boundary layer and tropopause of the WP region must be connected by a moist adiabat. For simplicity, Miller assumed that the lapse rate of the WP region is moist adiabatic. Following P95, atmospheric dynamics were implicitly included by assuming a uniform free-tropospheric temperature profile across the WP and CP regions.

In order to diagnose the temperature and moisture profiles for the boundary layer in the CP region (CPBL), M97 adopted the mixing line model (Betts and Ridgeway 1989). Before we continue our review of M97, a description of the mixing line model is required because it plays an important role in the behavior of M97 and other models discussed later. In order to discuss the mixing line model, we define the following parameters: dry static energy, $s \equiv c_p T + gz$, moist static energy, $h = s + Lq$, and liquid water static energy, $s_l = s - Ll$, where c_p is the heat capacity of air at constant pressure, g is the acceleration of gravity, L is the latent heat of condensation, q is the water vapor mixing ratio, and l is the liquid water mixing ratio. When evaluated at the saturation pressure, these properties, denoted here as $s = s^*$, $s_l = s^*_l$, and $h = h^*$ are approximately conserved for air parcels undergoing adiabatic motion or isobaric mixing (Betts 1973). The saturation pressure (SP) is defined as the pressure of a parcel in which $l = 0$ and $q = q_{sat}$, where q_{sat} is the saturation mixing ratio. Because the SP describes the parcel's conserved properties, only the SP has to be considered for mixing two parcels (Betts 1982). If equal masses of two parcels with different SPs are mixed, then the s_{SL}, $s_{l,SL}$, and h_{SL} of the mixed parcel is the simple arithmetic average of the two unmixed parcels. This is part of the basis for the mixing line model.

Following Betts (1985), we define a parameter β (different from the one in SL) as

$$\beta(p) = \frac{\partial}{\partial p}p^*, \tag{1.9}$$

where p^* denotes the saturation pressure level. The parameter β describes the amount of mixing between convecting parcels and the environment. If $\beta = 0$, the layer is well mixed. As β increases, the mixing decreases until $\beta = 2$, in which case essentially no mixing occurs. Betts (1985) asserts that β is virtually constant for shallow vertical layers, and so the various thermodynamic gradients can be computed from

$$\frac{\partial s}{\partial p} = \beta\left(\frac{\partial}{\partial p^*}s^*\right); \; \frac{\partial h}{\partial p} = \beta\left(\frac{\partial}{\partial p^*}h^*\right). \tag{1.10}$$

For the mixing line model, thermodynamic quantities are computed for assumed values of β. The use of an assumed value for β obviously provides a simplified representation of mixing processes in nature, which are complicated functions of stability, the divergence profile, SST gradient, and wind speed. This method has become popular due to its realistic representation for the current tropical climate, but there is no guarantee that the value of β would not change with the climate, e.g. in a doubled-CO_2 environment.

Several key differences distinguish the results of M97 from those of P95. First, M97 included a simplified moisture budget, although like P95, the relative humidity profiles for the CP and WP were assumed. For P95, moisture exchange between the CP and WP was parameterized in terms of CP surface temperature and relative humidity, which was specified. M97 explicitly calculated the moisture transport between the WP and CP. Second, the dry static energy difference between the top and bottom of the troposphere was calculated in M97, but fixed for P95. This difference allows for a lapse rate feedback to operate in Miller's model, but not in Pierrehumbert's model. Last and most importantly, M97 empirically parameterized cloud radiative effects over the WP and CP, while P95 neglected them.

The main finding of M97 is that low clouds act as a thermostat for tropical SST. Without a realistic distribution of stratus clouds, the SST was too warm beneath the subsiding branch of the tropical circulation. Although low clouds reduce the surface-absorbed solar radiation locally, M97 also found that the temperature drop in the WP region was nearly as large as that in the CP region. In order to obtain a realistic WP SST, an additional -5 W m^{-2} forcing for the CP, and -12 W m^{-2} forcing for the WP were needed. This suggests that additional cloud types contribute to the surface forcing. In contrast, cloud radiative forcing was not required for the model of P95 to simulate realistic SST. This discrepancy suggests that the crude radiative transfer parameterization adopted in P95 likely canceled the impact of not including cloud radiative effects.

Larson et al. (1999; hereafter referred to as L99) investigated the interactions between the depth of the CPBL and the tropical circulation. L99 used a two-box model which is very similar to that used by M97, except for two primary differences: First, L99 allowed the depth of the CP boundary layer to adjust to changes of the tropical circulation, while M97 specified the depth. Second, L99 accounted for moisture flux divergence at all levels of the WP free troposphere, while M97 assumed that the transport occurs in a pipeline just below the tropopause. M97 ignored the detrainment of water vapor by convective updrafts except at the top. A further difference is that L99 did not include a separate energy budget for the updraft region as M97 did. An important similarity between the two studies is that both adopted the mixing line model for the CPBL.

To the extent that the mixing line model is valid, L99 showed that the height of the trade-wind inversion (TWI) adjusts to changes of q_{invp}, the specific humidity just above the CPBL. As q_{invp} increases, the radiative cooling of the CPBL decreases, which causes the mean temperature of the CPBL to increase. Because potential temperature in the free troposphere increases with height, the depth of the CPBL must decrease as q_{invp} increases in order to reduce θ_{invp}, the potential temperature at the inversion top, sufficiently to achieve a balance among subsidence warming, sensible heating and radiative cooling of the CPBL. In order to maintain moisture balance for the CPBL, the vertical-mean specific humidity for the CPBL must increase as q_{invp} increases. Because the specific humidity in the boundary layer decreases with height, the depth of the CPBL must decrease in order for the vertical-mean specific humidity to increase. In summary, moisture and temperature balances require the CPBL depth to decrease as q_{invp} increases. For doubled-CO_2 experiments, the negative feedback of the CPBL depth due to an increase of q_{invp} was largely suppressed. Although q_{invp} increased, the subsidence rate decreased. The response of the CPBL depth to these effects are opposing, and the net effect was small.

Another important finding of L99 is that if the high-cloud fraction over the WP is increased by 50%, the WP SST decreases by only 1.7 K. This finding provides evidence which contradicts the thermostat hypothesis proposed by Ramanathan and Collins (1991). However, the SST-surface air temperature (SAT) difference is allowed to vary for L99's model; as the cloud fraction increases this difference decreases from 4.2 K to 0 K. As a result, the evaporation rate strongly weakens, and so the surface energy budget reaches balance. If the SST-SAT difference were relatively constant, then the SST decrease might have to be significantly larger in order to achieve the dominant surface balance, which is between the evaporation rate and the shortwave flux.

TABLE: 1.1: Inter-Comparison of Recent Box Models

Parameter	P95	SL96	M97	L99
number of boxes	2	3	2 1/2	2
moisture profile	specified RH, constant profile	N/A	specified RH, vertically varying	specified RH, vertically varying
cloud radiative forcing	neglected	Considered in calculation of T_e	empirical	empirical
lapse rate	fixed	N/A	moist adiabat	moist adiabat
boundary layer T, q profiles	effective temperature	N/A	mixing line	mixing line
radiation	Simple flux-emissivit y model	Considered in calculation of T_e	GISS GCM radiation model	STREAMER radiation model
oceanic dynamics	specified horizontal energy transport	explicit	specified horizontal energy transport	specified horizontal energy transport
atmospheric temperature advection	uniform air T above CPBL, explicit transport between boxes	uniform air T_e for CP and WP	uniform air T above CPBL, explicit transport between boxes	uniform air T above CPBL, explicit transport between boxes
Momentum equation for CPBL	No	No	No	No
convective detrainment (below cloud top)	neglected	N/A	neglected	explicit
depth of trade-wind boundary layer	implicit	N/A	specified	computed

Table 1.1 summarizes the characteristics of the box models which we have discussed thus far. The number of boxes assumed for each model varies between two and three. SL 96 differs from the others in that an undercurrent box is included. Although M97 includes individual boxes for both convective updrafts and for the WP, his calculations are for the limit in which the surface area covered by the updrafts is negligible. In this limit, the area-weighted mass flux and precipitation rate are non-negligible even though the surface area is negligible compared to the CP and WP surface areas.

For the calculation of radiative fluxes, the relative humidity (RH) profile for each model is specified, with the only difference being that P95 assumed that the RH is independent of height. However, as mentioned previously, P95 neglected cloud radiative effects altogether, while M97 and L99 parameterized the cloud optical thickness for boundary-layer clouds over the CP in terms of the lower-tropospheric stability. Lower tropospheric stability is calculated based on the potential temperature difference at 700 mb and 1000 mb. With the uniform free-tropospheric temperature assumption, the 700-mb potential temperature is determined by the WP, while air temperature in the boundary-layer is determined from the mixing-line model. Hence, the mixing-line model influences the intensity of cloud radiative effects in the boundary layer. Neither M97 nor P95 included cloud radiative effects over the WP. L99 specified the cloud optical thickness of cirrus anvil clouds over the WP so as to enforce the observed near-cancellation of shortwave and longwave cloud radiative effects for their base case. As discussed in Chapter 3, we examine the validity of neglecting cloud radiative effects over the WP.

For radiative transfer, M96 and L99 used relatively sophisticated parameterizations for their models which treat the effects of absorbing gases, water vapor, and various types of cloud water, while P95 resorted to using a much simpler parameterization for his model. Although P95 derived OLR over the WP with the CCM2 radiative transfer parameterization, he assumed effective emission temperatures for the free troposphere and boundary layer in order to calculate the radiation budget for the atmosphere over the CP. There is no doubt that the radiative-transfer calculations from M96 and L99 are more accurate than those of P95. But given the simple nature and relatively extreme assumptions of box models, the additional accuracy given by the sophisticated radiative transfer parameterization seems out of balance. In fact, a simple parameterization is to be preferred despite the sacrifice of accuracy, because it allows for insight into the interactions among the components of the system.

From our literature review, it is clear that several important unanswered questions remain about the tropical climate. For instance, it is assumed in the box models of the atmosphere (P95, M97, L99) that the WP region must export heat to the CP region. However, P95 showed that in the limit as the area of the WP becomes negligible, the lateral transports between the two regions is negligible, and the WP must be in radiative-convective equilibrium. Chapter 2 examines the conditions under which the WP can establish radiative-convective equilibrium.

M97 and L99 both found that high clouds do not significantly influence the SST of the WP. As we described in detail, the limitations of their two models make their conclusions suspect. Although the cloud fraction over the WP is specified for our model, the cloud optical depth is calculated. For our coupled model, the surface wind stress is calculated from a momentum budget, while the evaporation rate is calculated from a bulk parameterization. Using our model, we will vary the specified high-cloud fraction to settle the question of a high-cloud thermostat effect for the WP. We will explore the mechanisms which influence the equilibrium value of SST for the WP.

Sun and Liu (1996) showed that the SSTs of the CP and WP decrease as the intensity of the ocean circulation increases. M97 and L99 showed that the SST of the CP decreases as the stratus cloud fraction increases. However, SL emphasized processes in the ocean, and so their representation of the atmosphere is highly simplified. Likewise, M97 and L99 concentrated on atmospheric processes, and simply specified the flux divergence of energy in the ocean. Because the representations for the non-emphasized interactions in the previous studies are so idealized, no judgement can be made at present as to whether one dominates over the other. Consequently, it is still an open question as to whether ocean dynamical processes or radiative effects of stratus clouds significantly influence CP SST in nature. We will try to answer this question with our fully coupled model.

As mentioned previously, in Chapter 3 we present the formulation and results of a two-box model of the Walker circulation. We include a momentum budget for the CPBL which determines the mean boundary-layer wind speed. We also improve the treatment of the hydrologic cycle by avoiding the dependence on assumed RH profiles, relying instead on a water-vapor closure based on the observations. The radiative effects of clouds over the WP are considered much more carefully than in previous box models so as to determine their effects on the Walker circulation. Over the CP, the cloud fraction for boundary-layer clouds is computed diagnostically from a stability relationship (Klein and Hartmann 1993). The effects of ocean dynamics are included with the incorporation of a simple ocean model which contains a momentum budget. Although previous box models have explicitly treated dynamics in either the ocean or the atmosphere, ours is the first to include both.

The organization of this report is as follows. Chapter 2 presents the formulation and results for the ocean-atmosphere model over the WP. Results are discussed for the case in which the model is in either radiative-convective equilibrium, or the horizontal moisture and energy transports are specified. Chapter 3 presents the development of and stand-alone results from the ocean and atmosphere models for the CP. We describe how the height of the trade-wind inversion is computed, and present our derivation of a simplified vertically integrated momentum budget. Chapter 4 discusses results from the fully coupled model, and describes the effects of various perturbations of the system. Chapter 5 gives our summary and conclusions with an emphasis on future work that needs to be done.

CHAPTER 2

The Warm-pool Convective Column

2.1 Introduction

A variety of different model types have been used to study climate, including general circulation models (GCMs; e.g. Randall et al. 1989), radiative-convective models (Manabe and Wetherald, 1967; Ramanathan and Coakley, 1978), and energy-balance models (e.g., North 1975). Atmospheric and coupled ocean-atmosphere GCMs provide the most comprehensive and detailed climate simulations, but GCMs are expensive to run and their results are often difficult to interpret. Untangling the connections among the various physical processes in GCMs can be almost as difficult as untangling those in nature.

Energy-balance models and radiative-convective models offer simplicity and low computational cost but with much less quantitative accuracy. These simple models provide some qualitative insights which can be compared to observations and to GCM simulations. On the other hand, their simplicity severely limits their realism. In particular, energy-balance models do not represent the atmosphere's vertical structure, which means that quantities such as meridional energy transport must be parameterized in terms of the surface temperature only; and most energy-balance models lack a hydrological cycle.

Radiative-convective models use multiple layers (often several tens of them) to explicitly represent the vertical structure of the atmosphere. Although early versions contained no hydrological cycle, modern radiative-convective models have corrected this deficiency (e.g., Renno et al. 1994; Emanuel 1991). Many radiative-convective models, however, still exclude cloud radiative effects, which strongly influence climate. Current radiative-convective models also tend to be too complicated to study analytically.

The fundamental role of the hydrological cycle in determining the tropical climate is now widely recognized (e.g. Webster 1994). The connection between clouds and the tropical energy budget is particularly important - a connection that involves a number of complex processes. It is of paramount importance to understand the processes that establish how the large-scale environment controls convection and the extent to which the convection modulates radiative transfer (e.g. Lau et al. 1994, Wong et al. 1993).

Our goal in this chapter is to develop the simplest possible model that can represent the tropical WP of Earth. We are using the model to develop ideas about the interactions of various physical processes, which can then be tested against observations and by simulations with more realistic models. In this spirit, we have made some rather extreme assumptions in order to keep the model as simple as possible. For instance, our model represents the vertical structure of the tropical WP atmosphere by a single thermodynamic sounding, which may be considered as a representative sounding for the Intertropical Convergence Zone.

In keeping with this goal, we introduce a simplified cloud radiative transfer scheme. We ignore the radiative effects of liquid water clouds and parameterize the formation of ice clouds in terms of the precipitation rate. While this approach seems reasonable, since observations show that clouds with more intense precipitation tend to be optically thicker and brighter, we realize that both non-precipitating ice clouds and liquid water clouds have substantial radiative effects in the tropics. Our objective here is to describe the radiative effects of cold, precipitating cirrus clouds on the climate of the tropical WP. The effects of other cloud types will be addressed in a future study.

Through the application of this model, we have been able to identify and investigate a number of issues concerning the links between convection and radiation in the tropical atmosphere. We show that the ocean-atmosphere system cannot reach equilibrium in the absence of cloud radiative effects. The column water vapor reaches extremely large values, and a "runaway greenhouse" results (Ingersoll 1969). We also show that the addition of cloud radiative effects allows the model to reach equilibrium for low wind speeds and with relatively efficient removal of ice water path by stratiform precipitation. We show that the model's equilibrium solutions are quite sensitive to the shortwave and longwave cloud optical depths, which are parameterized as functions of the ice water path. A current practice is to assume that the ratio of these optical depths is near two, but as discussed later, measurements of this ratio vary considerably.

The effects of radiatively active clouds on the depth and thermal structure of the tropical troposphere are still not well understood. Recently, Thuburn and Craig (1997) compared results from a general circulation model and a radiative-convective model to show that the tropopause height is sensitive to the specified surface temperature and to the specified water vapor distribution. Only clear-sky results were reported, however, so the influence of cloud radiative effects on tropopause height remain unknown. This chapter seeks to explore aspects of these issues in a rudimentary way using a simple model of convection and cloud radiative processes. We show how the cloud radiative effects influence the tropopause height and tropopause temperature in the model. We also demonstrate a sensitivity to the specified ratio of longwave and shortwave optical depths.

This chapter presents the formulation and results from the WP model run in stand-alone mode. We discuss the hydrological cycle, the radiatively active clouds, and the simple but explicit cumulus parameterization that allows for a variable lapse rate and variable absolute and relative humidities. We also describe our model for the tropopause height and temperature, which is based on the requirement for temperature continuity at the tropopause for a two-layer stratosphere in radiative equilibrium.

2.2 Basic Structure

Consider a layer of air that is convectively coupled to the tropical ocean, extending from the surface, $z = 0$, to a height, $z = z_T$, below which the convection is confined. We describe this physical system using two prognostic variables, representing the ocean surface temperature, T_S, the precipitable water, W. As discussed later, the radiatively active clouds are associated with detrainment of ice by deep convection.

We enforce energy conservation for the convectively active layer of the atmosphere. The moist static energy is defined by

$$h \equiv s + Lq\,, \tag{2.1}$$

where the dry static energy is represented by $s \equiv c_p T + gz$, L is the latent heat of condensation, c_p is the heat capacity of air at constant pressure, g is the acceleration of gravity, and q is the water vapor mixing ratio. Recall that h is approximately conserved under both moist and dry adiabatic processes, and that s is approximately conserved under dry adiabatic processes. The vertically integrated moist static energy, H, is defined by

$$H \equiv \int_0^{z_T} h\rho dz = \int_0^{z_T} s\rho dz + LW \tag{2.2}$$

and satisfies

$$\frac{dH}{dt} = \mathcal{N}_\infty - \mathcal{N}_S + \rho_T h_T \frac{dz_T}{dt} + \mathcal{F}_H \tag{2.3}$$

where $\mathcal{N}_\infty \equiv \mathcal{S}_\infty - \mathcal{R}_\infty$ is the net downward energy flux at the top of the atmosphere (TOA), $\mathcal{N}_S \equiv \mathcal{S}_S - \mathcal{R}_S - L\mathcal{E} - Q_{\mathcal{H}}$ is the net downward energy flux at the surface, $\mathcal{F}_H$ is the mean horizontal energy transport into the atmosheric column, $\mathcal{S}_\infty$ is the net solar radiation absorbed at and below the TOA, and $\mathcal{R}_\infty$ is the outgoing longwave radiation (assuming that the incoming longwave radiation at the TOA is zero). $\mathcal{S}_S$ is the solar radiation absorbed by the ocean; $\mathcal{R}_S$ is the net upward infrared radiation at the sea surface; Q_H is the surface sensible heat flux; and $\mathcal{E}$ is the rate of evaporation of sea water. There are no latent heating terms on the right-hand-side (RHS) of (2.3), since moist static energy is conserved under moist adiabatic processes. The second term on the left-hand side (LHS) represents the effects of z_T moving with respect to the air. Since the vertical integral is between z_C and zero, the first term on the right-hand side (RHS) should actually be $\mathcal{N}_C$.

However, we assume that the stratosphere is in radiative equilibrium, and so $\mathcal{N}_C = \mathcal{N}_\infty$. A derivation of (2.3) in pressure coordinates is given in Appendix 1. As discussed later, (2.3) is used diagnostically rather than prognostically.

We assume that the tropopause occurs at level z_C and that the stratosphere is in radiative equilibrium. As described in Section 2.5, the constraints of stratospheric radiative equilibrium and temperature continuity are used to determine the tropopause temperature and height.

The prognostic equation for the surface temperature is

$$\rho_w C \delta z_D \frac{dT_S}{dt} = \mathcal{N}_S + \mathcal{F}_O, \tag{2.4}$$

where ρ_W is the density of water, C is the heat capacity of ocean water per unit depth, δz_D is the depth of the ocean mixed layer (specified and assumed constant), and $\mathcal{F}_O$ is the mean energy transport by the WP mixed layer.

The moisture budget of the atmosphere is expressed by

$$\frac{d}{dt}(W + IWP) - \rho_T q_{N,T} \frac{dz_T}{dt} = \mathcal{E} - \mathcal{P} + \mathcal{F}_q, \tag{2.5}$$

where IWP is the ice water path, $\mathcal{P}$ is the precipitation rate, $\mathcal{F}_q$ is the mean horizontal transport of moisture into the atmospheric column, and ρ_T, $q_{N,T}$, and z_T are the air density, total water mixing ratio, and height at the top of the convectively active layer, respectively. The second term on the left-hand-side of (2.5) represents the effect of the movement of z_T with respect to the air. Here we do not include a liquid water path, because we limit the cloud types under consideration to precipitating upper-tropospheric convective anvils which are composed of ice crystals only. We assume for simplicity that the convective layer is sufficiently deep so that $q_{N,T}$ is very small; then (2.5) reduces to

$$\frac{d}{dt}(W + IWP) = \mathcal{E} - \mathcal{P} + \mathcal{F}_q. \tag{2.6}$$

We assume that the stratiform ice cloud is produced by convective detrainment, so that the rate of ice production is proportional to the convective precipitation rate, $\mathcal{P}_C$. Cloud ice removal is due to stratiform precipitation, at rate $\mathcal{P}_S$, which in turn depends upon the amount of cloud ice. Neglecting the conversion of IWP to W by sublimation, we can write a prognostic equation of the form

$$\frac{d}{dt} IWP = \chi \mathcal{P}_C - \mathcal{P}_S, \tag{2.7}$$

where χ is a non-dimensional parameter. We assume that the stratiform precipitation rate satisfies

$$\mathcal{P}_S = IWP/(ft_{prec}), \tag{2.8}$$

and

$$\mathcal{P} = \mathcal{P}_C + \mathcal{P}_S, \tag{2.9}$$

where t_{prec} is the "autoconversion" time-scale for the removal of *IWP* by stratiform precipitation and f is the fractional cloudiness. The fractional cloudiness is a specified parameter in this model, chosen small enough so that the upward longwave flux into the stratosphere will be strong enough to produce realistic values of $\mathcal{R}_T$ and T_T. The cloud fraction appears in the denominator of (2.8) because *IWP* represents the area-averaged ice-water path, while it is the *local* ice water path that is relevant for conversion of cloud ice to snow. Figure 2.1 schematically summarizes these ideas.

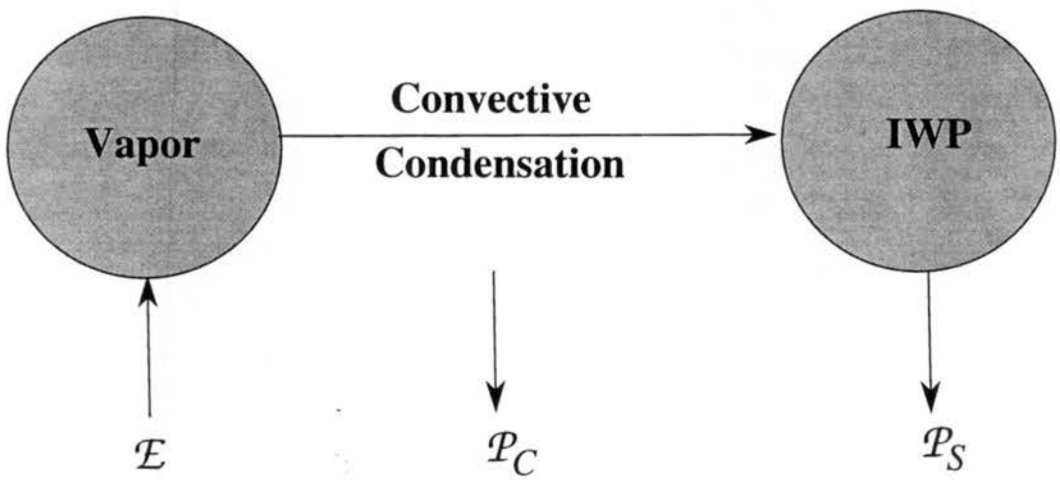

FIGURE 2.1: This graphically illustrates the process by which cirrus ice clouds form due to convective detrainment.

Using (2.8) and (2.9) in (2.7), we obtain

$$\begin{aligned}\frac{d}{dt}IWP &= \chi(\mathcal{P} - \mathcal{P}_S) - IWP/(ft_{prec}) \\ &= \chi(\mathcal{P} - IWP/t_{prec}) - IWP/(ft_{prec}) \\ &= \chi\mathcal{P} - (1+\chi)IWP/((ft_{prec})).\end{aligned} \tag{2.10}$$

When the source and sink terms are in quasi-balance, (2.10) reduces to

$$IWP \cong \left(\frac{\chi f t_{prec}}{1+\chi}\right)\mathcal{P}. \tag{2.11}$$

We could have written down (2.11), i.e. a simple proportionality between the total precipitation rate and the ice water path, by direct assumption, but the brief derivation given above allows some interpretation in terms of specific physical processes. Because the autoconversion time is expected to be short, on the order of 10^3-10^4 s (e.g. Fowler et al. 1996), solutions of the prognostic equation should remain close to the quasi-equilibrium solution given by (2.11). Note that for $f = 0$, (2.11) gives $IWP = 0$. Under the assumption that (2.11) is valid, (2.6) reduces to

$$\frac{dW}{dt} \cong \mathcal{E} - \mathcal{P} + \mathcal{F}_q. \tag{2.12}$$

2.3 Hydrological cycle

The atmospheric branch of the hydrological cycle is a fundamental component of the climate system (e.g. Webster 1994), because it transports energy, controls latent heat release and precipitation, and produces radiatively active clouds. A key goal of our study has been to construct an extremely simple model of the hydrological cycle.

We assume that the surface evaporation rate, $\mathcal{E}$, satisfies

$$\mathcal{E} = \mathcal{V}Max\{[q_{sat}(T_S, p_S) - q_S], 0\}, \tag{2.13}$$

where $\mathcal{V}$ is a "ventilation mass flux,"

$$q_{sat}(T, p) \cong \frac{\varepsilon e_0 exp(A_e - B_e/T)}{p} \tag{2.14}$$

is the saturation mixing ratio at temperature T and pressure p, and q_S is the surface air mixing ratio. Methods to determine q_S are discussed later.

For the stand-alone WP model, we assume that $\mathcal{V}$ is simply proportional to a prescribed wind speed, i.e.

$$\mathcal{V} = \rho_S c_T |V_S| . \quad \textbf{(2.15)}$$

Previous studies of this type (e.g. Pierrehumbert 1995) have also relied on this assumption, but it is not very satisfactory for two reasons. First, we expect *a priori* that $\mathcal{V}$ should be related to the vigor of the hydrological cycle, i.e. that there should be some relationship between $\mathcal{V}$ and, for example, $\mathcal{P}$. Second, surface and atmospheric energy balance depend sensitively on the values of $\mathcal{V}$ prescribed. For both of these reasons, $\mathcal{V}$ should be an internal variable of the model, rather than an externally imposed parameter. This generalization is implemented in future chapters.

We now adopt a very simple model for the cumulus clouds. We assume that the top of the convective layer, at $z = z_T$, occurs at the neutral buoyancy level for non-entraining parcels consisting of surface air. Moist static energy is conserved within these ascending, non-entraining parcels. Assuming that the environment at z_T has a saturation water vapor mixing ratio which is negligible compared to q_S, we can express the neutral buoyancy condition by $h_S = s_T$, which implies that

$$z_T = g^{-1}[c_p(T_S - T_T) + Lq_S] . \quad \textbf{(2.16)}$$

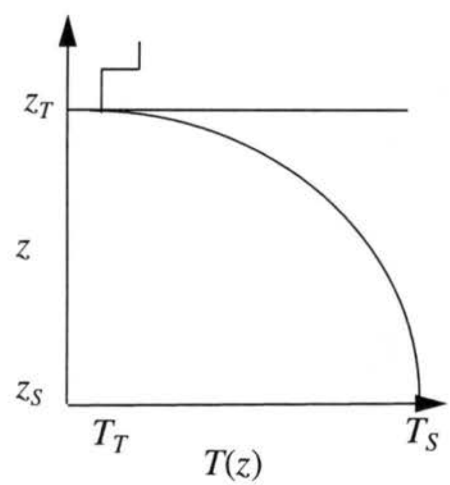

FIGURE 2.2: Schematic of the idealized tropical temperature profile in a convecting region of the tropical WP.

We assume that the tropical temperature profile has the form

$$T = T_S - \Gamma_0 z - \Upsilon z^2 , \quad \textbf{(2.17)}$$

where Γ_0 is the average lapse rate of the lower troposphere, and Υ is a parameter which allows the lapse rate to vary with height. Figure 2.2 presents the idealized temperature structure for our model. Figure 2.3 shows a typical sounding (solid line) over the WP from TOGA COARE (Parsons et al. 1994). As is well known, the observed tropical lapse rate closely follows a moist adiabat (dashed line). Note that the lapse rate steepens near $z = 9$ km and remains steep up to the tropopause. Our method to determine Γ_0 and Υ is discussed later.

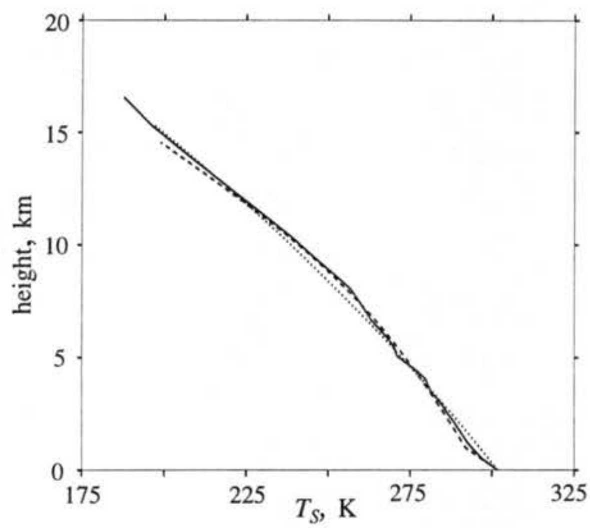

FIGURE 2.3: Observed area-mean temperature profile (solid line) for the TOGA COARE intensive flux array region. The dashed line is the moist adiabat; the dotted line is the temperature profile for the model.

Convection plays three roles in the climate system and in our model. It releases latent heat, it leads to precipitation which dries the atmosphere, and it transports energy and water upward from the surface. Following Arakawa and Chen (1987; see also Arakawa 1993) we assume that the convective state of the tropical atmosphere can be characterized by a point in the $(\Gamma_n, q/q_{sat})$ plane, which is considered as a phase space. Here

$$\Gamma_n \equiv \frac{\Gamma_0 - \Gamma_{mS}}{\Gamma_d - \Gamma_{mS}}, \tag{2.18}$$

where $\Gamma_d = g/c_p$ is the dry adiabatic lapse rate, and Γ_{mS} is the moist adiabatic lapse rate at the surface, given by

$$\Gamma_{mS} = \Gamma_d \left[\frac{1 + \frac{Lq_{sat}(T_S, p_S)}{RT_S}}{1 + \frac{\varepsilon L^2 q_{sat}(T_S, p_S)}{c_p R T_S^2}} \right] \tag{2.19}$$

evaluated at the surface temperature and pressure. In (2.19), R is the gas constant.

In their analysis of various observations, Arakawa and Chen (1987) took the lapse rate Γ_0 which appears in (2.18) to be the average lapse rate between the surface and 500 mb. In the case with $\Upsilon = 0$, Γ_0 is the average lapse rate between the surface and the top of the convective layer. Arakawa and Chen also discussed an idealized model, however, in which the lapse rate was assumed to be independent of height (see their Fig. 8). In the second case, Γ_0 is the lapse rate near the surface.

The four panels in the lower part of the figure, which are taken from Arakawa (1993), show observations plotted in the (Γ_n, q_S/q_{sat}) plane, which is a kind of phase space. As discussed by Arakawa, during periods of active convection the observations tend to fall along a line which runs from the lower right to upper left; a theoretical interpretation, discussed in detail by Arakawa (1993) and Arakawa and Chen (1987), is that points along this diagonal line represent convectively neutral states toward which convection drives the system.

A state of the model is represented by a point in the phase space depicted in the upper panel of Fig. 2.4. In this panel, points below the diagonal line, e.g. drier soundings, represent convectively stable states. Points above the line represent convectively unstable states, and are forbidden in the sense that convection immediately acts to remove the instability so that it is not observed. Radiation tries to increase the lapse rate (for optically thick atmospheres), and surface evaporation tries to increase the precipitable water. Convection fights back by warming aloft and drying. Points on the stable side of the line are allowed, and are not accompanied by convection. Such points will be driven toward the unstable portion of the domain, however, by the combined effects of radiation and surface evaporation. As soon as the system tries to cross the diagonal line, convection responds to prevent it from doing so; this is a kind of convective adjustment. We therefore expect that convectively active equilibria will lie along the line, and time-dependent solutions may even stay entirely on the line. The model's position along the line can change with time as a result of a tug-of-war among convection, radiation, and surface evaporation. Hu and Randall (1995) used a very similar parameterization.

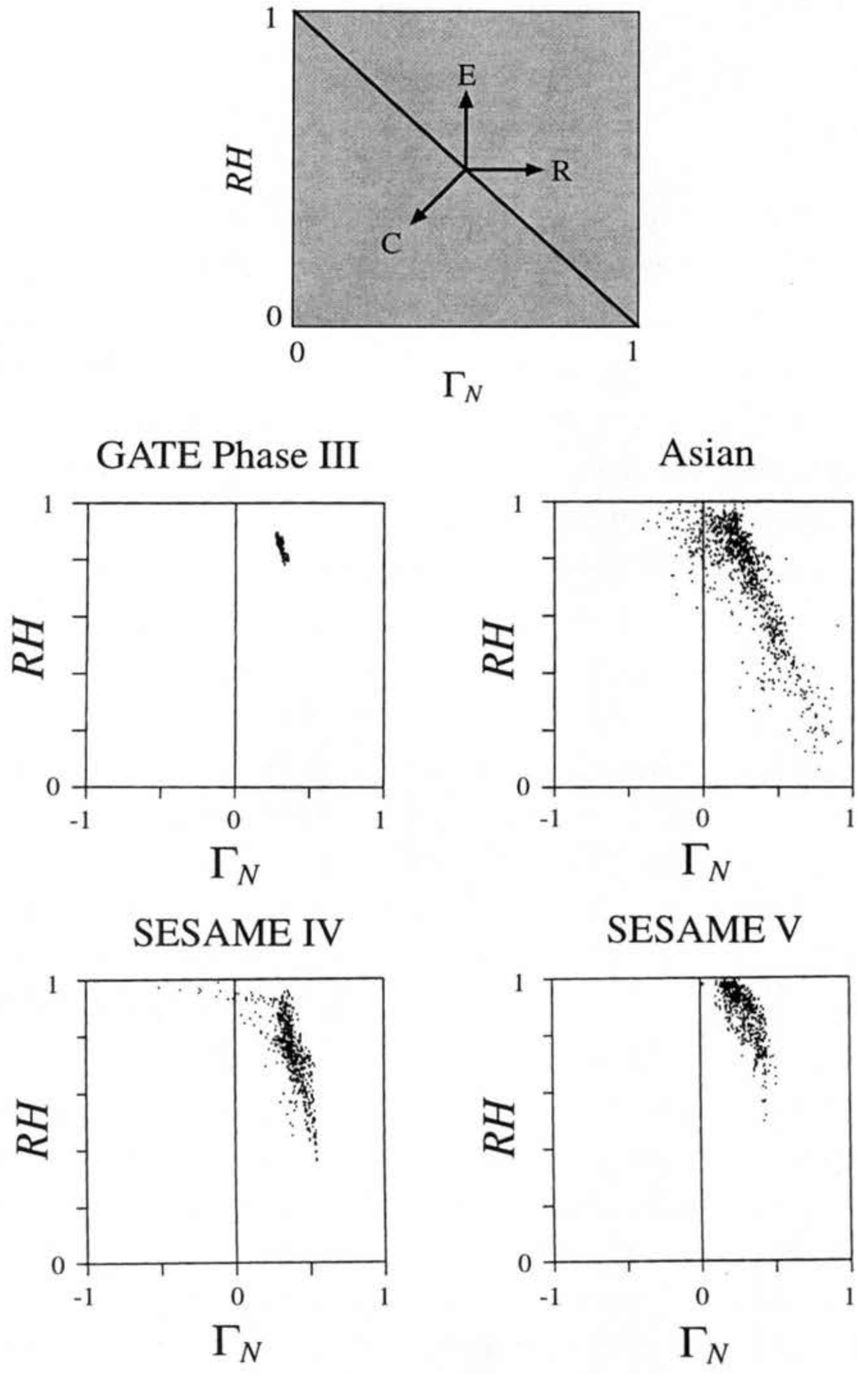

FIGURE 2.4: The top panel is a diagram illustrating the cumulus parameterization of the model. The vertical axis is a measure of the relative humidity. The horizontal axis is a measure of the lapse rate. When convection is active, the model state lies along the diagonal line; this constraint is expressed by (2.20) and (2.21). The lower four panels are taken from Arakawa (1993; see also Arakawa and Chen 1987). They show that data obtained in GATE Phase III, Asia, SESAME IV, and SESAME V all lend support to the closure assumption illustrated in the top panel.

To describe this closure mathematically, we define a parameter G, which passes through zero along the diagonal line in Fig. 2.4:

$$G \equiv \frac{q_S}{q_{sat}} - \frac{\Gamma_d - \Gamma_0}{\Gamma_d - \Gamma_{mS}}. \tag{2.20}$$

The region $G > 0$, which is "above the line," corresponds to convective instability; and the region $G < 0$, which is "below the line," corresponds to convective stability, i.e. conditions under which convection is suppressed. Essentially, the model allows $G \leq 0$, but forbids $G > 0$. When convection is active, the model "toes the line," with

$$\frac{dG}{dt} = 0 \text{ and } G = 0. \tag{2.21}$$

This simply means that during periods of active convection, the convective available potetial energy (CAPE) remains close to zero. In other words, (2.21) is an expression of quasi-equilibrium in the spirit of Arakawa and Schubert (1974).

For $G = 0$, (2.20) reduces to

$$\frac{q_S}{q_{sat}} = \frac{\Gamma_d - \Gamma_0}{\Gamma_d - \Gamma_{mS}}. \tag{2.22}$$

This result means that, given the relative humidity at the surface, we can determine the mean lapse rate over the lower troposphere. The lapse rate Γ_0 obtained from (2.22) represents an approximation to the moist adiabatic lapse rate in the lower troposphere, and in fact (2.22) can be derived directly from a moist adiabatic assumption. Figure 2.3 shows that the temperature profile obtained using Γ_0 matches the observed profile and the moist adiabat rather well. The advantage of using (2.22) is computational simplicity: we avoid explicitly computing the temperature for multiple layers as is usually done in radiative-convective models.

To determine the total precipitation rate, we start from (2.3), which is the budget equation for the vertically integrated moist static energy. We approximate the moist static energy at z_T, which appears in the second term on the left-hand side of (2.3), by the dry static energy at z_T, i.e. s_T. This is justified if the upper-level water vapor mixing ratio is sufficiently small. Recall that the dry static energy at level T is approximately equal to the moist static energy of the surface air, i.e. $s_T = h_S$, because the convective clouds detrain at their level of neutral buoyancy, z_T. This allows us to rewrite (2.3) as

TABLE: 2.1: Definitions, numerical values, and units of various parameters used in the model.

Para meter	Definition	Value and Units
p_S	Surface pressure	1000 mb
A_e	Used to compute saturation mixing ratio	21.656
B_e	Used to compute saturation mixing ratio	5418 K
ε	Ratio of molecular weights of water vapor and dry air	0.622
e_0	Used to compute saturation mixing ratio	1 mb
c_T	Transfer coefficient used to compute the evaporation rate	0.001
ρ_W	Density of liquid water	1000 kg m^{-3}
C	Heat capacity of liquid water	4200 J kg^{-1}
D	Depth of the ocean mixed layer	60 m (nominal)
σ	Stefan-Boltzman constant	5.67×10^{-8} W m^{-2} K^{-4}
a_0	Parameter used to relate the clear-sky downward surface longwave radiation to the outgoing longwave radiation	0.38532
a_1	Parameter used to relate the upward surface longwave radiation to the outgoing longwave radiation	1.38532
c_1	Parameter used to relate the upward surface longwave radiation to the outgoing longwave radiation	0.005238 m^2 kg^{-1}
a_2	Parameter used to relate the clear-sky downward surface longwave radiation to the outgoing longwave radiation	0.9369
c_2	Parameter used to relate the clear-sky downward surface longwave radiation to the outgoing longwave radiation	0.0102 m^2 kg^{-1}
d	Used to obtain $(\mathcal{R}_{dn})_{S,clr}$	0.25 m^2 kg^{-1}
μ_0	"Average" cosine of the solar zenith angle	0.5
δp_u	Pressure depth of upper sublayer in stratosphere	2 mb
k_l	Constant used to determine IR optical thickness of the lower stratospheric sublayer	0.001 mb^{-1}
k_u	Constant used to determine IR optical thickness of the upper stratospheric sublayer	0.004 mb^{-1}

$$\frac{dH}{dt} - \rho_T h_S \frac{dz_T}{dt} = \mathcal{N}_\infty - \mathcal{N}_S + \mathcal{F}_H . \tag{2.23}$$

Now we derive analytical expressions for the vertically integrated dry static energy, S, and the vertically integrated moist static energy, H. Given the assumed distribution of T with height, we can integrate the RHS of (2.2), as follows. First, by combining the assumed temperature distribution with hydrostatics and the ideal gas law, $p = \rho RT$, we can show that the pressure approximately varies with height according to

$$p = p_S \left(1 - \frac{z\Gamma_0}{T_S}\right)^{\frac{g}{R\Gamma_0}} . \tag{2.24}$$

The exponent in (2.21) is independent of height, but through Γ_0 it depends on T_S and W (as discussed later). We assume that p_S is a constant over the WP (Table 2.1 lists all the parameters and constants used for this study). The temperature and pressure profiles given by (2.17) and (2.24), respectively, can be used in (2.2) to obtain

$$H = \frac{(\kappa + 1) T_S p_S}{\Gamma_0 \kappa + \Gamma_d} \left[1 - \left(1 - \frac{\Gamma_0 z_T}{T_S}\right)^{\frac{g}{R\Gamma_0} + 1} \right] - z_T p_T + LW . \tag{2.25}$$

Because the surface pressure p_S is assumed to be constant, H is a function of T_S and W only, i.e.

$$H = H(T_S, W) . \tag{2.26}$$

Part of the W-dependence of H comes from Γ_0 [see (2.37), discussed later]. Because T_S and W are governed by their own prognostic equations, (2.26) seems to imply that there is no room to enforce (2.23) as an additional constraint on H. In fact, however, we *can* enforce (2.23), because the precipitation rate has not yet been determined. The precipitation rate must be consistent with (2.23), given dT_S/dt and dW/dt from (2.4) and (2.12) respectively. From (2.26), we can write

$$\frac{dH}{dt} = \frac{\partial H}{\partial T_S}\frac{dT_S}{dt} + \frac{\partial H}{\partial W}\frac{dW}{dt} . \tag{2.27}$$

Substituting for each term of (2.27), we obtain

$$\mathcal{N}_\infty - \mathcal{N}_S + \rho_T h_S \frac{dz_T}{dt} + \mathcal{F}_H = \\ \frac{\partial H}{\partial T_S}\left(\frac{\mathcal{N}_S + \mathcal{F}_O}{\rho_w CD}\right) + \frac{\partial H}{\partial W}(\mathcal{E} - \mathcal{P} + \mathcal{F}_W). \tag{2.28}$$

We can also show that z_T in our model is a function of T_S and W only. Hence, we can write a differential equation for z_T which is similar to (2.27), except that z_T replaces H. The details are omitted here for brevity. Using the resulting expression for dz_T/dt in (2.28), we find that

$$\mathcal{N}_\infty = \Lambda_1 \mathcal{N}_S + (\Lambda_1 - 1)\mathcal{F}_O + \Lambda_2(\mathcal{E} - \mathcal{P} + \mathcal{F}_W) - \mathcal{F}_H, \tag{2.29}$$

where, for convenience, we define

$$\Lambda_1 \equiv 1 + \frac{1}{\rho_w CD}\left(\frac{\partial H}{\partial T_S} - \rho_T h_S \frac{dz_T}{dT_S}\right), \tag{2.30}$$

$$\Lambda_2 \equiv \frac{\partial H}{\partial W} - \rho_T h_S \frac{dz_T}{dW}. \tag{2.31}$$

Solving (2.29) for $\mathcal{P}$, we obtain

$$\mathcal{P} = \mathcal{E} + \mathcal{F}_W + \{\Lambda_1 \mathcal{N}_S + (\Lambda_1 - 1)\mathcal{F}_O - \mathcal{N}_\infty - \mathcal{F}_H\}\Lambda_2^{-1}. \tag{2.32}$$

In equilibrium, $\mathcal{P} = \mathcal{E} + \mathcal{F}_W$, $\mathcal{N}_S + \mathcal{F}_O = 0$, and $\mathcal{N}_\infty - \mathcal{N}_S + \mathcal{F}_E = 0$. According to (2.32), precipitation is driven by surface evaporation, by moisture flux convergence in the atmosphere, by surface warming, by energy flux convergence in the ocean, by radiative energy losses at the top of the convective layer, and by energy flux divergence in the atmosphere.

We assume that when convection is active the surface air mixing ratio satisfies

$$q_S = \frac{W}{W_{max}} q_{sat}(T_S, p_S), \tag{2.33}$$

where W_{max} is the precipitable water that would exist if the relative humidity were 100% throughout the depth of the tropical atmosphere. The relationship (2.33) resembles the climatological relationship between q_S and W employed by Liu (1986) in his attempt to retrieve ocean surface energy fluxes from satellite measurements. We have performed a similar analysis using different data. The results are shown in Fig. 2.5. For purposes of comparison with observations, we represent q_S by the 1000-mb mixing ratio, which is conveniently available in radiosonde reports. The points in Fig. 2.5 were derived by matching the 1000-mb mixing ratio with the precipitable water obtained by vertically integrating the surface observations and balloon soundings taken at Kavieng and Nauru during TOGA COARE (Parsons et al. 1994), and at Porto Santo during ASTEX (Albrecht et al. 1995). Satellite observations of precipitable water as a function of sea surface temperature (Jackson and Stephens 1995) were used to evaluate the assumption (2.33) as follows. We calculated q_{sat} from (2.33) and W_{max} from (2.19) and (2.36) (presented later), both as functions of observed sea surface temperature. The satellite-observed W and the derived q_{sat} and W_{max}, all corresponding to the same sea surface temperature, were then inserted into (2.33) to obtain the curve plotted in Fig. 2.5.

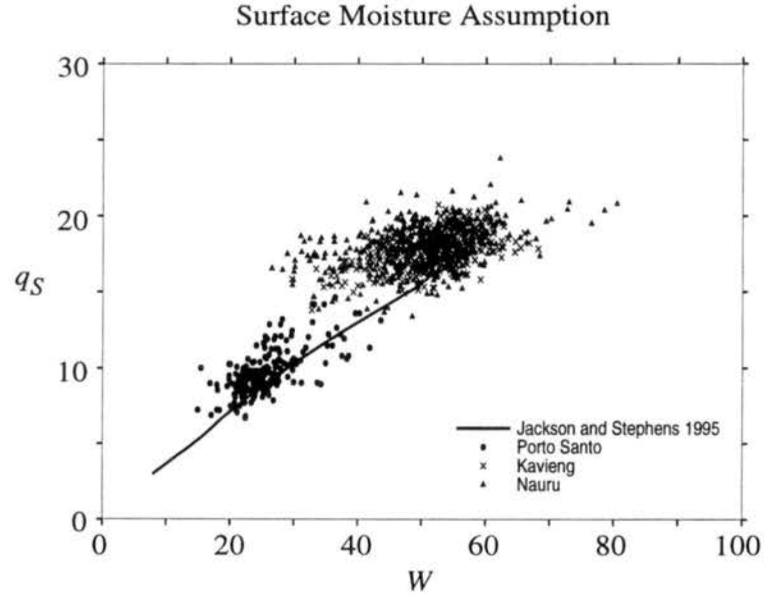

FIGURE 2.5: The relationship between q_S and W, as determined from radiosonde data by Liu (1986). The solid line in the figure represents the relationship derived using (2.33) and a relationship between sea surface temperature and W, as discussed by Jackson and Stephens (1995).

The fact that the line passes through the data reasonably well supports the use of (2.33) in our model, even though both Liu's data and our results suggest that q_S "flattens out" at large values of W. A plausible interpretation is that over warm oceans with large W, vigorous deep convection distributes moisture through a deeper layer, effectively drying the lower layers and moistening the air aloft. A consequence of this assumption is that the dependence of $\mathcal{E}$ on q_{sat} and q_S in (2.13) can be replaced by a dependence on W and W_{max}. Since q_S flattens out for large values of W in nature, the evaporation rate becomes independent of W at these large values. For our model, the evaporation rate continues to decrease for a given Υ as W increases, even for large values of W. In nature, as W increases, the radiative effect of water vapor destabilizes the lapse rate by cooling the upper troposphere and warming the lower troposphere (Webster 1994). This destabilization can intensify convection.

Given z_T, the lapse rate Γ_0 and the surface temperature, we are now able to evaluate W_{max}, using

$$\begin{aligned} W_{max} &= \int_0^{z_T} \frac{\varepsilon e_0 exp[A_e - B_e/T(z)]}{p(z)} \rho(z) dz \\ &= \frac{\varepsilon e_0}{R} \int_0^{z_C} \frac{exp[A_e - B_e/T(z)]}{T(z)} dz \\ &\cong F(T_S)/\Gamma_0, \end{aligned} \tag{2.34}$$

where

$$F \equiv \frac{\varepsilon e_0 T_0}{R B_e} exp(A_e - B_e/T_S) \tag{2.35}$$

The exponential function in (2.34) arises from the Clausius-Clapeyron equation; the values of the constants A_e and B_e are given in Table 2.1. We have used (2.17) with $\Upsilon = 0$ to do the integral in (2.34). The reference temperature T_0 used in (2.35) is set to 300 K. In the last line of (2.34), we have neglected the W-dependence of $T(z)$. This approximation introduces an error of 10% or less for T_S in the range 290 K to 310 K.

By combining (2.34) with our convection closure, (2.22), and our surface humidity assumption, (2.33), we can solve for Γ_0 and W_{max} as functions of W and T_S only:

$$W_{max} \cong \frac{F(T_S) + W(\Gamma_d - \Gamma_{mS})}{\Gamma_d}; \tag{2.36}$$

$$\Gamma_0 \cong \frac{\Gamma_d F(T_S)}{F(T_S) + W(\Gamma_d - \Gamma_{mS})}. \tag{2.37}$$

2.4 Radiation parameterization

We now describe parameterizations for the infrared and solar radiative fluxes that appear in our prognostic equations.

2.4.a Longwave

Infrared fluxes are calculated using the approach of Stephens and Greenwald (1991), in which the clear-sky infrared emission at the surface and the clear-sky infrared emission at the top of the atmosphere (TOA) are related by a simple function of W, i.e.

$$(\mathcal{R}_{up})_{S,\,clr} = \sigma T_S^4 = (a_1 + c_1 W)\mathcal{R}_{\infty,\,clr}\,. \tag{2.38}$$

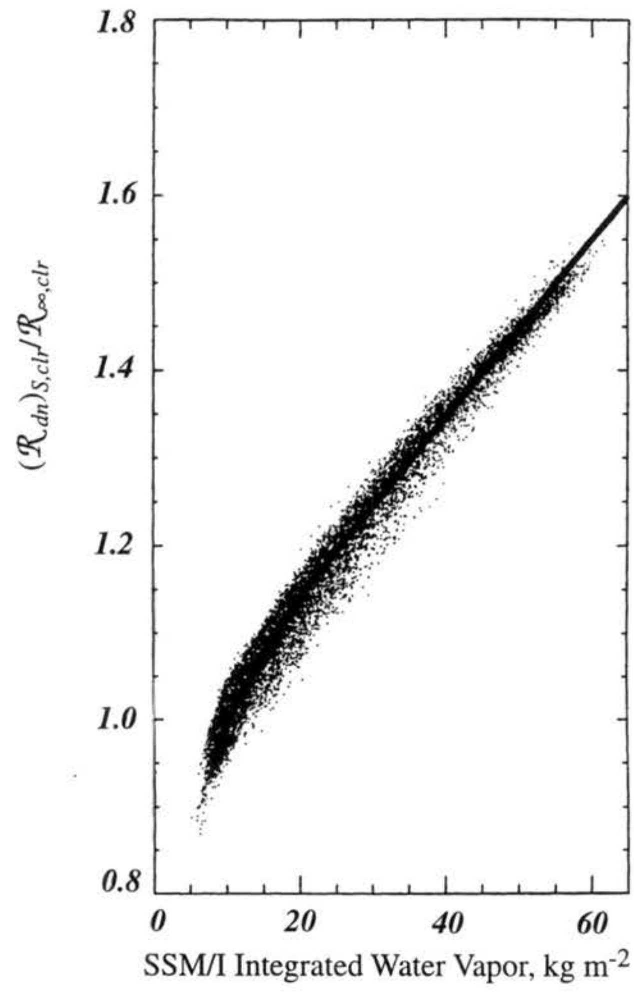

FIGURE 2.6: Results obtained with (2.39) in terms of the ratio $(\mathcal{R}_{dn})_{S,clr}/\mathcal{R}_{\infty,clr}$, as compared with the simulations described in Stephens et al. (1994).

Here a_1 and c_1 are approximately constant and their values are given in Table 2.1. In addition, following Stephens et al. (1994), we assume that the clear-sky downward infrared radiation at the surface is related to $(\mathcal{R}_{up})_{\infty, clr}$ by a simple function of W, i.e.

$$\begin{aligned}(\mathcal{R}_{dn})_{S,\,clr} &= \{[(a_2 - a_0) + c_2 W](1 - e^{-dW}) + a_0\}\mathcal{R}_{\infty,\,clr} \\ &= \left\{\frac{[(a_2 - a_0) + c_2 W](1 - e^{-dW}) + a_0}{a_1 + c_1 W}\right\}\sigma T_S^4,\end{aligned} \tag{2.39}$$

where a_0, a_2, and c_2 are approximately constant and are given in Table 2.1. Figure 2.6 presents results obtained with (2.39), expressed in terms of the ratio $(\mathcal{R}_{dn})_{S,\,clr}/\mathcal{R}_{\infty,\,clr}$, as compared with the radiative-transfer simulations described by Stephens et al. (1994). The assumed simple relationship between $(\mathcal{R}_{dn})_{S,\,clr}/\mathcal{R}_{\infty,\,clr}$ and W fits the simulations adequately for the purposes of this study.

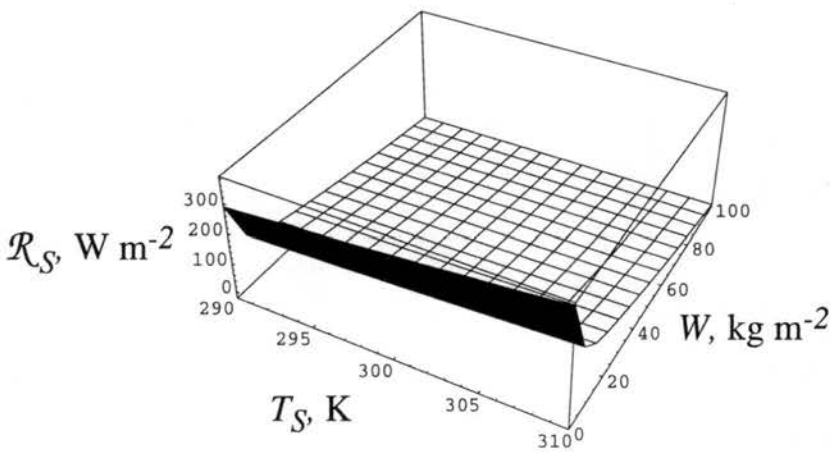

FIGURE 2.7: The net clear-sky longwave radiation at the surface, as a function of T_S and W.

By combining (2.38) and (2.39), we find that the net clear-sky longwave radiation at the surface satisfies

$$\mathcal{R}_{S,\,clr} = \sigma T_S^4 \left\{\frac{(a_1 - a_0 + c_1 W) - [(a_2 - a_0) + c_2 W](1 - e^{-dW})}{(a_1 + c_1 W)}\right\}. \tag{2.40}$$

Simply by rearranging (2.38), we obtain an expression for the net clear-sky longwave radiation at the TOA. Using these simple equations, we can determine the clear-sky net longwave radiation at the surface and the TOA in terms of T_S and W. Figure 2.7 shows the results for the net radiation at the surface. When W is small, $\mathcal{R}_S$ decreases sharply as W

increases. Beyond $W = 40$ kg m^{-2}, T_S and W variations affect $\mathcal{R}_S$ only moderately.

With 100% cloudiness or "overcast" skies, the upward longwave radiation at the top of the convective layer is assumed to satisfy

$$(\mathcal{R}_{up})_{T,\,ovc} = (\mathcal{R}_{up})_{T,\,clr}(1-\varepsilon_{cld}) + \varepsilon_{cld}\sigma T_T^4. \tag{2.41}$$

where ε_{cld} is the longwave emittance of the cloud. The value for $(\mathcal{R}_{up})_{T,clr}$ can be obtained from (2.63) (presented later) with $\mathcal{R}_\infty = \mathcal{R}_{\infty,clr}$.

Having determined a value for $(\mathcal{R}_{up})_{T,clr}$, cloudy-sky values of z_T and T_T can be calculated by following the procedure described in Section 2.5. The cloudy-sky values of z_T and T_T differ from their clear-sky values because clouds reduce the upward longwave flux at level z_T thereby causing the stratosphere to cool. The overcast OLR follows as

$$\mathcal{R}_{\infty,\,ovc} = (\mathcal{R})_{C,\,ovc}(1-\varepsilon_l)(1-\varepsilon_u) + (1-\varepsilon_u)\varepsilon_l\sigma T_l^4 + \varepsilon_u\sigma T_u^4, \tag{2.42}$$

where ε_l and ε_u are the emissivities of the upper and lower stratospheric layers. We adopt a simplified form of the emissivity given by

$$\varepsilon_{l,\,u} = 1 - e^{-k_{l,\,u}\delta p_{l,\,u}}, \tag{2.43}$$

where $k_{l,u}$ is a constant of each layer, and $\delta p_{l,u}$ is a pressure scale. For the upper stratospheric layer, we set $\delta p_u = 2$ mb. For the lower stratospheric layer, $\delta p_l = p_C - 2$ mb, where p_C is the hydrostatic pressure that corresponds to z_C. This idealized form represents an effective emissivity in each sub-layer of the stratosphere. We estimated values of $k_{l,u}$ from more detailed radiative transfer calculations.

The overcast net surface longwave radiation is assumed to satisfy

$$(\mathcal{R}_S)_{ovcst} = \mathcal{R}_{S,\,clr} - (1-\varepsilon_{clr})\varepsilon_{cld}\sigma T_T^4, \tag{2.44}$$

where ε_{clr} is the emissivity of the atmosphere below the cloud. For simplicity, we assume

$$\varepsilon_{clr} = 1 - e^{-kW}, \tag{2.45}$$

where k is a constant whose value is discussed below. Use of (2.45) in (2.44) gives

$$(\mathcal{R}_S)_{ovcst} = \mathcal{R}_{S,\,clr} - e^{-kW}\varepsilon_{cld}\sigma T_T^4. \tag{2.46}$$

Although the emission temperature T_T in (2.44) generally differs from that in (2.41), W is typically large enough so that the second term on the right-hand side of (2.46) is small. Observations (e.g. Stephens et al. 1994) show that for large W the cloud has little effect on the surface longwave fluxes. Nevertheless, we do not neglect the second term. The value $k = 1/8\ \mathrm{m}^2\ \mathrm{kg}^{-1}$, used above, is consistent with the observations.

We use the adjective "all-sky" to denote the actual radiation that occurs for whatever cloud fraction is specified in the model. The all-sky longwave radiation fields are assumed to satisfy

$$\mathcal{R} = \mathcal{R}_{clr} - C_{LW}, \tag{2.47}$$

where C_{LW} is the cloud longwave forcing, which is discussed in Subsection 2.4.c. Equation (2.47) holds for the flux of longwave radiation at the top and bottom of the atmosphere.

2.4.b Shortwave

The reflected overcast shortwave radiation at the TOA is assumed to satisfy

$$(\mathcal{S}_{up})_{ovcst,\ \infty} = (\mathcal{S}_{dn})_C[\alpha_C + (1-\alpha_C)^2\alpha_S\Im^2], \tag{2.48}$$

where α_C is the cloud albedo, α_S is the surface reflectivity, $\Im$ is the transmissivity of the troposphere, and $(\mathcal{S}_{dn})_C = (1\text{-}A)\mathcal{S}_\infty$. The first term in (2.48) is the contribution to the upwelling flux due to direct reflection by the cloud, and the second term allows for reflection by the surface. Making $\Im$ a function of water vapor only, we adopt a standard parameterization for water vapor absorption (Lacis and Hansen 1974). The surface reflectivity is specified to be 0.07, and cloud albedo is parameterized in terms of the *IWP*. For $\alpha_C = 0$, (2.48) gives the reflected clear-sky shortwave radiation at the TOA.

The downward solar radiation at the surface under overcast skies is assumed to satisfy

$$(\mathcal{S}_{dn})_{ovcst,\ S} = (\mathcal{S}_{dn})_C\Im(1+\alpha_C\alpha_S\Im^2)(1-\alpha_C). \tag{2.49}$$

The overcast upward solar radiation at the surface is assumed to be

$$(\mathcal{S}_{up})_{ovcst,\ S} = \alpha_S(\mathcal{S}_{dn})_{ovcst,\ S} = \alpha_S(\mathcal{S}_{dn})_C\Im(1+\alpha_C\alpha_S\Im^2)(1-\alpha_C). \tag{2.50}$$

Hence, the overcast net solar radiation at the surface is

$$\mathcal{S}_{ovcst,\ S} = (\mathcal{S}_{dn})_C\Im(1+\alpha_C\alpha_S\Im^2)(1-\alpha_C)(1-\alpha_S). \tag{2.51}$$

This reduces to the clear-sky net solar radiation at the surface for $\alpha_C = 0$.

As W increases from 0 to 100 kg m^{-2} in Fig. 2.8, the absorbed shortwave radiation at the TOA increases by less than 10 W m^{-2}; and the surface shortwave absorption increases by about 60 W m^{-2}. Hence, the model's atmosphere absorbs an increasingly greater proportion of $\mathcal{S}_{\infty,clr}$ as the column water vapor increases.

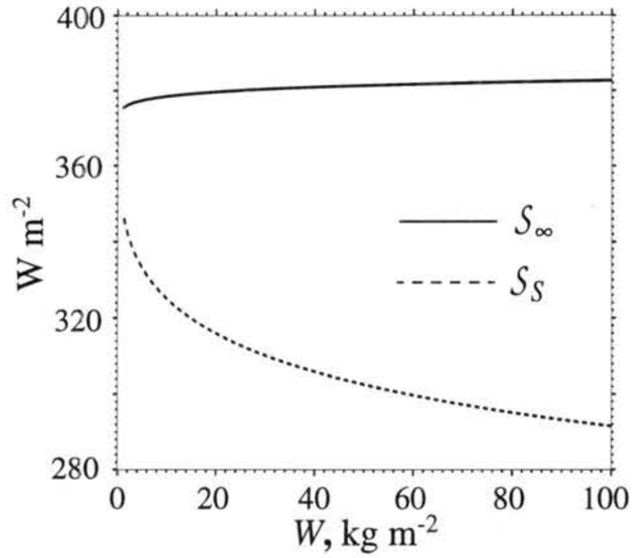

FIGURE 2.8: The net shortwave radiation at the top of the atmosphere (solid curve) and at the surface (dashed curve), as a function of *W*.

The all-sky shortwave radiation fields are assumed to satisfy

$$\mathcal{S} = \mathcal{S}_{clr} + C_{SW}, \tag{2.52}$$

where C_{SW} is the shortwave cloud forcing, which is discussed in the next section. Equation (2.52) holds for shortwave fluxes at the TOA and surface.

2.4.c Cloud properties

The shortwave and longwave cloud radiative forcing at the surface and the TOA are assumed to satisfy:

$$(C_{SW})_{\infty} = f[\mathcal{S}_{ovcst,\infty} - (\mathcal{S}_{\infty})_{clr}], \tag{2.53}$$

$$(C_{SW})_{S} = f[\mathcal{S}_{ovcst,S} - (\mathcal{S}_{S})_{clr}], \tag{2.54}$$

$$(C_{LW})_{\infty} = f[(\mathcal{R}_{\infty})_{clr} - \mathcal{R}_{ovcst,\infty}], \tag{2.55}$$

$$(C_{LW})_{S} = f[(\mathcal{R}_{S})_{clr} - \mathcal{R}_{ovcst,S}]. \tag{2.56}$$

In order to determine the longwave and shortwave cloud radiative forcings defined above, the cloud albedo and emittance must be determined. We assume that the clouds are non-absorbing in the shortwave. Since the clouds in question are produced by detrainment from deep cumuli, we suppose that they are composed of ice crystals. Following Stephens (1984), we assume that

$$\varepsilon_{cld} = 1 - e^{-k_{cld}IWP}. \tag{2.57}$$

The quantity $k_{cld}IWP$ is the infrared optical depth of the cloud. The "standard value" of k_{cld} used here is 75 $m^2\ kg^{-1}$, which is taken to be characteristic of cirrus clouds according to a gross fit of the observed albedo - emittance relationship of FIRE data as reported by Stackhouse and Stephens (1991). For $IWP = 0.06\ kg\ m^{-2}$, $\varepsilon_{cld} \cong 0.99$. Further increases of the *IWP* have little effect on the cloud emissivity, so for $IWP > 0.06\ kg\ m^{-2}$ we have emissivity *saturation*.

To determine the cloud albedo, we modify the relation obtained in a two-stream relationship (e.g. Twomey 1991), i.e.

$$\alpha_C = \frac{(\alpha_C)_{max}\tau/\mu_0}{\tau_0 + \tau/\mu_0}, \tag{2.58}$$

where $(\alpha_C)_{max}$ is a predetermined maximum possible cloud albedo, τ is the shortwave optical thickness of the cloud, μ_0 is the effective cosine of the solar zenith angle, and τ_0 is a parameter that can be related to particle scattering asymmetry. When τ becomes large, α_C approaches its maximum value, which we set to 0.8 in this study. We assume $\mu_0 = 0.5$ throughout this study, although the form of (2.58) accounts for the variation of α_C with μ_0 in a realistic way. The shortwave cloud optical depth τ is parameterized according to

$$\tau = c_{cld}IWP, \tag{2.59}$$

where c_{cld} is a parameter which can be specified or calculated. Equation (2.59) can be derived using the same set of assumptions that define a linear relation between optical depth and cloud liquid water path, as introduced by Stephens (1978).

According to (2.57) and (2.59), the infrared and shortwave optical depths of the ice clouds are proportional to *IWP*, with respective proportionality constants k_{cld} and c_{cld}. Values of these parameters can be discussed in terms of the ratio

$$c_{cld}/k_{cld} \equiv \gamma. \tag{2.60}$$

It is often assumed that $\gamma = 2$ (e.g. Platt 1979), although in reality the broadband value of this quantity is not well known. We show later how the solutions of the model depend on both the value of γ, and the individual values of k_{cld} and c_{cld}. The albedo-emittance relationship, with the parameter values mentioned above, are compared with the FIRE data in Fig. 2.9. The albedo-emittance relationship of the FIRE data is subject to considerable variability, particularly in the high emittance region of the domain. For values of the emittance greater than 0.7, our parameterization and the radiative-transfer models significantly underestimate the cloud albedo, relative to some of the aircraft observations.

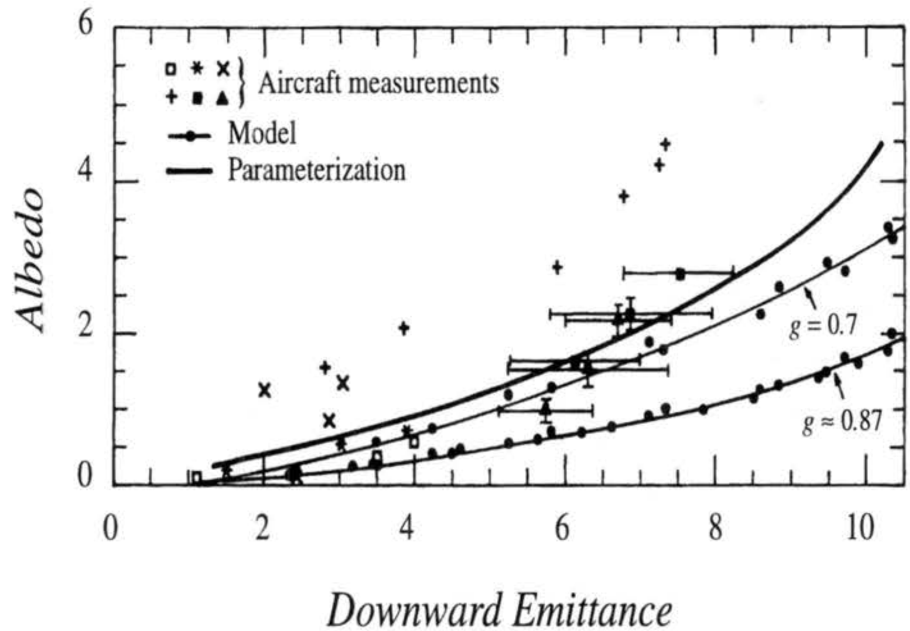

FIGURE 2.9: The albedo and emittance of cirrus clouds deduced from aircraft radiometric measurements summarized in Stackhouse and Stephens (1991; points) and model calculations (lines). The heavy solid curve represents the parameterization embodied in (2.57) through (2.60) with k_{cld} = 75 m^2 kg^{-1}.

2.5 Solution for the tropopause height and temperature

We now consider the calculation of tropopause height and temperature. We define the tropopause to be the maximum altitude reached by convecting parcels. It is also the altitude above which the atmosphere is in radiative equilibrium, rather than in radiative-convective equilibrium (RCE). Since we have assumed that the amount of CAPE in the tropical atmosphere is negligible, the buoyancy constraint would seem to provide no limitation on the depth of the convective layer. That is, convecting parcels could rise indefinitely. In nature, however, the convecting parcels become negatively buoyant as they reach the lower stratosphere. How can we model this in a simple way?

Goody and Yung (1989) described a radiative constraint imposed by the stratosphere which suffices to determine the depth of the troposphere. For a gray-absorbing atmosphere in RCE, the tropopause height is adjusted until the troposphere can deliver the radiative flux required to keep the stratosphere in radiative equilibrium. In contrast, Manabe and Strickler

(1964) and Manabe and Wetherald (1967) calculated the time rate of change of temperature due to radiative heating at each level for a non-gray atmosphere, and then adjusted convectively unstable levels to an assumed lapse rate of 6.5 K km^{-1}. As the upwelling radiative fluxes across an interface (tentatively labeled as the tropopause) increase, the temperature of the layer above increases, and so the static stability increases. As the upwelling fluxes across the interface decrease, the temperature of the layer above decreases, and therefore the static stability decreases so that convective adjustment may become necessary.

These results suggest that the interactions between the stratosphere and troposphere must be modeled in order to realistically determine the tropopause height and temperature. Our model incorporates aspects of the approaches of Goody and Yung (1989) and Manabe and colleagues, plus the constraint of moist static energy conservation for convecting parcels. Given the OLR and the distribution of shortwave heating due to ozone absorption, we find values for z_T and T_T which give temperature continuity across the tropopause, are consistent with radiative equilibrium of the stratosphere, and satisfy (2.16). We will discuss how this is done shortly.

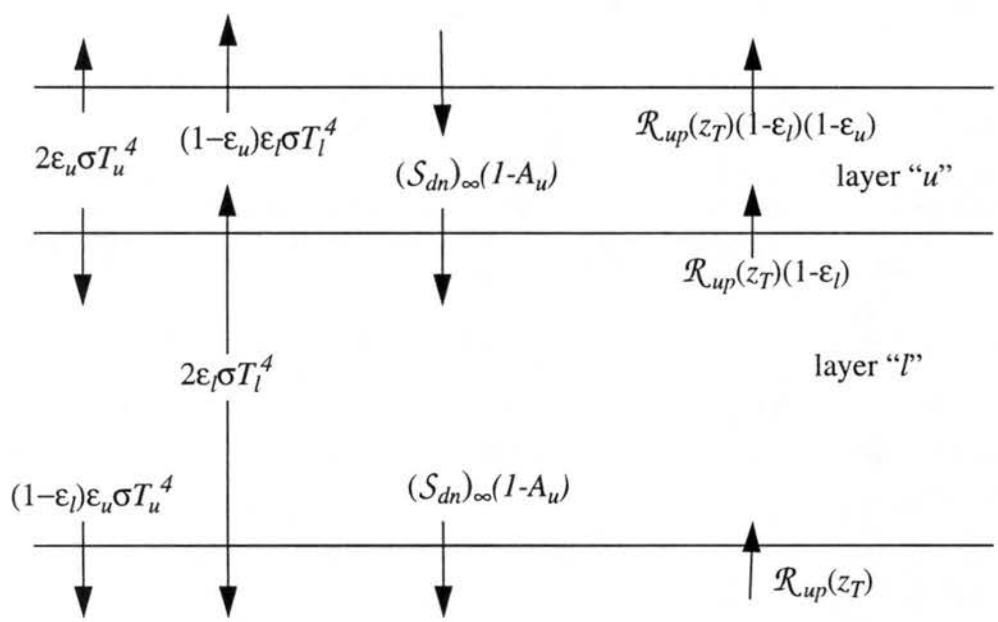

FIGURE 2.10: A schematic that describes the stratospheric radiative balance assumed in this study.

We model the stratosphere as two layers which are both in radiative equilibrium (Fig. 2.10). We assume that the heating due to ozone shortwave absorption occurs only in the upper stratospheric layer, and is balanced by thermal emission. The temperature of the lower stratosphere is assumed to be such that there is a balance between longwave absorption and emission. Scattering in the stratosphere is neglected. For a two-layer stratosphere in radiative equilibrium, we can show that

$$\sigma T_u^4 = \frac{S_\infty \mu_0 A/\varepsilon_u + (1 - \varepsilon_l/2)(\mathcal{R}_{up})_T}{2 - \varepsilon_l \varepsilon_u/2} \tag{2.61}$$

and

$$\sigma T_l^4 = \frac{S_\infty \mu_0 A/2 + (\mathcal{R}_{up})_T\left[1 + \frac{\varepsilon_u}{2}(1 - \varepsilon_l)\right]}{2 - \varepsilon_l \varepsilon_u/2}, \tag{2.62}$$

where ε is the emissivity, A is the shortwave absorptivity of the upper stratospheric sublayer, μ_0 is the solar zenith angle, S_∞ is the mean downward flux of solar radiation at the top of the atmosphere (TOA), and $(\mathcal{R}_{up})_T$ is the upward longwave flux at level z_T. The subscripts u and l refer to the upper and lower sub-layers of the stratosphere, respectively. Since we have an expression for $\mathcal{R}_\infty$ [(2.38)], but not for $(\mathcal{R}_{up})_T$, we write $(\mathcal{R}_{up})_T$ as

$$(\mathcal{R}_{up})_T = \frac{\mathcal{R}_\infty(2 - \varepsilon_l \varepsilon_u/2) - S_\infty \mu_0 A\left[1 + \frac{\varepsilon_l}{2}(1 - \varepsilon_u)\right]}{2 - \varepsilon_u - \varepsilon_l + \varepsilon_l \varepsilon_u/2}, \tag{2.63}$$

i.e, in terms of $\mathcal{R}_\infty$.

We adopt the parameterization of Lacis and Hansen (1974) for shortwave absorption due to ozone. We assume that ozone absorption occurs in the layer between 40 and 55 km. Given values of $\mathcal{R}_\infty$ and p_T, we can determine the temperature as a function of height in the stratosphere from (2.61) and (2.62), and also (2.63) from which we diagnose $(\mathcal{R}_{up})_T$.

The method of solution for T_T and z_T is as follows. We have three equations, (2.16), (2.17), and (2.62), and three unknowns, z_T, T_T, and Υ. To enforce temperature continuity across the tropopause, we set $T_T = T_l$ in (2.62). Given an initial guess for Υ, we compute z_T and T_T from (2.16) and (2.17), and T_l from (2.62). The pressure at the tropopause, p_T, which is needed to calculate the emissivity of the lower stratospheric sublayer, is calculated from (2.24). If $T_T \neq T_l$, the guess for Υ is updated as a weighted average of the old value and a new value obtained from (2.17) for $T = T_l$. The iteration is repeated until the values of T_T and T_l differ by less than 0.01 K; approximately 5 to 10 iterations suffice.

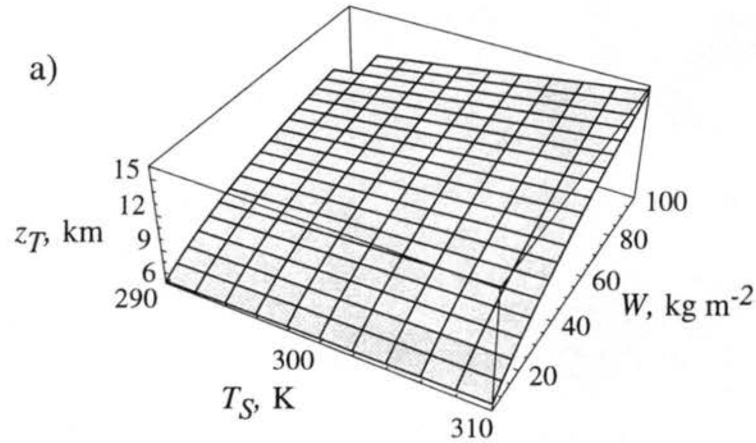

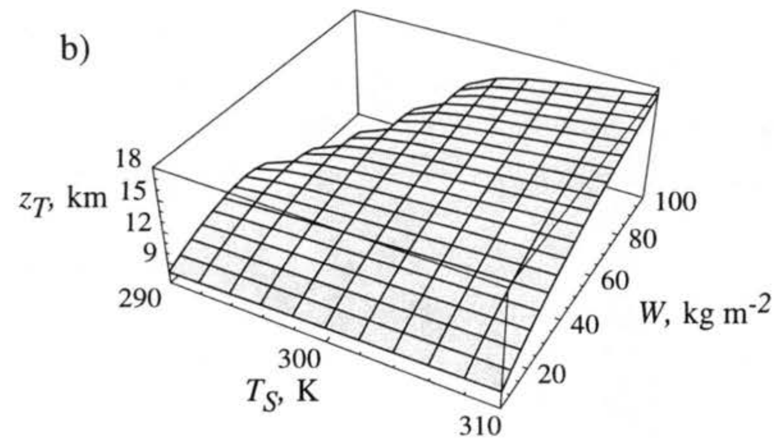

FIGURE 2.11: A contour plot of z_T as a function of T_S and W with a) $f = 0$, b) $f = 0.4$ with t_{prec} = 1000 s. Values are not plotted for T_S-W combinations that W exceeds W_{max} or the lapse rate becomes superadiabatic at the tropopause.

The stratospheric temperature profile depends on the upwelling longwave flux from the troposphere in our model, just as it does for the model of Manabe and colleagues. Since T_T explicitly appears in (2.16), we see that the temperature of the lower stratosphere limits the height of the tropopause; as T_T increases in (2.16), z_T decreases, if T_S and q_S remain fixed. Instead of using a prescribed lapse rate as Manabe and his colleagues did, we use our convective closure to obtain Γ_0. From (2.17) with $T = T_T$, $z = z_T$ and $\Upsilon = 0$, we find that $z_T = (T_S - T_T)/\Gamma_0$. Using $T_S = 303$ K, $T_T = 215$ K, and $\Gamma_0 = 6.5$ K km^{-1}, taken from Fig. 5 in Manabe and Wetherald (for their case of fixed relative humidity), we obtain $z_T = 13.5$ km. In this context, with the lapse rate fixed and constant, our results agree with those of Manabe and his colleagues. Given z_T, T_S and T_T, we can diagnose q_S from (2.16). Equation (2.33) is not needed here because the lapse rate has been prescribed. The value of

q_S that we obtain implies that $RH = 0.66$ in our model, compared to $RH = 0.77$ assumed by Manabe and Wetherald. The RH values differ because we require convecting parcels to conserve moist static energy, but Manabe and Wetherald do not. Water vapor influences their model only through radiative effects, while our model also couples the water vapor to z_T through our convection parameterization. If T_T from their Fig. 5 were smaller, e.g. $T_T = 195$ K, then both the tropopause height and relative humidity for our model would increase, e.g. $z_T = 16.6$ km and $RH = 0.81$. Thus our method probably gives better results for the tropics.

Figure 2.11b shows that if cloud-radiative effects are neglected, then z_T depends strongly on W. For fixed T_S, the upwelling flux at the tropopause increases as W decreases. As depicted in Fig. 2.12b (below), for a given T_S, stronger longwave upwelling causes T_T to increase, which in turn causes z_T to decrease. With W fixed, z_T increases slightly with T_S. We expect z_T to rise as T_S increases if T_T remains constant. T_T increases, however, due to the increase of the upwelling longwave flux with T_S.

2.6 Radiative-convective equilibria

For this section, we assume that $\mathcal{F}_H = 0$, $\mathcal{F}_q = 0$, and $\mathcal{F}_O = 0$, i.e. that there are no horizontal energy or moisture transports out of the convective column. This implies that, in equilibrium, the net energy flux at the TOA, across the atmosphere, and at the surface must be zero. In equilibrium, the evaporation rate has to be balanced by the precipitation rate.

Given values of T_S and W imply an evaporation rate via (2.13). Once $\mathcal{P}$ is known, the IWP follows from (2.11). From T_S, W, and IWP, all of the radiative fluxes can be computed. All the cloudy-sky results were generated with $t_{prec} = 5000$ s, a wind speed of 5 m s^{-1}, and $f = 0.4$ unless otherwise indicated. The upper left-hand quadrants are blacked out because W exceeds W_{max} there, which by (2.33) and (2.13) implies unphysical negative evaporation and precipitation rates.

Figures 2.11 and 2.12 compare the clear-sky values of z_T and T_T with their all-sky counterparts. Comparing Fig. 2.11a with Fig. 2.11b, we see that clouds cause z_T to increase by about 2 km for fixed T_S-W pairs, relative to the clear-sky solutions. Of course, when cloud radiative effects are added we would expect the model to evolve to a T_S-W state different from that obtained with clear skies. As discussed later, increasing the fractional cloudiness also causes z_T to increase. Figure 2.12 shows that clouds cause T_T to decrease by between 5 and 20 K, relative to the clear-sky results. The response of T_T to increasing T_S depends on the value of the IWP in a particular region of the T_S-W domain. In the high-W part of the domain, ε_{cld} has not yet saturated. As T_S increases, the *IWP* and, therefore, the cloud emissivity increase, which implies [from (2.41)] that the longwave upwelling into the stratosphere decreases. Thus, in the high-W part of the domain, T_T must decrease as T_S increases, which is what we see in the figure. Near the blacked-out region of the domain, the *IWP* is small, so cloud radiative effects cause T_T to decrease by only 5 to 10 K. In the low-W portion of the domain, the emissivity is saturated; and as a result, the tropopause temperature follows the surface temperature.

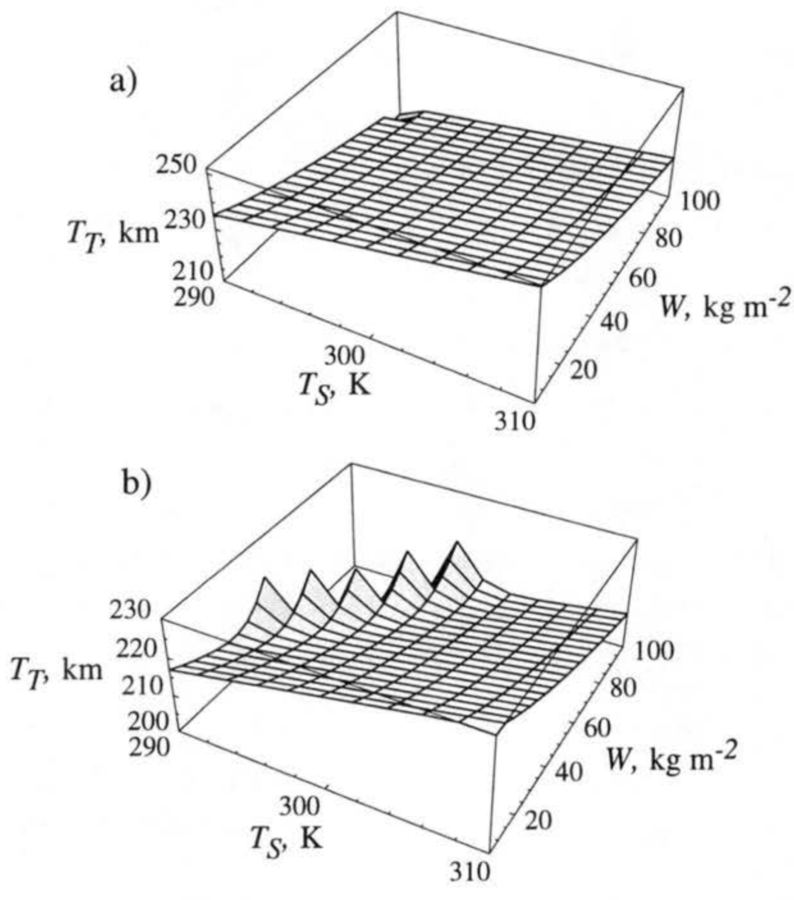

FIGURE 2.12: A contour plot of T_T as a function of T_S and W with a) $f = 0.4$, b) $f = 0$. Values are not plotted for T_S-W combinations that W exceeds W_{max} or the lapse rate becomes superadiabatic at the tropopause.

In Fig. 2.13, the shortwave cloud forcing is negative for all values of T_S and W, and generally increases as the surface temperature increases and as the precipitable water decreases. As expected, the difference in the shortwave cloud forcing at the TOA and at the surface is small, approximately 15 W m^{-2}. As the surface temperature increases, more evaporation is needed to maintain surface energy balance. This requires more precipitation, which results in more *IWP* and brighter clouds. As the precipitable water increases for fixed surface temperature, the evaporation rate decreases, and, in equilibrium, so must the precipitation rate. As a result, increased precipitable water implies weaker convection and optically thinner clouds, which produce less shortwave forcing. The largest plotted values of the shortwave forcing are greater than -100 W m^{-2}, which agrees well with ERBE measurements (Harrison et al. 1990).

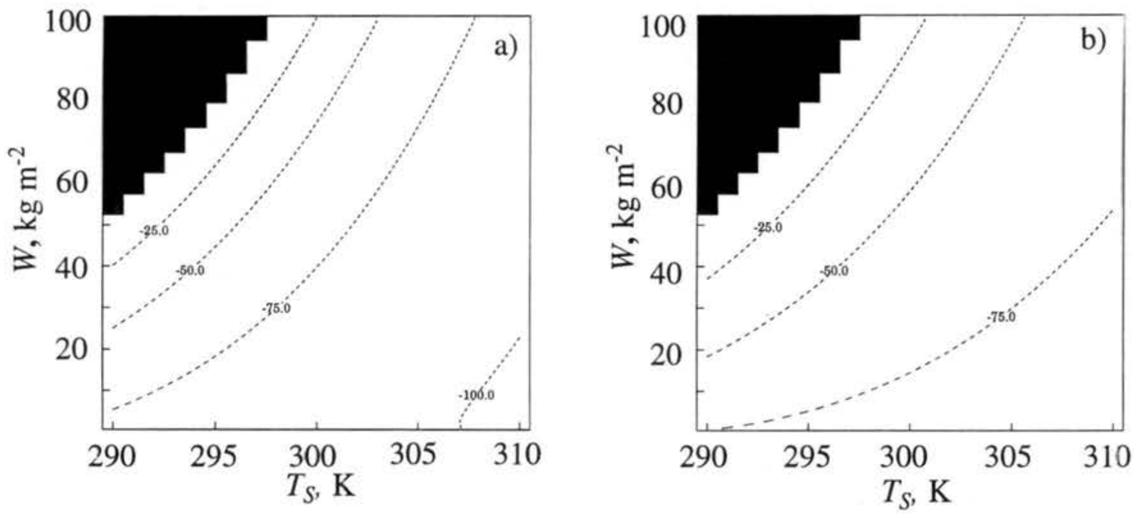

FIGURE 2.13: The shortwave cloud radiative forcing at a) top of the atmosphere, and b) the surface, for the case of uniform cloudiness, as functions of *W* and T_S.

As shown in Fig. 2.14, the longwave cloud forcing increases as the surface warms and as the precipitable water decreases. We expect the longwave cloud forcing to increase as ε_{cld} increases and T_T decreases. Except for the high-*W* part of the domain, T_T basically increases as T_S increases and *W* decreases, which implies that the variations of the cloud forcing induced by ε_{cld} and T_T are opposing. Near the blacked-out region, the rapid increase of cloud emissivity as T_S increases and *W* decreases gives rise to a relatively strong gradient of longwave cloud radiative forcing. Beyond this region, the cloud emissivity has saturated, and T_T increases as T_S increases and *W* increases, which seems to imply that the cloud radiative forcing should decrease. The clear-sky OLR increases at a slightly greater rate than the overcast-sky OLR, however, and for this reason the cloud radiative forcing continues to gradually increase. By design, the longwave forcing at the surface is small when the precipitable water exceeds 40 kg m^{-2}. For $W < 10$ kg m^{-2}, as the surface warms, the surface longwave forcing increases.

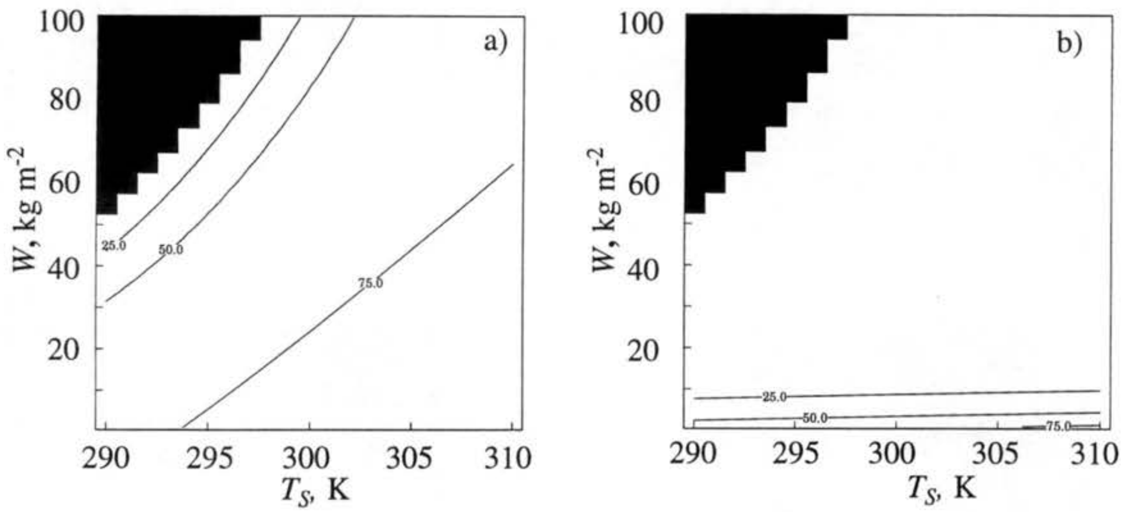

FIGURE 2.14: The longwave cloud radiative forcing at a) top of the atmosphere, and b) the surface, for the case of uniform cloudiness, as functions of W and T_S.

The variations of the net cloud radiative forcing (Fig. 2.15) as a function of T_s and W are complex. The net cloud forcing at the surface is negative, as expected, if W is greater than about 5 kg m^{-2}. The TOA net cloud forcing changes from negative to positive values as the surface temperature increases and the precipitable water decreases. It varies monotonically, but interestingly it remains relatively small across the entire domain. Analyses of ERBE data show that the TOA net cloud radiative forcing in the tropics is small (Harrison et al., 1990). Kiehl (1994) argued that the near-cancellation of the longwave and shortwave forcing results from the cold cloud-top emission temperatures of cumulonimbus towers in the tropics. The clouds trap energy radiated by the surface, and emit at much colder temperatures thereby reducing the OLR, relative to clear skies. In the tropics, the cloud-top emission temperatures are so cold that the longwave cloud radiative effects nearly balance the shortwave cloud albedo effects.

The clear-sky energy imbalances at the surface, at the TOA, and across the atmosphere are shown in Fig. 2.16. As W increases for fixed T_S, the planet and the surface tend to gain energy, but the atmosphere tends to lose energy. Two different processes contribute to these tendencies. First, as W increases for fixed T_S the surface evaporation rate decreases, and this reduced evaporation represents a relative gain of energy for the surface and a relative loss of energy for the atmosphere. Second, the atmosphere emits more longwave radiation to the surface as W increases, thus cooling the atmosphere and warming the surface; at the same time, $\mathcal{R}_\infty$ decreases, although the reduction in $\mathcal{R}_\infty$ is smaller than the increase in the emission to the surface (Stephens et al. 1994). These two effects together warm the surface and

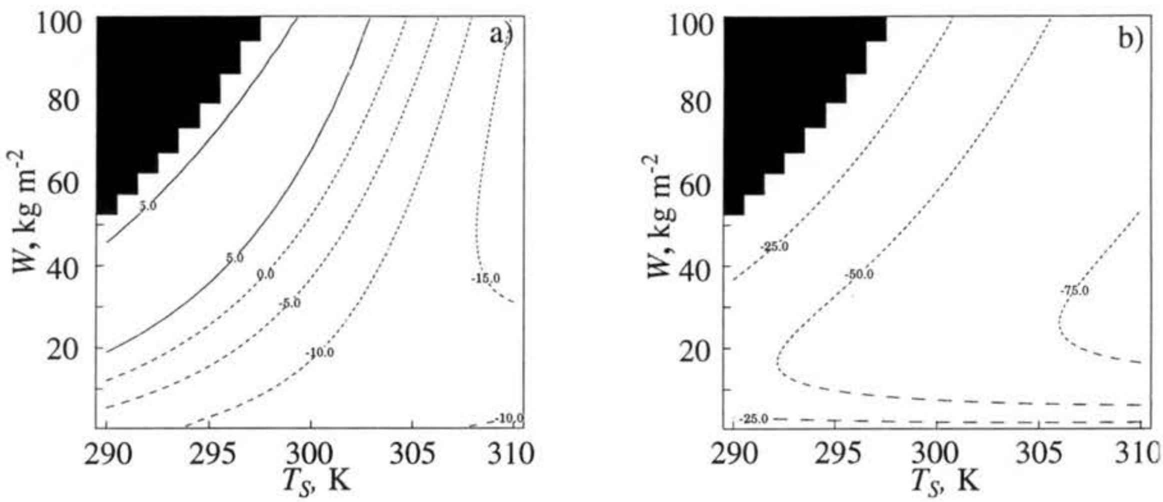

FIGURE 2.15: The net cloud radiative forcing at a) top of the atmosphere, and b) the surface, for the case of uniform cloudiness, as functions of *W* and T_S. Note the different contour intervals used in the panels.

the planet, and cool the atmosphere, which is what we see in Fig. 2.16.

The results shown in Fig. 2.17a are the same as those shown in Fig. 2.16, except that only the zero contours of the imbalances are plotted. We consider $\alpha_S = 0.07$ and $|V_S| = 5$ m s^{-1}. The black region in the upper left portion of each panel indicates where the "Max{ }" function has been triggered in the computation of the evaporation rate, i.e. $W > W_{max}$. Solutions in the black region are, therefore, physically meaningless, and so are not plotted. Figure 2.17 depicts three curves. Along the solid curve, the atmosphere is in energy balance. Along the dashed curve, the surface is in energy balance. Along the dotted curve, the net radiation at the TOA is zero. An equilibrium would exist if the three curves intersected, which they do not in this case.

To the right of their respective zero contours in Fig. 2.17a, the planet and surface lose energy, while the atmosphere gains energy. For the surface and the atmosphere, the values of W required for energy balance of each system increase as T_S increases, but at somewhat different rates. For example, as the surface temperature increases, more water vapor is needed to limit the rate at which the surface cools radiatively and by evaporation. Within the range plotted here, TOA radiation balance occurs only at very high T_S and low W. The TOA radiation balance depends, in the absence of clouds, on T_S, W, and α_S only. The dotted line in Fig. 2.17 is not affected by changing the wind speed.

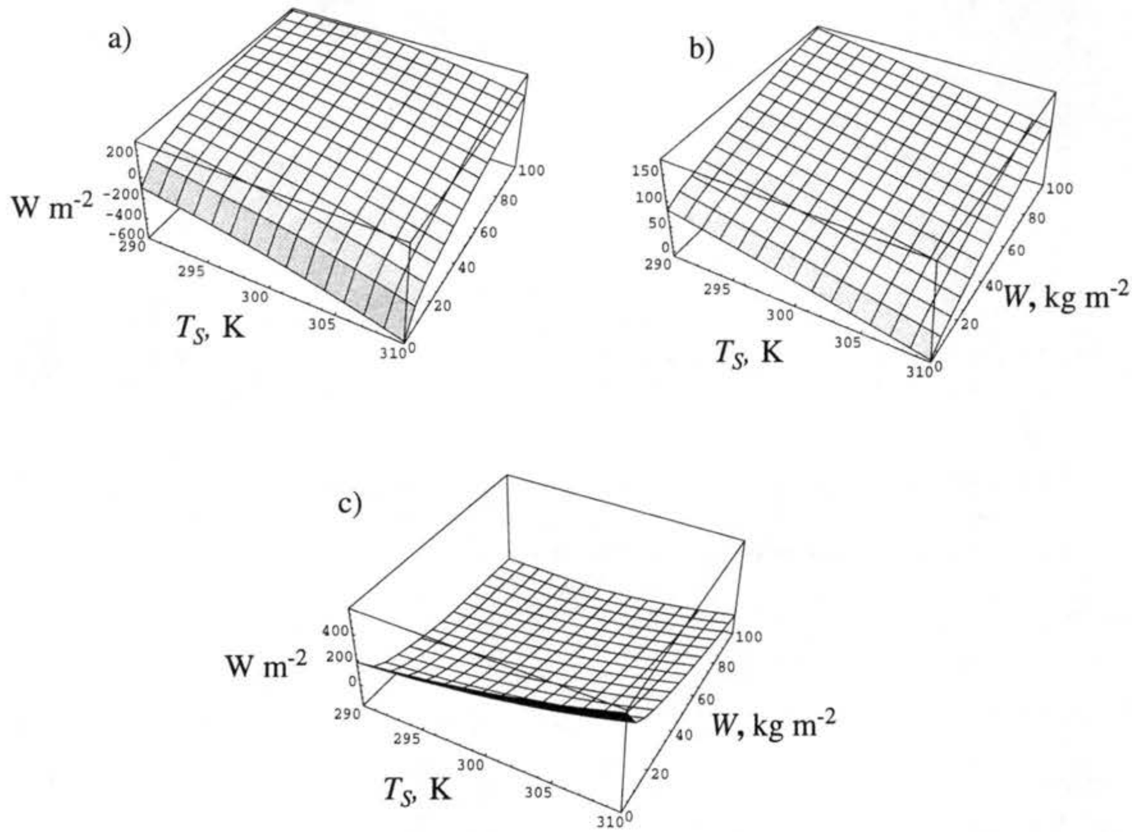

FIGURE 2.16: Energy imbalances for a) the surface, b) the planet, and c) the atmosphere, for a fixed wind speed of 5 m s^{-1}, as functions of W and T_S.

If we regard the surface temperature as given, then the solid curve in Fig. 2.17a, which indicates atmospheric energy balance, represents equilibria of the model. These equilibria would correspond to atmospheric general circulation model-simulated climates obtained with fixed sea surface temperatures; the literature is full of such studies. For a sea surface temperature of 300 K and a wind speed of 5 m s^{-1}, the model atmosphere is in equilibrium with a precipitable water close to 40 kg m^{-2}, which is quite realistic for the tropics.

Figures 2.17b and c show the zero-energy-balance contours obtained with t_{prec} = 5000 s (moderate cloud) and 10,000 s (thick cloud). No equilibria occur for either value of t_{prec}. As the clouds thicken, more column water vapor is required to balance the energy budget at all three levels, particularly at the TOA. Note the similarity between the clear-sky energy balances at the surface and across the atmosphere and those obtained with moderate and thick cloud. From Fig. 2.13, we see that the cloud shortwave forcing at the surface is nearly constant along the zero-balance contours for the surface in Fig. 2.17b and Fig. 2.17c. Since

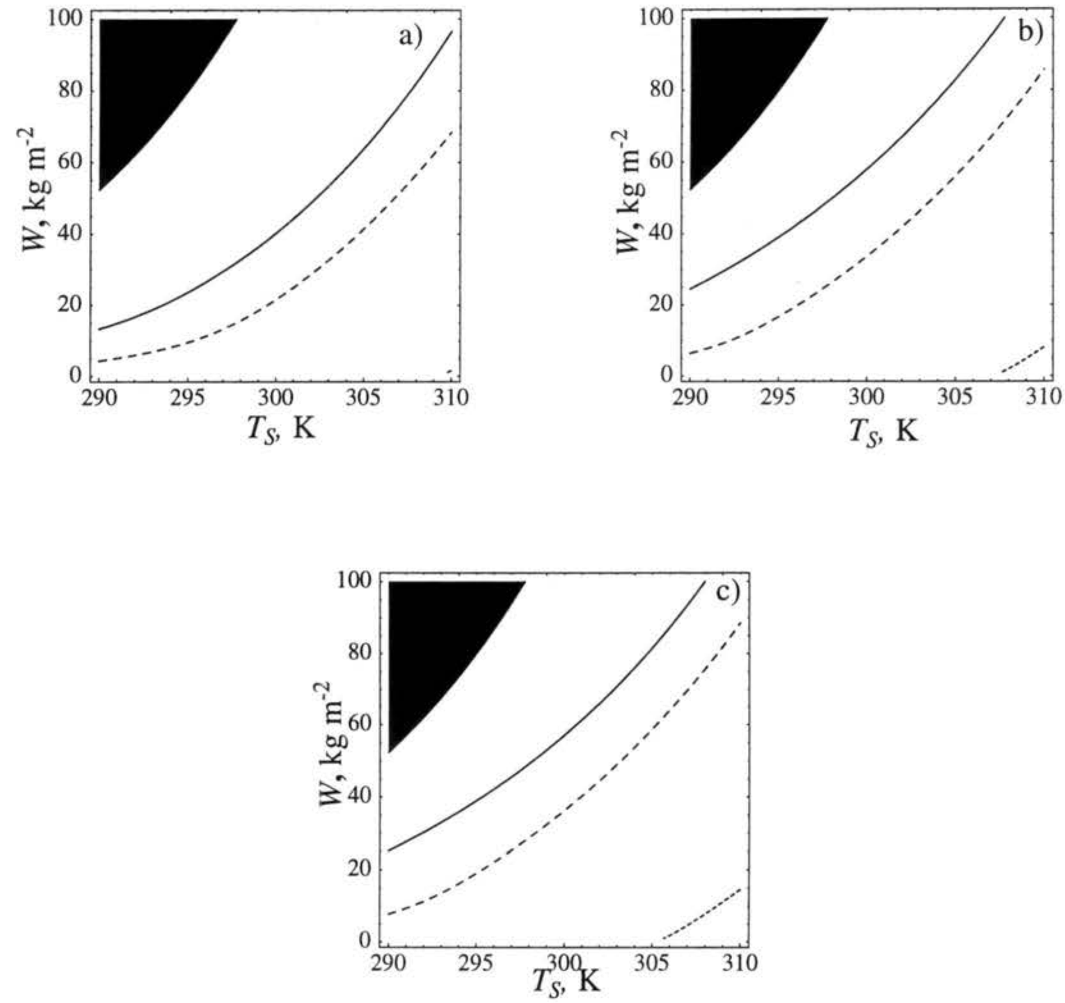

FIGURE 2.17: For α_S = 0.07, $|V|$ = 5 m s^{-1}, and f = 0.4, a progression, from t_{prec} = 0 s (clear sky) in a), to t_{prec} = 5,000 s (moderate cloud) in b), to t_{prec} = 10,000 s (thick cloud) in c) are shown. The contours depict the T_S-W pairs for which the atmosphere (solid line), the surface (dashed line), and the TOA (dotted line) are in energy balance.

longwave cloud radiative forcing contributes little to the surface energy balance, the clear-sky surface energy balance dictates the shape of the all-sky zero-balance contour at the surface. If we subtract the net cloud radiative forcing field at the TOA from that at the surface, we can show that the same conclusion approximately holds for the energy balance across the atmosphere.

We computed the energy budgets for various combinations of cloud fractions and wind speeds. The model is in equilibrium for t_{prec} = 15 000 s, a very weak prescribed wind speed of 1 m s^{-1}, T_S = 313 K and W = 12 kg m^{-2}. Since energy balance must be achieved locally, this warm, dry equilibrium does not seem altogether unreasonable. The low column water

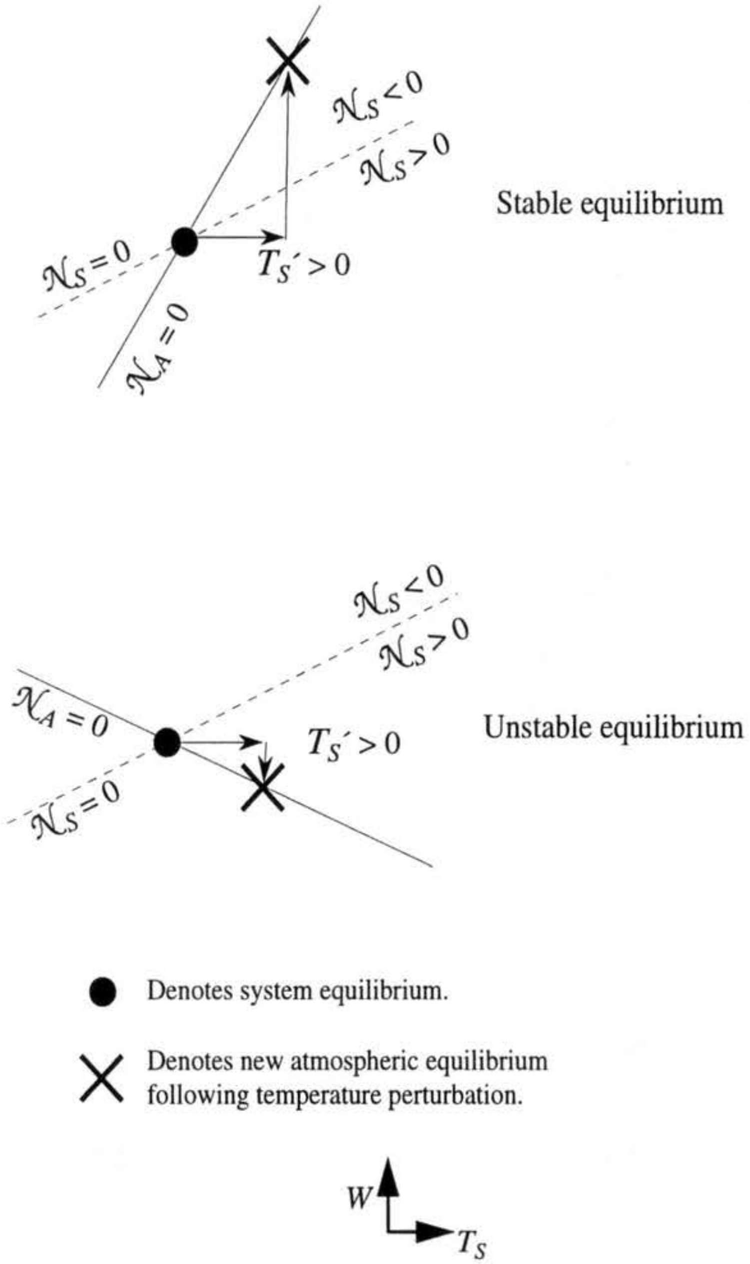

FIGURE 2.18: This schematic graphically illustrates unstable and stable equilibria of the earth-atmosphere system.

vapor makes the atmosphere's greenhouse effect small, so that radiation is very efficient at transporting heat to space.

The equilibrium solution discussed above is unstable in a coupled model, as can easily be demonstrated by time integration of the equations. Figure 2.18 graphically illustrates the mechanism of the instability. If we perturb the equilibrium by increasing the sea surface temperature, the atmosphere will quickly equilibrate, long before the ocean can cool off again, so that the model will find itself along the solid line (which denotes atmospheric equilibrium). As we move up the solid line, the surface energy imbalance becomes positive, i.e. the surface tends to warm. The initial positive perturbation of the sea surface temperature is thus amplified, and the system moves away from equilibrium; in other words, instability occurs. This happens whenever the solid line is to the left of the dashed line on the "warm" side of equilibrium, as it is in the upper left-hand panel of Fig. 2.18.

When the wind speed is increased to 5 m s^{-1}, the water vapor amount increases and the greenhouse effect becomes too strong for the system to reach equilibrium. Results from time integrations of the model provide a basis for an interpretation of the model's inability to reach equilibrium of the ocean-atmosphere system. As the surface warms, the precipitable water increases and leads to more surface warming. The evaporative cooling cannot balance the radiative heating and the surface temperature increases without bound. We identify this condition as a runaway greenhouse (Ingersoll 1969). Although our model produces a warm and dry equilibrium, it is unstable, so our results tend to confirm those of Pierrehumbert (1995); in order to find an equilibrium that resembles the observed climate, a second mostly non-convecting, low-water-vapor region is needed to receive and radiate to space the excess energy of the convecting region.

2.7 Equilibria with prescribed lateral energy and moisture transports

We have argued above that lateral energy and moisture transports are required to account for the observed mean climate of the deep tropics. As shown schematically in Fig. 2.19, the RCE state is quite different from the observed state, in terms of lateral moisture and energy transports.

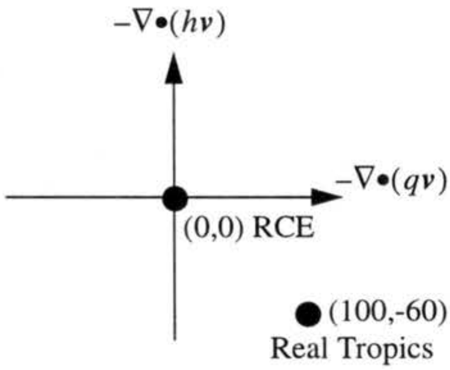

FIGURE 2.19: Schematic phase diagram showing the lateral flux convergences of moisture (*x* axis) and moist static energy (*y* axis) in the tropics.

To show how the model responds to realistic transports, we alter its hydrological and energy budgets to include prescribed transports.For the following runs, we have prescribed the moisture and energy transports as $\mathcal{F}_q = 100$ W m^{-2} (Trenberth and Guillemot 1995) and $\mathcal{F}_H = -60$ W m^{-2} (Ramanathan and Collins 1987), respectively. We set $\mathcal{F}_O = 0$ for simplicity.

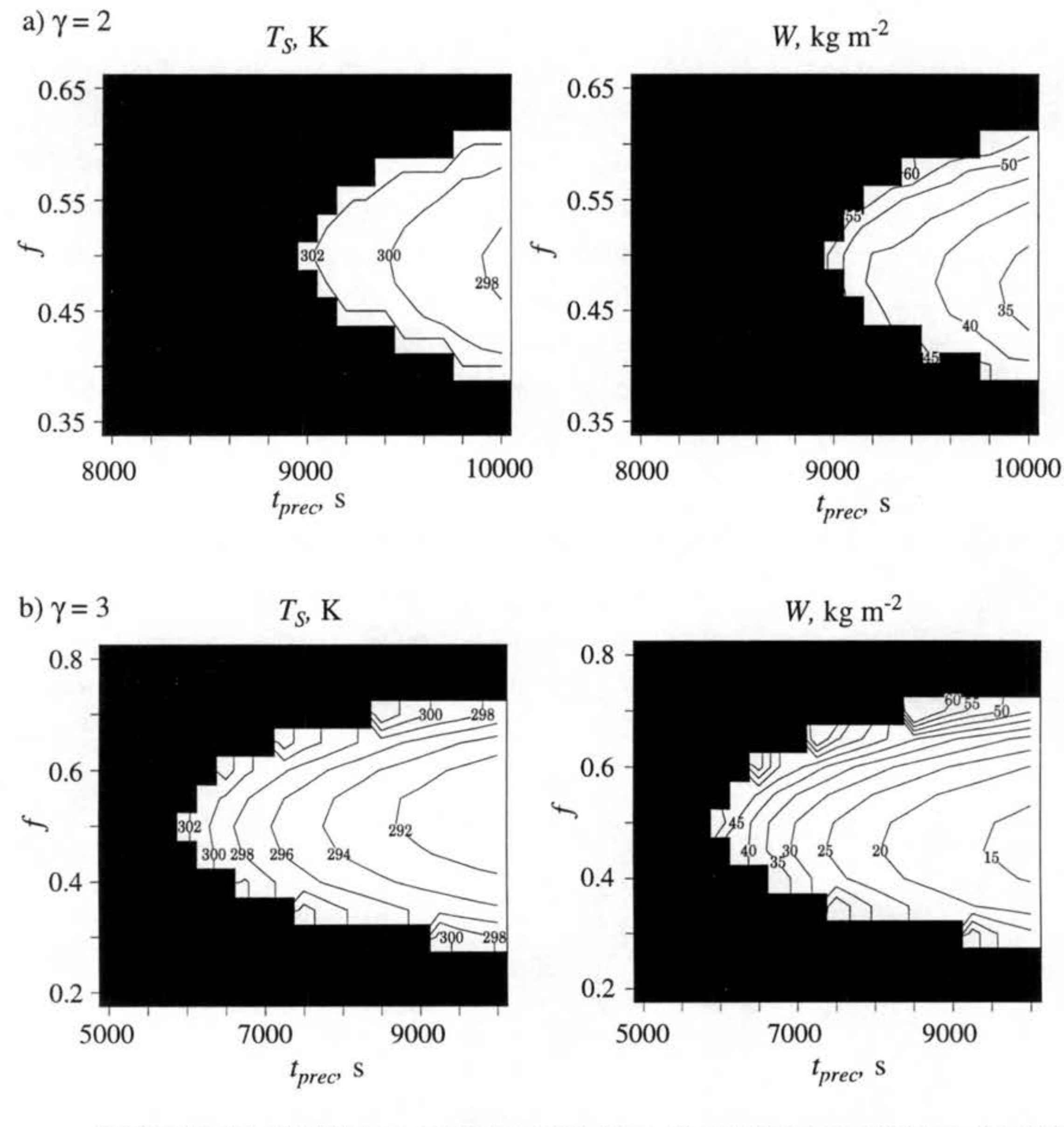

FIGURE 2.20: Equilibrium solutions with prescribed lateral energy and moisture transports are presented. The plots show T_S and W as functions of t_{prec} and f for $\gamma = 2$ (upper plots) and $\gamma = 3$ (lower plots). Values are not plotted for T_S-W combinations for which no solution was found.

The equilibrium results are presented in Fig. 2.20 for $\gamma = 2$ (upper panels), for $\gamma = 3$ (lower panels), and for a wind speed of 5 m s^{-1} in both cases. If the model did not reach equilibrium for a given f-t_{prec} combination, results were not plotted. In contrast to the radiative-convective simulations, the model now can find equilibria for a range of f and t_{prec}. In general, T_S and W decrease as t_{prec} increases, for fixed f. For fixed t_{prec}, minima of both fields are evident near $f = 0.45$. For $\gamma = 2$, T_S lies between 295 and 302 K, while W ranges between 35 and 50 kg m^{-2}. With $\gamma = 3$, values for both fields are somewhat lower. Given the simplicity of the model, these values seem sufficiently realistic.

The model reaches equilibrium for a greater range of f-t_{prec} combinations with $\gamma = 3$ than with $\gamma = 2$. As suggested by Fig. 2.15 and Fig. 2.21, the net TOA cloud forcing becomes more negative as γ increases from two to three. Consequently, with larger γ, the net radiative flux at the TOA balances the prescribed lateral energy transport over a wider range of f-t_{prec} combinations. In overlapping regions in which the model reaches equilibrium for both values of γ, the equilibrium values of T_S and W are smaller for $\gamma = 3$ than for $\gamma = 2$. With relatively brighter clouds for $\gamma = 3$, the lower $\mathcal{R}_*$ that results from a lower surface temperature is sufficient for the net radiation at the TOA to balance the prescribed lateral energy transport. Although brighter clouds reduce the shortwave radiation absorbed by the ocean, the lower surface temperature tends to reduce the upward longwave radiation and evaporation. In order to cool the surface sufficiently, the model decreases W which leads to a larger evaporation rate and a smaller downward longwave flux at the surface.

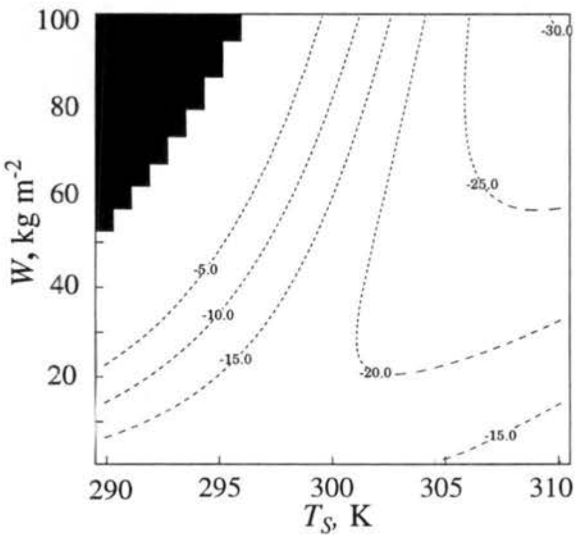

FIGURE 2.21: Contour plot of net cloud radiative forcing at the TOA for $\gamma = 3$.

To understand this behavior of the model for a given value of γ, consider Fig. 2.22 which shows the net atmospheric radiative cooling (*ARC*) as a function of t_{prec} and f, where

$$ARC = \mathcal{S}_S - \mathcal{S}_\infty + \mathcal{R}_\infty - \mathcal{R}_S. \quad \textbf{(2.64)}$$

Holding f fixed, the *ARC* decreases as t_{prec} increases. From (2.11), the *IWP* is proportional to both $\mathcal{P}$ and t_{prec}, whose changes oppose each other. With lateral flux convergences included in these simulations, $L\mathcal{P}$ no longer equals the *ARC*, although $\mathcal{P}$ still decreases as the *ARC* decreases. The net effect is that the *IWP* increases slightly across the range of t_{prec} for which equilibria occur. Since the *IWP* ranges between 0.25 and 0.35 kg m^{-2}, the cloud emissivity has saturated and the *IWP* increase causes the clouds to brighten without affecting the OLR. As a result, the surface temperature must fall in order to reduce the OLR and maintain energy balance at the TOA. Since $\mathcal{P} = \mathcal{E} + \mathcal{F}_W$ in equilibrium, and $\mathcal{F}_W$ is fixed, changes of the evaporation rate follow those of the *ARC*. Hence, the evaporation rate decreases as t_{prec} increases, which implies from (2.13) that W/W_{max} increases as t_{prec} increases. The surface temperature decrease implies that W_{max} must decrease, and thus W must fall rather strongly in order for the evaporation rate to decrease. Despite the lower surface temperature, the net upward longwave radiation actually increases, because the decrease in W makes the atmosphere more transparent to longwave radiation. Hence, the increase in $\mathcal{R}_S$ is actually the main contributor to the decrease in the *ARC*.

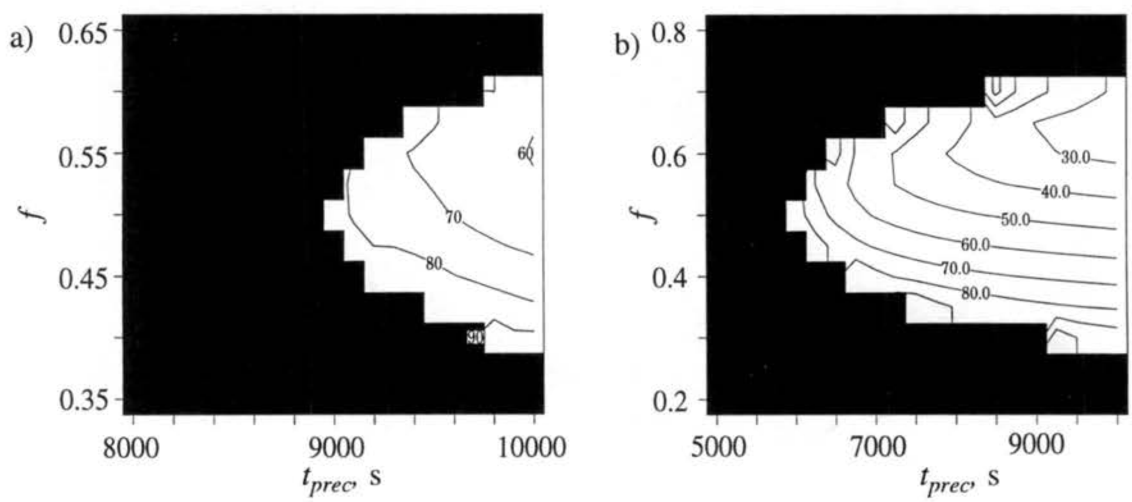

FIGURE 2.22: Contour plots of atmospheric radiative cooling for $\gamma = 2$ (a) and $\gamma = 3$ (b). Values are not plotted for T_S-W combinations for which no solution was found.

For fixed t_{prec}, the minima of T_S and W for $f = 0.45$ are also quite interesting. With f relatively large, the *ARC* is weak which implies that the latent heating of the atmosphere is relatively weak. In order to balance the hydrological cycle, the evaporation rate must decrease. The model accomplishes this by increasing W to approximately 40 kg m^{-2}, which makes the atmosphere more opaque to longwave radiation, and therefore causes T_S to increase. With a higher W, the surface must radiate at a higher temperature in order for the TOA net radiation to achieve the proper balance. In the middle range of the cloud fractions, the *ARC* is stronger and $\mathcal{P}$ is higher. The model adjusts by decreasing W. With smaller W, the surface evaporative and radiative cooling increase and cause the surface temperature to decrease. At the lowest cloud fractions, the *ARC* is strong and $\mathcal{P}$ is large. Nevertheless, the shortwave cloud radiative forcing is relatively weak because the cloud fraction is small. Correspondingly, T_S increases.

2.8 Summary

We have presented an idealized but physically based radiative-convective model with a hydrological cycle. The prognostic variables of the model are the precipitable water and the sea surface temperature. Cumulus convection is parameterized using a very simple closure assumption based on the work of Arakawa and Chen (1987) and Arakawa (1993). Surface evaporation is parameterized using a bulk aerodynamic formula, in which the surface wind speed is prescribed. Surface sensible heat flux is neglected. Radiative transfer is parameterized using simple methods suggested by the work of Stephens et al. (1994) and others cited in the text. The atmospheric lapse rate is also determined by the model.

Our clear-sky results show that realistic quasi-tropical equilibria occur for realistic (warm) prescribed sea surface temperatures and surface wind speeds, but realistic clear-sky equilibria of the tropical atmosphere-ocean system do not occur. When the surface temperature is allowed to vary, the model runs away. This imbalance indicates the need for lateral energy transports and/or radiatively active clouds.

We have shown that simulating realistic cloud radiative effects allows the model to reach very warm, dry equilibrium. Because the radiative-convective equilibrium solutions do not resemble the observed tropical climate, we tested prescribed realistic lateral energy and moisture transports. With tropical moisture and energy convergence specified as 100 W m^{-2} and -60 W m^{-2}, respectively, and for t_{prec} = 9500 s, f = 0.5, γ = 2, and a wind speed of 5 m s^{-1}, the equilibrium solution occurs for T_S = 300 K and W = 40 kg m^{-2}, which are quite reasonable.

We also found that the tropopause height and temperature are sensitive to cloud radiative effects. The decreased upward longwave flux that results when cloud radiative effects are included causes the tropopause temperature to fall as cloud optical thickness or cloud fraction increase. Reinforcing this trend is the concurrent increase of column water vapor, which reduces the clear-sky contribution to the OLR.

As either the cloud optical thickness or cloud fraction increase, the shortwave radiation absorbed by the surface decreases. To reach energy balance, the column water vapor must increase in order to reduce surface evaporative and radiative cooling. The buoyancy condition for non-entraining parcels, (2.16), dictates that for fixed T_S, the tropopause height must increase as the tropopause temperature decreases and the surface relative humidity increases, both of which occur as the cloud optical depth and cloud fraction increase. The cloud fraction strongly affects the height and temperature of the tropopause because it affects the longwave radiation upwelling into the stratosphere. The effects of cloud optical thickness are self limiting, however, because the emissivity is greater than 0.999 for *IWP* larger than 0.1 kg m^{-2}.

The key sensitivities in this model are to the prescribed wind speed, to γ, and to the values of c_{cld} and k_{cld}, and t_{prec}. Equilibrium solutions with prescribed lateral energy and moisture transports showed a marked sensitivity to γ, the ratio of shortwave to longwave optical depths, and to f. In the next chapter, we shall add a "radiator fin" and model-predicted surface wind speeds.

CHAPTER 3

Walker Circulation

3.1 Introduction

The literature review in Chapter 1 shows that the steady tropical ocean-atmosphere general circulation remains inadequately understood. Many of the previous studies illustrate sensitivities of the tropical climate (Lindzen and Nigam 1987; Ramanathan and Collins 1991), or describe the linear response of the tropical climate to small perturbations (Gill 1980; Geisler 1981; Rosenlof et al. 1986). Their value was primarily to show the processes and interactions which must be considered in a theory of the steady tropical climate. Recent studies with box models (P95, SL96; M97; L99) have improved our understanding because they actually simulate the tropical ocean-atmosphere circulation in a simplified way. However, their applicability is somewhat limited due to their extreme simplifications. For example, P95 neglected cloud radiative effects and specified the potential temperature difference between the upper and lower branches of the tropical circulation. A momentum budget was not incorporated in P95, M97, and L99, and for SL96, the speed of the ocean currents was assumed to be a quadratic function of the east-west temperature difference.

In Chapter 2, we presented and discussed results from our model of the tropical WP. We showed that clear-sky radiative convective equilibria do not occur. As the surface temperature increases, the precipitable water tends to increase, and so the longwave trapping effect of water vapor reduces the OLR and prevents equilibrium. When cloud radiative effects are included, the model produces a very warm, very dry equilibrium. This high-T_S, low-W combination results in a relatively large value of the OLR which can balance the incoming solar radiation. We also showed that realistic prescribed horizontal transports of energy and moisture make it possible to find a realistic equilibrium. Because the horizontal transports and wind speed were specified, however, the results presented in Chapter 2 are far short of a simulation of the tropical climate. In order to simulate the climate, we must compute the exchanges of moisture, energy, and momentum between the WP and CP regions of the model. The primary goal of this chapter is to add additional physics to make it possible to compute the energy and moisture transports and the wind speed.

In this chapter, we formulate a model which includes a simplified momentum budget for the CPBL, which parameterizes the radiative effects of stratocumulus and trade cumulus clouds, and which explicitly calculates the potential temperature or dry static energy difference between the upper and lower branches of the simulated Walker circulation. Throughout this chapter, we contrast and compare the formulation of our model with those of P95, SL96, M97, and L99. In Sections 3.2, 3.3, and 3.4, we describe the equations and assumptions used to simulate the atmosphere in the WP and CP regions, and the ocean, respectively. Section 3.5 describes the radiation and cloud parameterizations used for the atmospheric model in the CP region. In each section, we present stand-alone results for the different components in order to illustrate their various sensitivities. Because our model of the atmosphere for the WP region was fully discussed in Chapter 2, it is only briefly described here.

3.1.a Overview of our model

As discussed in Chapter 1, the Walker circulation consists of a convectively driven upper-tropospheric outflow from the WP to the CP, and a near-surface inflow from the CP trade-wind boundary layer to the WP (Fig. 3.1). The boundary-layer mass flux over the CP is forced by a horizontal pressure gradient which is induced by an SST gradient. The air exiting the CPBL is replaced by free-tropospheric air entrained into the boundary layer. Over the WP, the westward horizontal mass flux decreases to zero at the western boundary, as the mass flow turns upward and departs the boundary layer in the convectively active region. As the convective outflow travels eastward over the CP, it undergoes radiative cooling and subsidence warming. A positive zonal pressure gradient decelerates the wind as it crosses the CP. We require that the eastward mass flux decrease to zero at the eastern boundary of the upper troposphere.

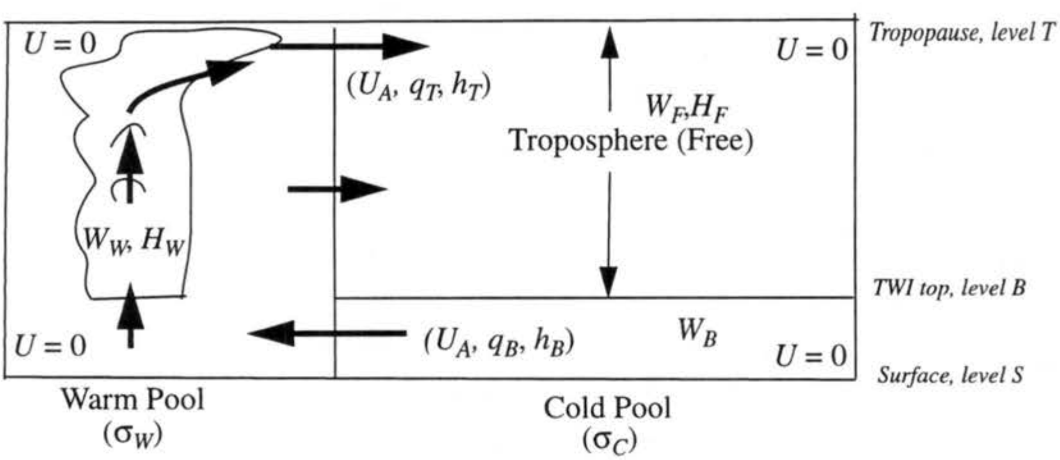

FIGURE 3.1: Schematic of the two-box atmosphere model. Heavy arrows denote winds; thin arrows depict the vertical boundaries of the free troposphere.

As discussed by Philander et al. (1996), idealized GCM simulations suggest that the Intertropical Convergence Zone (ITCZ) occurs in the NH primarily due to the slope of NH land masses with respect to lines of constant longitude. In the present study, we consider an idealized flow in which the WP lies on the equator. This idealization allows us to assume that the Coriolis effect plays no role, i.e. $f = 0$. Our assumption is similar to that of Sun and Liu (1996), in which the Coriolis effect is not taken into account.

As shown in Fig. 1.1, sea surface temperature (SST) gradients across the tropical Pacific ocean are very small, especially in the WP. We assume that the SST is uniform across the WP, and varies linearly across the CP. To the extent that the local SST controls the zonal pressure gradient in the tropics, the pressure is horizontally uniform across the WP. Horizontal temperature gradients in the free tropical troposphere are small due to the weak rotation (Charney 1963). Consistent with these findings, we assume that temperature is uniform across the WP atmosphere. Although a small temperature gradient is required to produce a realistic horizontal pressure gradient above the CPBL, we neglect the temperature gradient for simplicity. Figure 3.2 shows the assumed temperature profile in the two regions. We represent the TWI of the CP region as a discontinuous jump in temperature.

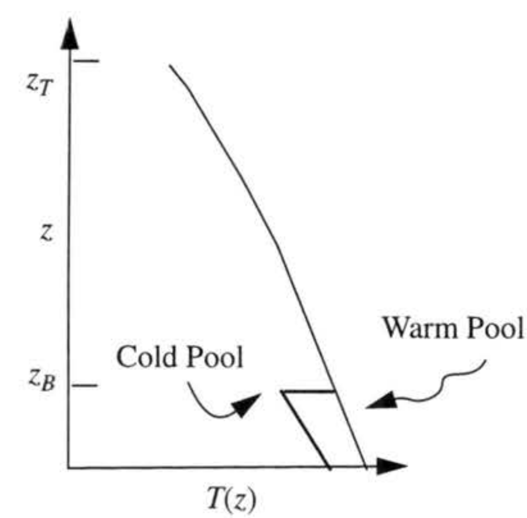

FIGURE 3.2: Schematic illustrating the idealized vertical temperature profiles in the CP and WP.

3.2 Warm-pool model

3.2.a Equations

The governing equations for the atmosphere in the WP region are

$$\mathcal{N}_{\infty W} - \mathcal{N}_{SW} + \mathcal{F}_H = 0\,, \tag{3.1}$$

$$\mathcal{E}_W - \mathcal{P}_W + \mathcal{F}_q = 0, \tag{3.2}$$

$$-u_{BI}\frac{\Pi_{BI}}{g} = U_A, \tag{3.3}$$

which are the steady moist static energy budget for the atmosphere, the moisture budget, and continuity equation. The subscripts I and B denote quantities at the interface between the WP and CP and in the boundary layer, respectively. U_A is the mass flux from the WP region to the CP region in the free troposphere, u_{BI} is the mean wind speed across the depth of the boundary layer, and $\Pi_{BI} = p_S - p_B$. The pressure p_B represents the level of the trade-wind inversion. For a true mass flux, the units should be kg s^{-1}, but the units of U_A are kg m^{-1} s^{-1}. This difference occurs because our equations are for motions in the x-z equatorial plane, and so motions and variations in the meridional direction have not been considered. In order to get the right units, we could simply multiply the equations by 1 m. There is no momentum budget for the WP region because u_{BI} is determined by the SST gradient in the CP.

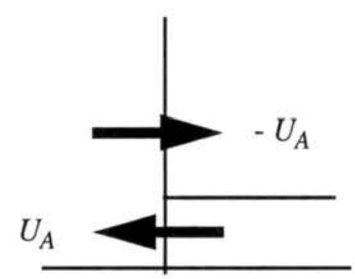

FIGURE 3.3: Schematic illustrating the mass fluxes for the model.

The steady moist static energy and moisture budget equations can be obtained from (2.23) and (2.12), respectively, by neglecting the time derivatives. To avoid confusion, we introduce the subscripts C and W to denote quantities above the CP and WP, respectively. A derivation of (3.1) is given in Appendix 1. As shown in Appendix 1, if the horizontal averaging of the vertically integrated moist static energy equation is taken over the entire width of the WP, then

$$\mathcal{F}_H \equiv \frac{U_A(h_{BI} - h_{FI})}{\sigma_W}, \tag{3.4}$$

where the symbols h_{FI} and h_{BI} denote the values of h which correlate with U_A to give the vertical-mean horizontal energy transport in the free troposphere and boundary layer, respectively, and σ_W is the width of the WP. We use the subscript F to represent quantities in the free troposphere, which is defined as the layer between the TWI and tropopause. Table 3.1 describes the symbols used in the coupled model. In deriving (3.4), we have assumed that u vanishes at the western boundary of the WP, and so the net flux is determined by the flow at the eastern boundary of the WP. Similarly, the vertically and horizontally integrated water vapor flux convergence for the WP is defined as

$$\mathcal{F}_q \equiv \frac{U_A(q_{BI} - q_{FI})}{\sigma_W} , \tag{3.5}$$

where q_{BI} and q_{FI} are defined analogously to h_{FI} and h_{BI}. The two quantities $\mathcal{F}_H$ and $\mathcal{F}_q$ are calculated, as discussed later. The widths of the WP and CP satisfy

$$\sigma = \sigma_C + \sigma_W , \tag{3.6}$$

where σ is the width of the tropical Pacific basin.

Equation (3.2) turns out to be extremely important in determining the climate of the WP and the intensity of the Walker circulation. The evaporation rate is determined locally (although the wind stress is determined by the SST gradient), and the net inflow of moisture to the WP region is influenced remotely by the CP. Hence the precipitation rate follows as that which balances the moisture added by evaporation and advection. From Chapter 2, recall that the optical thickness of cirrus clouds in the WP region is determined by the precipitation rate. Because we fix the cloud fraction and thereby eliminate any feedbacks associated with cloud fraction, the precipitation rate, and hence the radiative properties of clouds, can vary due to local and remote influences.

Our parameterization for cloud radiative properties over the WP is far different from the approaches taken for previous box models. Pierrehumbert (1995) neglects the radiative effects of cirrus clouds over the WP altogether, arguing that the net radiative effect at the TOA is small compared to the net TOA energy imbalance. Miller (1997) simply specifies cloud radiative effects over the WP, while Larson et al. (1999) specify the cloud optical properties for cirrus anvils over the WP so that the net cloud radiative forcing at the TOA is nearly zero. Because the net radiation at the TOA governs the horizontal energy transport from the sides of the ocean-atmosphere column, the results from these studies rest on the observed near-cancellation of shortwave and longwave radiative effects of cirrus clouds. However, the primary shortwave cloud radiative effect is to cool the surface, while the main longwave effect is to warm the atmosphere. With the exception of L99, the other box models do not realistically account for the differing regions of influence of the shortwave and longwave cloud radiative effects.

TABLE: 3.1: Symbols used in the Coupled Model.

Symbol	Definition	Value
σ	width of the Pacific basin	1.5×10^7 m
$\mathcal{N}_S$, $\mathcal{N}_\infty$	surface/TOA energy balance	calculated
$\mathcal{F}_H$, $\mathcal{F}_q$, $\mathcal{F}_O$	net exchanges of energy by the atmosphere, of moisture, and of energy by the ocean between boxes, normalized by WP width	calculated
U_A, U_O	atmospheric/oceanic mass fluxes	calculated
u_{BI}	vertical-mean boundary-layer wind speed at interface between the WP and CP	calculated
Π_{BI}, p_{BW}	pressure thickness/pressure level of trade wind layer/inversion	calculated
u_O, u_{O-}	mixed-layer current/undercurrent	calculated
z_T	depth of the thermocline	calculated
δz_T	layer over which surface wind stress is mixed	160 m
$\mathcal{M}_O$	divergence of the oceanic mass flux	calculated
T_U	undercurrent temperature	293 K

Pierrehumbert (1995) argued that the shortwave effect at the surface is largely compensated by changes of the evaporation rate, but in his analysis, cloud radiative effects are not linked to convection or a moisture budget. Miller (1997) computed the evaporation rate as that which gives surface energy balance, and thus implicitly assumed that the evaporation rate compensates for cloud radiative effects at the surface. Larson et al. (1999) concluded that changing the WP cloud fraction has little effect on the surface energy budget, because the evaporation rate in their model decreases to compensate for the decreased surface insolation. But L99 assumed a constant surface wind stress, and so possible cloud radiative forcing-evaporation feedbacks are suppressed. These earlier studies concluded that high-cloud radiative forcing over the WP plays no role in the regulation of SST and the tropical circulation, based on rather strong assumptions. With our model, we can explicitly explore these interactions to reach more defensible conclusions.

3.2.b Method of solution

Starting with a guess for the mean surface wind speed and the horizontal flux convergences of energy and moisture in the WP, we find the T_{SW}-W combination which gives surface and atmospheric energy balance using methods explained in Chapter 2. Assuming that $\mathcal{F}_H$ = -95 W m^{-2} and $\mathcal{F}_q$ = 125 W m^{-2} and the surface wind speed is 5 m s^{-1}, the WP is in equilibrium for T_{SW} = 297 K and W = 35 kg m^{-2}. Figure 3.4 illustrates this equilibrium graphically.

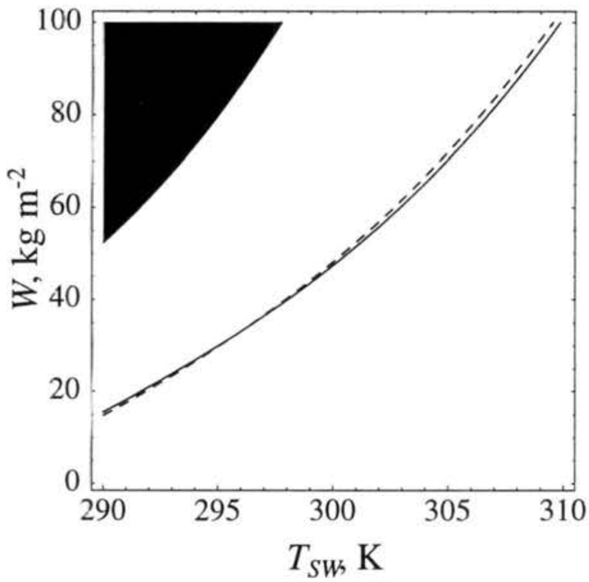

FIGURE 3.4: Atmospheric(solid) and mixed-layer (dashed) energy balance for the ocean-atmosphere column in the WP region for f = 0.5, $\mathcal{F}_q$ = 125 W m^{-2} and $\mathcal{F}_H$ = -95 W m^{-2}. An equilibrium for the WP occurs at the point where the two contours cross, which is approximately T_{SW} = 297 K and W = 35 kg m^{-2} for this case.

As discussed later, the WP would be in equilibrium for these values, but the CP would not. The guesses for $\mathcal{F}_H$, $\mathcal{F}_q$ and the surface wind speed would therefore have to be altered, and the WP equilibrium would have to be re-computed. As discussed previously, the equilibrium T_{SW}-W combination for the WP region gives the lapse rate as a function of height for the tropical free troposphere and establishes the tropopause height and temperature for the model. The free-tropospheric relative humidity profile at the CP-WP boundary is assumed to be independent of height. Thus, the temperature profile above the WP determines the rate at which moisture and energy are transported to the free troposphere in the CP region. As described later, we assume that no cirrus clouds are present over the CP, and therefore the export of ice is neglected. These WP inputs determine the mass and moisture fluxes at the top of the CP TWI, and so the wind speed, east-side SST, boundary-layer mass fluxes and CP width can be calculated using equations which are discussed later in this chapter. Then the fluxes of moisture and energy can be computed. If the net fluxes (free tropospheric + boundary layer) do not match those assumed initially for the WP, then a new WP equilibrium is computed using the calculated fluxes, and the process is repeated until convergence occurs. Figure 3.5 graphically illustrates this process.

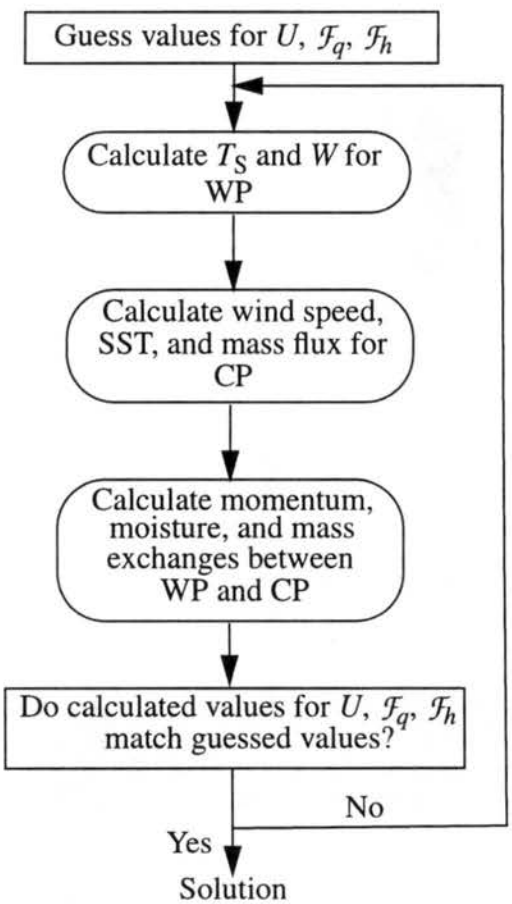

FIGURE 3.5: Flow chart illustrating the process by which an equilibrium solution is found.

We assume that horizontal variations of surface pressure, density and SST can be neglected for the WP region, and that the surface wind speed decreases from its maximum at the eastern boundary to zero at the western boundary of the WP. For the calculation of the mean surface evaporation rate, the wind speed is therefore assumed to be one-half of the vertical-mean CPBL wind speed at the boundary between the CP and WP. We specify a transfer coefficient in our bulk parameterization for evaporation which relates the CPBL vertical-mean wind speed rather than the usual 10-m wind speed to the surface fluxes of momentum and heat. As discussed later in the chapter, the SST and precipitable water for the WP, T_{SW} and W_W, are assumed to be those which give $\mathcal{N}_{SW} = 0$ and $\mathcal{N}_{\infty W} + \mathcal{F}_H = 0$. The cloud fraction is specified.

3.3 Cold-Pool model

The subsiding branches of the tropical circulation are called radiator fins by Pierrehumbert (1995) because they efficiently radiate to space excess energy that has been advected from the WP. Stratocumulus and trade cumulus clouds are assumed to be the only cloud types present in the CP region.

The governing equations for the atmosphere in the CP region are

$$u_{BI} = \left[g\mathcal{M}_{BI} - \left\{(g\mathcal{M}_{BI})^2 + 4g\rho C_D\left(-\langle\frac{\partial}{\partial x}\phi\rangle\Pi_{BI}\right)\right\}^{1/2}\right](2g\rho C_D)^{-1}, \tag{3.7}$$

$$(h_{BI} - h_{FI})U_A = (\overline{\mathcal{N}_{TC}} - \overline{\mathcal{N}_{SC}})\sigma_C, \tag{3.8}$$

$$q_{BI}U_A = q_{FI}U_A + \Delta\overline{\mathcal{E}_C}\sigma_C, \tag{3.9}$$

$$\omega_B = g\frac{(\mathcal{N}_{R\infty} - \mathcal{N}_{RB})}{s_B - s_F}, \tag{3.10}$$

$$\frac{\partial U_A}{\partial x} - \mathcal{M}_B = 0, \tag{3.11}$$

where s_F represents the vertical mean of s over the free troposphere in the CP region. The symbol Δ denotes the evaporation efficiency which is defined as $(\mathcal{E} - \mathcal{P})/\mathcal{E}$. Each of these equations will be discussed below.

3.3.a Momentum equation

Equation (3.11) is derived by substituting 1 for a in the vertically integrated generic conservation equation (A4). $\mathcal{M}_B$ is defined as

$$-g\mathcal{M}_B \equiv \frac{\partial p_B}{\partial t} + u_{B+}\frac{\partial p_B}{\partial x} - \omega_B, \tag{3.12}$$

where u_{B+} and ω_B are the pressure, zonal wind, and vertical velocity at the TWI. As p_B decreases, the boundary layer depth increases, and so $\mathcal{M}_B$ is positive. As discussed later, this equation can and will be simplified.

This is another point at which our model diverges from those of Pierrehumbert (1995), Miller (1997), and Larson et al. (1999). In these three previous studies and in our study, the mass flux through the TWI is estimated based on the relationship between subsidence and radiative cooling [(3.22), discussed later in this chapter]. For P95 and M96, the pressure level of the TWI is assumed, and so the mean wind speed follows directly from (3.3). L99 calculate the pressure depth of the CPBL based on energy and moisture balance constraints. The vertical-mean wind speed in her model then follows also from (3.3) and (3.11). Using values for the subsidence rate and the relative area of the CP for the base case of L99, the implied vertical-mean wind speed at the CP-WP boundary is 39 m s^{-1}, which is very unrealistic. In our model, we compute the vertical-mean wind speed directly from a simplified momentum equation, which is explained below. Therefore, the pressure depth of the CPBL of our model follows from (3.3). As a result, we can use the energy and moisture balance constraints to compute the ratio of the CP and WP widths, which are free parameters in the previous studies mentioned above.

Based on arguments in Appendix 2, we assume that advection in the momentum equation may be neglected. Hence, we have

$$g\mathcal{M}_{BI}(u_{B+} - u_{BI}) - \langle\frac{\partial}{\partial x}\phi\rangle\Pi_{BI} + g\rho C_D u^2_{BI} = 0, \tag{3.13}$$

which is a quadratic equation for u_{BI}. The last term on the LHS is the surface wind stress. For the CP model, the drag coefficient, C_D, was chosen to parameterize the surface stress in terms of the vertical-wind speed in the trade-wind boundary layer. Following Deardorff (1972), we specify $C_D = 8 \times 10^{-4}$. Since we expect $u_{BI} < 0$, we have set $|u_{BI}| = -u_{BI}$ in order to get (3.13). This means that the model breaks down if u_{BI} ever becomes positive. The solution of (3.13) is (3.7), in which the negative square root has been taken to ensure that u_{BI} is negative. Given the vertical-mean boundary-layer pressure gradient and the mass flux through the boundary-layer top, we can use (3.7) to calculate the zonal wind at the western boundary of the CP. While we could, in principle, use (3.7) to calculate u_B as a function of x, this would require us to determine $\mathcal{M}_B$ as a function of x. We wish to avoid making a crude assumption for $\mathcal{M}_B$. We return to this point later.

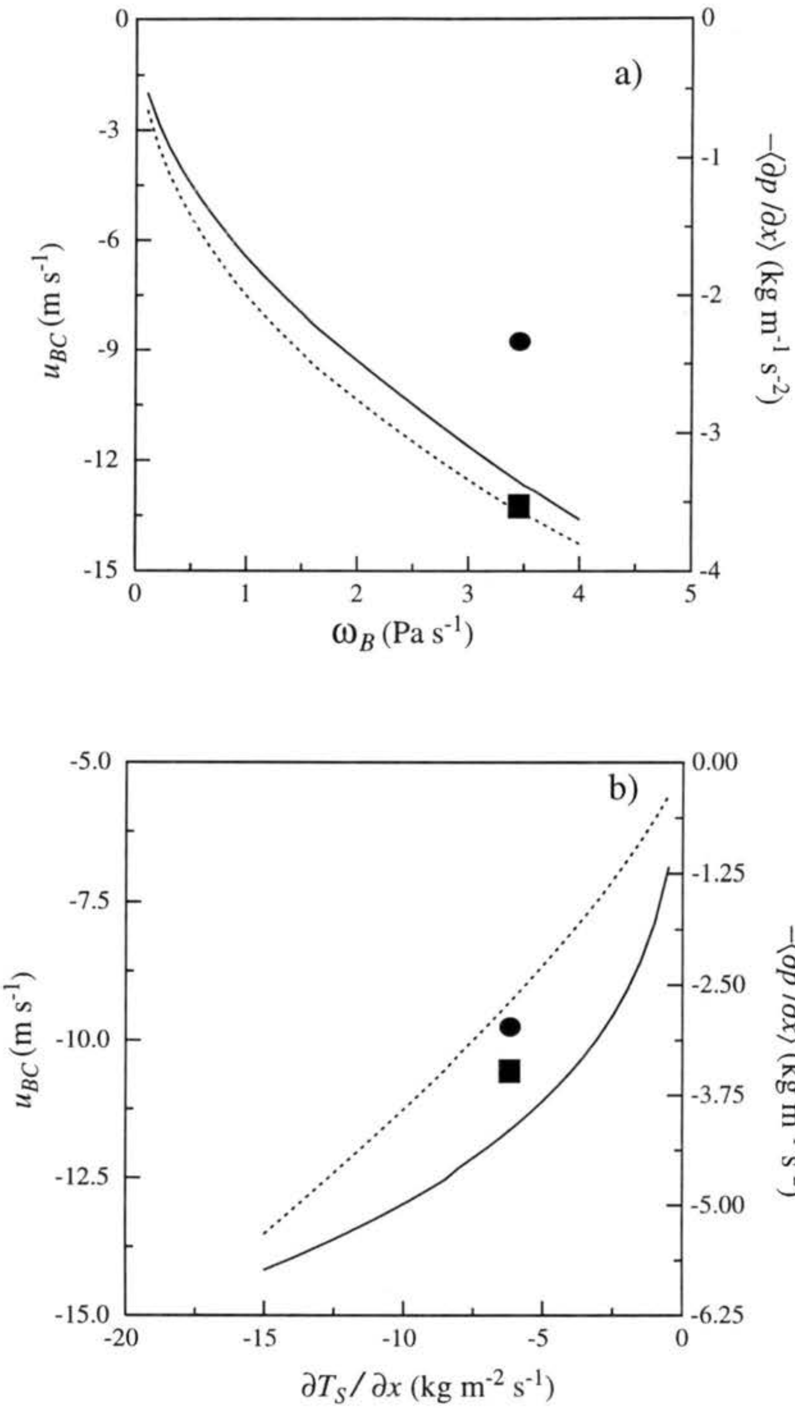

FIGURE 3.6: The zonal wind (solid line) and horizontal pressure gradient force ($\times 10^5$; dashed line) are plotted for $u_{B+} = 0$ as functions of a) the subsidence rate ($\times 10^2$) for a specified SST gradient of -6 $\times$ 10^{-7} K m^{-1}, and b) the SST gradient ($\times 10^7$) for $\omega_B = 3.5 \times 10^{-2}$ kg m^{-2} s^{-1}. The dot represents the mean wind speed from the observations; the square is the mean observed pressure gradient.

The sensitivities of the boundary-layer wind speed are examined in Fig. 3.6 above. The solid lines in Fig. 3.6a and Fig. 3.6b show that the speed of the zonal wind increases as the mass flux and the magnitude of the east-west temperature gradient increase, respectively. The squares in each plot denote the estimated real-world value for the right-hand y-axis, while the circles denote the real-world value for the left-hand y-axis. Compared to observations discussed by Hastenrath (1998), the mean wind speed is overestimated by 30-50%. This error may seem large; but when it is compared to the implied value from Larson et al. (1999), our estimate does not seem too bad. Of course, the reason for the overestimate is that no mass diverges meridionally from the boundary layer of our model, in contrast to what occurs in nature.

With u_{BI} from (3.7) and the definition of U_A, the horizontal mass flux, we can integrate (3.7) and solve for Π_{BI}, the pressure depth of the trade-wind boundary layer. The result is

$$\Pi_{BI} = u_{BI}^{-1}\int_{\sigma}^{\sigma_W} \mathcal{M}_B(x')dx' . \tag{3.14}$$

If we know the surface pressure, then (3.14) gives the pressure at the base of the TWI. Because Π_{BI} and u_{BI} are present in (3.7) and (3.14), we presently solve for these quantities by iterating. We discuss our iteration method shortly.

We show in Appendix 4 that the mean boundary-layer pressure gradient is

$$-\left(\frac{\partial\phi}{\partial x}\right)_M = 0.5\Pi_B\frac{R}{p_S}\frac{\partial T_{SC}}{\partial x} . \tag{3.15}$$

For a temperature gradient which is constant with x, (3.15) indicates that the pressure-gradient force varies horizontally due to the variation of the boundary-layer pressure depth and surface pressure. The dashed lines in Fig. 3.6a and Fig. 3.6b show that the magnitude of the pressure gradient force increases with the mass flux and SST gradient, respectively. From (3.14), as the mass flux increases, Π_{BI} increases, and so the pressure gradient, which is proportional to Π_{BI}, must also increase. We see that the pressure gradient is estimated fairly well.

There is an additional simplification that we can make. As can be seen from (3.15), the mean CPBL pressure gradient is inversely proportional to the surface pressure, p_S. Figure 3.7 shows that the variation of surface pressure across the equatorial Pacific is less than 1%. Taking advantage of this small variation, we may write

$$\frac{1}{p_S} = \frac{1}{\bar{p}_S + p'_S} = \frac{1}{\bar{p}_S\left(1 + \frac{p'_S}{\bar{p}_S}\right)} \approx \frac{1}{\bar{p}_S}\left(1 - \frac{p'_S}{\bar{p}_S}\right), \tag{3.16}$$

where in this case the overbar represents the zonal average for the CP and the prime denotes deviations from the average. We used a one-term binomial expansion for the approximation on the RHS of (3.16). Referring to Fig. 3.7, for a zonal average of about 1010 mb, the deviations about this mean are no larger than 3 mb, which means that $p'_S/\bar{p}_S \ll 1$ and neglect of this term is justified. Even if the deviation were as large as 25 mb, the error introduced by this approximation would still be less than 2.5%. Because we assumed in Chapter 2 that the surface pressure over the WP is 1000 mb, and Fig. 3.7 suggests that the typical difference in surface pressure between South America and Indonesia is about 6 mb, we assume that $\bar{p}_S = 1003$ mb. To determine the pressure level of the TWI at the CP-WP boundary, we assume that $p_{SI} = p_{SW}$, which in Chapter 2 was specified as 1000 mb, and p_{BI} follows as $p_{SI} - \Pi_{BI}$.

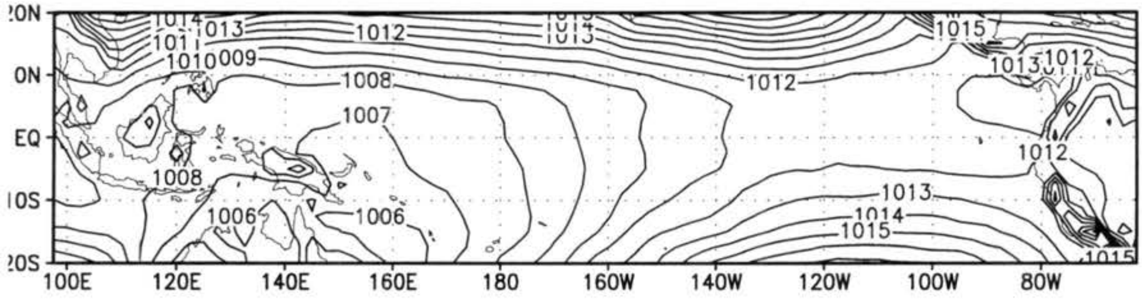

FIGURE 3.7: Surface pressure for January 1989 from the ECMWF reanalysis dataset obtained from NCAR. Contour interval is 1 mb.

Our solution method for u_{BI} and Π_{BI} is as follows. Given an initial guess for Π_{BI}, the pressure gradient and u_{BI} are computed from (3.15) and (3.7), respectively. From our calculation of $\mathcal{M}_B$, discussed later, Π_{BI} can then be computed from (3.14) with our new value of u_{BI}. If the error between the calculated and guessed values of Π_{BI} is less than 1%, then the solution is accepted. If not, then the new value of Π_{BI} is taken as a weighted sum of the calculated and guessed values, and the process is repeated. Convergence usually results within 10 iteration cycles. There appears to be only one solution for a given radiative cooling rate and SST gradient. Convergence fails only if the subsidence rate and hence $\mathcal{M}_B$ are so small that the square root factor in (3.7) is negative.

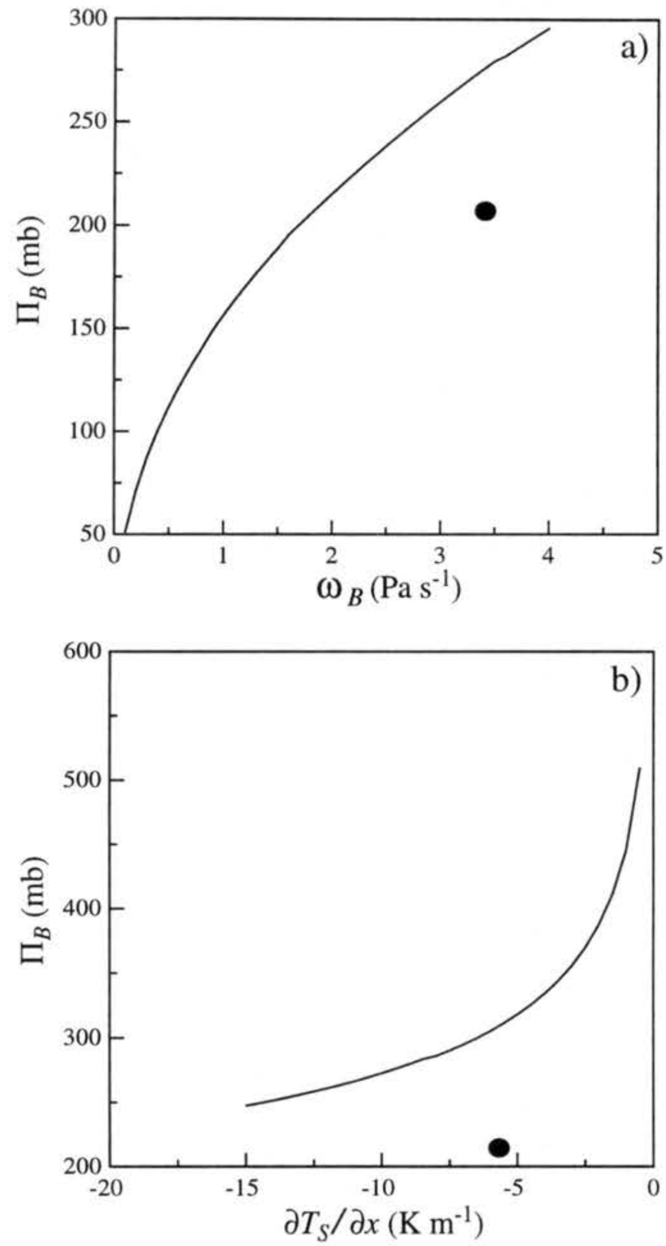

FIGURE 3.8: For the same parameters as in Fig. 3.6, the boundary-layer depth is plotted in millibars (mb) as a function of a) mass flux $\times\ 10^3$ at the top of the CPBL and b) CP SST gradient $\times\ 10^7$. The dots represents mean values from the observations.

The height of the TWI is calculated based on mass continuity considerations, rather than on the effects of turbulence. In equilibrium, the subsidence rate at the TWI must equal the CPBL mass flux at the boundary between the CP and WP. For a given SST gradient, the vertical-mean wind speed follows, and thus the product of the CPBL depth and the mean wind speed must balance the product of the subsidence rate and the width of the CP.

For a given subsidence rate and CP area, the depth of the CPBL must decrease as the wind speed increases in order to preserve mass continuity. Although such an assumption would not be valid for a diurnal time scale, it should be approximately valid for an equilibrium solution since we are not attempting to predict the time evolution of TWI height. In effect, we have combined the trade-wind boundary layer with the layer of easterlies above. This produces a 100-mb error in the pressure level of the TWI.

Results for u_{BI} were already presented in Fig. 3.6. Figure 3.8 shows the sensitivity of Π_{BI} to changes of the mass flux and of the SST gradient. As discussed later, the mass flux is controlled by the radiative cooling rate over the CP. The depth of the boundary layer increases as the mass flux through the TWI increases (holding the SST gradient constant) and as the SST gradient increases (holding the vertical mass flux constant). Note that as the SST gradient becomes very small, the boundary-layer depth increases quite strongly. This happens because, when the wind speed (Fig. 3.6b) is very weak, a deep boundary layer is demanded by mass continuity for a given subsidence rate. The subsidence rate is driven by the radiative cooling in the upper troposphere. The dots show the approximate mean observed values. Our model overestimates the depth of the boundary layer for two reasons. First, we have assumed for simplicity that easterly flow in the tropics is confined below the TWI. Figure 1.3 shows that weak easterly flow extends up to approximately 600 mb, which is the zero-wind level discussed by Geisler (1981) and Rosenlof (1986). Second, we have assumed that the Walker circulation is closed, and so the meridional Hadley cell cannot remove air from the boundary layer.

Our solution method gives Π_{BI}, but not individual values of p_S and p_B, which are needed to compute the height in meters of the TWI from (2.24). As discussed in Section 3.5.b, the height of the TWI is needed in order to determine the liquid water path for boundary-layer clouds. Recall that we assumed a value for $\bar{p}_S$ in (3.15). Because p_S varies so little, compared to the variation of p_B, we set $p_B \cong \Pi_B - \bar{p}_S$.

3.3.b Subsidence warming in the free troposphere of the CP region

Following previous box studies (e.g. P95), we assume that the radiative cooling of the free troposphere is balanced by adiabatic compression and sinking, i.e.

$$\omega\frac{\partial s}{\partial p} = -g\frac{d\mathcal{N}_R}{dp}, \tag{3.17}$$

where $\mathcal{N}_R$ is the net downward radiative flux. As described in Section 3.5, our radiative transfer parameterization requires the vertically integrated water vapor as input, and returns the net radiative flux for the slice of the atmosphere over which the column water vapor was computed. Given the simplified nature of this radiation parameterization, it does not seem prudent to use (3.17) to compute the vertical velocity level-by-level for the free troposphere in the CP region. Instead, we compute the radiative flux divergence for the entire free troposphere, and use (3.17) to compute ω_B for a simplified free-tropospheric divergence profile. Although we could assume that the vertical velocity is independent of height as in M97, it seems somewhat more realistic to assume that $\partial\omega/\partial p$ is constant with height. Integrating (3.17) over the depth of the free troposphere, under the assumption that $\omega = 0$ at the tropopause and $\partial\omega/\partial p$ is constant, the result is (3.10).

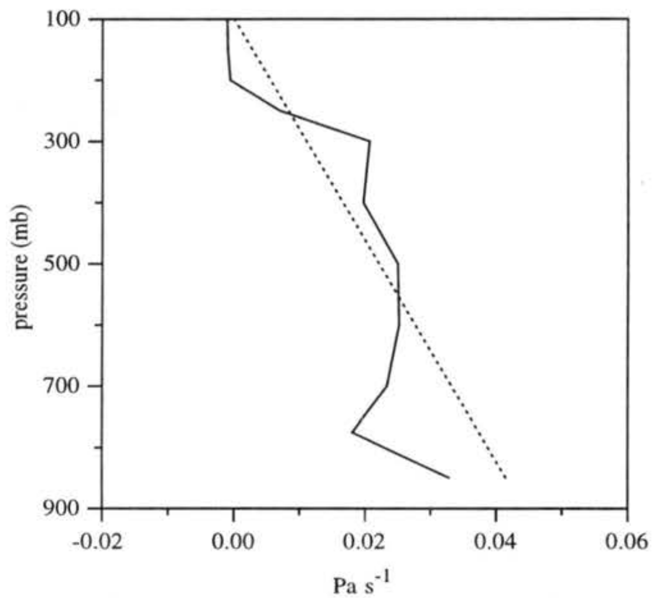

FIGURE 3.9: Vertical velocity over the eastern, equatorial Pacific as a function of pressure. The solid curve shows monthly mean values for January 1989 from the ECMWF reanalysis dataset. The dashed curve shows values computed from (3.10).

For a typical moisture and temperature profile from the ECMWF reanalysis dataset, we have computed the profile of ω using (3.17) and (3.10). We calculated the radiative fluxes in (3.10) from NCAR's CCM3 radiation code using ECMWF temperature and moisture profiles as input. Figure 3.9 shows that the monthly mean vertical velocity profile from the ECMWF reanalysis dataset (solid curve) and the vertical velocity profile obtained using (3.10) agree fairly well in the middle and upper troposphere. Our parameterization overestimates the vertical velocity by 25% compared to the ECMWF reanalysis dataset at lower levels, but slightly underestimates the subsidence rates compared to Betts and Ridgeway (1989) and L99. Estimates of vertical velocity are highly uncertain.

3.3.c Budget Equations for the CPBL

Substituting s for a in the vertically integrated conservation equation, the budget equation for dry static energy in the CPBL follows as

$$\frac{\partial H_B}{\partial t} = -\frac{\partial}{\partial x}(U_B h_B) + h_{B+}\mathcal{M}_B + \mathcal{N}_B - \mathcal{N}_S \ , \tag{3.18}$$

where $\mathcal{N}_B$ is the net flux of energy at the TWI. The energy stored in the boundary layer is a balance between the horizontal flux convergence of moist static energy, subsidence warming through the TWI, radiative cooling, and surface evaporation. We have set the air-sea temperature difference to zero, which means that we are neglecting sensible heating.

Because we want steady-state solutions, we drop the LHS of (3.18). Equation (3.11) gives U_B as a function of x, assuming that the horizontal distribution of $\mathcal{M}_B$ is known. Integrating (3.18) from σ to σ_W, we find that

$$h_{BI}U_{BI} + [\overline{h_{B+}\mathcal{M}_B} - \overline{(\mathcal{N}_B - \mathcal{N}_S)}]\sigma_C = 0 \, . \tag{3.19}$$

The goal is to evaluate (3.19) analytically. In equilibrium, it can be shown from the moist static energy budget for the free troposphere that $\overline{h_{B+}\mathcal{M}_B}\sigma_C = U_A h_{FI} - \overline{(\mathcal{N}_T - \mathcal{N}_B)}\sigma_C$, where $\mathcal{N}_T$ is the net energy flux at the tropopause. Substituting the RHS of this expression in (3.19), the moist static energy budget reduces to (3.8). As described later, we compute the horizontal-mean vertical flux convergence of energy for the CP atmosphere [i.e. the RHS of (3.8)] at the horizontal center of the CP region. We use an approach which determines the longwave radiative cooling based on an effective emissivity and effective emission temperature.

We determine the LHS of (3.8) independently of the RHS. U_A is known, and h_{BI} and h_{FI} can be calculated. As discussed in Chapter 2, we assume that the moist static energy for convecting parcels is conserved. Thus, $h_{FI} \equiv c_p T_{SW} + Lq_{SW}$. The parcel originates from near the surface, and so the potential energy part of the moist static energy is negligible. In order to calculate $h_{BI} \equiv s_{BI} + Lq_{BI}$, we assume that the air has been heated sufficiently from below so that the lapse rate and surface temperature at the CP-WP boundary are identical to those in the WP, i.e. there is no temperature discontinuity. Hence $h_{BI}\Pi_{BI}/g$ can be computed from (2.25), with z_{BI} and p_{BI} replacing z_T and p_T, respectively. The moisture contribution of the moist static energy [LW in (2.25)] is computed as $Lq_{BI}\Pi_{BI}/g$, where q_{BI} is the vertical-mean specific humidity in the CPBL at the CP-WP boundary.

Given the net energy balance on the LHS of (3.8), we can then solve for σ_C. In the previous box models (P95, SL96, M97, L99), σ_C was specified rather than calculated. As discussed later, we calculate the zonal wind speed from a simplified momentum equation. Because the product of the subsidence rate and the width of the CP must balance $U_A \equiv u_{BI}\Pi_{BI}/g$, we must solve for the CP width which satisfies the constraints imposed by mass continuity and energy balance. The previous box models do not have to satisfy this constraint, because u_{BI} is not calculated.

To calculate q_{BI}, we substitute q for a in the vertically integrated conservation equation to derive

$$\frac{\partial W_B}{\partial t} = -\frac{\partial}{\partial x}(U_B q_B) + q_{B+}\mathcal{M}_B + \Delta\mathcal{E}_C, \tag{3.20}$$

which is the vertically integrated budget equation for water vapor in the CPBL. Here q_{B+} is the water vapor mixing ratio just above the trade inversion. We compute the evaporation rate, $\mathcal{E}_C$, from (2.13) just as in Chapter 2, except that q_B, p_{SC}, and T_{SC} vary with x in the CP region. At the east side of the CP, we compute the evaporation rate under the assumptions that the surface relative humidity is 90% and that the minimum wind speed is 5 m s^{-1}. The minimum wind-speed assumption is made in order to account for the underestimated evaporation rate, which results from the bulk evaporation formula for low observed wind speeds. We specify an evaporation efficiency, and so $\Delta\mathcal{E}$ is just the amount of the evaporated water vapor which is available for export to the WP.

Following the same procedure as for the dry static energy budget, we find

$$q_{BI}U_{BI} + \overline{q_{B+}\mathcal{M}_B}\sigma_C + \Delta\overline{E}_{CS}\sigma_C = 0. \tag{3.21}$$

In equilibrium, $\overline{q_{B+}\mathcal{M}_B}\sigma_C = U_A q_{FI}$, and so (3.21) reduces to (3.9). From (3.5) and (3.9), $\mathcal{F}_q$ is proportional to the net evaporation rate in the CP. If we specify the vertical variation of relative humidity and zonal wind at the CP-WP boundary, then we compute q_{FI} from $q_{FI} = U_A^{-1}\int_{\Pi_{FI}} uq\,dp/g$ and estimate the pressure level to which q_{FI} corresponds. Figure 3.10 shows an example for which the zonal wind decreases linearly to zero at the TWI from its maximum at the tropopause and the relative humidity is constant with pressure. Under these conditions, $q_{FI} = 2.26$ g kg^{-1}, which for the given relative humidity profile, implies that the effective level from which U_A transports water vapor is approximately 400 mb. This effective transport level is not very sensitive to lapse rate variations, which in turn depend on the WP SST, precipitable water, and cloud cover. For SST = 302 K and an $\partial T_{SW}/\partial x = -6.4 \times 10^{-7}$ K m^{-1}, the effective water vapor transport level increases by 25 mb as the precipitable water decreases by 20 kg m^{-2}; for $W = 55$ kg m^{-2} and $\partial T_{SW}/\partial x$ = -6.4 × 10^{-7} K m^{-1}, the effective water vapor transport level increases by 5 mb as the SST decreases by 4 K. For SST = 302 K and W = 55 kg m^{-2}, the effective transport level increases by 23 mb and decreases by 10 mb as the SST gradient is doubled and halved, respectively. Given its relatively small variation, we fix the effective water vapor transport level at 400 mb. For the fully coupled model, we obtain the relative humidity at the WP surface from (2.33), and then assume that the relative humidity is independent of height in the troposphere above. This assumption broadly agrees with the observations from TOGA COARE (Brown and Zhang 1997) that were taken during convectively active periods. This is also roughly consistent with the equatorial RH profile at 120°E from the ECMWF reanalysis dataset (Fig. 3.11) for Jan. 1989. Recall from Fig. 1.3 that 120° E is in the rising branch of the Walker circulation.

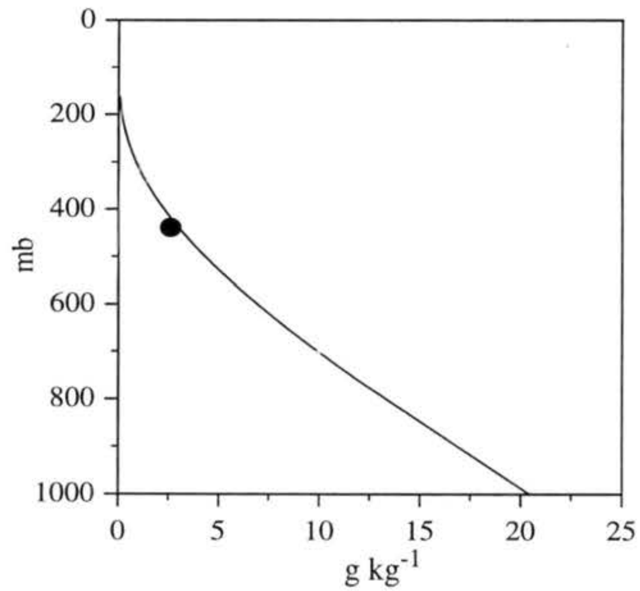

FIGURE 3.10: The specific humidity profile which results for T_{SW} = 302 K, W = 65 kg m^{-2} and RH = 80%.The black dot represents the effective pressure level from which the free-tropospheric mass flux transports water vapor.

The next step in evaluating (3.9) analytically is to determine the mean evaporation rate for the CP. We somewhat simplistically assume that the mean evaporation rate is given by the arithmetic average of the evaporation rates at the eastern and western borders of the CP. As described above, the bulk parameterization has been implemented, and so the wind speed, surface temperature, surface pressure, and vertical-mean specific humidity for the CPBL are generally required in order to calculate the evaporation rate.

As stated previously, our model simulates a closed Walker circulation, and so water vapor advected from nearby convection over South America is not allowed. This assumption contrasts with the findings of Newell et al. (1996) who showed that mixing from the east contributes to the properties of air parcels above the tropical eastern Pacific. We assume that $q_{SE} = 0.9\ q_{sat}(T_{SE}, p_S)$, i.e. we assume that the surface RH = 0.9 on the east side of the CP. Because the horizontal mass flux is identically zero at the eastern boundary of the CP, we must assume a minimum wind speed for the calculation of the evaporation rate. It is well known that the bulk parameterization underestimates the evaporation rate at low wind speeds, and so an assumed minimum wind speed is commonly used. For our model, we assume that the minimum wind speed is 5 m s^{-1}. Thus the mean evaporation rate above the CP follows as

$$\begin{aligned}\overline{\mathcal{E}}_{CS} = 0.5\rho c_T\Bigg\{ & |u_{SI}|\, q_{sat}(T_{SW}, p_{SW})\left(1 - \frac{q_{SI}}{q_{sat}(T_{SW}, p_{SW})}\right) \\ & + |u_{min}|\, q_{sat}(T_{SE}, p_{SE})\left(1 - \frac{q_{SE}}{q_{sat}(T_{SE}, p_{SE})}\right)\Bigg\},\end{aligned} \quad (3.22)$$

and is simply the arithmetic average of the evaporation rates at the eastern and western borders of the CP. The first term on the RHS is approximately four times larger than the second.

The task remains to relate the surface evaporation rate to the mean boundary-layer quantities u_B and q_B, which are diagnosed by the model. L99 and M97 adopted the mixing line model (described in Chapter 1), which predicts the vertical variation of q and T based on prescribed mixing rates. Rather than relying on such an elaborate method, which in the end still prescribes the vertical variation of moisture and temperature, we substitute q_{BI} for q_{SI} in (3.22) and modify (reduce) the transfer coefficient c_T so as to compute the evaporation rate from the mean boundary-layer wind speed and specific humidity rather than from their 10-m values (Deardorff 1972). We specify the heat transfer coefficient to be $c_T = 2.0 \times 10^{-4}$.

Although we must specify the transfer coefficient, we specify neither the surface mass flux as L99 did, nor the surface relative humidity as P95 did. Although M97 avoided making assumptions regarding the surface wind speed or relative humidity, he calculated the evaporation rate as that which balances the moisture budget and the surface energy budget. Rather than explicitly calculating the surface energy balance, SL96 included ocean-atmosphere heat exchange as Newtonian relaxation to a specified equilibrium temperature.

Despite the use of a specified transfer coefficient, our approach is more physically based than any of the previous box models.

In order to calculate q_{B+} (and all the other quantities that follow from mass exchange between the WP and CP regions), we considered following the approach of Held and Hou (1980), who assumed that the mass flux is confined to narrow pipelines at the top and bottom of the troposphere. This would mean that $q_{B+} = q_T$. Subsidence over the CP region would then be assumed to be horizontally invariant and would imply that the water vapor distribution is uniform throughout the free troposphere in the CP region. In the eastern part of the CP region, this approach does not seem unreasonable. Water-vapor mixing ratios decrease drastically above the TWI for regions far from deep convective activity (Hastenrath 1998). Over the western part of the CP region, q_{B+} is much larger than q_T due to stronger moistening from adjacent WP convective zones.

Figure 3.11 demonstrates this point reasonably well. Note how the relative humidities between 700 mb and 800 mb over the central Pacific are reduced, compared to adjacent values. Moreover, note the strong minimum in relative humidity (< 20%) in the middle troposphere near 110° W. Figure 3.12 shows that the 0.5 g kg^{-1}contour of specific humidity slopes downward by 200 mb between 120° E and 100° W. This indicates that, to very good approximation, the specific humidity of the air in the middle troposphere is conserved as it traverses the equatorial Pacific ocean (Salathé and Hartmann 1997). In the lower part of the troposphere (above the level of the TWI ~ 800 mb), the specific humidity of the air increases at a given pressure level as we move westward. This indicates that the air is being moistened as it moves westward, and thus meridional exchanges are implicated. Without meridional exchanges, we would expect the specific humidity of the air to remain relatively constant following the motion. We would therefore expect extremely low relative and specific humidities at low levels if meridional exchanges could somehow be suppressed.

As mentioned previously, we assume that the free-tropospheric relative humidity (RH) vertical profile above the CP-WP boundary is uniform. Given values for the precipitable water and SST from the WP, we calculate the surface relative humidity. Essentially, we assume that the specific humidity vertical profile rotates to become the specific humidity horizontal profile just above the TWI in the CP region. Thus, $q_{B+}(\sigma) = q_T(\sigma_W)$ and $q_{B+}(\sigma_{W/})$ is obtained from the uniform relative humidity profile. The specific humidity at the middle altitude of the specified vertical profile would then be the specific humidity at the middle point of the CP for level $B+$. This approach assumes that advection controls the specific humidity of the free troposphere in the CP region, and therefore follows Salathé and Hartmann (1997). Figure 3.13 schematically summarizes this discussion.

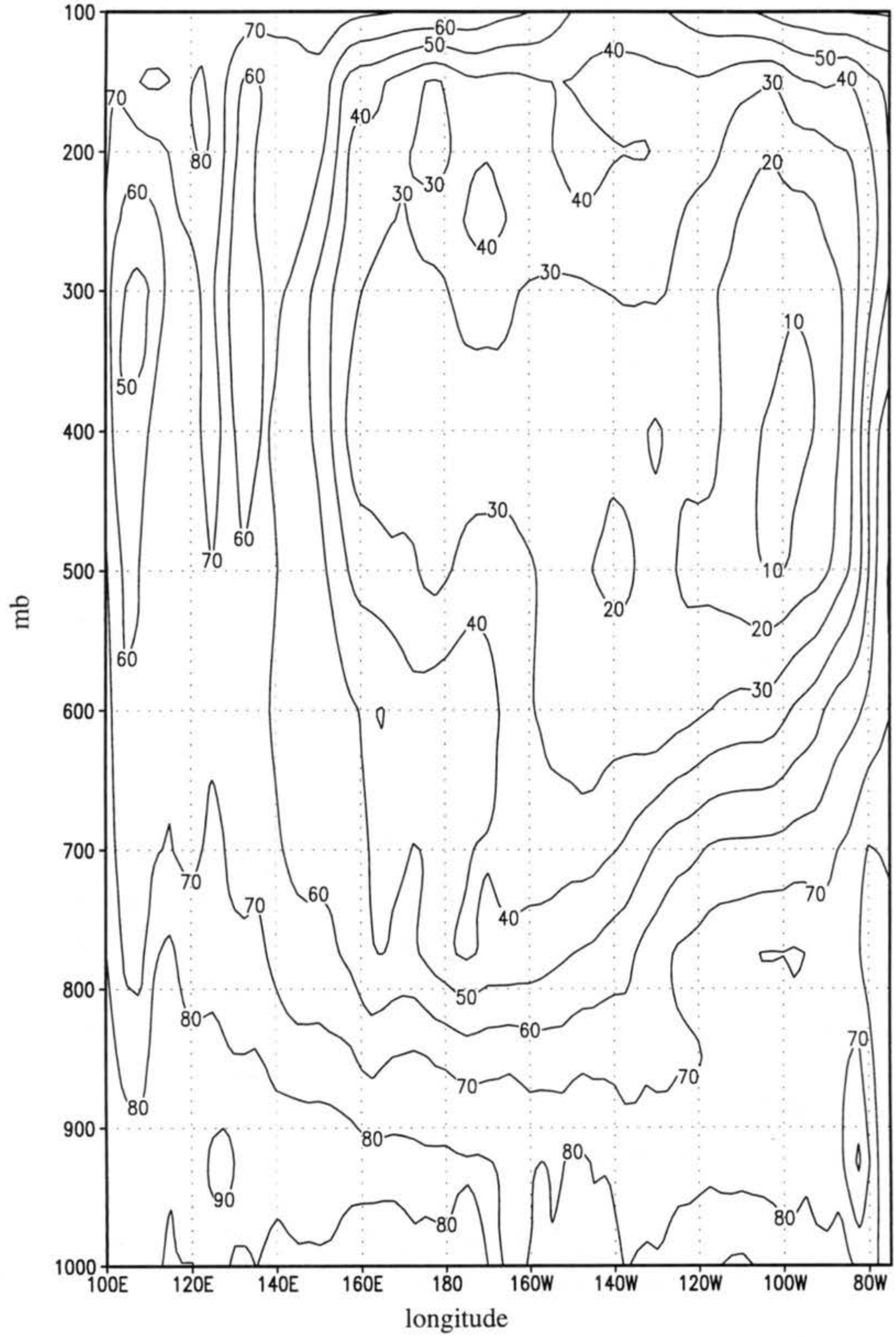

FIGURE 3.11: Relative humidity in % in the *x-p* plane along the equator. Contour interval is 10%. Data are from the ECMWF reanalysis dataset for January 1989.

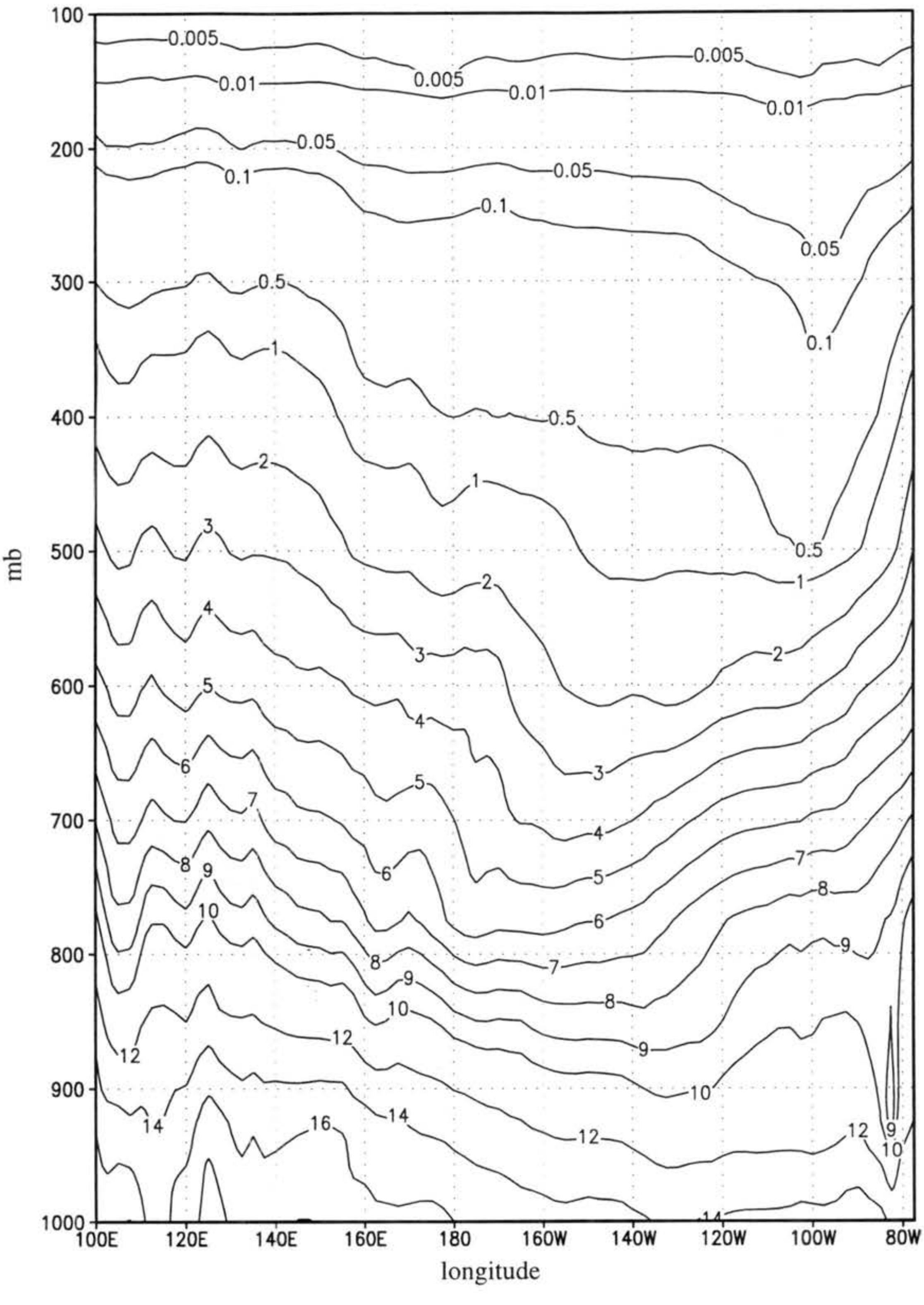

FIGURE 3.12: Specific humidity in g kg^{-1} in the *x-p* plane along the equator. Contour interval varies from 0.005 g kg^{-1} near the tropopause to 2 g kg^{-1} near the surface. Data are from the ECMWF reanalysis dataset for January 1989.

Above the upper-most trajectory (see Fig. 3.13) that begins just below the tropopause at the CP-WP boundary, there is essentially a "dead zone" in the model in which the water-vapor assumption does not apply. We would not expect the specific humidity for this zone to be higher than that in lower-altitude regions of the CP. For convenience, we assume that the lower limit for specific humidity for the CP is $q_{TC}(\sigma_C)$. Therefore, on the east side of the CP region, our assumption is that the specific humidity in the free troposphere is constant with height and very dry, so that $q = q_{B+}(\sigma_C) = q_{TC}(\sigma_W)$. Based on this assumption and the advective model described above, the precipitable water can be computed as a function of x above the CPBL.

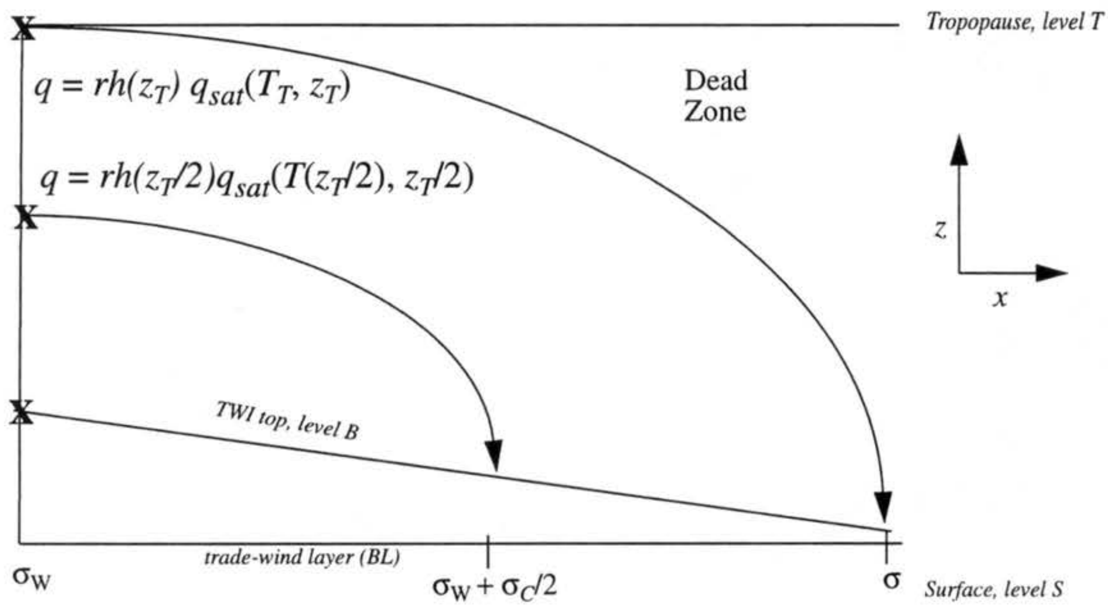

FIGURE 3.13: Schematic illustrating an idealized cross section of specific humidity above the TWI in the CP region

Under the assumption that the height of the trade-wind inversion (TWI) is steady (consistent with previous derivations), from (3.12), the mass flux $\mathcal{M}_B$ can be simplified to

$$g\mathcal{M}_B = \omega_B - u_{B+}\frac{\partial p_B}{\partial x}. \tag{3.23}$$

This means that in a time average, the turbulent entrainment is balanced by subsidence and advection. As described previously, we calculate the pressure of the TWI based on mass continuity and the assumption that the depth of the trade-wind layer approaches zero at the east boundary of the CP. For consistency, we must set $u_{B+} = 0$. Recall that we have assumed that easterly and westerly winds occur below and above the TWI, respectively. The ECMWF reanalysis dataset (not shown) shows that the winds between the top of the TWI and 500 mb are predominately from the east, and seem to originate as convective outflow from South America. However, since we are interested in simulating a closed circulation, we choose not to represent this flow. With this choice, the mass flux at the TWI for our model is given by the large-scale vertical velocity obtained from (3.10), i.e.

$$g\mathcal{M}_B = \omega_B . \qquad \textbf{(3.24)}$$

3.3.d Cloud parameterization

Following Suarez et al. (1983), we assume that the condensation level of the stratocumulus and towering cumulus clouds is given by

$$p_{CL} = p_B + \Pi_B \frac{(q_S - q_{sat}(T_B, p_B))}{(q_{sat}(T_S, p_S) - q_{sat}(T_B, p_B))} , \qquad \textbf{(3.25)}$$

where T_B is the temperature at the base of the TWI. Our method varies from that of Suarez et al. (1983), however, because we allow the lapse rate to vary from dry adiabatic. On the east side of the CP, we assume that the lapse rate is dry adiabatic. But in the center of the CP, we assume that the lapse rate satisfies

$$\Gamma = \Gamma_d RH + \Gamma_{mS}(1 - RH) . \qquad \textbf{(3.26)}$$

Below cloud base, the lapse rate should be dry adiabatic, but above cloud base the lapse rate should be more stable than moist adiabatic. Equation (3.26), which can be derived from (2.22), should provide a reasonable estimate of the mean lapse rate for the layer, and so the cloud top temperature $T_B = T_S - \Gamma z_B$. Then the LWP satisfies

$$LWP = g^{-1} q_S(p_{CL} - p_B) - \int_{z_{CL}}^{z_B} q_{sat}(T, p)\rho dz . \qquad \textbf{(3.27)}$$

Substituting the version of the Clausius-Clapeyron equation used in Chapter 2 for q_{sat} in (3.27), and evaluating the integral, we find that

$$LWP = g^{-1} qs(p_{CL} - p_B) - \frac{\varepsilon e_0 T_0 exp(A_e)}{R\bar{\Gamma} B_e}\left[exp\left(\frac{-B_e}{T_{CL}}\right) - exp\left(\frac{-B_e}{T_B}\right)\right], \qquad \textbf{(3.28)}$$

where $\varepsilon = 0.622$, $e_0 = 1$ mb, R is the gas constant for dry air, T_0 is a reference temperature, and A_e and B_e are constants in our approximate Clausius-Clapeyron equation.

3.4 Ocean model

The ocean is represented by three boxes: the WP, the CP, and the undercurrent. As Fig. 3.14 shows, z_S is the top of the ocean, i.e. the bottom of the atmosphere, and z_D is the depth of the thermocline. We assume that these interfaces slope due to the effects of wind stress, and for simplicity, that the slopes are approximately linear and equal in the WP and CP. We also assume that the equatorial circulation is closed. For a westward surface current, upwelling must occur in the CP and downwelling must occur in the WP in order to maintain a closed loop. As a result, the ocean current may be characterized by a single ocean mass flux, U_O, between ocean regions, as described below.

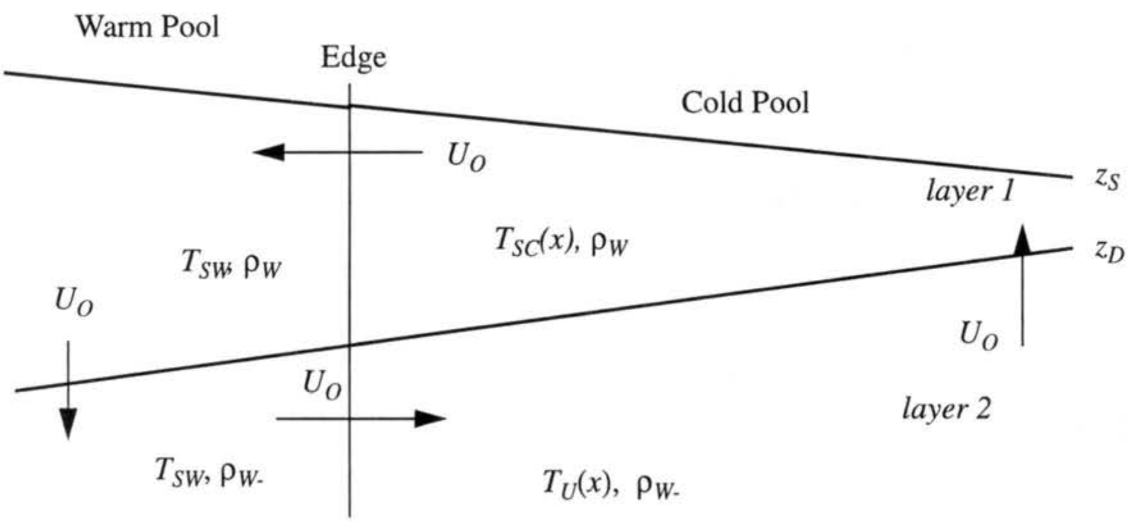

FIGURE 3.14: Schematic illustrating the distribution of temperature and thermocline depth in the tropical Pacific ocean.

The governing equations for the ocean model are

$$\mathcal{N}_{SW} + \mathcal{F}_O = 0, \tag{3.29}$$

$$\mathcal{N}_{SC} + C\mathcal{M}_O(T_U - T_{SE}) = 0, \tag{3.30}$$

$$T_U = T_\infty + \delta T_0 (u_{O-}/u_{O-,max})^{1/(lt_r)}, \tag{3.31}$$

$$-\frac{\partial U_O}{\partial x} = \mathcal{M}_O, \tag{3.32}$$

$$u_{O-} = \left(2\int_{\sigma_W}^{\sigma}\left(\frac{1}{\rho_{W-}}\frac{\partial p}{\partial x}\right)dx\right)^{0.5}, \tag{3.33}$$

where $\mathcal{M}_O$ is the vertical mass flux through the thermocline, T_U is the undercurrent temperature, T_∞ is the specified minimum temperature of the undercurrent, u_{O-} is the undercurrent, ρ_{W-} is the density of the water in the undercurrent. Equations (3.29) and (3.30) are the mixed-layer energy balance equations for the WP and CP, respectively. Equation (3.31) is the temperature equation for the undercurrent, in which t_r is a time scale for relaxation of T_U to T_∞, $l = -\partial u_{O-}/\partial x$, $\delta T_0 = T_{SW} - T_\infty$. and $u_{O-,max}$ is the speed of the undercurrent at the CP-WP boundary. Equations (3.32) and (3.33) are the mass continuity and zonal momentum equations for the undercurrent, respectively. Each of these equations will be discussed below.

3.4.a Prognostic equations

Although we used time-marching methods to obtain a solution in Chapter 2, we were interested in the steady, equilibrium solution for the WP. Since we are now including a model for the atmosphere and ocean in the CP region, the procedure for finding a solution is more involved. Moreover, there are additional time scales involved for the various ocean-atmosphere interactions, and so time-marching is no longer a practical solution technique. For these reasons, we now construct steady-state equations by explicitly neglecting all time derivatives. The steady equation for WP surface temperature is obtained by neglecting the LHS of (2.4) to get (3.29). In Chapter 2, for simplicity, we considered solutions for which $\mathcal{F}_O = 0$. Such solutions continue to be valid, since the WP is a region of maximum SST with a negligible SST gradient. Furthermore, estimates of the net surface energy flux indicate a mean energy input of less than 20 W m^{-2} into the ocean (Weller and Anderson 1996, Philander 1990). Because of the relatively small observed surface energy flux for the tropical WP, we continue to neglect it.

In analogy to the atmospheric mass flux, the ocean mass flux is defined as

$$U_O \equiv -\rho_W u_O \delta z_D = \rho_{W-} u_{O-} \delta z_U . \tag{3.34}$$

Here, δz_U and δz_D are the thicknesses of the undercurrent and mixed layer, respectively, and u_O is the zonal current in the mixed layer. As discussed later, we specify the thickness of the undercurrent layer, but solve for the depth of the mixed layer. Because we assume that the zonal ocean circulation in the tropics is closed, the mass flux in the mixed-layer must balance that in the undercurrent. Furthermore, the divergence of the mass flux must balance the upwelling through the thermocline [(3.32)].

If we let $a = T_S$ in the steady-state mixed-layer budget equation for the ocean (Appendix 3), then the CP SST satisfies

$$\mathcal{N}_{SC} - C\frac{\partial}{\partial x}(U_O T_S) + C\mathcal{M}_O T_U = 0 \; . \qquad \textbf{(3.35)}$$

Since we assume that the CP temperature gradient is linear, we need the SST at the east and west boundaries of the CP. Since $T_S = T_{SW}$ at the west boundary of the CP, we need only solve (3.35) at the east boundary of the CP. At this boundary, $U_O = 0$. Using (3.32), (3.35) reduces to (3.30), from which we can simply solve for T_{SE}. Equation (3.30) says that the equilibrium SST results from a balance between the net surface energy flux and cold-water upwelling.

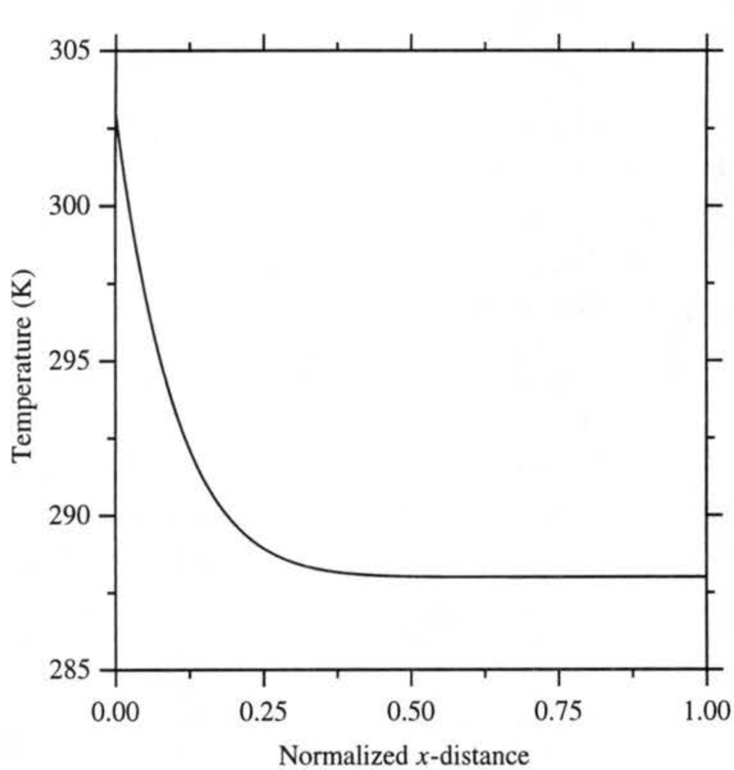

FIGURE 3.15: Temperature of the undercurrent as a function of *x*-distance from the WP-CP boundary. This distance has been normalized by an assumed length for the CP of 1.75 × 10^4 km. We have also assumed that $u_{O\text{-},max}$ = 50 cm s^{-1}, T_∞ = 288 K, and t_r = 30 days.

We assume that the temperature of the undercurrent satisfies

$$-u_{O\text{-}}\frac{\partial T_U}{\partial x} - \frac{(T_U - T_\infty)}{t_r} = 0 \, . \qquad \textbf{(3.36)}$$

The equilibrium temperature for the undercurrent results from a balance between advection and relaxation. For simplicity, we assume that the $T_U = T_{SW}$ beneath the WP. With this choice, the solution of (3.36) is (3.31). As shown in the next subsection, the variation of u_{O-} is assumed to be linear across the eastern half of the tropical Pacific ocean, and so l can be calculated easily if we assume that the undercurrent vanishes at the eastern boundary of the CP. Assuming that $u_{O-,max} = 50 \text{ cm s}^{-1}$ and $T_{\infty} = 288$ K, and that the WP and CP have equal widths, the temperature variation as a function of x is shown in Fig. 3.15. The undercurrent basically occurs in the thermocline, so the undercurrent slopes upward from west to east. This suggests that the temperature of the undercurrent should be almost uniform across the basin. Fig. 3.15 indicates that our model gives this result.

3.4.b Horizontal momentum equations

Our derivation in Appendix 3 shows that the steady-state momentum budget for the ocean mixed layer satisfies

$$\rho_W \delta z_D \frac{\partial}{\partial x}\left(\frac{u_O^{\,2}}{2}\right) + (u_O - u_{O-})\mathcal{M}_O = -(\mathcal{F}_u)_S - \delta z_D\left(\frac{\partial p}{\partial x}\right)_M, \tag{3.37}$$

where $(\mathcal{F}_u)_S$ is the surface wind stress. According to Neelin et al. (1998), the primary balance for the momentum budget of the surface mixed layer is between the surface wind stress and the horizontal pressure gradient force so that

$$0 = -(\mathcal{F}_u)_S / \delta z_D - \left(\frac{\partial p}{\partial x}\right)_M. \tag{3.38}$$

We are interested in finding the thickness of the thermocline at the CP-WP boundary, which we can do by integrating (3.38). This will be done later after the discussion of the mixed layer pressure gradient.

For the undercurrent, we assume that the momentum equation is characterized by a balance between the gradient of zonal kinetic energy and the horizontal pressure gradient force:

$$\frac{\partial}{\partial x}\left(\frac{u_{O-}^{\,2}}{2}\right) = -\frac{1}{\rho_{W-}}\frac{\partial p}{\partial x}. \tag{3.39}$$

Integrating (3.39) across the CP under the condition that $u_{O-} = 0$ on the eastern boundary, we obtain (3.33), where the positive root was taken since the undercurrent is westerly. As noted by McCreary (1981), reflection at the eastern boundary of the tropical Pacific generates waves which have westward group velocities. McCreary found linear solutions for the undercurrent as sums of Hermite functions. For the bounded response (i.e.

boundaries on both sides of the ocean basin). McCreary chose the amplitude of the given Hermite mode so that the zonal components which are proportional to Hermite function cancel at the boundary. McCreary found that the maximum speed of the undercurrent occurs to the east of the wind stress maximum. For simplicity, we assume that the maximum speed of the undercurrent occurs at the CP-WP boundary, i.e. at $x = \sigma_W$. Hence the undercurrent should slow to the east of the CP-WP boundary due to an interaction with westward-propogating waves and to the decrease of the wind stress. We assume that the speed of $u_{O\text{-}}$ decreases linearly, and hence U_O decreases linearly due to our assumption of contant undercurrent thickness. From (3.32), this implies that the rate of upwelling is constant across the CP. Based on estimates provided by McCreary (1981), we assume that the mean pressure gradient in the thermocline [in (3.33)] is about 50% of that in the mixed layer, which is described below.

A derivation in Appendix 5 shows that the vertical-mean mixed-layer pressure gradient satisfies

$$\left(\frac{dp}{dx}\right)_M = -\frac{g}{2}\frac{\partial}{\partial x}(\ln\rho_W) - g\frac{\partial z_S}{\partial x}, \tag{3.40}$$

where $\rho_W = \rho_0(1-\xi T)$, is an assumed equation of state for the ocean. Because we have assumed that there are no horizontal temperature gradients beneath the WP, the first term on the RHS vanishes. If the pressure gradient is approximately constant with height in the mixed layer, then it can be shown that

$$\Delta\rho\frac{\partial z_D}{\partial x} = \frac{\partial z_S}{\partial x}, \tag{3.41}$$

where $\Delta\rho$ is the jump in density across the thermocline, which we compute explicitly. For this model, we assume that $T_\infty = 293$ K based on the observed vertical temperature variation through the equatorial thermocline (Philander 1990). Substituting (3.41) in (3.40), and neglecting the first RHS term in (3.40), the horizontal pressure gradient force in the thermocline beneath the WP satisfies

$$\left(-\frac{1}{\rho_W}\frac{dp}{dx}\right)_M = g\frac{\Delta\rho}{\rho_W}\frac{\partial z_D}{\partial x}. \tag{3.42}$$

In order to determine the depth of the thermocline, we substitute the RHS of (3.42) for the second term on the RHS of (3.38). This gives

$$0 = -(\mathcal{F}_u)_S/\delta z_D + g\Delta\rho\frac{\partial z_D}{\partial x}. \tag{3.43}$$

We argue that δz_D is the thickness of the layer over which momentum can be mixed, while z_D can be thought of as the depth of the 293 K isotherm. We assume a value for $\delta z_D = 160$ m. Neglecting the small variation of the surface elevation (~ 0.5 m across the equatorial Pacific), we assume $z_D = 0$ at the eastern boundary of the CP. Under the assumption that the slope of the thermocline is linear across the tropical Pacific, we find that

$$z_D = \frac{-(\overline{\mathcal{F}}_u)_S\sigma_C}{\overline{\delta z_D} g\Delta\rho}, \tag{3.44}$$

i.e. the thermocline depth on the west side of the CP is proportional to the mean wind stress. The overbar denotes the horizontal average, which for $(\mathcal{F}_u)_S$, is taken as the wind stress in the middle of the CP. We have assumed a value for $\overline{\delta z_D}$, which is too large compared to the observations (~ 60 m; Philander 1990). However, as described in the next chapter, we find that z_D on the west side of the WP is between 95 m and 170 m, which is not too bad (~ 150 m; Philander 1990).

3.5 Radiative transfer

In order to calculate the moisture and energy budgets in the radiator fin, we must set up the radiative transfer equations. Consider a boundary layer topped by stratocumulus clouds and/or trade wind cumuli with cloud fraction f_B and liquid water path *LWP* which are diagnosed from the sea surface temperature and the relative humidity of the boundary layer.

3.5.a Longwave radiation

Just as in Chapter 2, we parameterize the net longwave radiation at the TOA and surface in terms of the surface temperature and precipitable water. We assume that the longwave flux at the TOA and surface are given by (2.38) and (2.40), respectively.

Under cloudy skies, we assume that

$$\mathcal{R}_{S,\,cld} = \mathcal{R}_{S,\,clr} - (1-\varepsilon^{-}_{B})\varepsilon_{SC}\sigma T_{CL}^{4}. \tag{3.45}$$

Here ε^{-}_{B} is the downward emissivity of the boundary-layer atmosphere. The cloud emissivity is assumed to satisfy $\varepsilon_{SC} = 1 - e^{-\tau_{SC}}$, where τ_{SC} is the longwave cloud optical depth. Following Stephens (1978), $\tau_{SC} = k_{SC}LWP$ and $k_{SC} = 150\ \mathrm{m^2\,kg^{-1}}$. The cloud-base temperature T_{CL} is assumed to be the temperature of the environment at the lifting consensation level.

For cloudy skies, the OLR is assumed to satisfy

$$\mathcal{R}_{\infty,\,cld} = \sigma T^4{}_B/(a_1 + c_1 W_{FC}), \tag{3.46}$$

where, as mentioned previously, W_{FC} is the column water vapor above the CPBL. This equation is identical to (2.38), except that T_B and W_{FC} replace the SST and total precipitable water. Basically, we are assuming that the cloud emits as a blackbody and that the important variable absorber is water vapor. This assumption requires boundary-layer clouds in our model to be optically thick.

We define the net longwave flux for level i as

$$\mathcal{R}_i \equiv \mathcal{R}^+{}_i - \mathcal{R}^-{}_i, \tag{3.47}$$

where the + and - denote upward and downward fluxes, respectively.

For partially cloudy skies, the longwave radiation at level i is given by

$$\mathcal{R}_i = f_B \mathcal{R}_{i,\,cld} + (1 - f_B)\mathcal{R}_{i,\,clr}. \tag{3.48}$$

In order to compute the radiative cooling rate of the free troposphere, we write the clear-sky longwave fluxes at the TOA and surface as

$$\mathcal{R}_{\infty,\,clr} = \sigma T_{SC}{}^4(1 - \varepsilon_B{}^+)(1 - \varepsilon_F{}^+) + \sigma T_E{}^4 \varepsilon_B{}^+(1 - \varepsilon_F{}^+) + \sigma T^+{}_F{}^4 \varepsilon_F{}^+, \tag{3.49}$$

$$\mathcal{R}_{S,\,clr} = \sigma T_{SC}{}^4 - \sigma T_E{}^4 \varepsilon_B{}^- - (1 - \varepsilon_B{}^-)\varepsilon_F{}^- \sigma T^-{}_F{}^4, \tag{3.50}$$

respectively. In general, the upward and downward emissivities of the free troposphere and boundary layer differ (Rodgers 1967). We assume for simplicity that T_E, the emission temperature of the boundary layer, is the arithmetic mean of temperatures at the top and bottom of the boundary layer. The emissivities can be evaluated, as described below. Then we can solve for $T^+{}_F$ and $T^-{}_F$, which are the upward and downward emission temperatures of the free troposphere.

Neglecting shortwave absorption, the radiative cooling rate of the free troposphere follows as

$$\Delta R_F = \varepsilon_F{}^+ \sigma T^+{}_F{}^4 + \varepsilon_F{}^- \sigma T^-{}_F{}^4 - \varepsilon_F{}^+(\sigma T_{SC}{}^4(1 - \varepsilon_B{}^+) + \sigma T_E{}^4 \varepsilon_B{}^+). \tag{3.51}$$

For this model, we assume that $\Delta \mathcal{R}_F = \mathcal{N}_{R\infty} - \mathcal{N}_{RB}$, i.e. that shortwave absorption has a negligible effect on the radiative cooling rate of the free troposphere. We neglect the effect of CPBL clouds on the radiative cooling of the free troposphere, as they have only a marginal effect (Stephens and Webster 1979). The clear-sky emissivity for the CPBL is parameterized as

$$\varepsilon^{+-} = \sum_{i=1}^{4} (a_i^{+-} \log W)^i , \tag{3.52}$$

where the coefficients a_i are described in Rodgers (1967) and Stephens and Webster (1979). This form of the emissivity was proposed by Rodgers (1967) and then extended by Stephens and Webster (1979) to include water vapor continuum absorption. Plots of the emissivity as a function of water vapor are shown in Rodgers (1967) and in Stephens and Webster (1979).

3.5.b Shortwave radiation

Following Chapter 2, the transmissivity $\Im$ of shortwave radiation through the atmosphere is given by

$$\Im = 1 - \frac{2.9(0.1 W_C/\mu_0)}{[1 + 141.5(0.1 W_C/\mu_0)]^{0.635} + 5.925(0.1 W_C/\mu_0)} , \tag{3.53}$$

where μ_0, the solar zenith angle, is assumed to be 0.5. With reference to Fig. 3.16, $\Im_F$ and $\Im_B$ are the transmissivities of the free atmosphere and boundary layer, respectively. These transmissivities are calculated by replacing W_C in (3.53) by W_F or W_B. As depicted in Fig. 3.16, α_{SC} and α_S are the albedos of the cloud and surface, respectively.

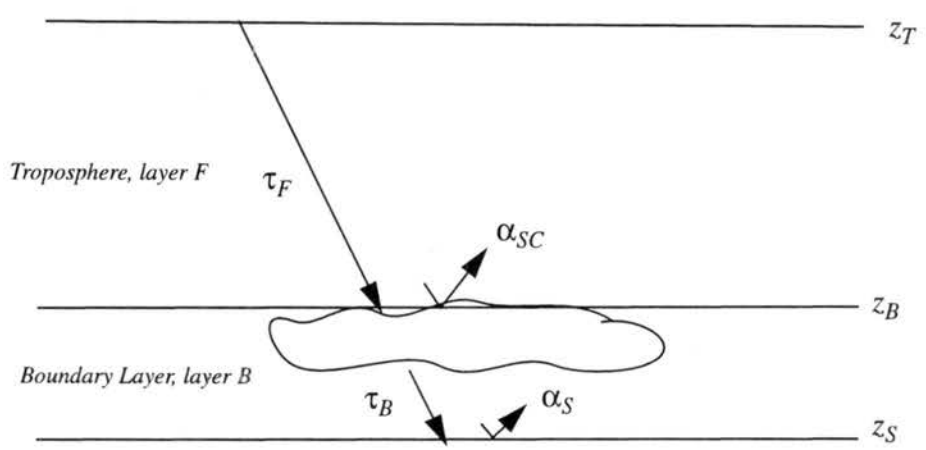

FIGURE 3.16: Schematic illustrating cloudy shortwave radiative transfer over the CP.

We assume that the upward shortwave radiation at the TOA satisfies

$$S^{+}_{\infty,\,cld} = S^{-}_{\infty}(1-A)\Im_F^2[\alpha_{SC} + \alpha_S \Im_B^2 (1-\alpha_{SC})^2], \tag{3.54}$$

where A represents the absorptivity of shortwave radiation by the stratosphere, and we have assumed that reflected shortwave radiation is not absorbed in the stratosphere. Given the downward shortwave radiation at the TOA, S^{-}_{∞}, we have

$$S_{\infty,\,cld} = S^{-}_{\infty}\{1-(1-A)\Im_F^2[\alpha_{SC} + \alpha_S \Im_B^2 (1-\alpha_{SC})^2]\}. \tag{3.55}$$

Again, following Chapter 2, the cloud albedo, α_{SC} is given by

$$\alpha_{SC} = \frac{(\alpha_{SC})_{max}\tau_{SW}/\mu_0}{\tau_0 + \tau_{SW}/\mu_0}, \tag{3.56}$$

and $(\alpha_{SC})_{max}$ is a predetermined maximum possible cloud albedo, τ_{SW} is the shortwave optical depth of the stratocumulus cloud, and τ_0 is a parameter that can be related to particle scattering asymmetry. The shortwave cloud optical depth is parameterized according to

$$\tau_{SW} = c_{SC} LWP, \tag{3.57}$$

where $c_{SC} = 150\ \mathrm{m^2\,kg^{-1}}$.

For overcast skies, the shortwave radiation absorbed by the surface is given by

$$S_{S,\,cld} = S^{-}_{\infty}(1-A)\Im_F(1-\alpha_S)\Im_B(1-\alpha_{SC}), \tag{3.58}$$

where $S^{-}_{\infty}(1-A)\Im_F$ is the shortwave radiation which has been transmitted down to cloud top, $1-\alpha_{SC}$ represents the fraction of the radiation which emerges from the bottom of the cloud, and $1-\alpha_S$ represents the fraction of radiation which is absorbed by the surface.

The net shortwave flux for level i is defined as

$$S_i = S^{-}_i - S^{+}_i. \tag{3.59}$$

For partly cloudy skies, the net downward shortwave at level i is

$$S_i = f_B S_{i,\,cld} + (1-f_B) S_{i,\,clr}, \tag{3.60}$$

where $S_{i,clr}$ is described in Chapter 2.

3.6 Summary of the solution method for the coupled system

Up to this point, we have been discussing the energy and moisture balance equations for the CP and WP separately. However, for equilibrium to exist, the coupled system must have energy and moisture balance.

The energy and moisture balance equations for the Walker circulation are given by

$$\sigma_W(\overline{\mathcal{N}_{\infty W}} - \overline{\mathcal{N}_{SW}}) + \sigma_C(\overline{\mathcal{N}}_{\infty C} - \overline{\mathcal{N}}_{SC}) = 0, \tag{3.61}$$

$$\sigma_W(\overline{\mathcal{E}}_W - \overline{\mathcal{P}}_W) + \sigma_C\Delta\overline{\mathcal{E}}_C = 0. \tag{3.62}$$

In deriving these equations, we have neglected meridional exchanges of moisture and energy.

Substituting from (3.1) and (3.2) in order to eliminate the quantities for the WP region, (3.61) and (3.62) become

$$\sigma_C(\overline{\mathcal{N}}_{\infty C} - \overline{\mathcal{N}}_{SC}) - \sigma_W\mathcal{F}_H = 0, \tag{3.63}$$

$$\sigma_C\overline{\mathcal{E}}_C - \sigma_W\mathcal{F}_q = 0. \tag{3.64}$$

Equations (3.63) and (3.64) are actually equivalent to (3.8) and (3.9), respectively. We have just re-derived them to show that they follow from moisture and energy balance for the entire system. We need not consider (3.64) further, because we have shown previously that $\mathcal{F}_q$ is derived directly from the mean evaporation rate for the CP. Thus (3.64) is identically satisfied. As discussed previously, $\mathcal{F}_H$ is derived independently of the atmospheric energy balance for the CP, and so (3.63) may not be satisfied. This provides a constraint on the system which we can use to compute σ_W.

Table 3.2 lists all the equations and unknowns in the atmosphere and ocean models, except for those from the radiation and cloud parameterizations. The equation denoted by *adv* refers to the water vapor advection model described earlier in this chapter. As shown below, the atmosphere model contains 21 equations and 21 unknowns, and the ocean model has 7 equations and 7 unknowns.

Due to non-linearities in the model, we have not yet found an analytical solution and so iteration was used to find a solution. Although iteration is a perfectly acceptable solution method, uniqueness of the solution is not guaranteed. In fact, multiple equilibria are a distinct possibility for a simple box model (i.e SL96). As described later in Chapter 4, the equilibrium solution is insensitive to differing initial conditions for the limited number of cases that we have tried.

TABLE: 3.2 a: Equations and Unknowns in the Atmosphere Model

Atmosphere

Equation	Unknown	Definition
2.11	IWP	ice water path
2.13, 3.23	$\mathcal{E}_W$, $\mathcal{E}_{CS}$	mean evaporation rate in the WP and at the center of the CP
2.16, 2.17, 2.62	z_T, T_T, Υ	tropopause height, tropopause temperature, lapse rate parameter
2.33	q_{SW}	specific humidity in the WP region
adv[a]	W_{FE}	precipitable water in the free troposphere above the CP
3.1	W_W	precipitable water in the WP region
3.3	$\mathcal{P}_W$	precipitation rate in the WP region
3.5, 3.6	$\mathcal{F}_H$, $\mathcal{F}_W$	lateral moist static energy and latent heat transports
3.7, 3.9	σ_W, σ_C	widths of the WP and CP
3.8, 3.15	u_{BI}, Π_{BI}	vertical-mean wind speed and pressure thickness of the TWI
3.10	q_{BI}	vertical-mean boundary-layer specific humidity at the CP-WP boundary
3.11	ω_B	subsidence rate at the top of the TWI
3.12, 3.25	U_A, $\mathcal{M}_B$	mass flux from the WP to CP/mass flux through the TWI
3.16	atmosphere HPGF	horizontal pressure gradient force

a. Refers to water vapor advection model.

TABLE: 3.2 b: Equations and Unknowns in the Ocean Model

Ocean

Equation	Unknown	Definition
3.30	T_{SW}	SST in the WP
3.31	T_{SE}	SST on the east side of the CP
3.32	T_U	undercurrent temperature
3.34, 3.35	u_{O-}, u_O	undercurrent/mixed-layer current
3.43	ocean HPGF	horizontal pressure gradient force
3.45	z_D	depth of the thermocline

The method of solution is as follows. We first find a solution for the WP region. That is, we guess initial values for $\mathcal{F}_q$, $\mathcal{F}_H$, T_{SE}, and the surface wind speed. From these, T_{SW} is computed as that which gives surface energy balance for the WP. Based on the SST difference between the WP and CP, we compute the boundary-layer wind speed and the ocean currents. If the wind speed does not match the guessed value, an iteration is carried out until the SST difference and wind speed are mutually consistent. The CP SST is then calculated. If the calculated value does not match the previously guessed value, then the boundary-layer wind speed must be re-calculated and the process repeated until the error between a previous value and the current calculation is less than 0.1 K. Similar iterations are carried out so that the differences between the current and previous calculations of horizontal moisture and energy fluxes are small.

At this point, the calculation is consistent, but we do not yet have a solution for the WP. We must check to see if the horizontal transport of moist static energy from the WP region balances the net heating of the atmosphere in the WP region. If the horizontal energy transport from the WP is smaller than the net heating of the atmosphere, we must increase q_S. Recall from Chapter 2 that our surface humidity assumption relates q_S to the precipitable water, W. Through the radiative effects of increased W, an increase of q_S can also affect the TOA energy balance of the WP. If q_S must be changed, then the entire process must be repeated until the calculation is consistent and the horizontal energy transport balances the net heating of the atmosphere in the WP region. The result is a WP solution for a given σ_W. The boundary-layer wind speed, the ocean currents, T_{SW} and T_{SE} are all known following this calculation. However, (3.63), which is the condition for energy balance of the CP, may not be satisfied. Hence this iteration is

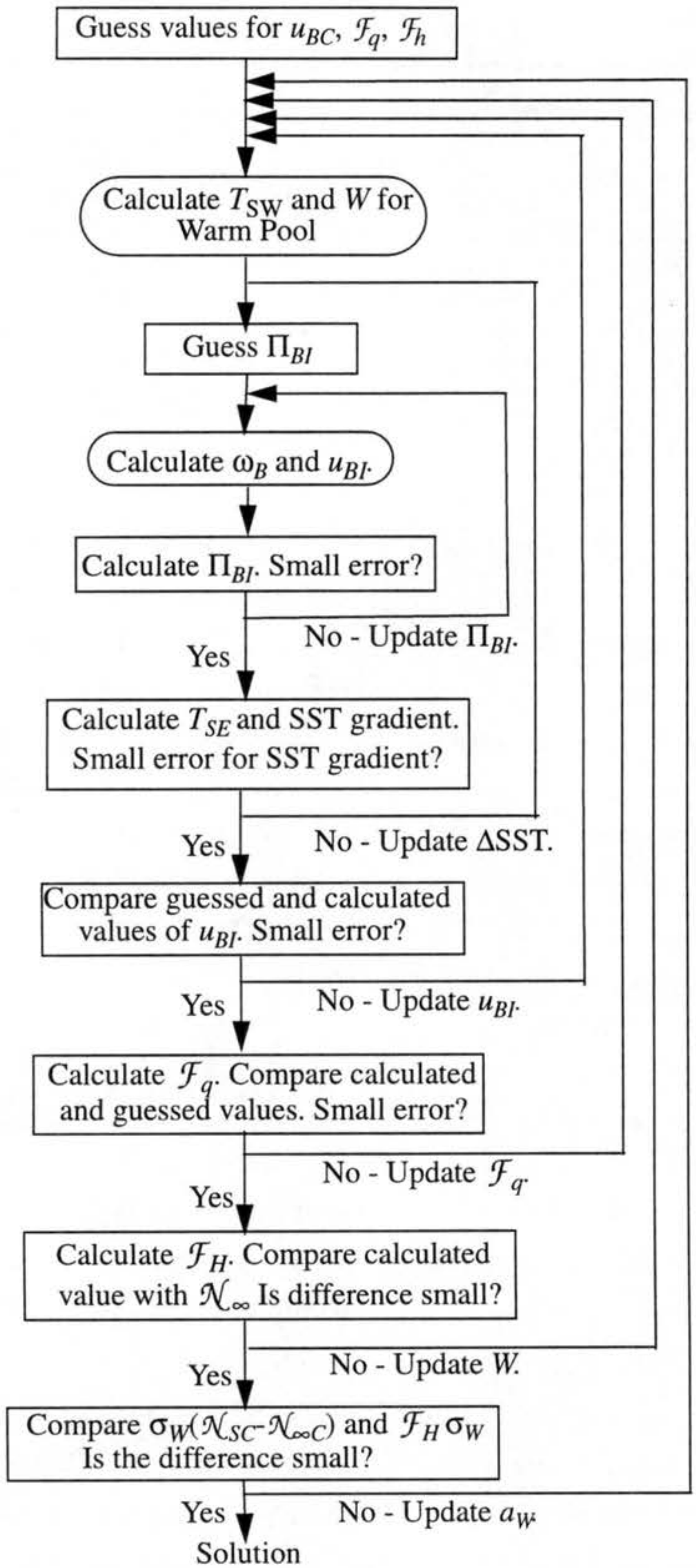

FIGURE 3.17: Flow chart illustrating the detailed process by which an equilibrium solution for the coupled model is found.

is repeated for a range of σ_W values; and both terms of (3.63) [or, equivalently (3.8)] are plotted as a function of σ_W. Figure 3.17 illustrates this iterative process graphically. Fig. 3.18 displays an equilibrium solution obtained using this method. A solution is given by an intersection of the two curves, which, for this example, is $a_W = 0.33$. Characteristics of the solution are discussed in Chapter 4.

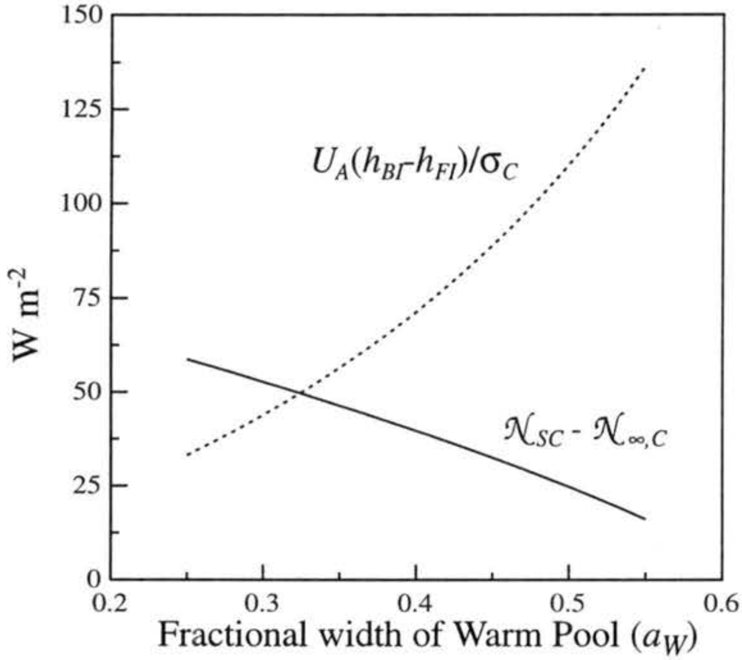

FIGURE 3.18: Energy balance for the CP as a function of WP relative area. The dashed line shows the horizontal energy flux per unit area into the CP. The solid line depicts the vertical energy flux divergence for the CP. An equilibrium is denoted by the intersection of the two curves.

CHAPTER 4

Results

4.1 Introduction

In this section, we describe and compare and contrast our results with the recently published box models discussed in Chapter 1. Our objective is to show the roles of the components of the ocean-atmosphere coupled system. For instance, we compare results in which cloud radiative effects are alternatively included and excluded from the simulations. The influence of cloud radiative effects over the CP has already been investigated in a very simple way by Miller (1997) and by Larson et al. (1999). The cloud fraction in their models, as well as in ours, is determined from an observed linear relation (Klein and Hartmann 1993) between low-level stability, as measured by the 700 mb-surface potential temperature difference, and cloud fraction.

Miller and Larson et al. assumed a value for the horizontal energy flux divergence in the CP, and so the interactions between atmosphere and ocean circulations were suppressed. With our model, we are able to simulate such interactions explicitly, and therefore it is interesting to see how our results differ from theirs. It seems evident that cloud radiative effects in the CPBL can be modulated by the ocean circulation. As the cloud cover/optical depth increases, the flux of shortwave radiation at the surface decreases, and so the SST decreases. Assuming that SST for the WP remains constant, the decrease of SST for the CP would increase the surface wind stress and the intensity of the ocean circulation. If the SST of the CP were to decrease, we would expect the trade-wind inversion to intensify, assuming that the temperature in the free troposphere remained constant. Such a perturbation might lead to an increase of CPBL cloud cover, which in turn, could intensify the initial perturbation. These interactions are explored in depth in Section 4.4b.

We also describe the radiative effects of high clouds over the WP, which were largely neglected by Pierrehumbert (1995) under the observationally based assumption that longwave and shortwave cloud radiative forcings cancel at the TOA. Because of the observed near-cancellation for the current climate, high clouds over the WP do not affect the total amount of energy which must be exported to the CP region and mid-latitudes. However, the clouds do impact the vertical distribution of radiation fluxes compared to clear skies. The radiative effects of clouds reduce the shortwave flux absorbed by the ocean and reduce the longwave radiative cooling of the atmosphere. Based on the dominant surface balance between the surface evaporation rate and the net surface shortwave flux

(Cornejo-Garrido and Stone 1977), it has been proposed that the evaporation rate decreases to compensate for the reduction of absorbed shortwave radiation produced by optically thick high clouds (Pierrehumbert 1995; Larson et al. 1999). Results from their two-box models support this conclusion.

In our model, the friction velocity is based on the calculated wind speed and an assumed transfer coefficient. Although we do assume that the sea surface-surface air temperature difference is small for the equilibrium climate, our model includes a much larger range of ocean-atmosphere interactions than do previous box models. Our model should therefore provide more definitive evidence on the role of high-cloud radiative feedbacks over the WP in modulating the tropical climate. We present results for the simulated Walker circulation in which high-cloud radiative effects for the WP are alternatively included and excluded.

This chapter is organized as follows. Section 4.2 describes results from our base case in which there are clear skies over the CP, while Section 4.3 discusses the sensitivities of our solution. In Section 4.4, we examine how cloud radiative effects influence the solution. Section 4.5 describes the feedbacks on SST when the solar constant is perturbed.

4.2 Base case

Table 4.1 shows the specified parameters which were assumed for all cases unless otherwise noted. The assumptions of a zero-temperature difference between SST and SAT and an autoconversion rate for *IWP* were described in detail in Chapter 2. A cloud fraction of 0.5 for the WP region was chosen to be in rough agreement with the observations, although our specification is slightly low. Basically we chose $f = 0.5$ because it gives better results than for a larger cloud fraction. The bulk evaporation and momentum coefficients were specified based on Deardorff (1972). We prescribe a much lower transfer coefficient than that suggested by Deardorff because we parameterize the evaporation rate as a function of the mean specific humidity in the trade-wind layer, rather than in the well-mixed planetary boundary layer. The evaporation efficiency, defined as $\Delta = (\mathcal{E} - \mathcal{P})/\mathcal{E}$, determines the fraction of evaporated water vapor, which is transported into the WP region. The sensitivity of the solution to Δ will be discussed later.

Figure 4.1 depicts the horizontal energy flux convergence (dashed line) and vertical energy flux divergence (solid line) for the CP. As discussed in the previous chapter, an intersection of these curves denotes an equilibrium solution for the Walker circulation. As a_W increases from 0.2 to 0.6, horizontal energy export from the WP increases from 25 W m^{-2} to 160 W m^{-2}. The vertical energy flux divergence decreases from 50 W m^{-2} to -50 W m^{-2} for the same range of a_W values. As can be seen from the figure, our solution occurs for $a_W = 0.27$ and $\mathcal{N}_{\infty C} - \mathcal{N}_{SC} = 35$ W m^{-2}. The reasons for this behavior will become clear shortly. For a given set of parameters, our iterative technique has resulted in only a single solution. Although we certainly have not proved that no additional solutions exist, we have yet to find any additional solutions. For at least some cases, an identical solution results for different initial conditions.

TABLE: 4.1: Specified parameters

Variable	Value
SST-SAT temperature difference	0 K
autoconversion rate for ice water path	2,000 s
WP cloud fraction	0.5
bulk evaporation coefficient	0.2×10^{-3}
bulk momentum coefficient	0.8×10^{-3}
length of the ocean basin	1.5×10^{7} m
minimum undercurrent temperature (T_U)	293 K
Evaporation efficiency	0.4

The solution is summarized in Table 4.2. As can be seen from the Table, the SST difference across the equatorial ocean basin is approximately 10.3 K, which is somewhat larger than observed. As Philander (1990) shows, the maximum SST difference on the equator is about 6 K, but the difference increases to 8 K at 5° S. McCreary (1981) estimates the maximum intensity of the undercurrent to be greater than 1.2 m s^{-1}. As shown in Fig. 4.2, the undercurrent in the central Pacific varies between 1.9 m s^{-1} and approximately -0.5 m s^{-1}. Nevertheless, the mean seems to hover near 1.1 m s^{-1}. As shown in Table 4.2, our model diagnoses the mass flux to be 1.34×10^5 kg m^{-1} s^{-1}, which for a 100-m thick undercurrent and $\rho_W = 1000$ kg m^{-3}, implies that the maximum undercurrent is 1.34 m s^{-1}. Although the simulated current is somewhat stronger than those depicted in Fig. 4.2, this value represents the maximum current for our model, and thus may not be an overestimate.

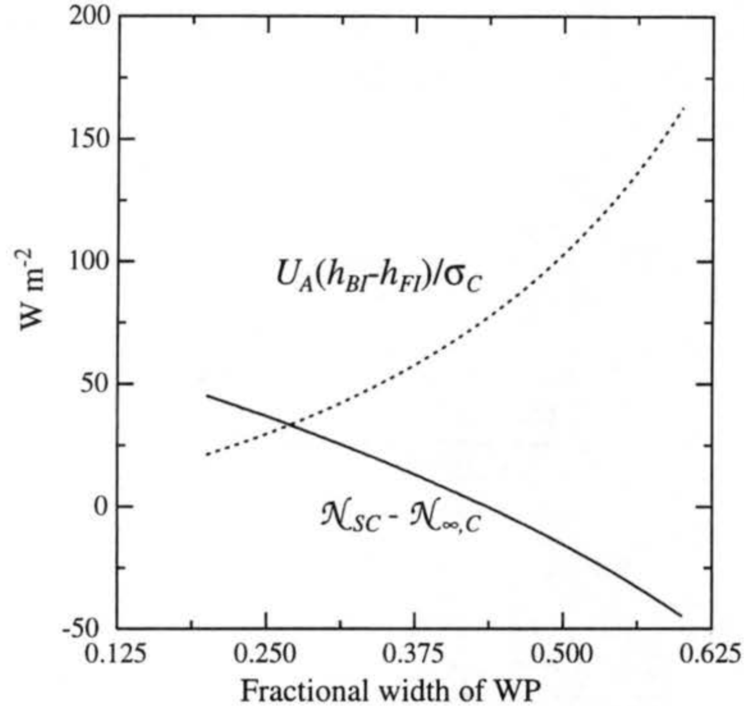

FIGURE 4.1: Energy balance for the CP as a function of WP fractional width.The dashed line shows the horizontal energy flux per unit area into the CP. The solid line depicts the vertical energy flux divergence for the CP. An equilibrium is denoted by the intersection of the two curves.

This result demonstrates that ocean dynamics are sufficient to produce a realistic equilibrium solution which does not depend on cloud radiative effects over the CP. The result depends on the specified value of T_∞, which for the base case is 293 K and which represents the minimum vertical-mean temperature for the undercurrent. We derived an expression for the undercurrent temperature (3.31), but Fig. 3.15 shows that $T_U = T_\infty$ for most of the x domain east of the CP-WP boundary. Because the simulated current for the coupled model is nearly three times more intense than that assumed to derive Fig. 3.15, $T_U = T_\infty$ for an even larger fraction of the x domain. Because $T_U = T_\infty$ for most of the x domain, hereafter we refer to T_U and T_∞ interchangeably. In deriving our results, the temperature T_U was tuned; simulations with $T_U = 293$ K were found to give better results than those with $T_U = 288$ K. However, the sensitivity of our results to the assumed value for T_U shows the importance of ocean dynamical effects on the equilibrium solution.

TABLE: 4.2: Base Case Results

Variable	Value
Fractional width of the WP (a_W)	0.270
T_{SW}	306.5 K
Warm-Pool W	64.9 kg m^{-2}
T_{SE}	296.2 K
Cold-Pool W	23.6 kg m^{-2}
Maximum depth of the CPBL	219 mb
Maximum vertical-mean zonal wind in the CPBL	-9.6 m s^{-1}
Surface Latent heat flux in CPBL	106.9 W m^{-2}
Ocean mass flux	1.34×10^5 kg m^{-1} s^{-1}
Mixed-layer thickness	94 m
Net cloud radiative forcing at WP TOA	-1.5 W m^{-2}
Lateral moist static energy transport ($\mathcal{F}_{\mathrm{H}}$)	90.3 W m^{-2}
Lateral latent heat transport ($\mathcal{F}_{\mathrm{q}}$)	-121.5 W m^{-2}

The precipitable water for the WP simulated by the model is about 30% larger than that observed by satellite (Fig. 4.3). The dataset shown below is an average of Januaries between 1988 and 1991. For the WP region, the mean precipitable water appears to be near 50 kg m^{-2}. As compared with the subsiding regions of the tropics, the simulated precipitable water for the CP region is quite realistic. As we discuss later, the model's overestimate of precipitable water for the WP leads to an overestimate of T_{SW}. As shown in Fig. 1.1, a reasonable large-scale average for T_{SW} is approximately 302 K, and so the SST simulated by our model is 4.5 K too warm.

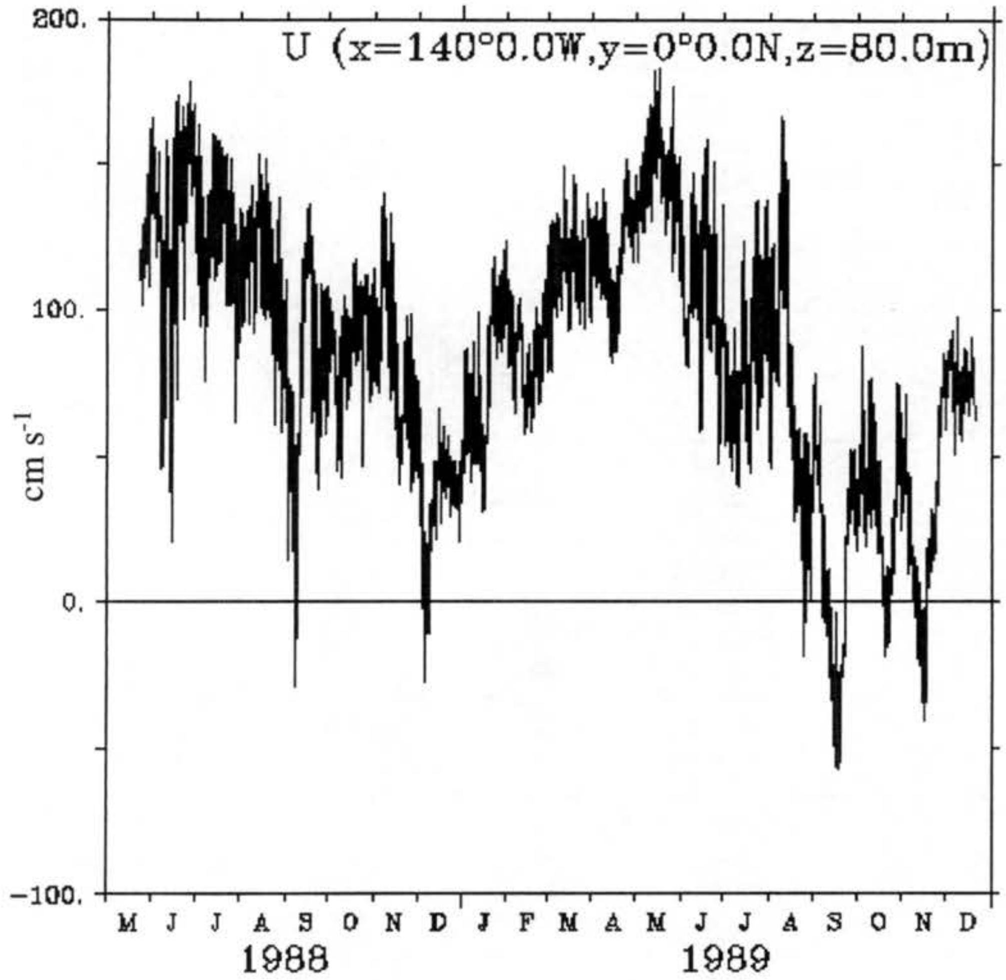

FIGURE 4.2: Plot taken from the TOGA TAO web site. Hourly data for the zonal current on the equator at longitude 140° W and a depth of 80 m.

The inversion height for our solution is 781 mb, which makes the CPBL only about 19 mb deeper than is generally observed (Haraguchi 1968). There are cases, however, in which Haraguchi found the lowest inversion height to be higher than 750 mb. As discussed in Chapter 3, we have combined the trade-wind boundary layer with a layer of easterlies above. In nature, the layer of easterlies extends 200 mb above the CPBL, while the CPBL itself is about 200 mb thick. For our model, the pressure thickness for this idealized layer should be about 300 mb. When Π_{BI} decreases to significantly less than 300 mb, the boundary-layer pressure gradient tends to be somewhat weak. As a result, the surface wind stress is relatively weak (< 10 m s^{-1}), even though the SST gradient is too strong. Thus, a shallow thermocline (94 m) is a consequence of a weak pressure gradient.

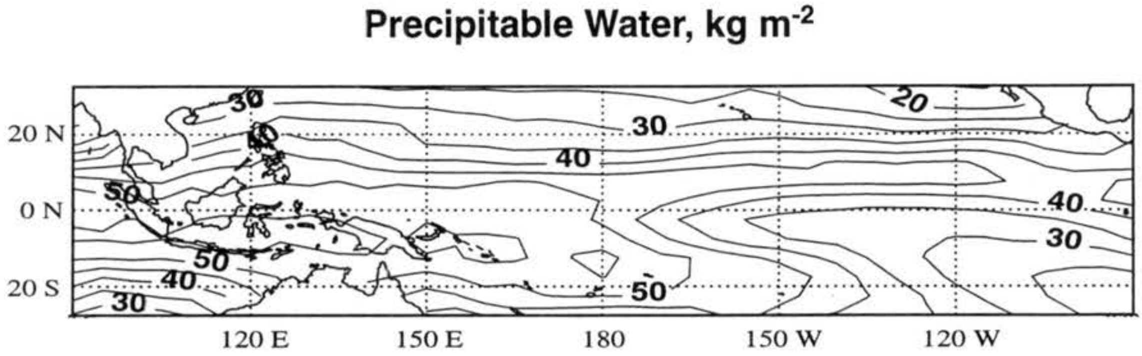

FIGURE 4.3: Contour plot of precipitable water in kg m^{-2} from SSM/I satellite observations for an average of Januaries between 1988 and 1991. The contour interval is 5 kg m^{-2}.

The simulated evaporation rate for the CP is not too different from the observed value, i.e. 107 W m^{-2} compared to 98 W m^{-2} obtained from the TOGA TAO buoys (Zhang and McPhaden 1995). We have assumed that 40% of the water vapor evaporated from the CP is transported to the WP. Although this assumption provides a realistic simulation, Webster (1994) estimated that the net freshwater flux ($\mathcal{P}$ - $\mathcal{E}$) in the ocean is slightly positive in the central and eastern equatorial Pacific. Thus, we may be underestimating the precipitation rate over the CP. Although strong precipitation events are somewhat rare over the CP, drizzle is a frequent occurrence off the coast of South America. As shown in Fig. 4.4, the precipitation rate on the equator and to the east of 150° W is approximately 1 mm day^{-1}, which equates to a latent heating of 29.2 W m^{-2}. Even though this value is small, the surface latent heat flux in this region is of order 30 to 50 W m^{-2}. Hence, a significant proportion of the water vapor supplied by evaporation is not available for export to the WP.

Our results differ from those of M97 and L99 in that we specifically include the effects of precipitation on the CPBL moisture budget. Miller solved for the evaporation rate as that which balances the moisture budget, based on a prescribed relative humidity profile. Because the relative humidity in the CP region would have to be much larger without precipitation, an assumed relative humidity profile based on the observations implicitly includes the effects of precipitation. Larson et al. did not specifically account for precipitation, but parameters in the moisture and energy budgets were tuned to provide tropics-like solutions. For instance, the relative humidity for the WP region is computed based on an assumed fraction by which eddy fluxes augment the large-scale flux of water vapor. There is no justification for such a parameter other than that it gives good results.

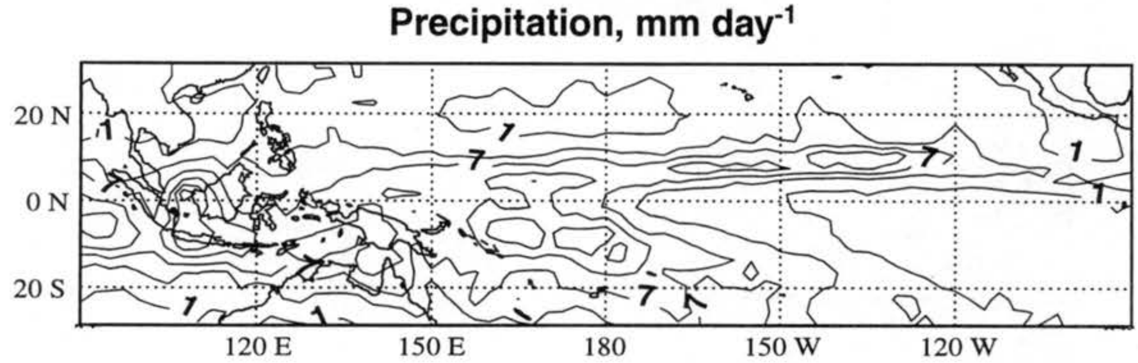

FIGURE 4.4: Tropical precipitation rate in mm day^{-1} from the Global Precipitation Climatology Product for an average of Januaries between 1988 and 1992. The data were derived from the SSM/I algorithm. The contour interval is 3 mm/day.

One point of note here is that the simulated net cloud radiative forcing at the TOA for the WP is approximately -1.5 W m^{-2}, which agrees extremely well with observations from the Earth Radiation Budget Experiment (Kiehl 1994). As described in our literature review, meridional energy export by the Hadley circulation reduces the total amount of energy which must be transported either zonally by the Walker circulation or vertically by radiative cooling. Previous box models (e.g. Larson et al. 1999) have assumed a horizontal energy flux divergence of 20 to 25 W m^{-2} from the simulated tropical circulation. Noting that $\mathcal{F}_q$ = -121 W m^{-2} and $\mathcal{F}_H$ = 90 W m^{-2}, which are about 20% and 50%, respectively, larger than the values assumed in Chapter 2, the model must adjust so as to cool the WP region sufficiently to reach energy balance.

Even though we compute the relative width of the WP, we show a series of plots as a function of a_W. In order to do this, we must violate the constraint imposed by (3.63); that is, the vertical flux divergence of energy in the CP region no longer balances the energy imported laterally from the WP. Despite the violation of this constraint, the plots are of interest in order to illustrate the basic mechanisms which control the equilibrium solution of the WP.

From Fig. 4.5, we see that T_{SW} and T_{SE} increase and decrease, respectively, as a_W increases. The precipitable water for the WP region (not shown) more than doubles, increasing from 55 kg m^{-2} to 130 kg m^{-2} as a_W increases from 0.2 to 0.6. Figure 4.1 shows that the rate of lateral heat transport from the WP atmosphere increases with a_W. Because we assume that the surface energy budget in the WP is in equilibrium, the heat transported laterally from the WP must balance the net flux of energy at the TOA of the WP region. As the rate of lateral heat transport increases, the energy absorbed at the TOA of the WP region increases, because the greenhouse effect intensifies as a_W increases. The surface temperature at the east side of the CP decreases due to the effects of cold-water upwelling. Although the column water vapor increases by 20 kg m^{-2} above the CP and causes the long-wave radiative cooling rate at the surface to decrease, its effect on the surface energy budget is negated by a doubling of the ocean mass flux. The large heat capacity of the cold water overwhelms the radiative effect of more water vapor; and so T_{SE} decreases.

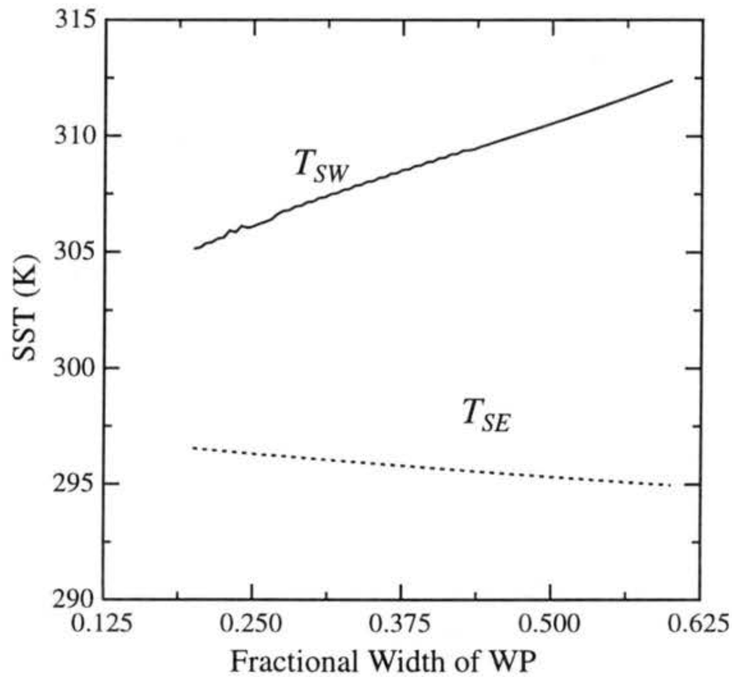

FIGURE 4.5: SST for the WP (solid line) and eastern boundary of the CP (dashed line) as a function of WP relative area. The equilibrium value is given by the intersection in Fig. 4.1.

We must now interpret the changes of precipitable water with a_W. Figure 4.1 shows that the horizontal energy import per unit area for the CP increases by more than a factor of five as a_W increases. This occurs due to an increase in heating of the WP region and due to a decrease in the width of the CP. An analysis of the moist static energy flux, $U_A(h_{FI} - h_{BI})$, and the latent heat flux, $U_A L(q_{FI} - q_{BI})$, indicates that the magnitudes of the fluxes increase as a_W increase, even if the precipitable water is initially held constant. Although the subsidence rate remains approximately constant initially (for constant precipitable water), σ_C decreases and so $U_A \equiv \omega_B \sigma_C / g$ decreases. In addition, $\sigma_W \equiv a_W \sigma$, which is in the denominators of $\mathcal{F}_q$ and $\mathcal{F}_H$, increases as a_W increases. As result, the magnitudes of $\mathcal{F}_q$ and $\mathcal{F}_H$ increase. The increase of $\mathcal{F}_q$, which amounts to a decrease in the amount of moisture imported from the CP to WP, causes the precipitation rate in the WP to decrease and therefore the cloud albedo to decrease. As a result, the net radiation flux at the TOA in the WP region increases slightly. In order to balance the WP region energetically, the precipitable water above the WP region must increase, and so the net flux of radiation above the WP column decreases and $\mathcal{F}_H$ increases. As mentioned above, a stronger greenhouse effect is induced by an increase of precipitable water, which causes the SST for the WP to increase as a_W increases.

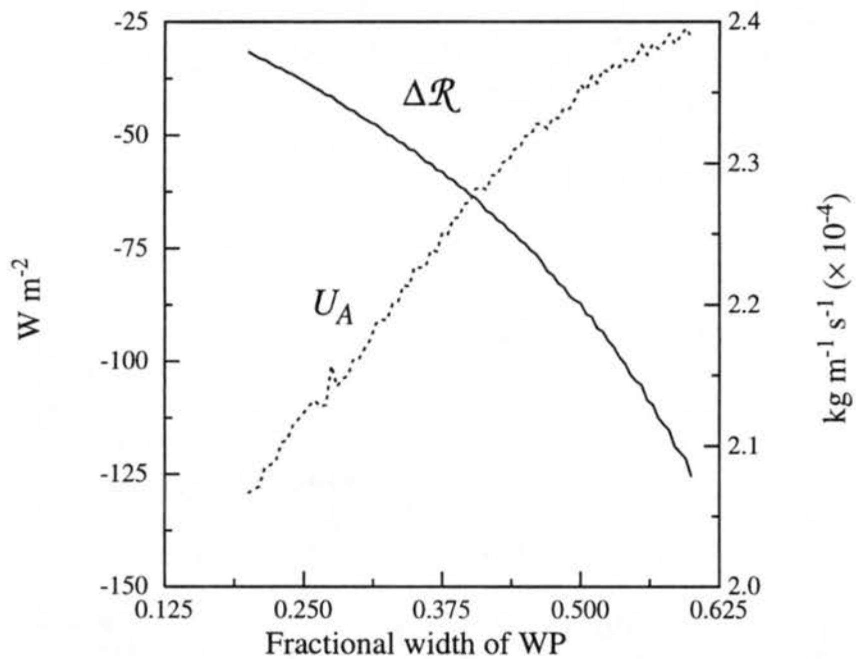

FIGURE 4.6: Radiative heating (solid line; left axis) in units of W m^{-2} above the CPBL and horizontal mass flux (right axis; dashed line) in units of kg m^{-1} s^{-1} as functions of WP fractional width.

Although T_{SE} decreases with a_W, the precipitable water above the CPBL increases with a_W. Additional water vapor is advected to the CP region because the precipitable water over the WP increases as a_W increases. As can be seen from Fig. 4.6, the radiative cooling rate increases by 100 W m^{-2} due to the increase of free-tropospheric water vapor. As described in Chapter 3, the atmospheric mass flux, U_A, is proportional to the radiative cooling, and so it increases by 12.5% as a_W increases from 0.2 to 0.6. The increase of U_A is limited, despite an increasing radiative-cooling rate, because the width of the CP and the pressure thickness of the trade-wind boundary layer decrease as a_W increases. As the width of the CP decreases, U_A decreases for a fixed radiative cooling rate, since the area through which the air is cooled decreases. The subsidence rate decreases as the denominator in (3.10) increases. The difference between s_B, the dry static energy at the top of the TWI, and s_{avg}, the vertical-mean dry static energy of the free troposphere, which is in the denominator of (3.10), increases as the pressure thickness of the TWI layer decreases. These two effects combine to give a decrease of U_A.

4.3 Sensitivities of the solution to parameters

The next step is to examine how the solution varies with the parameters specified in Table 4.1. In particular, we wish to determine the response of the tropical climate to varying the specified minimum undercurrent temperature and the specified evaporation efficiency. Discussion of the sensitivity of the solution to t_{prec}, the autoconversion rate for WP cirrus clouds, and f, the cloud fraction over the WP, will be deferred to Section 4.4, where cloud radiative effects are discussed in detail.

As shown in Fig. 4.7a, T_{SW} is sensitive to Δ, but not to T_U. Holding T_U constant, T_{SW} increases by 10 K as Δ increases from 0.2 to 1. As Fig. 4.7d shows, T_{SW} and W are well-correlated. Comparing Fig. 4.7a and Fig. 4.7c, it can be inferred that T_{SE} is relatively insensitive to Δ. The mass flux of the ocean prevents T_{SE} from departing from T_U by more than 4 K. For fixed T_U, as Δ increases, the east-west temperature difference increases. This occurs mainly due to the increase of T_{SW} with Δ, which was mentioned above. As the east-west temperature difference increases, we might expect the surface wind stress to increase. However, the thickness of the TWI layer shrinks as a_W increases, and so the surface wind stress increases only slightly. Hence, the ocean mass flux increases only slightly, and for fixed T_U, T_{SE} decreases by only 0.5 K as Δ increases from 0.2 to one.

From Fig. 4.7b, we note that for a_W, the fractional width of the WP, the dependence on T_U is stronger than that for Δ. However, for fixed T_U, a_W has a maximum near $\Delta = 0.6$. What is going on here? The solution for a_W must simultaneously satisfy several constraints. Even though T_{SW} and T_{SE} are predicted based on their own surface energy budgets, a_W determines the intensity of the SST gradient. It also determines the CP width through which air subsides into the CPBL, and thus ensures that the constraint of mass continuity holds. Finally, a_W must adjust so that the energy transported laterally from the WP balances the vertical flux divergence of energy from the CP region. In general, the radiative cooling rate (not shown) increases as Δ increases, and so a_W is relatively constant. The increase in radiative cooling rate explains the increase of U_A with Δ. Holding Δ constant, the radiative cooling rate decreases slightly as T_U increases. Because U_A is relatively constant with T_U, the decrease in radiative cooling rate implies that a_W must increase as T_U increases, which is what we see in Fig. 4.8a. Note that the changes of a_W are relatively small across the entire phase space.

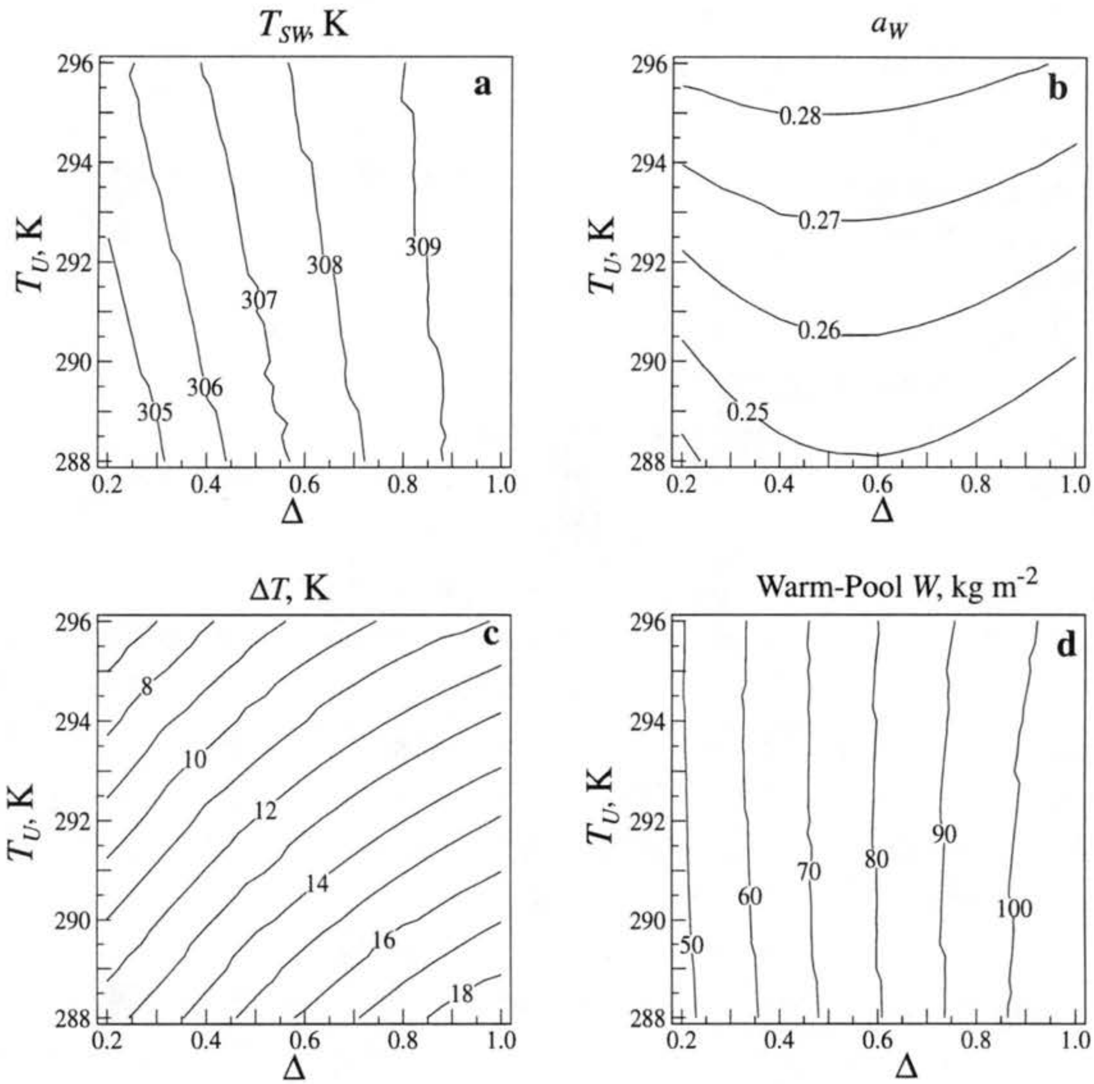

FIGURE 4.7: Contour plots of a) T_{SW} in units of K, b) a_W, which is unitless, c) east-west SST difference in units of K, and d) WP precipitable water in units of kg m^{-2}, as functions of the evaporation efficiency (Δ; unitless) and undercurrent temperature (T_U; K). The contour intervals for a, b, c, and d are 1 K, 0.01, 1 K, and 10 kg m^{-2}, respectively.

As mentioned previously, our results differ from previous studies with box models in that we solve for a_W. The interactions among the subsidence rate, the mass flux, and the relative width of the WP are not seen in Pierrehumbert (1995), Sun and Liu (1996), Miller (1997), and Larson et al. (1999). Because none of these previous studies included a momentum budget for either the ocean or the atmosphere, a_W was a free parameter which could simply be specified.

In order to understand the dependencies of the solution on these parameters, consider Fig. 4.7d. We see that the precipitable water over the WP is quite sensitive to Δ. As Δ increases, the CP exports a greater proportion of its evaporated water vapor to the WP. In order to balance the moisture and energy budgets, which depend on the latent heat transported laterally from the CP region, the precipitable water over the WP must increase as Δ increases. Due to the increasing greenhouse effect as the precipitable water increases, T_{SW} must increase as Δ increases.

To see why W varies with Δ for fixed T_U, consider Fig. 4.8. For fixed T_U, the intensity of the Walker circulation, as represented by U_A, increases as Δ increases. For fixed Δ, its dependence on T_U is negligible. Figure 4.8b shows that the net energy flux at the TOA of the WP region decreases slightly as Δ increases. One would think that the circulation could weaken as Δ increases, since the precipitable water over the WP also increases with Δ. The reason this does not happen is that the water vapor supplied from the CPBL increases strongly as Δ increases. The mean evaporation rate for the CPBL varies by only 20 W m^{-2} across the entire phase space depicted in Fig. 4.8. But the net latent heat flux (that is, the evaporated water which is available for transport to the WP) increases from 20 W m^{-2} for $\Delta = 0.2$ to 120 W m^{-2} for $\Delta = 1$. The net result is that W, and to a lesser extent, U_A must increase as Δ increases.

U_A increases with Δ because the radiative cooling rate increases with Δ. As Δ increases, the radiative cooling rate triples and therefore contributes to a much larger subsidence rate. It can be shown that $U_A = \omega_B \sigma_C / g$. Because $\sigma_C = (1 - a_W)\sigma$ does not vary strongly with Δ, U_A is essentially proportional to ω_B as Δ increases. As can be seen from Fig. 4.8b, $\mathcal{N}_\infty$ is essentially independent of Δ (and of T_U for that matter), and so $\mathcal{F}_H$ must remain constant as Δ increases. Recall that the water vapor budget controls the lateral transport of moist static energy, since we have assumed that no temperature gradient exists at the CP-WP boundary. Because U_A increases as Δ increases, $h_{FI} - h_{BI}$ must decrease. As mentioned previously, q_{BI} increases strongly as Δ increases, which implies that q_S must still increase as Δ

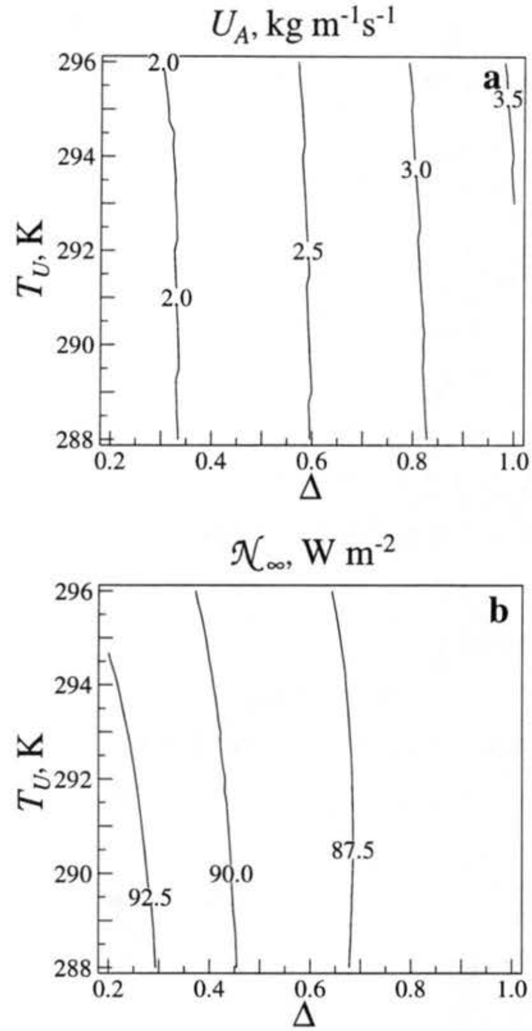

FIGURE 4.8: Contour plot of a) U_A in kg m^{-1}s^{-1} and b) $\mathcal{N}_\infty$ in W m^{-2} as functions of the evaporation efficiency (Δ; unitless) and undercurrent temperature (T_U; K). The contour intervals are 0.5 kg m^{-1}s^{-1} and 2.5 W m^{-2}.

increases. Our surface humidity assumption [(2.33)] relates the precipitable water to q_S. As a result, W increases as Δ increases.

Our advection model can be modified to give much better results. As described in Chapter 3, we assume that the precipitable water over the CPBL advects from the WP region. Due to sinking motion in the CP free troposphere, precipitable water advected from the lower troposphere of the WP region cannot reach the central or eastern part of the CP region before it is entrained into the CPBL. For our simple advection model, we have assumed that the column water vapor over the central part of the CP free troposphere originates from the upper half of the troposphere at the CP-WP boundary. For the results presented above, this level is $p_{mid} = 457$ mb. Suppose we assume that the distribution of winds change such that the precipitable water comes from the upper 70% of the WP free troposphere, rather than from the upper 50%. As can be seen from Table 4.3, the solution is much improved. The values for T_{SW} and T_{SE} are quite realistic, as are the values for the precipitable water. Although we tried to moisten the CP region, the model responded by drying. Even the maximum depth of the thermocline is much closer to the observed value of 150 m (Philander 1990). The water vapor originated from pressure level p_{mid} = 550 mb, which differs from the original solution by less than 100 mb.

The reason for this difference derives from the increased radiative cooling rate for a given value of the WP precipitable water. For the "wet troposphere" solution, a stronger

TABLE: 4.3: Wet troposphere solution

Variable	Value
Fractional width of the WP (a_W)	0.279
T_{SW}	301.7 K
Warm-Pool W	43.5 kg m^{-2}
T_{SE}	295.8 K
Cold-Pool W	22.0 kg m^{-2}
Maximum depth of the CPBL	236 mb
Maximum vertical-mean zonal wind in the CPBL	-10.2 m s^{-1}
Surface latent heat flux in CPBL	96.7 W m^{-2}
Ocean mass flux	1.42×10^5 kg m^{-1} s^{-1}
Mixed-layer thickness	163 m s^{-1}
Net cloud radiative forcing at WP TOA	-3.5 W m^{-2}
Lateral moist static energy transport ($\mathcal{F}_H$)	93.4 W m^{-2}
Lateral latent heat transport ($\mathcal{F}_q$)	-104 W m^{-2}

radiative cooling rate produces a stronger subsidence rate and hence contributes to an intensified Walker circulation. As a result, the model reaches equilibrium for a much lower value of precipitable water in the WP region. Our result suggests that water vapor over the CP originates from a lower level than that assumed in our advection model. It also demonstrates the extreme sensitivity of the solution to the amount and vertical distribution of water vapor over the CPBL.

4.4 Cloud radiative effects

We next wish to consider the effects of cloud radiative forcing on the solution. Recall that Miller (1997) specified the cloud radiative forcing, while Larson et al. (1999) specified the cloud optical depths over both the WP and CP and the cloud fraction over the WP. Although we specify the cloud fraction for the WP region, we calculate the optical depths for clouds in the WP and CP regions.

4.4.a Cloud radiative forcing over the Warm Pool

We examine the response of our solution as a function of specified cloud fraction and autoconversion rate. Figures 4.9a, b, c, and d show the equilibrium values for T_{SW}, a_W, $\Delta T_S \equiv T_{SW} - T_{SE}$, and precipitable water in the WP region (W), respectively, as functions of f and t_{prec}. For low t_{prec} and f, T_{SW} and ΔT_S increase as t_{prec} and f increase. For $0.6 \leq f \leq 0.4$, ΔT_S and T_{SW} are insensitive to changes of t_{prec}. The largest values for these two quantities occur for $t_{prec} = 1000$ s and $f = 0.85$. For $f > 0.6$, T_{SW} and ΔT_S decrease as t_{prec} increases, but only slightly. For fixed f, a_W increases monotonically as t_{prec} increases. For fixed t_{prec}, a maximum value of a_W occurs near $f = 0.55$. Precipitable water over the WP increases as f and t_{prec} increase, although its response to increasing f is larger than that for increasing t_{prec}. The maximum value of W is approximately 101 kg m^{-2}, which is extremely large.

It is somewhat surprising that T_{SW} increases as the cloud fraction increases. As discussed previously, the cloud optical depth for anvil cirrus over the WP is proportional to t_{prec}. For thin clouds and low cloud fraction, the surface shortwave heating is at a maximum. Nevertheless, the ocean reaches its coldest temperatures there due to the relatively weak greenhouse effect of the water vapor and the cloud. This is the point in the f-t_{prec} phase space at which the evaporative and longwave radiative cooling are at their maxima. As we move from the lower left-hand quadrant to upper right-hand quadrant in Fig. 4.9a, the shortwave flux into the ocean decreases by 150 W m^{-2} and the surface latent heat flux decreases by 60 W m^{-2}. From Fig. 4.9d, the precipitable water increases by 50 kg m^{-2} across this range. Even though the longwave radiative cooling must decrease by 90 W m^{-2}

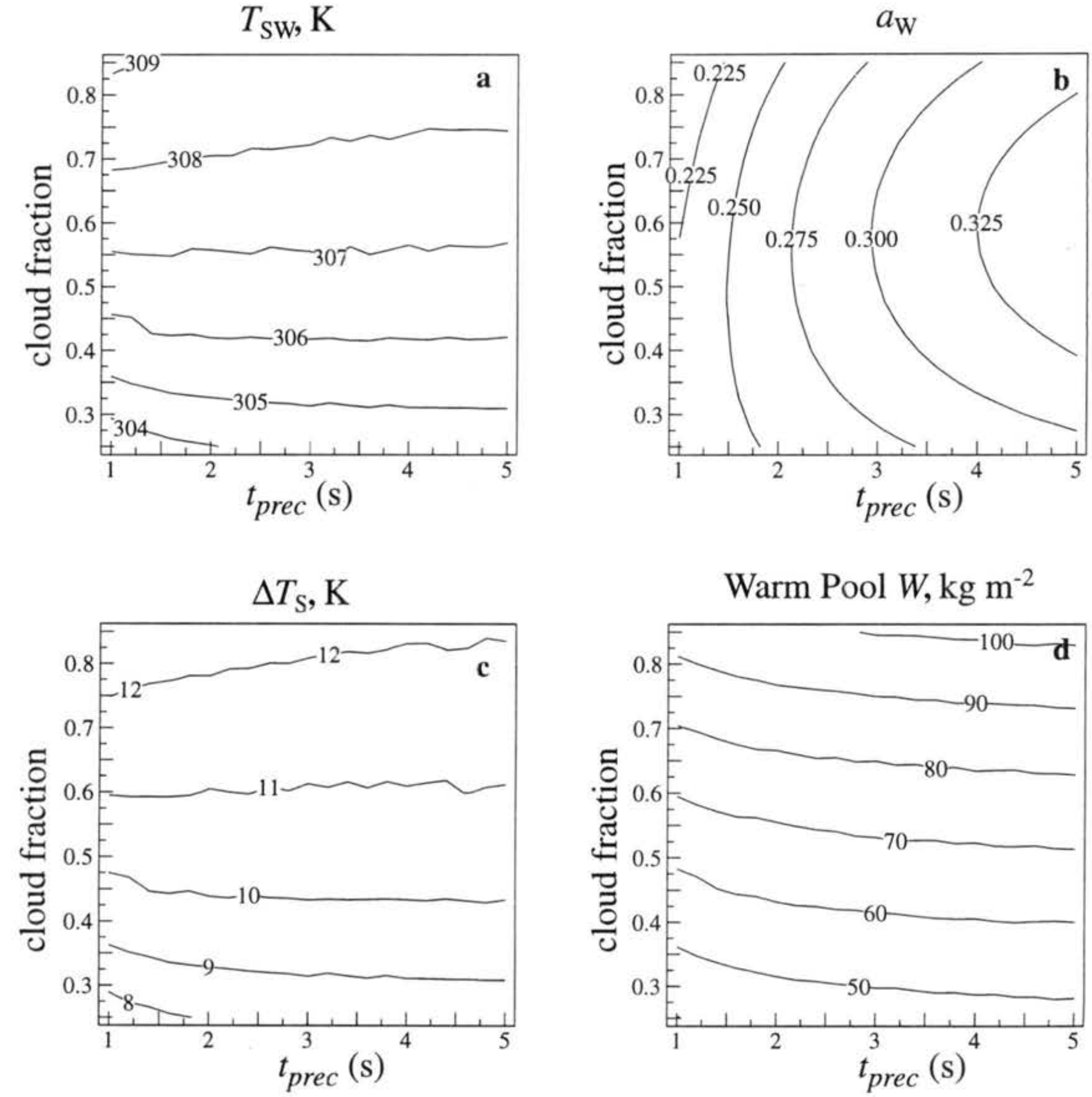

FIGURE 4.9: Contour plots of a) T_{SW} in units of K, b) a_W, which is unitless, c) east-west SST difference in units of K, and d) precipitable water in units of kg m^{-2}, as functions of autoconversion rate (t_{prec}; $\times 10^3$ s) and WP cloud fraction (f). The contour intervals for a, b, c, and d are 1 K, 0.025, 1 K, and 10 kg m^{-2}, respectively.

(and, in fact, becomes negative) in order to maintain surface energy balance, the large increase of precipitable water, as f and t_{prec} increase, requires that T_{SW} must increase.

This behavior can be explained with reference to the IWP as a function of t_{prec} and f (Fig. 4.10c). Recall from our discussion in Chapter 2 that the IWP is proportional to cloud optical depth. By design, the IWP increases as t_{prec} and f increase. As discussed in Chapter 2, for $IWP > 0.075$ kg m^{-2}, $\varepsilon_{cld} = 0.99$, and so the emissivity of the cloud is saturated for values of the *IWP* larger than this threshold. For $f = 0.25$, the cloud emissivity increases from 0.75 to 0.99 and the cloud albedo increases from 0.3 to 0.56, as t_{prec} increases from 1,000 s to 5,000 s. The precipitable water increases by 7.5 kg m^{-2} over this t_{prec} range. As a result, the intensity of the greenhouse effect increases more than that of the cloud albedo effect, and so T_{SW} increases slightly. For large f, the emissivity has saturated. Despite a similar increase of the precipitable water, the cloud albedo effect dominates so that T_{SW} decreases slightly as t_{prec} increases.

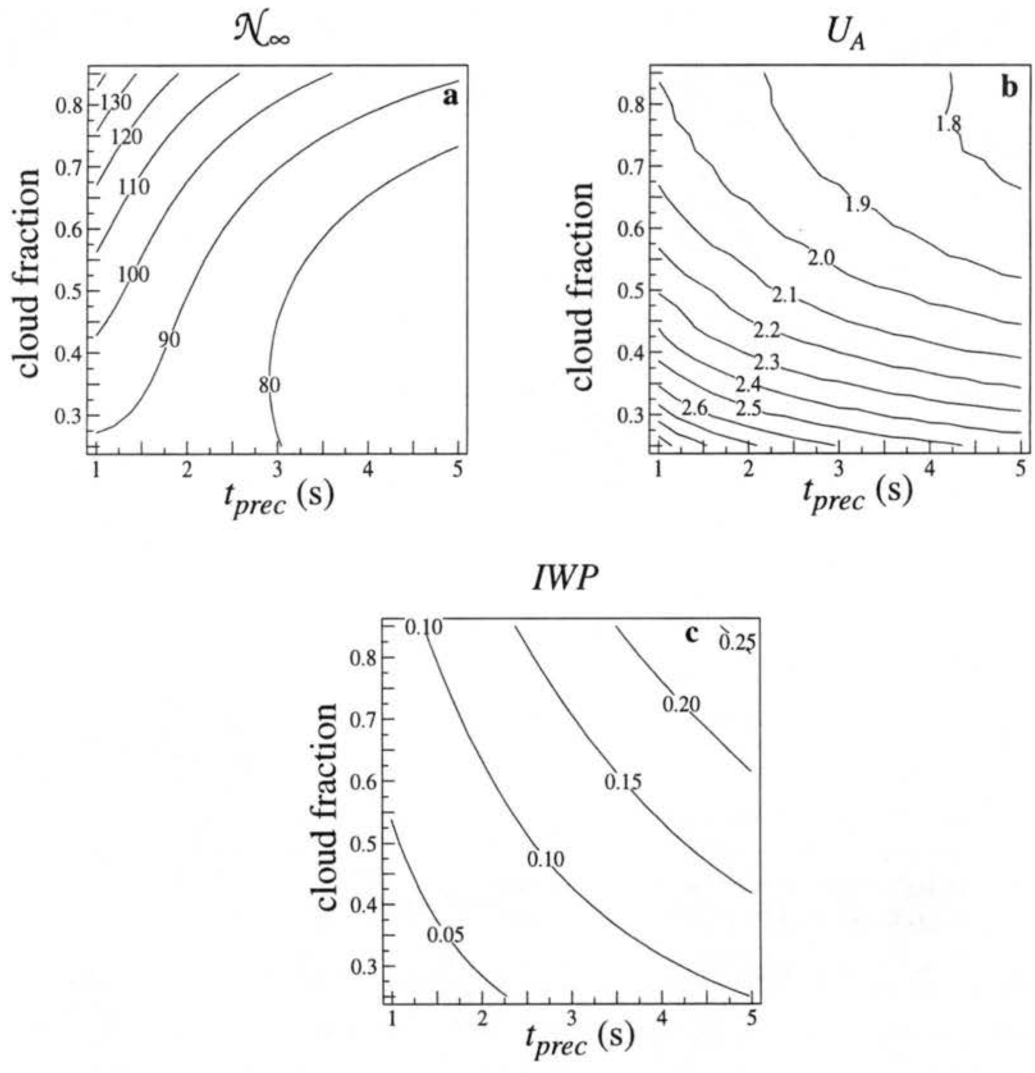

FIGURE 4.10: Contour plots of a) $\mathcal{N}_\infty$ for the WP in units of W m^{-2}, b) U_A in units of kg m^{-1} s^{-1} ($\times 10^4$) and c) *IWP* in units of kg m^{-2} as functions of autoconversion rate (t_{prec}; $\times 10^3$ s) and WP cloud fraction (*f*). The contour intervals are 10 W m^{-2}, 0.2 kg m^{-1}s^{-1} and 0.05 kg m^{-2}, respectively.

On the other hand, the precipitable water has an even larger impact for increases of the cloud fraction. For constant t_{prec}, the albedo cloud effect would dominate as the *IWP* gets larger than 0.075 kg m^{-2} if the precipitable water were to remain fixed. However, from Fig. 4.9d, the precipitable water increases by more than 50 kg m^{-2} and the resulting increase of the greenhouse effect prevents the albedo effect from reducing T_{SW}. Thus, the tendency for the temperature to decrease as the cloud fraction increases is counteracted by the increase of precipitable water.

The area fraction, a_W, and the east-west SST difference vary in order for the lateral heat transport between boxes to balance the vertical energy flux convergence of the WP region. Because we have assumed that the surface energy budget for the WP is balanced, the vertical energy flux convergence in the WP region is given by $\mathcal{N}_\infty$. Figure 4.10a shows that it varies as a complicated function of t_{prec} and f, which actually depend on T_{SW}, W, and the cloud optical depth. Comparing Fig. 4.9b with Fig. 4.10a, we note that the shapes of the contours are similar, although a_W has a maximum for $f = 0.55$. For specified t_{prec} and f, the model finds values of T_{SW} and W which give surface energy balance. The mass flux (Fig. 4.10b), the WP area fraction (Fig. 4.9b), and the SST difference (Fig. 4.9c) all adjust so that the horizontal energy export balances the net energy flux at the TOA, which must also balance the net cooling of the CP region.

The increase of precipitable water with f is required due to the increase of $\mathcal{N}_\infty$ and the decrease of U_A as f increases. As the cloud fraction increases, the flux of longwave radiation into the stratosphere decreases. As described in Chapter 2, the reduced longwave upwelling causes the troposphere height to increase and the tropopause temperature to decrease. As the tropopause rises, the air transported laterally to the CP region originates from higher levels in the upper troposphere of the WP, and is therefore much dryer than air that originated from lower levels. As a result of dry air being advected over the CP region, the radiative cooling rate decreases. Comparing the small change of a_W in Fig. 4.9b and the large change of U_A in Fig. 4.10b as functions of f, we deduce that changes in U_A occur mainly due to changes in the subsidence rate. In addition, q_{BI} increases in response to increasing the cloud fraction, because U_A is in the denominator of the expression for q_{BI} [(3.9)]. As a result of these changes, q_S must increase strongly. Considering Fig. 4.9d and our surface moisture assumption, we infer that q_S does adjust strongly.

The response of our model to increasing cloud fraction can be compared to the feedback mechanism proposed by Lindzen (1990) for a doubled CO_2 climate. In response to a doubling of CO_2, Lindzen hypothesized that cloud tops associated with convective activity would rise, and so dryer air would be detrained and subsequently advected into the subsiding regions of the tropics. As a result, a weakened greenhouse effect and diminished surface warming would result. Thus, convective activity would act as a remote negative feedback on surface temperature. In nature, however, the mid-level drying would also lead to a decreased radiative cooling rate, and hence, to a decreased subsidence rate. As suggested in Fig. 4.9, the precipitable water and SST of the WP must increase in order to compensate for the reduced intensity of the circulation. Thus, our findings suggest that this mechanism would act as a positive feedback on surface temperature, rather than as a negative feedback.

The sensitivity of our model to increasing cloud fraction is also different than those of Larson et al. (1999), Miller (1997), and Pierrehumbert (1995). Recall that Miller (1997) specified the cloud radiative forcings over the WP, while Pierrehumbert (1995) neglected them altogether. In Larson's model, the SST of the WP decreased by 3 K as the high-cloud fraction increased from 0.2 to one. However, the relative humidity in their model was determined by an assumed closure relationship for the water vapor budget. A parameter is included in their closure which relates the large-scale upward flux of moisture to the eddy flux of moisture. Although their model gives good results, there appears to be no theoretical justification for their closure relationship. We employ a closure relationship in which the surface relative humidity is related to the total precipitable water in the convective column [(2.33)]; but ours is based on the observations. Despite this observational basis, it appears that the column water vapor in our model increases too strongly as the cloud liquid water changes.

4.4.b Boundary-layer cloud radiative effects

Following Miller (1997) and Larson et al. (1999), we now examine the influence of boundary-layer cloud radiative effects on the Walker circulation. The unique aspect of our study is that we explicitly include momentum budgets for the ocean and atmosphere. We expect that cold-water upwelling may feedback to influence our results.

In order to first examine the sensitivities of the solution, we show results as functions of f_B, the specified boundary-layer cloud fraction, and τ_B, the specified cloud optical depth for boundary-layer clouds. Although in nature we expect the cloud optical depth to decrease and the cloud fraction to increase with x in the CPBL, results in this section are first shown for the case in which the cloud fraction and optical depths are horizontally invariant in the CPBL. Our purpose is to show the sensitivity of our solution to boundary-layer clouds, without the complication of horizontally varying cloud properties.

Figure 4.11 shows contour plots of T_{SE} in a, of a_W in b, of the east-west SST difference in c, and precipitable water in the WP region in d, all as functions of CPBL cloud fraction and cloud optical depth. For constant optical depth, T_{SE} decreases as f_B increases. As a function of optical depth, T_{SE} is relatively invariant for $f_B < 2$. The small response occurs because the cloud liquid water path remains small, no matter how large τ_B becomes. For larger cloud fractions, T_{SE} decreases with optical depth for $30 < \tau_B < 10$, but then decreases only slightly for larger cloud optical depths. As the cloud optical depth increases from 10 to 30, the cloud albedo increases from 0.42 to 0.57. As the cloud optical depth increases from 40 to 100, the cloud albedo increases from 0.52 to 0.65. The smaller rate of increase for the cloud albedo for larger τ_B explains the diminished response of T_{SE} to increasing τ_B. For the entire f_B-τ_B domain depicted in Fig. 4.11, $\varepsilon_B > 0.999$. Because the precipitable water

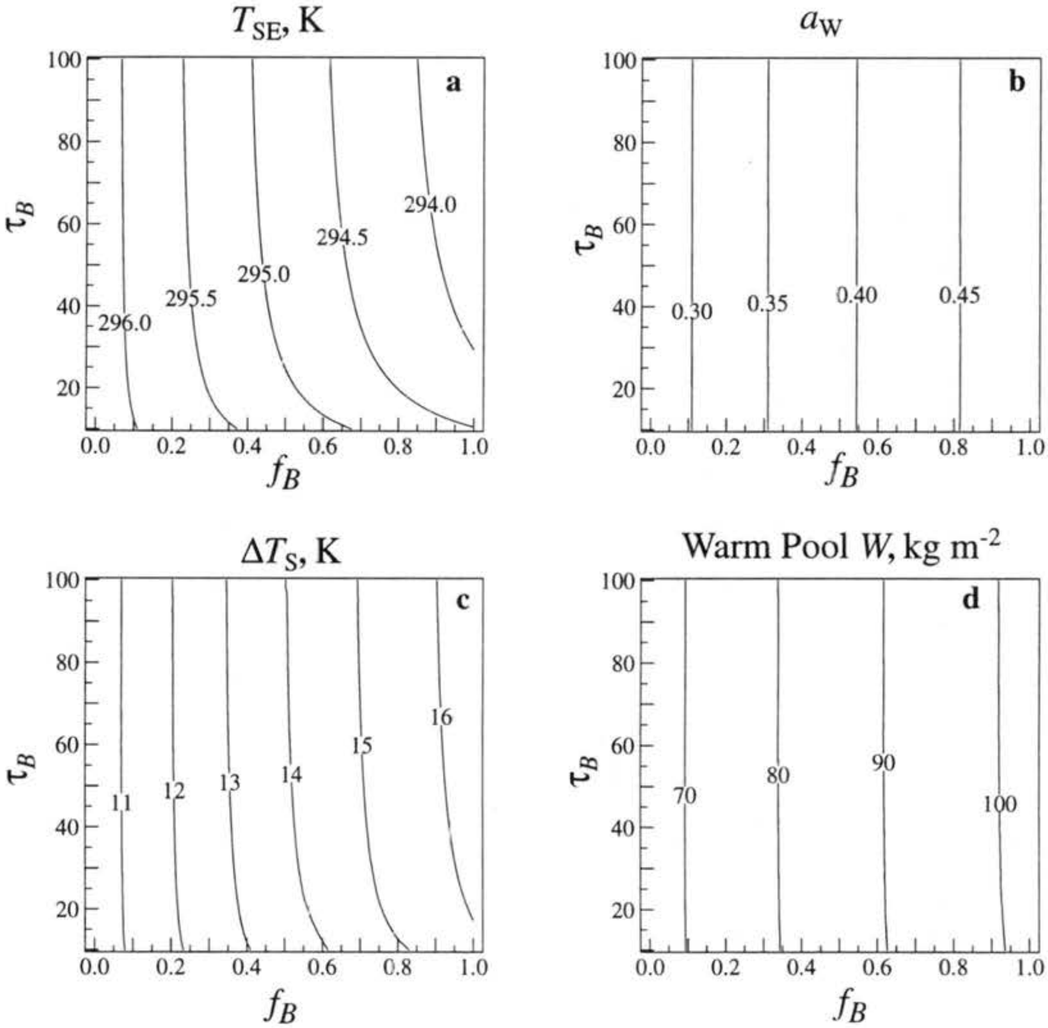

FIGURE 4.11: Contour plots of a) T_{SE} in units of K, b) a_W in fractional area, c) WP precipitable water in units of kg m^{-2}, and d) T_{SW} - T_{SE} in units of K. The contour intervals are 0.5 K, 0.05, 0.5 K, and 10 kg m^{-2} for a, b, c, and d, respectively.

remains constant in response to changing τ_B, the decrease of T_{SE} as τ_B increases is thus attributable to an intensifying the cloud albedo effect. The relatively small change in SST is due to the relatively small change in cloud albedo. Note that τ_B must be larger than 10 for our model, because our radiative transfer parameterization assumes that the cloud emits as a blackbody. Since the cloud is assumed to be optically thick, we do not expect a large response to increasing τ_B further.

For fixed τ_B, T_{SE} decreases by at most 3 K, as f_B increases from zero to one. The longwave radiative effect of the boundary-layer cloud plays a role in the small response. Even though the cloud emissivity does not change, the mean liquid water path for the region increases because f_B increases. As Fig. 4.11d suggests, the greenhouse effect of the clear-sky atmosphere increases too. The net effect is depicted in Fig. 4.12. Because the surface latent heat flux remains approximately constant, the surface energy balance is determined by the difference between the surface shortwave flux and surface longwave flux. The shortwave flux into the ocean decreases by 190 W m^{-2}, while the longwave radiative cooling decreases by 90 W m^{-2}. As seen from Fig. 4.12b, the net energy balance at the surface decreases by as much as 100 W m^{-2} as f_B increases. The clouds have a large impact on the net energy flux at the surface, due to the small amount of water vapor above the eastern part of the CP ($W_E \sim 12$ kg m^{-2}). The reason for the small response of T_{SE} to changing the surface energy balance will be explained shortly.

Figure 4.11 also shows that a_W and W are insensitive to changes of τ_B and sensitive to changes of f_B, This can be explained as follows. The vertical flux divergence of energy for the CP region is largely unaffected by changing the optical depth (since the clouds emit as blackbodies). As the cloud fraction for the CPBL increases, the vertical energy flux divergence of the atmosphere increases, due to the longwave cloud radiative effect at the surface. For the sake of energy balance, this requires the CP width to decrease (a_W increases). However, the change in a_W causes the SST gradient to change. In order to maintain energy and moisture balance for the WP, the precipitable water must increase, just as before. This increase of precipitable water causes T_{SW} to increase, as deduced by comparing Fig. 4.11a and c. The increase of precipitable water leads to an increase of the radiative cooling rate (not shown), and thus, to an increase of the subsidence rate. The depth of the boundary layer does not change very much. Despite the decrease in CP width, the increase in subsidence rate causes U_A to increase slightly as f_B increases (Fig. 4.12c).

As can be seen from Fig. 4.12b and c, the east-west temperature contrast increases with f_B at a faster rate than the CP width decreases, which implies the CPBL pressure gradient increases with f_B. As a result, the surface wind stress increases with f_B, which causes the upwelling flux in the ocean to increase with f_B (Fig. 4.12d).

The question remains as to why T_{SE} decreases only slightly as f_B increases. As mentioned previously, the net energy flux at the ocean surface increases by more than 100 W m^{-2} as f_B increases from zero to one. To see why the changing surface energy balance has only a small effect on SST, consider

$$T_{SE} = \frac{\mathcal{N}_{SE} + C\mathcal{M}_O T_U}{C\mathcal{M}_O}, \tag{3.65}$$

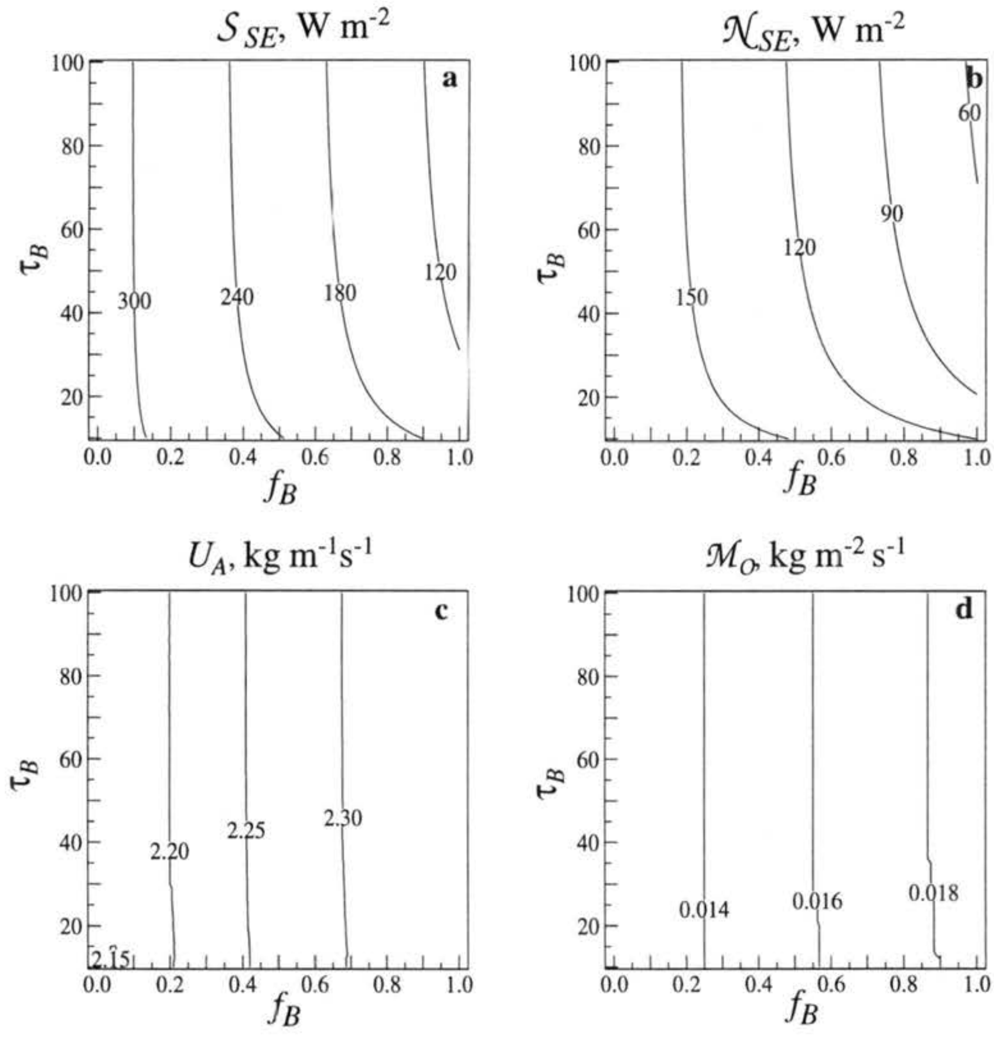

FIGURE 4.12: Contour plots of a) net shortwave radiative flux at the surface in W m^{-2}, b) net energy flux at the surface in W m^{-2}, c) atmospheric mass flux ($\times$ 10^4, units: kg m^{-1} s^{-1}) between the WP and CP regions, and d) the net upwelling ocean flux in kg m^{-2} s^{-1} as functions of the CPBL cloud fraction and cloud optical depths. The contour intervals are 40 W m^{-2}, 50 W m^{-2} and 0.002 kg m^{-2} s^{-1} for a, b, and c, respectively.

which derives from (3.30). The term $C\mathcal{M}_O T_U$ is approximately 1.85×10^4 W m^{-2}, $\mathcal{N}_{SE}$ is at most 150 W m^{-2}, and the denominator is approximately 63 W m^{-2} K^{-1}. In order to derive these values, we have assumed that $\mathcal{M}_O = 0.015$ kg m^{-2} s^{-1}. Because $\mathcal{N}_{SE} \ll C\mathcal{M}_O T_U$, the effect of changing the surface energy balance is relatively small. Near the eastern boundary of the CP, where the undercurrent should be relatively small, $\mathcal{M}_O \approx \rho_W w_T$, and w_T is the rate of upwelling across the thermocline. Assuming that $\rho_W \cong 1000$ kg m^{-3}, the upwelling rate for our model is approximately 130 cm day^{-1}. Philander (1990) presented results from an ocean general circulation model in which the coastal upwelling rate appears to be between 50 - 100 cm day^{-1}. McCreary (1981) suggests that the upwelling rate for the Pacific ocean is between 40 and 400 cm day^{-1}. Clearly, our simulated upwelling rate is in the ball park, although the GCM results suggest that our estimate is a factor of two to three too large. Holding $\mathcal{M}_O = 0.015$ kg m^{-2} s^{-1}, T_{SE} decreases by 1.6 K if $\mathcal{N}_{SE}$ decreases by 100 W m^{-2}. If $\mathcal{M}_O$ is reduced by a factor of three, T_{SE} decreases by 4.8 K, a factor of three larger, for the same surface energy flux decrease. For the range of $\mathcal{M}_O$ values obtained in Fig. 4.12d, the ocean acts as a buffer to limit the decrease of T_{SE} as the cloud optical depth increases.

These results also provide the basis for interpreting the variation of T_{SE} with f_B for fixed τ_B. From Fig. 4.12, the absorbed shortwave radiation at the surface decreases more rapidly with f_B than the surface longwave cooling. Consequently, the net flux of energy into the ocean decreases as f_B increases, and so T_{SE} decreases. Because the precipitable water over the WP increases with f_B, T_{SW} also increases. This causes the east-west temperature difference to increase, which leads to stronger wind stress and a faster ocean circulation. A more intense ocean circulation limits the decrease of T_{SE} with increasing f_B.

Our result differs from those of Miller (1997) and Larson et al. (1999), who found that the CP SST decreases by 4 to 5 K as the cloud fraction increased from 0 to 0.5. Although neither of these previous studies includes ocean currents, the energy flux divergence for the ocean is prescribed from observations. Because of the strong buffering effect of the simulated ocean currents, T_{SE} may be too insensitive to changes of the surface energy balance, compared to results from coupled ocean-atmosphere GCM simulations (Ma et al. 1996). In the next section, we describe results in which the ocean has been arbitrarily slowed down.

4.4.b(i) Results with predicted cloud fraction and cloud water

The next step is to find the solution in which the cloud fraction and cloud water are calculated rather than specified. As described in Chapter 3, our solution is obtained using the method of Suarez et al. (1983) to predict cloud water and the method of Klein and Hartmann (1993; hereafter KH) to predict the boundary-layer cloud fraction.

The column denoted "standard" in Table 4.4 presents our solution with diagnosed cloud water and cloud fraction. Recall that the vertical energy flux divergence for the CP region is computed using the mean SST in the CP and the mean CPBL column water vapor. The mean precipitable water above the CPBL is calculated based on the simple advection model described in Chapter 3. The effect of clouds on the vertical flux divergence of energy for the CP region is taken into account using the cloud fraction and the cloud liquid water calculated at the center of the CP region.

TABLE: 4.4: Solution with diagnosed CPBL clouds

Variable	Standard	Slow ocean	Wet troposphere
Fractional width of the WP (a_W)	0.350	0.334	0.268
T_{SW}	308.0 K	307.9 K	301.7
Warm-Pool W	78.8 kg m^{-2}	74.5 kg m^{-2}	43.3
T_{SE}	295.3 K	297.7 K	295.7
Cold-Pool W	27.4 kg m^{-2}	27.6 kg m^{-2}	21.9
Maximum depth of the CPBL	204 mb	215 mb	289
Maximum vertical-mean zonal wind in the CPBL	-10.7 m s^{-1}	-10.0 m s^{-1}	-10.2
Surface latent heat flux in CPBL	125 W m^{-2}	121 W m^{-2}	96.6
Ocean mass flux, U_O	1.41×10^5 kg m^{-1} s^{-1}	1.34×10^5 kg m^{-1} s^{-1}	1.43×10^5 kg m^{-1} s^{-1}
Mixed-layer thickness	107 m	92.0 m	166 m
Net cloud radiative forcing at WP TOA	-2.9 W m^{-2}	-1.9 W m^{-2}	3.7 W m^{-2}
Lateral moist static energy transport ($\mathcal{F}_H$)	88.0 W m^{-2}	93.3 W m^{-2}	93.4 W m^{-2}
Lateral latent heat transport ($\mathcal{F}_q$)	-97.9 W m^{-2}	-101.3 W m^{-2}	-104 W m^{-2}

The cloud fraction and cloud optical depth for the center of the CP region, f_{BC} and τ_{BC}, are 0.6 and 10.4, respectively. The cloud fraction and cloud optical depth for the east side of the CP, f_{BE} and τ_{BE}, are 0.29 and 107, respectively. From our cloud parameterization, these values imply that the cloud albedos are 0.66 for the central CP region and 0.43 for the eastern boundary of the CP region. Comparing Table 4.1 and Table 4.4, the addition of CPBL clouds results in a 0.9-K decrease of T_{SE}. The solutions are quite different, as the water vapor transport decreases significantly and the width of the WP increases significantly for the cloudy CPBL case. As explained earlier, the change in a_W occurs due to the change in the vertical energy flux convergence, which of course, is induced by the cloud radiative effects. The latent heat flux between boxes decreases due to the increase of a_W (which is in the denominator), even though the precipitable water increases. As discussed earlier, the precipitable water must increase in order to maintain temperature balance. The other quantities in the table are similar for the clear- and cloudy-sky cases. As explained in the previous section, the main reason for this similarity is the buffering effect of the ocean.

As we noted earlier, the upwelling rate may be overestimated by our model. To explore the effect of varying the upwelling rate, we conduct an experiment in which $\mathcal{M}_O = 0.5\overline{\mathcal{M}}_O$. Although we previously assumed that U_O varies linearly, and so $\mathcal{M}_O$ is constant, we argue that a reduced value of $\mathcal{M}_O$ near the coast would occur over a relatively small strip of ocean. Thus, $\overline{\mathcal{M}}_O$ would not be significantly affected. Examining results from an ocean GCM (Philander 1990), our idealization for this experiment is not really too different from what the ocean GCM simulates. The upwelling rate is quite small near the coast, and then abruptly increases and remains large across most of the tropical Pacific. The column denoted "Slow ocean" in Table 4.4 present the results for this case. T_{SE} increases by 2.4 K compared to the standard run. As compared with the standard case, the cloud fractions decrease by 0.09 and 0.15 for the central and eastern parts of the CP region, respectively. However, the cloud optical depths increase by 75 and 4.5 in the central and eastern parts of the CP region. The upwelling rate for this slow-ocean case is approximately 58 cm day^{-1}, which is quite reasonable. In order to compare results between clear- and cloudy-sky cases, we also ran the model with $\mathcal{M}_O = 0.5\overline{\mathcal{M}}_O$ and with no CPBL cloud radiative effects (not shown). For the case without cloud radiative effects, $T_{SE} = 299.4$ K, which is still only 1.7 K warmer than the case with cloud radiative effects. The upwelling rate and the surface energy flux decreased by 7 cm day^{-1} and by 26 W m^{-2}, respectively, compared to the slow-ocean all-sky case. Although the decrease in T_{SE} under cloudy skies was damped by the buffering effect of the ocean, the SST difference seems realistic, given the relatively small decrease of the surface energy flux.

Recognizing that the amount of precipitable water over the CP may affect the intensity of the circulation, we designed an experiment to examine the effect of increasing the free-tropospheric column water vapor. As discussed for the clear-sky case (Table 4.3), allowing the CP to receive water vapor from lower levels in the WP region causes the free troposphere over the CPBL to moisten and the Walker circulation to intensify. As before, the advection model was altered so that water vapor from the lower 30%, rather than from the lower 50%, of the WP free troposphere is excluded from reaching the central part of the CP free troposphere. Results for the clear- and all-sky cases are compared in Section 4.5.

As shown in the column denoted "Wet troposphere," the effect of the added water vapor was to decrease T_{SW} by 6.3 K, compared to the standard case. Despite the decrease of the SST gradient, the surface wind speed decreased by only 0.5 m s^{-1}. Because the depth of the CPBL expanded, the mean boundary-layer pressure gradient did not change very much, despite the smaller SST gradient. The precipitable water decreased, compared to the standard case, for the same reason as for the clear-sky wet-troposphere case. The radiative cooling rate intensifies as the precipitable water over the CP increases (which occurs because the water vapor originates from a lower level over the WP), and so U_A becomes relatively larger. As a result, the precipitable water over the WP does not have to increase as much in order to balance the energy budget. Comparing clear-sky and the all-sky wet-troposphere solutions, we immediately note that the solutions are virtually identical. The diagnosed cloud fractions for the all-sky case are 0.13 and zero for the eastern and central parts of the CPBL, respectively. Recall that we tuned the KH cloud fraction diagnostic based on our standard results. Because T_{SW} decreases so much compared to the standard solution, the cloud fraction becomes too small for a more realistic solution.

4.5 Perturbation of the coupled solution

Our goal is to examine the effect of cloud radiative forcing on the climate sensitivity. In order to do this, we have conducted experiments in which the solar constant was increased by 1% with and without cloud radiative forcing. In our first attempt to find a clear-sky solution, the precipitable water over the WP decreased to less than 10 kg m^{-2} and $T_{SW} < T_{SE}$. In our model, convective and boundary-layer processes have been parameterized only in the WP and CP regions, respectively. If $T_{SW} < T_{SE}$, then the solution is no longer valid. In principle, we could generalize the model to include parameterizations for both regions, but little understanding of the tropical circulation is gained by doing so.

The model broke down for our first attempt because we continued with our base-case assumption that $\Delta = 0.4$. For such a clear-sky case, the WP atmosphere is in equilibrium for a relatively low value of the precipitable water. However, the vertical energy flux divergence for the CP region is smaller than the lateral energy transport from the WP. In order to balance the two fluxes, a_W and W have to get smaller. As W decreases, so does T_{SW}. As a_W and W become smaller, the vertical energy flux divergence for the CP region approaches the lateral energy transport for the WP. However, for $\Delta = 0.4$, balance cannot be reached for $T_{SW} > T_{SE}$. As Δ increases, precipitable water over the WP increases and the lateral energy transport from the WP region decreases. We were able to find solutions for cases in which $\Delta = 0.8$.

Table 4.5 shows the clear-sky solutions, while Table 4.6 presents the all-sky solutions. The standard case refers to the solution in which the standard solar constant was used. Comparing the standard runs in Table 4.5 and Table 4.6, the precipitable water is 56.2 kg m^{-2} larger for the all-sky case than for the clear-sky case. The stronger greenhouse effect due to the additional water vapor causes T_{SW} to increase by 5.6 K compared with the clear-sky simulation.

When the solar constant is increased by 1%, T_{SW} increases by 0.25 K and Warm-Pool W increases by 1.1 kg m^{-2} for fixed a_W. However, the vertical energy flux divergence of the CP region no longer balances the lateral heat transport from the WP region. Therefore, a_W and W must adjust. After a_W decreases to 0.177 and W decreases to 53.2 kg m^{-2}, the solution in the "Clear-sky perturbed" column of Table 4.5 results. Allowing a_W to adjust results in a solution in which T_{SW} and W decrease slightly in response to a 1% increase of the solar constant.

As can be seen in Table 4.6, the all-sky response to a 1% perturbation of the solar constant is even smaller than the clear-sky response. When the solar constant is increased by 1% but a_W is held constant, the SST increases by 0.15 K and the precipitable water increases by 1 kg m^{-2}. The intense greenhouse effect, due to the large amount of water vapor and optically thick clouds over the WP, prevents a large response to a perturbed solar constant, even if a_W is held fixed. When a_W is allowed to adjust, the response to the perturbation becomes even smaller. This behavior implies that the effect of the clouds is to damp out an already small response. However, note that the column water vapor is so large that its adjustment dominates any effect that the clouds could have. In Chapter 2, we defined a parameter γ, which is the ratio of the shortwave and longwave cloud optical depths. For perturbation experiments of the solar constant in which γ was varied between 1.5 and 2.5, the

TABLE: 4.5: Clear-sky comparison

Variable	Clear-sky Standard	Clear-sky perturbed
Relative length of the WP (a_W)	0.1895	0.1770
T_{SW}	304.8	304.6 K
Warm-Pool W	54.8 kg m^{-2}	53.2 kg m^{-2}
T_{SE}	295.4 K	295.5 K
Cold-Pool W	25.2 kg m^{-2}	25.7 kg m^{-2}
Maximum depth of the CPBL	322 mb	331 mb
Maximum vertical-mean zonal wind in the CPBL	-13.5 m s^{-1}	-13.6 m s^{-1}
Surface Evaporative Cooling in CPBL	117 W m^{-2}	117 W m^{-2}
Ocean mass flux, U_O	1.99 $\times 10^5$ kg m^{-1} s^{-1}	2.02 $\times$ 10^5 kg m^{-1} s^{-1}
Mixed-layer thickness	211 m	218 m
Horizontal moist static energy transport ($\mathcal{F}_H$)	85.5 W m^{-2}	92.1 W m^{-2}
Horizontal latent heat transport ($\mathcal{F}_q$)	-431 W m^{-2}	-468.0 W m^{-2}

solution was virtually unchanged. The precipitable water is so large for these experiments that clouds do not influence the solution.

There seems to be little doubt that the water vapor budget in our model is too sensitive to changes of the different parameters and to cloud radiative effects. A key difference between our model and the previous box models is that cold air advection does not play a major role for ours. We assume that the profile of dry static energy for air at the boundary between the CP and WP regions is identical to that for air in the interior of the WP region. Our viewpoint has been that the ocean sufficiently heats the air so that the temperature gradient is negligible at the CP-WP boundary. In contrast, P95, SL96, M97, and L99 assumed

TABLE: 4.6: All-sky comparison

Variable	All-sky Standard	All-sky Perturbed
Fractional width of the WP (a_W)	0.3760	0.3665
T_{SW}	310.4 K	310.4 K
Warm-Pool W	111 kg m^{-2}	111 kg m^{-2}
T_{SE}	294.6 K	294.6 K
Cold-Pool W	39.8 kg m^{-2}	31.3 kg m^{-2}
Maximum depth of the CPBL	222 mb	223 mb
Maximum vertical-mean zonal wind in the CPBL	-13.5 m s^{-1}	-13.6 m s^{-1}
Net cloud radiative forcing at WP TOA	-21 W m^{-2}	-22 W m^{-2}
Surface latent heat flux in CPBL	137 W m^{-2}	137 W m^{-2}
Ocean mass flux, U_O	1.74×10^5 kg m^{-1} s^{-1}	1.75×10^5 kg m^{-1} s^{-1}
Mixed-layer thickness	142 m	142 m
Horizontal moist static energy transport ($\mathcal{F}_H$)	95.2 W m^{-2}	97.1 W m^{-2}
Horizontal latent heat transport ($\mathcal{F}_q$)	-198 W m^{-2}	-206 W m^{-2}

that advection between boxes is proportional to the product of the mass flux and the east-west SST difference. If our viewpoint is correct (and the observations show that the air-sea temperature difference is usually small), then advection into the WP is clearly overestimated in their models.

But the advantage of their assumption, however incorrect it may be, is that it reduces the burden on the water vapor budget for achieving energy and moisture balance. Pierrehumbert (1995) assumed both a relative humidity profile and the potential temperature difference between the upper and lower branches of the circulation, and so only the mass flux could adjust. Miller (1997) assumed a relative humidity profile, and so only the temperature difference and the mass flux could adjust. Except at the top of the CPBL, Larson et al. (1999) assumed a relative humidity profile for the free troposphere in the CP region. At the level of the TWI in the CP region, the specific humidity was calculated as the vertical mean of that in the free troposphere of the WP region. Their method does not realistically account for the effects of subsidence, however, because water vapor from all levels of the free troposphere were included in the mean. Our "wet-troposphere" solution demonstrated the strong sensitivity of the tropical climate to the vertical distribution of water vapor. In addition, Larson et al. calculated the relative humidity for the WP region at the level of the TWI from an assumed closure relationship, which has no theoretical or observational justification.

Although these previous models give better results in some instances, our model includes more realistic physics. Our poor results give some indication of the difficulty of simulating the ocean-atmosphere system with a simple model. Extreme assumptions are often required in order to constrain the behavior of a simple model. We chose not to follow this route. Our model contains simplified, but realistic physical processes which may have a limited range of applicability. Although the experiments conducted with their models have been constrained to better resemble the current climate, there is no evidence to suggest that their solutions are valid if the current climate state is perturbed.

CHAPTER 5

Summary and Conclusions

5.1 Summary

In Chapter 1, we reviewed several papers which present observations of the tropical climate (Newell et al., 1974; Cornejo-Garrido and Stone, 1977; Newell et al., 1996; Hastenrath 1998). These papers are important because their descriptions of the tropical climate can be used to test the various theories and models of the tropical climate which have emerged during the past 20 years. In particular, several theoretical studies have proposed various feedbacks and sensitivities as mechanisms which strongly modulate the tropical climate (Lindzen and Nigam 1987; Ramanathan and Collins 1991), while others have examined the linear response of the tropical climate to small perturbations (Gill 1980; Geisler 1981; Rosenlof et al. 1986). These early studies identified the physical processes and ocean-atmosphere interactions which must be successfully simulated by a simple model of the steady tropical climate. Recent studies with box models (P95, SL96; M97; L99) have improved our understanding because they actually simulate the tropical atmospheric or oceanic circulation.

As discussed previously, the applicability of previous box models is limited for two reasons. First, several interactions and feedbacks among key elements of the tropical circulation have been specified. For instance, P95 neglected cloud radiative effects at the TOA and specified the potential temperature difference between the upper and lower branches of the tropical circulation. Although his assumptions are valid for the current climate, they may not be valid if the system were perturbed. The models of P95, M97, and L99 do not include a momentum budget, and so interactions between the SST gradient and the surface wind stress were not simulated. This contrasts with the findings of Lindzen and Nigam (1987) who showed that the SST gradient modulates the boundary-layer wind speed. SL96 assumed somewhat arbitrarily that the intensity of the ocean circulation is proportional to a quadratic function of the CP-WP SST difference. Second, none of these previous box models include fully interactive components for *both* the ocean and the atmosphere. SL96 simulated the interaction of the atmosphere with the ocean by specifying an equilibrium temperature toward which the surface temperature relaxes. P95, M97, and L99 incorporated a surface energy budget for each of their models, but the oceanic energy transports were specified.

In Chapter 2, we presented an idealized but physically based model, which represents the tropical WP region. The model includes an interactive hydrologic cycle. Cumulus convection is parameterized using a very simple closure assumption which follows from Arakawa and Chen (1987) and Arakawa (1993). Surface evaporation is parameterized using a bulk aerodynamic formula, in which the surface wind speed is prescribed. Consistent with our assumption of a negligible air-sea temperature difference, the surface sensible heat flux is neglected. Radiative transfer is parameterized based on the work of Stephens et al. (1994) and others cited in the text.

Our results from the WP model show that quasi-tropical equilibria occur for prescribed (warm) SSTs and surface wind speeds, but realistic clear-sky equilibria do not occur for the tropical ocean-atmosphere column. When the surface temperature is allowed to vary, a runaway greenhouse develops. We also showed that incorporating realistic cloud radiative effects allows the model to reach an unrealistically warm, dry radiative-convective equilibrium. These results indicate that lateral energy transports and/or radiatively active clouds are required in order to find a realistic, tropical solution. With lateral moisture and energy convergence for the WP region specified as 100 W m^{-2} and -60 W m^{-2}, respectively, and for $t_{prec} = 9500$ s, $f = 0.5$, $\gamma = 2$, and a surface wind speed of 5 m s^{-1}, the model equilibrates with $T_{SW} = 300$ K and $W = 40$ kg m^{-2}, which are quite reasonable.

We also found that the longwave radiative effect of cirrus anvil clouds causes the tropopause height and temperature to increase and decrease, respectively, compared to their clear-sky values. The tropopause cools because the upward longwave flux at level z_T decreases as the cloud optical thickness and/or cloud fraction increase. This cooling is reinforced by the concomitant increase of precipitable water, which reduces the clear-sky part of the OLR.

Based on results from our model, the mechanism for the response of the tropopause to increasing cloud cover can be described as follows. As the cloud optical thickness and/or cloud fraction increase, the shortwave flux at the surface decreases. To balance the surface energy budget, the precipitable water must increase in order to reduce the surface evaporative and radiative cooling. For fixed T_{SW}, the neutral buoyancy condition for non-entraining parcels states that the tropopause height must increase as the tropopause temperature decreases and the surface relative humidity increases, both of which occur as the cloud optical depth and cloud fraction increase. As the cloud fraction and cloud optical thickness increase, the longwave radiative flux into the stratosphere decreases, and so the tropopause cools. The effects of cloud optical thickness on tropopause height and temperature are self limiting, however, because the emissivity saturates as the *IWP* increases beyond 0.1 kg m^{-2}.

In Chapter 3, we described the coupling of models of the WP and CP regions. The surface wind speed for the WP region is calculated based on the mass flux from the CPBL. Simplified but physically based momentum budgets were derived for the ocean and CPBL. The parameterization for the free-tropospheric radiative cooling rate above the CPBL derives from the work of Stephens et al. (1994); the emissivity calculation follows Rodgers (1967) and Stephens and Webster (1979). The subsidence rate over the CPBL is computed based on the balance between adiabatic subsidence and radiative cooling. The hydrologic cycle of the coupled model is fully interactive; the evaporation rate does not depend on a prescribed wind stress as in Larson et al. (1999), nor is it calculated as that which balances the surface energy budget as in Miller (1997). The effects of precipitation in the CPBL are prescribed. As described in Chapter 2, the radiative effects of cirrus clouds over the WP are explicitly calculated, without assuming the cloud optical depth. In addition, the cloud fraction and cloud optical depths of boundary-layer clouds over the CPBL are computed in a physically consistent way so that cloud radiative effects on the solution could be explored.

Chapter 4 presents our results for the Walker Circulation. For the case with clear skies in the CPBL, $T_{SW} = 306.5$ K, $T_{SE} = 296.2$ K, and precipitable water in the WP region is 64.9 kg m^{-2}. The vertical-mean wind speed for the boundary layer is -9.6 m s^{-1}, which compares well with the equatorial jet noted by Battisti and Ovens (1995). The relative width of the WP was found to be 0.270. The simulated values of W and SST in the WP region are rather high compared with those from ECMWF analyses and SSM/I observations. The observed values for SST and precipitable water in the WP region are 302 K and 50 kg m^{-2}, respectively. This difference may result from our assumption of zero SST-SAT temperature difference across the equatorial Pacific ocean. If the SST-SAT temperature difference for air transported from the CPBL were larger than that in the WP region, then cold-air advection might play a role in the energy budget of the WP region. Because the SST-SAT temperature difference is assumed to be zero, adjustment of the precipitable water in the WP region is the primary mechanism for the model to reach energy and moisture balance.

For fixed t_{prec}, T_{SW} increases strongly as the cloud fraction in the WP region increases. As noted previously, the tropopause height increases and tropopause temperature decreases as the cloud fraction for the WP region increases. As the height of the tropopause increases, air which is advected to the CP region must come from higher levels in the WP region. As a result, the advected air is much drier, which contributes to a decreased radiative cooling rate over the CPBL, and so the Walker circulation slows down. In order to maintain energy balance in spite of a weaker circulation, the precipitable water over the WP must increase. Although the cloud albedo also increases as f increases, the greenhouse effect intensifies due to increasing precipitable water and completely dominates the changes of T_{SW}.

We also found that the solution is sensitive to the value of Δ, which specifies the proportion of evaporated water vapor which is precipitated in the CPBL. For $\Delta = 1$, the precipitation rate in the CP region is zero, and all evaporated water vapor is transported laterally to the WP region. For $\Delta = 0$, the precipitation rate is 100%, and so none of the evaporated water vapor is transported to the WP region. In previous box models, the effects of precipitation in the CP region were not explicitly discussed, although parameters in the moisture and energy budgets were tuned to give tropics-like results, and so the effects of precipitation were implicitly included. As shown in Fig. 4.7, the precipitable water and SST in the WP region increase strongly as Δ increases. As the precipitation rate in the CP region decreases, the precipitable water and SST of the WP region increase. Although the effect of precipitation rate in the CP region on precipitable water over the WP is somewhat obvious, our results give the first quantitative estimates of its influence.

We also found that T_{SE} is relatively insensitive to changes of the CPBL cloud fraction, but is very sensitive to changes of T_U. T_{SE} does not vary from T_U by more than 4 K. The influence of boundary-layer clouds on SST for our model is small compared to that noted by Miller (1997) and Larson et al. (1999), although the energy flux divergence of the ocean mixed layer was specified in these earlier studies. For the fully coupled solution, $T_{SW} = 308.0$ K and $T_{SE} = 295.3$ K, which represents a 1.5-K increase of WP SST and a 0.9-K decrease of CP SST, compared to the clear-sky solution. The relatively small effect on SST can be attributed to cold-water upwelling in the CP. The large heat capacity of the water prevents the SST of the CP from drifting too far from the undercurrent temperature. Although our model overestimates the upwelling rate, an experiment with the upwelling rate reduced by one-half shows that T_{SE} decreases by 1.7 K, compared to the analogous clear-sky case. Since the surface energy flux decreased by only 26 W m^{-2}, this decrease does not seem unreasonable. For our model, the effect of cold-water upwelling on SST is basically linear. If the upwelling rate were reduced to 0.2 of its base-case value, the T_{SE} difference between the clear- and all-sky cases would increase by a factor of five compared to the base-case difference. The linear increase in T_{SE} difference depends on the undercurrent temperature remaining constant.

Our "wet troposphere" experiment demonstrates the crucial connection between water vapor amount and vertical distribution, and the tropical climate. As the water vapor increases over the CPBL, the radiative cooling rate and hence the mass flux of the Walker circulation increase. The "wet-troposphere" solution therefore shows that if water vapor is advected to the CP region from a lower altitude in the WP region, the circulation speeds up.

Because the circulation is faster, the SST and precipitable water of the WP region must decrease in order to balance the energy and moisture budgets. In fact, when we try to moisten the atmosphere for this experiment, the model adjusts so as to dry out.

Finally, we examined the response of the tropical climate to a 1% perturbation of the solar constant. As explained previously, a solution could not be found for our base-case value of $\Delta = 0.4$, and so solutions were examined for $\Delta = 0.8$. When the fractional width of the WP is held constant, T_{SW} and T_{SE} increase for the clear-sky solution. When the fractional width is allowed to adjust, T_{SW} decreases by 0.2 K and T_{SE} increases by 0.1 K. When cloud radiative effects are simulated, the SSTs in the WP and CP do not respond to a perturbation of the solar constant. Thus, we conclude that the effect of the clouds is to damp out an already small response. However, the amount of precipitable water for the cloudy-sky simulation is so large that the response of the climate to the perturbation may be suspect.

To summarize, we have shown the following:

- The WP region can establish a very warm, very dry radiative-convective equilibrium in the presence of realistic cloud radiative effects;
- Horizontal energy flux divergence is required in order for the WP region to find a solution which resembles the current tropical climate;
- The longwave radiative effect of clouds contributes to an increase of tropical tropopause height and a decrease of tropical tropopause temperature, compared to their clear-sky values;
- In response to increased cloud cover over the WP, T_{SW} increases due to a feedback involving a higher and colder tropopause.
- Cold-water upwelling prevents T_{SE} from straying too far from the undercurrent temperature;
- The amount and vertical distribution of column water vapor strongly influences the radiative cooling rate and thus determines the intensity of the Walker circulation;
- The precipitation rate over the CPBL influences the amount of precipitable water over the WP.

5.2 Future Research

The next step in researching the Walker circulation should be to compare our results with a coupled ocean-atmosphere general circulation model. Because our model is physically based, it can be used to identify mechanisms which control the tropical climate. However, due to its simplicity, the relative strengths of these mechanisms may not be correct. It would be very useful to conduct idealized simulations with a coupled GCM in order to assess the accuracy of our model in identifying the relative intensities of the different mechanisms which control the tropical climate.

We would also like to expand the model to include a meridional circulation, i.e. a Hadley circulation. This addition would allow us to explicitly study the interactions between the Hadley and Walker circulations and would involve changing the momentum budgets for the ocean and atmosphere models to include the Coriolis acceleration. As shown by Gill (1980) and Geisler (1981), a zonal, Walker-like circulation results from convective heating which has been specified to be symmetric about the equator. Results presented in Chapter 4 have also demonstrated the sensitivity of the solution to the vertical distribution of water vapor. Our wet-troposphere experiment supports the notion that the subsiding branch of the Walker circulation is moistened by air which originated from the middle and upper troposphere of a convecting region. Because subsidence limits the length of trajectories travelled by air parcels in the subsiding branches of the tropics, it is unlikely that mid-tropospheric air parcels could travel from the WP region to the central and eastern parts of the CP region before being entrained into the CPBL. Thus, our wet-troposphere experiment seems to implicate a meridional circulation for moistening the free troposphere above the equatorial central and eastern Pacific. An expanded version of our model could be used to study the significance of such a north-south circulation for maintaining the observed vertical profile of water vapor in the subsiding branch of the Walker circulation.

The interactions in our model are also limited due to our specification of the cloud fraction over the WP and the evaporation efficiency over the CP. As we showed in Chapter 4, the response of the system to a 1% perturbation of the solar constant is highly dependent on the specified cloud fraction and on the evaporation efficiency. In principle, the cloud fraction could be calculated based on the area-averaged *IWP*, while the evaporation efficiency could be determined from lower tropospheric stability and the *LWP*. Thus, we might expect the cloud fraction and the evaporation efficiency to change in response to a solar perturbation, because the factors which control them might be expected to change. Diagnosing the cloud fraction in the WP region and the evaporation efficiency in the CP region would then allow us to more realistically calculate the equilibrium response of the tropical climate to a prescribed perturbation.

Our modeling assumption that the top of the layer of easterlies coincides with the trade-wind inversion should also be relaxed. This assumption introduced a feedback among the depth of the CPBL, the SST gradient, and the mean CPBL wind speed. As the SST gradient increased, the depth of the CPBL often decreased so that the pressure gradient and thus the mean wind speed did not increase as strongly as anticipated. We have found no evidence of similar behavior in nature. As shown in Fig. 1.3, weak easterly flow extends up to the 600-mb pressure level across the entire tropical Pacific ocean. For the sake of consistency, modifying this assumption would require other changes in the model. For instance, our neglect of u_{B+}, the wind speed just above the TWI, in (3.13) and (3.24) would no longer be justified. We would most likely have to assume a simple vertical dependence for the zonal wind in order to diagnose u_{B+}. We would also have to develop a new parameterization for calculating the pressure level of the TWI. Nevertheless, relaxing this assumption should be investigated since the feedback described above might be removed.

As discussed in Chapter 4, the water vapor budget in our model is very sensitive to changes of the different parameters and to cloud radiative effects. Our assumption that the vertical profile of dry static energy for air at the CP-WP boundary is identical to that for air in the interior of the WP region requires investigation. There is no doubt that the SST gradient in the WP is quite small. Nevertheless, air below the trade inversion at the CP-WP boundary should perhaps be slightly cooler than air in the interior of the WP region. For such a case, cold-air advection could play a role for establishing energy balance in the WP region. Thus, it would be interesting to explore the effect of allowing the air-sea temperature difference at the CP-WP boundary to vary from that in the interior of the WP region.

Finally, the time-dependent evolution of the model toward the equilibrium solution(s) must also be studied. As discussed above, the model exhibits several interesting feedbacks. Without any time dependencies, however, the model cannot be used to analyze the evolution of the atmosphere in response to a prescribed perturbation. The present model gives the equilibrium state only. Because we have found only one solution thus far, a time-dependent version of the model should be developed in order to aid the search for additional solutions and for oscillatory behavior.

References

Albrecht, B. A., C. S. Bretherton, D. Johnson, W. H. Schubert and A. S. Frisch, 1995: The Atlantic Stratocumulus Transition Experiment -- ASTEX. *Bull. Amer. Meteor. Soc.*, **76**, 889-904.

Anderson, D. L. T., and J. P. McCreary, 1985: Slowly propogating disturbances in a coupled ocean-atmosphere model. *J. Atmos. Sci.*, **42**, 615-629.

Arakawa, A., 1993: Closure assumptions in the cumulus parameterization problem. In *The Representation of Cumulus Convection in Numerical Models*, a Meteorological Monograph published by the American Meteorological Society, K. Emanuel and D. Raymond, Eds., 246 pp.

Arakawa, A., and J. -M. Chen, 1987: Closure assumptions in the cumulus parameterization problem. In *Short and Medium Range Numerical Weather Prediction.* Collection of Papers Presented at the WMO/IUGG Symposium on Numerical Weather Prediction, Tokyo, 4-8 August 1986, Special Vol. *J. Meteor. Soc. Japan*, 107-131.

Arakawa, A. and W. H. Schubert, 1974: Interaction of a cumulus cloud ensemble with the large-scale environment. Part I. *J. Atmos. Sci.*, **31**, 674-701.

Battisti, D. S., 1988: The dynamics and thermodynamics of a warming event in a coupled tropical atmosphere/ocean model. *J. Atmos. Sci.*, **45**, 2889-2919.

Battisti, D. S., and A. C. Hirst, 1989: Interannual variability in the tropical atmosphere/ ocean system: Influence of the basic state, ocean geometry and nonlinearity. *J. Atmos. Sci.*, **46**, 1687-1712.

Battisti, D. S., and D. D. Ovens, 1995: The dependence of the low-level equatorial jet on Hadley and Walker circulations. *J. Atmos. Sci.*, **52**, 3911-3931.

Betts, A. K., 1973: Nonprecipitating cumulus convection and its parameterization. *Quart. J. Roy. Met. Soc.*, **99**,178-196.

Betts, A. K., 1982: Saturation point analysis of moist convective overturning. *J. Atmos. Sci.*, **39**, 1484-1505.

Betts, A. K., 1985: Mixing line analysis of clouds and cloudy boundary layers. *J. Atmos. Sci.*, **42**, 2751-2763.

Betts, A. K., and W. Ridgway, 1989: Climatic equilibrium of the atmospheric convective boundary layer over a tropical ocean. *J. Atmos. Sci.*, **46**, 2621 - 2641.

Bjerknes, J., 1969: Atmospheric teleconnections from the equatorial Pacific. *Mon. Wea. Rev.*, **97**, 163-172.

Brown, R. G., and C. Zhang, 1997: Variability of midtropospheric moisture and its effect on cloud-top height distribution during TOGA COARE. *J. Atmos. Sci.*, **54**, 2760-2774.

Bunker, A. F., 1971: Energy transfer and tropical cell structure over the central Pacific. *J. Atmos. Sci.*, **28**, 1101-1116.

Cane, M. A., and S. E. Zebiak, 1985: A theory of El Niño and the Southern Oscillation. *Science*, **228**, 1085-1087.

Charney, J. G., 1963: A note on large-scale motion in the tropics. *J. Atmos. Sci.*, **20**, 607-609.

Cornedjo-Garrido, A. G. and P. H. Stone, 1977: On the heat balance of the Walker circulation. *J. Atmos. Sci.*, **34**, 1155-1162.

Deardorff, J. W., 1972: Parameterization of the planetary boundary layer for use in general circulation modes. *Mon. Wea. Rev.*, **100**, 93-106.

Emanuel, K. A., 1991: A scheme for representing cumulus convection in large-scale models. *J. Atmos. Sci.*, **48**, 1763-1775.

Fowler, L. D., D. A. Randall, and S. A. Rutledge, 1996: Liquid and Ice Cloud Microphysics in the CSU General Circulation Model. Part I. Model Description and Simulated Microphysical Processes. *J. Climate*, **9**, 489-529.

Geisler, J. E., 1981: A linear model of the Walker circulation. *J. Atmos. Sci.*, **38**, 1390-1400.

Gill, A. E., 1980: Some simple solutions for heat-induced tropical circulation. *Q. J. Roy. Met. Soc.*, **106**, 447-462.

Goody, R. M., and Y. L. Yung, 1989: *Atmospheric Radiation Theoretical Basis*, 2nd Ed., New York: Oxford Univ. Press, 519 pp.

Graham, N. E., and W. B. White, 1990: The role of the western boundary in the ENSO cycle: Experiments with coupled models. *J. Phys. Oceanogr.*, **20**, 1935-1948.

Haraguchi, P. Y., 1968: Inversions over the tropical eastern Pacific ocean. *Mon. Wea. Rev.*, **96**, 177-185.

Harrison E. F., P. Minnis, B. R. Barkstrom, V. Ramanathan, R. D. Cess, G. G. Gibson, 1990: Seasonal variation of the Earth Radiation Budget Experiment. *J. Geophys. Res.*, **95**, 18687-18703.

Hartmann, D. L., M. E. Ockert-Bell, and M. L. Michelson, 1992: The effect of cloud type on the Earth's energy balance: Global analysis. *J. Climate*, **5**, 1281-1304.

Hastenrath, S., 1971: On meridional circulation and heat budget of the troposphere over the equatorial central Pacific. *Tellus*, **23**, 60-73.

Hastenrath, S., 1998: Contribution to the circulation climatology of the eastern equatorial Pacific: Lower atmospheric jets. *J. Geophys. Res.*, **D16**, 19433-19451.

Heckley, W. A., 1985: Systematic errors of the ECMWF operational forecasting model in tropical regions. *Quart. J. R. Met. Soc.*, **111**, 709-738.

Held, I. M. and A. Y. Hou, 1980: Nonlinear axially symmetric circulations in a nearly inviscid atmosphere. *J. Atmos. Sci.*, **37**, 515-533.

Holton, J. R., 1992: *An introduction to dynamic meteorology*. 3rd Ed. Academic Press, 511 pp.

Hu, Q., and D. A. Randall, 1995: Low-frequency oscillations in radiative-convective systems: An idealized model. *J. Atmos. Sci.*, **52**, 478-490.

Ingersoll, A. P., 1969: The runaway greenhouse: A history of water on Venus. *J. Atmos. Sci.*, **26**, 1191-1198.

Jackson, D. L., and G. L. Stephens, 1995: A study of SSM/I derived precipitable water over the global oceans. *J. Climate*, **8**, 2025-2038.

Klein, S. A. and D. L. Hartmann, 1993: The seasonal cycle of low stratiform clouds. *J. Climate*, **6**, 1587-1606.

Kiehl, J. T., 1994: On the observed near cancellation between longwave and shortwave cloud forcing in tropical regions. *J. Climate*, **7**, 559-565.

Lacis, A., and J. E. Hansen, 1974: A parameterization for the absorption of solar radiation in the earth's atmosphere. *J. Atmos. Sci.*, **31**, 118-133.

Larson, K., D. L. Hartmann, and S. A. Klein, 1999: Climate sensitivity in a two box model of the tropics. *J. Climate*, In press.

Lau, W. K.-M., C.-H. Sui, M.-D. Chou, and W.-K. Tao, 1994: An inquiry into the cirrus cloud thermostat effect for tropical sea surface temperatures. *Geophys. Res. Let.*, **21**, 1157-1160.

Lau, K.-M., H.-T. Wu, and S. Bony, 1997: The role of large-scale circulation in the relationship between tropical convection and sea surface temperature. *J. Climate*, **10**, 381-392.

Lau, K.-M., and H. Lim, 1982: Thermally driven motions in an equatorial β-plane: Hadley and Walker circulations during the winter monsoon. *Mon. Wea. Rev.*, **110**, 336-353.

Lilly, D. K., 1968: Models of cloud-topped mixed layers under a strong inversion. *Quart. J. Roy. Meteor. Soc.*, **94**, 292-309.

Lindzen, R. S., 1990: Some coolness concerning global warming. *Bul. Amer. Met. Soc.*, **71**, 288-299.

Lindzen, R. S., and S. Nigam, 1987: On the role of sea surface temperature gradients in forcing low-level winds and convergence in the tropics. *J. Atmos. Sci.*, **44**, 2418-2436.

Liu, W. T., 1986: Statistical relation between monthly mean precipitable water and surface-level humidity over global oceans. *Mon. Wea. Rev.*, **114**, 1591-1602.

Liu, Z. and B. Huang: 1997: A coupled theory of tropical climatology: warm pool, cold tongue, and walker circulation. *J. Climate*, **10**, 1662-1679.

Ma, C.-C., C. R. Mechoso, A. W. Robertson, A. Arakawa, 1996: Peruvian stratus clouds and the tropical Pacific circulation: a coupled ocean-atmosphere GCM study. *J. Climate*, **9**, 1635-1645.

Manabe, S., and R. F. Strickler, 1964: Thermal equilibrium of the atmosphere with a convective adjustment. *J. Atmos. Sci.*, **21**, 361-385.

Manabe, S., and R. T. Wetherald, 1967: Thermal equilibrium of the atmosphere with a given distribution of relative humidity. *J. Atmos. Sci.*, **24**, 241-259.

Matsuno, T., 1966: Quasi-geostrophic motions in the equatorial area. *J. Meteor. Soc. Jap.*, **44**, 25-43.

McCreary, J. P., 1981: A linear stratified ocean model of the equatorial undercurrent. *Philos. Trans. R. Soc. London*, **298**, 603-635.

Miller, R. L., 1997: Tropical thermostats and low cloud cover. *J. Climate*, **10**, 409-440.

Neelin, J. D., D. S. Battisti, A. G. Hirst, F.-F. Jin, Y. Wakata, T. Yamagata, S. E. Zebiak, 1998: ENSO theory. *J. Geophys. Res.*, **103**, 14261-14,290.

Neelin, J. D., and I. M. Held, 1987: Modelling tropical convergence based on the moist static energy budget. *Mon. Wea. Rev.*, **115**, 3-12.

Neelin, J. D., and F.-F. Jin, 1993: Modes of interannual tropical ocean-atmosphere interaction-a unified view, II, Analytical results in the weak coupling limit, *J. Atmos. Sci.*, **50**, 3504-3533.

Newell, R. E., J. W. Kidson, D. G. Vincent and G. J. Boer, 1974: *The General Circulation of the Tropical Atmosphere*, Vol. 2, The MIT Press, 371 pp.

Newell, R. E., Y. Zhu, E. V. Browell, W. G. Read, J. W. Waters, 1996: Walker circulation and tropical upper tropospheric water vapor. *J. Geophys. Res.*, **101**, D1, 1961-1974.

North, G. R., 1975: Theory of energy balance climate models. *J. Atmos. Sci.*, **32**, 2033-2043.

Parsons, D., W. Dabberdt, H. Cole, T. Hock, C. Martin, A.-L. Barrett, E. Miller, M. Spowart, M. Howard, W. Ecklund, D. Carter, K. Gage and J. Wilson, 1994: The integrated sounding system: description and preliminary observations from Toga Coare. *Bull. Amer. Meteor. Soc.*, **75**, 553-567.

Philander, S. G. H., 1990: *El Niño, La Niña, and the Southern Oscillation*, Academic Press, Inc., 293 pp.

Philander, S. G. H., D. Gu, D. Halpern, G. Lambert, N.-C. Lau, T. Li, R. C. Pacanowski, 1996: Why the ITCZ is mostly north of the equator. *J. Climate*, **9**, 2958-2972.

Pierrehumbert, R. T., 1995: Thermostats, radiator fins, and the runaway greenhouse. *J. Atmos. Sci.*, **52**, 1784-1806.

Platt, C. M. R., 1979: Remote sounding of high clouds: I. Calculation of Visible and Infrared Optical Properties from Lidar and Radiometer Measurements. *J. App. Met.*, **18**, 1130-1143.

Ramanathan, V., and J. A. Coakley, Jr., 1978: Climate modeling through radiative-convective models. *Rev. Geophys. Space Phys.*, **6**, 465-489.

Ramanathan, V. and W. Collins, 1991: Thermodynamic regulation of ocean warming by cirrus clouds deduced from observations of the 1987 El Niño. *Nature*, **351**, 27-32.

Randall, D. A., Harshvardhan, D. A. Dazlich, and T. G. Corsetti, 1989: Interactions among radiation, convection, and large-scale dynamics in a general circulation model. *J. Atmos. Sci.*, **46**, 1943-1970.

Renno, N. O., K. A. Emanuel, and P. H. Stone, 1994: Radiative-convective model with an explicit hydrologic cycle. 1: Formulation and sensitivity to model parameters. *J. Geophys. Res.*, **99** (D7), 14429-14441.

Rodgers, C. D., 1967: The use of emissivity in atmospheric radiation calculations. *Quart. J. Roy. Met. Soc.*, **93**, 43-54.

Rosenlof, K. H., D. E. Stevens, J. R. Anderson, and P. E. Ciesielski, 1986: The Walker circulation with observed zonal winds, a mean Hadley cell, and cumulus friction. *J. Atmos. Sci.*, **43**, 449-467.

Salathé Jr., E. P. and D. L. Hartmann, 1997: A trajectory analysis of tropical upper-tropospheric moisture and convection. *J. Climate*, **10**, 2533-2547.

Schneider, E. K., 1977: Axially symmetric steady-state models of the basic state for instability and climate studies. Part II. Nonlinear calculations. *J. Atmos. Sci.*, **34**, 280-296.

Schneider, E. K., and R. S. Lindzen, 1977: Axially symmetric steady-state models of the basic state for instability and climate studies. Part I. Linearized calculations. *J. Atmos. Sci.*, **34**, 263-279.

Schopf, P. S., and M. J. Suarez, 1988: Vacillations in a coupled ocean-atmosphere model. J. Atmos. Sci., *J. Phys. Oceanogr.*, **20**, 629-645.

Schutz, C. and W. Gates, 1972: Global climatic data for surface, 800 mb, 400 mb, July. Rep. R-1029-ARPA, The Rand Corporation.

Sohn, B.-J., 1994: Temperature-moisture biases in ECMWF analyses based on clear sky longwave simulations constrained by SSMI and MSU measurements and comparisons to ERBE estimates. *J. Climate*, **7**, 1707-1718.

Stackhouse, Jr., P. W. and G. L. Stephens, 1991: A Theoretical and Observational Study of the Radiative Properties of Cirrus: Results from FIRE 1986. *J. Atmos. Sci.*, **48**, 2044-2059.

Stephens, G. L., 1978: Radiation profiles in extended water clouds II: Parameterization schemes. *J. Atmos. Sci.*, **35**, 2123-2132.

Stephens, G. L., 1984: Review: The Parameterization of Radiation for Numerical Weather Prediction and Climate Models. *Mon. Wea. Rev.*, **112**, 826-867.

Stephens, G. L., and T. J. Greenwald, 1991: The Earth's Radiation Budget and Its Relation to Atmospheric Hydrology. 1. Observations of the Clear Sky Greenhouse Effect. *J.*

Geophys. Res., **96**, 15311-15324.

Stephens, G. L., A. Slingo, M. J. Webb, P. J. Minnett, P H. Daum, L. Kleinman, I. Wittmeyer, and D. A. Randall, 1994: Observations of the Earth's radiation budget in relation to atmospheric hydrology. Part IV: Atmospheric column radiative cooling over the world's oceans. *J. Geophys. Res.*, **99**, 18585 - 18604.

Stephens, G. L., and Webster, P. J., 1979: Sensitivity of radiative forcing to variable cloud and moisture. *J. Atmos. Sci.*, **36**, 1542-1556.

Suarez, M. J., A. Arakawa, and D. A. Randall, 1983: The parameterization of the planetary boundary layer in the UCLA general circulation model: Formulation and results. *Mon. Wea Rev.*, **111**, 2224-2243.

Sun, D.-Z. and Z. Liu, 1996: Dynamic ocean-atmosphere coupling: A thermostat for the tropics. *Science*, **272**, 1148-1150.

Thuburn, J., and G. C. Craig, 1997: GCM theories for the height of the tropopause. *J. Atmos. Sci.*, **54**, 869-882.

Trenberth, K. E., and C. J. Guillemot, 1995: Evaluation of the global atmospheric moisture budget as seen from analyses. *J. Climate*, **8**, 2255 -2272.

Troup, A. J., 1965: The 'southern oscillation.' *Q. J. R. Meteorol. Soc.*, **91**, 490-506.

Twomey, S., 1991: Aerosol, clouds and climate. *Atmos. Env.*, **25A**, 2435-2442.

Webster, P. J., 1987: The variable and interactive monsoon. In *Monsoons*, ed. by J. S. Fein and P. L. Stephens. Wiley, New York, 269-330.

Webster, P. J., 1994: The role of hydrological processes in ocean-atmosphere interactions. *Rev. Geophys.*, **32**, 427-476.

Weller, R. A., and S. P. Anderson: 1996: Surface meterology and air-sea fluxes in the western equatorial Pacific warm pool during the TOGA coupled ocean-atmosphere response experiment. *J. Climate*, **9**, 1959-1990.

Wong, T., G. L. Stephens, and P. W. Stackhouse, Jr., and F. P. J. Valero, 1993: The Radiative Budgets of a Tropical Mesoscale Convective System During the EMEX-STEP-AMEX Experiment. 1. Observations. *J. Geophys. Res.*, 98, 8683-8693.

Yamagada, T., and Y. Masumoto, 1989: A simple ocean-atmosphere coupled model for the origin of warm El Niño Southern Oscillation event. *Philos. Trans. R. Soc. London A*, **329**, 225-236.

Zhang, G. J., and M. J. McPhaden, 1995: The relationship between sea surface temperature and latent heat flux in the equatorial Pacific. *J. Climate*, **8**, 589-605.

Zebiak, S. E., and M. A. Cane, 1987: A model of El Niño Southern Oscillation. *Mon. Wea. Rev.*, **115**, 2262-2278.

Appendices

Appendix 1

Derivation of conservation equations for the atmosphere

Consider a conservation equation for an arbitrary variable, a, written in pressure coordinates as

$$g^{-1}\left[\frac{\partial}{\partial t}a + \frac{\partial}{\partial x}(ua) + \frac{\partial}{\partial p}(\omega a)\right] = \frac{\partial F_a}{\partial p} + S_a, \tag{A1}$$

where F_a is the upward turbulent convective flux of a, and S_a is a source/sink of a per unit volume. The symbols u and ω refer to the horizontal wind and vertical pressure velocity, respectively. As discussed below, this model includes only two space dimensions. Integrating (A1) between pressures p_1 to p_2, we find that

$$\begin{aligned}\frac{\partial A}{\partial t} + \frac{\partial}{\partial x}\left((ua)\frac{\Pi}{g}\right) - \frac{a_1}{g}\left(\frac{\partial p_1}{\partial t} + u_1\frac{\partial p_1}{\partial x} - \omega_1\right) + \frac{a_2}{g}\left(\frac{\partial p_2}{\partial t} + u_2\frac{\partial p_2}{\partial x} - \omega_2\right) \\ = (F_a)_1 - (F_a)_2 + \int_{p_2}^{p_1} S_a dp.\end{aligned} \tag{A2}$$

Here, the subscripts 1 and 2 refer to pressure levels in the region under consideration, $A \equiv \int_\Pi a dp/g \equiv a_M \Pi/g$, where a_M is the mean over the pressure depth $\Pi = p_1 - p_2$. The quantity (ua) represents the vertical-mean of the product of the zonal wind u and variable a, taken between p_1 and p_2.

We define

$$-g\mathcal{M}_i = \frac{\partial p_i}{\partial t} + u_i\frac{\partial p_i}{\partial x} - \omega_i \tag{A3}$$

as the downward mass flux across a pressure surface $p = p_i$. Of course, when the interface under consideration is the Earth's surface, the mass flux must be zero. At the top of the convective layer, $z = z_T$, we assume that ω_T and $\partial p_T/\partial x$ are zero. At the base of the TWI, (A3) represents the net flux across the boundary-layer top. We define the boundary layer as the layer which extends from the surface to the base of the TWI.

Substituting (A3) into (A2), we find that

$$\frac{\partial A}{\partial t}+\frac{\partial}{\partial x}\left((ua)\frac{\Pi}{g}\right)-a_2\mathcal{M}_2+a_1\mathcal{M}_1 = (F_a)_1-(F_a)_2+\int_{p_2}^{p_1}S_a dp. \tag{A4}$$

If we set $a = 1$ in (A4), then $A = \Pi$, and we have

$$\frac{\partial}{\partial t}\Pi_W+\frac{\partial U_{WB}}{\partial x}+\frac{\partial U_{WF}}{\partial x} = 0, \tag{A5}$$

where $\Pi_W = p_{SW} - p_T$. The subscript W denotes quantities in the WP. In (A5), we have included two flux divergence terms in order to account for flow in the boundary layer, layer B, and flow in the free troposphere, layer F.

If we let $a = h$, the moist static energy, then from (A4) we obtain

$$\frac{\partial}{\partial t}H_W+\frac{\partial}{\partial x}\left\{(uh)_F\frac{\Pi_F}{g}\right\}+\frac{\partial}{\partial x}\left\{(uh)_B\frac{\Pi_B}{g}\right\}+h_T\frac{\partial p_T}{\partial t} = \mathcal{N}_{TW}-\mathcal{N}_{SW}. \tag{A6}$$

Integrating (A6) across the horizontal boundaries of the WP, we find that

$$\frac{d}{dt}(\overline{H}_W\sigma_W)-H_{WI}\frac{d\sigma_W}{dt}+(uh)_{FI}\frac{\Pi_{FE}}{g}+(uh)_{BI}\frac{\Pi_{BI}}{g}+\bar{h}_T\frac{d}{dt}(\bar{p}_T\sigma_W)-\bar{h}_T p_T\frac{d\sigma_W}{dt} = (\overline{\mathcal{N}}_{TW}-\overline{\mathcal{N}}_{SW})\sigma_W, \tag{A7}$$

where σ_W is the length of the WP and the subscript I refers to values at the boundary between the WP and CP. Expanding the first and fourth LHS terms and rearranging, we have

$$\sigma_W\frac{d}{dt}\overline{H}_W+(\overline{H}_W-H_{WI})\frac{d\sigma_W}{dt}+U_{FI}h_{FI}+U_{BI}h_{BI}+\bar{h}_T\sigma_W\frac{d\bar{p}_T}{dt} + \bar{h}_T(\bar{p}_T-p_T)\frac{d\sigma_W}{dt} = (\overline{\mathcal{N}}_{TW}-\overline{\mathcal{N}}_{SW})\sigma_W. \tag{A8}$$

where $U \equiv \int_{\Pi} udp/g$ is the mass flux for given vertical layer. Then h_{FI} or h_{BI} are given by $U_{F,B}h_{F,B} = \int_{\Pi_{F,B}} uhdp/g$. If we assume that temperature and moisture gradients are negligible in the WP, then $\overline{H}_W = H_W$ and $\bar{p}_T = p_T$. Dropping the overbars and dividing through by σ_W, (A8) reduces to (2.3) [or (3.1) for the steady state] if we define

$$\mathcal{F}_H \equiv \frac{-(U_{FI}h_{FI} + U_{BI}h_{BI})}{\sigma_W}. \tag{A9}$$

Considering the CPBL, the limits for the vertical integration in (A4) become p_S and p_B for p_1 and p_2, respectively. If we let $a = 1$ in (A4), then the steady-state continuity equation for the CPBL becomes

$$\frac{\partial}{\partial x}\left(\frac{u_B \Pi_B}{g}\right) = \mathcal{M}_B. \tag{A10}$$

From the definition of mass flux, $U_A \equiv u_B \Pi_B / g$, and so (A10) is equivalent to (3.11).

Appendix 2

Derivation of the CPBL steady-state momentum equation

We begin with

$$\frac{\partial}{\partial t}\left(\frac{u_{BC}\Pi_{BC}}{g}\right) + \frac{\partial}{\partial x}\left(u_{BC}^2 \frac{\Pi_{BC}}{g}\right) = u_{B+}\mathcal{M}_{BC} - \langle\frac{\partial}{\partial x}\phi\rangle\frac{\Pi_{BC}}{g} + \mathcal{F}_{uS}, \tag{A11}$$

$$\frac{\partial}{\partial t}\left(\frac{\Pi_{BC}}{g}\right) + \frac{\partial}{\partial x}\left(\frac{u_{BC}\Pi_B}{g}\right) = \mathcal{M}_{BC}, \tag{A12}$$

which are the vertically integrated momentum and continuity equations for a well-mixed boundary layer. The metric and rotational effects have been ignored in the momentum equation since both are generally small near the equator. Such a momentum equation could be used to represent an idealized Walker circulation. In (A11), $\mathcal{F}_{uS}$ is the surface wind stress, u_{B+} is the wind velocity just above the trade inversion, and $\Pi_{BC} = p_{SC} - p_B$. Multiplying (A12) by u_{BC} and subtracting from (A11), we obtain

$$\Pi_{BC}\left(\frac{\partial u_{BC}}{\partial t} + u_{BC}\frac{\partial}{\partial x}u_{BC}\right) = g\mathcal{M}_{BC}(u_{B+} - u_{BC}) - \langle\frac{\partial}{\partial x}\phi\rangle\Pi_{BC} + g\,\mathcal{F}_{uS}. \tag{A13}$$

Since we want steady-state results, we neglect the time-rate-of-change term on the LHS of (A13) to get

$$\overset{\mathrm{I}}{-\Pi_{BC}\frac{\partial}{\partial x}\left(\frac{u_B^2}{2}\right)} + \overset{\mathrm{II}}{g\mathcal{M}_B(u_{B+} - u_B)} - \overset{\mathrm{III}}{\langle\frac{\partial}{\partial x}\phi\rangle\Pi_B} + \overset{\mathrm{IV}}{g\,\mathcal{F}_{uS}} = 0. \qquad \textbf{(A14)}$$

To determine if any terms of (A14) may be neglected, we performed an order-of-magnitude analysis. Figure A1 displays the ECMWF reanalysis monthly mean zonal wind and geopotential heights at the 925-mb pressure level for Jan 1989. From these data, we choose a typical wind speed $u_B = -6\ \mathrm{m\,s^{-1}}$, a typical kinetic energy variation of $\delta(u^2/2) = 20\ \mathrm{m^2\,s^{-2}}$ and horizontal geopotential variation $\delta\phi = 200\ \mathrm{m^2\,s^{-2}}$ over the length scale $L_x = 5\,000$ km. We specify a typical boundary-layer depth for the CP as $\Pi_B = 100$ kPa (Haraguchi 1968). With these choices, we find that the magnitude of term I is

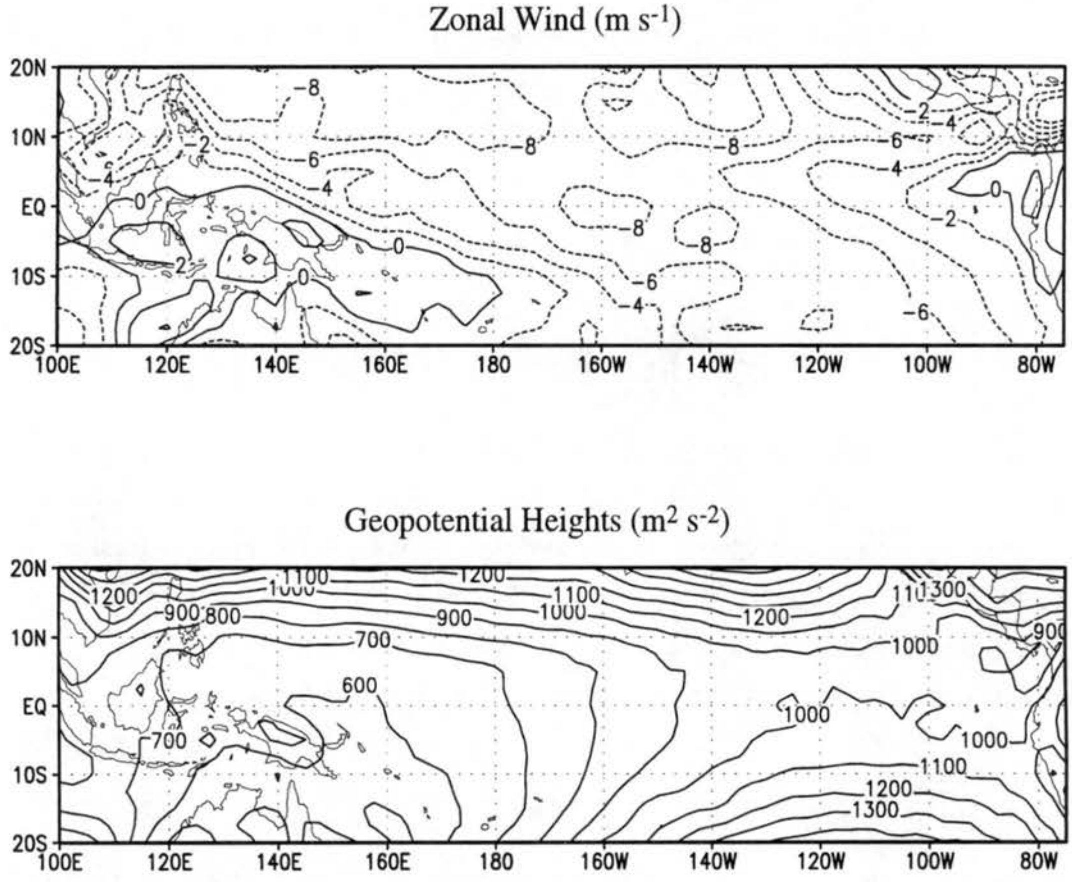

FIGURE A1: Monthly mean maps of 925-mb a) zonal wind and b) geopotential height for January 1989. Data are taken from the ECMWF reanalysis dataset.

$$-\Pi_B\frac{\partial}{\partial x}\left(\frac{u_B^2}{2}\right) \sim d_B\frac{\delta(u^2/2)}{L_x} = 4.0\times 10^{-2}. \quad \textbf{(A15)}$$

We further assume that the density ρ is 1.1 kg m^{-3}. Using (3.24) and Fig. A3.9 to estimate $g\mathcal{M}_B$, we find that terms II, III, and IV are of order 2.5×10^{-1}, 4.0×10^{-1} and 3.9×10^{-1}, respectively. Thus, we see that the primary balance is among terms II, III, and IV and the advection term (term I) is small enough to neglect. Neglecting term I gives

$$g\mathcal{M}_{BI}(u_{B+}-u_{BI}) - \langle\frac{\partial}{\partial x}\phi\rangle\Pi_{BI} + g\mathcal{F}_{uS} = 0. \quad \textbf{(A16)}$$

Appendix 3

Derivation of a general ocean mixed-layer budget

This derivation is analogous to that done in Appendix 1 for the atmosphere. Consider a conservation equation for an arbitrary variable a written in height coordinates as

$$\rho\left[\frac{\partial}{\partial t}a + \frac{\partial}{\partial x}(ua) + \frac{\partial}{\partial z}(wa)\right] = -\frac{\partial F_a}{\partial z} + S_a, \quad \textbf{(A17)}$$

where the symbols have the same meaning as in Appendix 1, and w is the vertical velocity. Integrating (A17) from z_D to z_S, we get

$$\frac{\partial}{\partial t}(\rho A\delta z_D) + \frac{\partial}{\partial x}(\rho u_O A\delta z_D) = -(F_a)_S + A_U\mathcal{M}_O + (S_A)_M\delta z_D, \quad \textbf{(A18)}$$

where $\delta z_D = z_S - z_D$, $A = (\delta z_D)^{-1}\int_{z_T}^{z_S} a dz$, u_O is the mean current of the mixed layer, A_U is the value of A in the undercurrent, $(S_A)_M$ is the vertical-mean source term in the mixed layer, and $\mathcal{M}_O$ is the mass flux through the thermocline, which is defined as

$$-\rho\left(\frac{\partial z_D}{\partial t} + u_D\frac{\partial z_D}{\partial x} - w_D\right) \equiv \mathcal{M}_O. \quad \textbf{(A19)}$$

If $\mathcal{M}_O$ is positive, then upwelling and downwelling occur in the CP and WP, respectively.

In order to derive (A18), we neglected the source terms in the layer between z_D and $z_D + \varepsilon$ and assumed that the temperature and density do not vary across depth the mixed layer. We have also assumed that no mass crosses the ocean surface.

Letting $a = 1$, (A18) gives

$$\frac{\partial}{\partial t}(\rho \delta z_D) + \frac{\partial}{\partial x}(\rho u_O \delta z_D) = \mathcal{M}_O, \tag{A20}$$

which is the mixed-layer continuity equation. Since we are looking for equilibrium solutions, we neglect the time-dependent part of (A20); and using the definition of mass flux (3.32), (A20) reduces to (3.34).

If we let $a = u$ in (A18), then a steady-state form of the zonal momentum equation is

$$\frac{\partial}{\partial x}(\rho_W {u^2}_O \delta z_D) = -(\mathcal{F}_u)_S + u_{O-}\mathcal{M}_O + \left(-\frac{\partial p}{\partial x}\right)_M \delta z_D. \tag{A21}$$

Multiplying the steady-state version of (A20) by u_O and subtracting from (A21), our zonal momentum equation finally becomes

$$\rho_W \delta z_D \frac{\partial}{\partial x}\left(\frac{{u_O}^2}{2}\right) = -(\mathcal{F}_u)_S + (u_{O-} - u_O)\mathcal{M}_O + \left(-\frac{\partial p}{\partial x}\right)_M \delta z_D. \tag{A22}$$

Appendix 4

Derivation of the CPBL pressure gradient

With the aid of the hydrostatic equation and the ideal gas law, we can show that

$$-\frac{\partial}{\partial p}\left(\frac{\partial \phi}{\partial x}\right)_p = \frac{R \partial T}{p \partial x}, \tag{A23}$$

where R is the gas constant for dry air.

We note that p decreases by about 20% between the surface and the top of the trade-wind inversion, and the temperature gradient decreases by 20 - 30% (Lindzen and Nigam 1987) over the same layer. The increase of $1/p$ compensates for the decrease of the temperature gradient over the depth of the trade-wind boundary layer. Thus, we assume that the RHS of (A23) is approximately constant with height. Integrating (A23) vertically from p_S to p_B, we find that

$$-\left(\frac{\partial \phi}{\partial x}\right)_S = -\left(\frac{\partial \phi}{\partial x}\right)_B + \Pi_B \frac{R \partial T}{p \partial x}. \tag{A24}$$

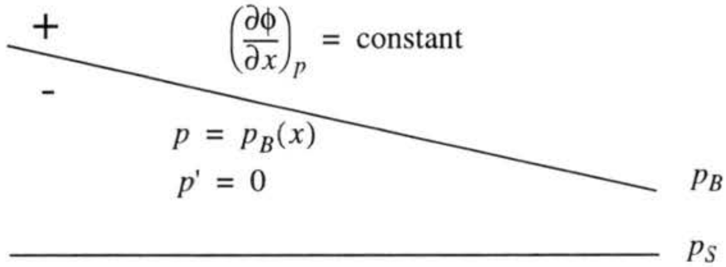

FIGURE A2: Schematic illustrating the assumptions used to derive the mean horizontal pressure gradient force in the tropical trade-wind boundary layer.

Based on ECMWF reanalyses, we assume that the geopotential gradient at the base of the TWI top is negligible compared to that the surface. Assuming that

$$-\left(\frac{\partial\phi}{\partial x}\right)_S = \Pi_{BC}\frac{R}{p_{SC}}\frac{\partial T_{SC}}{\partial x}, \qquad \textbf{(A25)}$$

which gives a reasonable estimate of the zonal pressure gradient at the surface, then the mean pressure gradient for the boundary layer follows as

$$-\left(\frac{\partial\phi}{\partial x}\right)_M = 0.5\Pi_{BC}\frac{R}{p_{SC}}\frac{\partial T_{SC}}{\partial x}. \qquad \textbf{(A26)}$$

In order to relate the mean horizontal pressure gradient force of the cold-pool boundary layer to the slope of the TWI, consider Fig. A2. Defining a new pressure coordinate as $p' \equiv p - p_B(x, t)$, then the horizontal pressure gradient force at level p is

$$\left(\frac{\partial\phi}{\partial x}\right)_p = \left(\frac{\partial\phi}{\partial x}\right)_{p'} - \frac{\partial\phi}{\partial p}\frac{\partial p_B}{\partial x}. \qquad \textbf{(A27)}$$

Applying (A27) at the top and bottom of the inversion, using the hydrostatic equation, and subtracting, we find that

$$-\left(\frac{\partial\phi}{\partial x}\right)_{p_B} + \left(\frac{\partial\phi}{\partial x}\right)_{p_{B+}} = -\left(\frac{\partial\phi}{\partial x}\right)_{p'=0} + \left(\frac{\partial\phi}{\partial x}\right)_{p'=0+} + \frac{R\Delta T}{p_B}\frac{\partial p_B}{\partial x}, \qquad \textbf{(A28)}$$

where ΔT is the jump in temperature across the inversion.

Continuity of pressure requires that $\left(\frac{\partial\phi}{\partial x}\right)_{p' = 0} = \left(\frac{\partial\phi}{\partial x}\right)_{p' = 0+}$. Thus,

$$-\left(\frac{\partial\phi}{\partial x}\right)_B + \left(\frac{\partial\phi}{\partial x}\right)_{B+} = \frac{R\Delta T}{p_B}\frac{\partial p_B}{\partial x}. \tag{A29}$$

As explained in Chapter 3, the second term on the LHS can be neglected. By methods described in Chapter 3, the slope of the TWI can be estimated, and so (A29) can be used to estimate the temperature jump across the inversion.

Appendix 5

Derivation of the ocean mixed-layer pressure gradient

We assume that the ocean is in hydrostatic balance. Integrating the hydrostatic equation, $\partial p/\partial z = -\rho_W g$, we find that the pressure in the mixed layer is given by

$$p(z) = p_S + g\rho_W(z_S - z), \tag{A30}$$

where z_S is the elevation of the ocean-atmosphere interface. We are interested in evaluating the mean pressure gradient in the mixed layer,

$$\langle\frac{\partial p}{\partial x}\rangle = \frac{1}{\delta z_D}\int_{z_D}^{z_S}\frac{\partial p}{\partial x}dx, \tag{A31}$$

where $\delta z_D = z_S - z_D$. Pulling out the derivative and using Leibniz's rule, we find that

$$\langle\frac{\partial p}{\partial x}\rangle = \frac{1}{\delta z_D}\frac{\partial}{\partial x}\int_{z_D}^{z_S} p\,dx - p_S\frac{\partial z_S}{\partial x} + p_D\frac{\partial z_D}{\partial x}. \tag{A32}$$

Substituting (A30) in (A32), evaluating the integral, and taking the derivative, we get

$$\langle\frac{\partial p}{\partial x}\rangle = \frac{\partial p_S}{\partial x} + \frac{g\delta z_D}{2}\frac{\partial\rho_S}{\partial x} - g\frac{\partial z_S}{\partial x}. \tag{A33}$$

The pressure gradient due to the atmosphere, $\partial p_S/\partial x$, is negligible compared to the other terms. Because we assume that the density depends only on temperature, and temperature in the mixed layer of the WP is horizontally uniform, the second term on the RHS is also negligible. Hence the pressure gradient is largely determined by the slope of the sea surface. The problem is that we do not really have a method to compute the sea-surface slope directly. However, we can compute the slope of the thermocline.

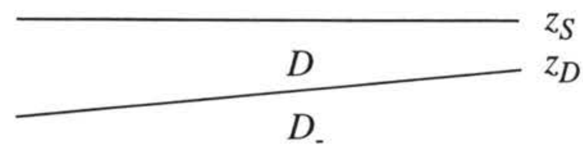

$$-\nabla_z p = 0$$

$$z = z_B(x)$$

$$z' = 0$$

FIGURE A3: Schematic illustrating the assumptions used to derive the mean horizontal pressure gradient force in the tropical-ocean mixed layer.

To derive the thermocline slope, we define a transformed coordinate as

$$z' \equiv z - z_D(x, t)\,. \tag{A34}$$

With reference to Fig. A3, the horizontal pressure gradient follows as

$$\begin{aligned}\left(\frac{\partial p}{\partial x}\right)_z &= \left(\frac{\partial p}{\partial x}\right)_{z'} - \left(\frac{\partial p}{\partial z}\right)\left(\frac{\partial z_T}{\partial x}\right); \\ &= \left(\frac{\partial p}{\partial x}\right)_{z'} + \rho g\left(\frac{\partial z_T}{\partial x}\right),\end{aligned} \tag{A35}$$

and the hydrostatic assumption has been used in the second line. The pressure gradients at levels D and D_- are given by

$$\begin{aligned}\left(\frac{\partial p}{\partial x}\right)_{z_D} &= \left(\frac{\partial p}{\partial x}\right)_D + \rho_W g\left(\frac{\partial z_D}{\partial x}\right); \\ \left(\frac{\partial p}{\partial x}\right)_{z_{D-}} &= \left(\frac{\partial p}{\partial x}\right)_{D-} + \rho_{W-} g\left(\frac{\partial z_D}{\partial x}\right).\end{aligned} \tag{A36}$$

The subscripts z_D and z_{D-} refer to quantities in z coordinates which are at depths that are just above and just below the thermocline, respectively. The D and D- subscripts refer to quantities in z' coordinates which are also slightly above and slightly below the thermocline, respectively. Subtracting the first equation from the second, and then dividing by ρ_W, we obtain

$$\frac{-1}{\rho_W}\left(\frac{\partial p}{\partial x}\right)_{z_D} = \frac{\Delta\rho}{\rho_W} g \frac{\partial z_D}{\partial x}\,, \tag{A37}$$

where $\Delta\rho = \rho_{W-} - \rho_W$. In the second of (A36), the LHS vanishes by assumption. We assume pressure continuity across the interface, and so the first terms on the RHS of each equation cancel when subtracted.

If we assume that the mixed-layer pressure gradient is independent of height, then from (A33),

$$\frac{-1}{\rho_W}\left(\frac{\partial p}{\partial x}\right)_{z_D} \approx \frac{-1}{\rho_W}\langle\frac{\partial p}{\partial x}\rangle, \tag{A38}$$

and the relationship between the thermocline slope and the sea-surface slope, (3.41), follows. To a good approximation, this relationship holds, even if there is an SST gradient.